Numerical Modeling of Geologic Carbon Dioxide Storage in Faulted Siliciclastic Settings

by

Lluís Saló Salgado

B.S. Geology, Universitat de Barcelona, 2014
M.S. Geotechnical and Earthquake Engineering, Universitat Politècnica de Catalunya, 2016

Submitted to the Department of Civil and Environmental Engineering
in partial fulfillment of the requirements for the degree of

DOCTOR OF PHILOSOPHY
IN GEOTECHNICAL AND GEOENVIRONMENTAL ENGINEERING

at the

MASSACHUSETTS INSTITUTE OF TECHNOLOGY

February 2024

Authored by:	Lluís Saló Salgado Department of Civil and Environmental Engineering September 21, 2023
Certified by:	Ruben Juanes Professor of Civil and Environmental Engineering Professor of Earth, Atmospheric and Planetary Sciences Thesis Supervisor
Accepted by:	Heidi Nepf Donald and Martha Harleman Professor of Civil and Environmental Engineering Chair, Graduate Program Committee

Numerical Modeling of Geologic Carbon Dioxide Storage in Faulted Siliciclastic Settings

by

Lluís Saló Salgado

Submitted to the Department of Civil and Environmental Engineering
on September 21, 2023 in partial fulfillment of the requirements for the degree of

DOCTOR OF PHILOSOPHY
IN GEOTECHNICAL AND GEOENVIRONMENTAL ENGINEERING

ABSTRACT

Carbon capture and storage (CCS) is a technology where CO_2 captured from point sources or the atmosphere is injected underground for permanent storage. CCS is part of a portfolio of technologies aimed at enabling the transition to a sustainable energy system with net-zero CO_2 emissions. This Thesis focuses on geologic CO_2 storage (GCS) in *faulted* siliciclastic sedimentary basins, and addresses the impact of uncertainty sources on forecasts of CO_2 migration made with physics-based numerical models. A key contribution of this work is the quantification of uncertainty on fault petrophysical properties and modeling of flow within clay-smeared faults, which play a central role on CO_2 storage effectiveness and safety.

We start by extending a reservoir simulator to increase fidelity in 3D numerical models of GCS. Extensions include a thermodynamic model to calculate PVT properties of CO_2-brine mixtures and relative permeability hysteresis. We then conduct numerical simulations and experiments of CO_2 injection and migration at the meter scale. Our experiments use tanks with transparent panels that allow recreating realistic basin geometries and CO_2 injection protocols. Using direct observations, we find that local measurements reduce model calibration time and that accurate deterministic forecasts are challenging. Next, recognizing the impact of faults on subsurface flow and shortcomings of previous models of fault architecture and hydraulic properties, we propose a probabilistic method to estimate the directional components of the fault permeability tensor. We extend previous efforts by modeling the fault core in 3D, using flow-based upscaling, and quantifying uncertainty. We then move to the field scale and apply this method to forecast fault CO_2 migration in the Miocene section offshore Texas. Faults are common in this area, and it is crucial to understand how they may limit storage capacity. Our modeling results indicate that, due to subsurface structure, stratigraphy and fault hydrogeology, updip CO_2 migration in listric growth faults is unlikely.

Our findings show that quantitative forecasts are uncertain due to limited subsurface knowledge and modeling choices. Efforts to quantify parameter uncertainty and its impact on modeling forecasts appear necessary, a task that requires development of reduced order models accounting for the limitations of simulation data. Forecasts based on numerical models will benefit from history-matching and updating as field data becomes available.

Thesis supervisor: Ruben Juanes
Title: Professor of Civil and Environmental Engineering
Professor of Earth, Atmospheric and Planetary Sciences

To my parents, Joan and Camino
My brother, Manel
And my partner, Riley

Contents

List of Figures xi

List of Tables xv

Acknowledgments xvii

1 Introduction 1
- 1.1 Background . . . 1
- 1.2 Goals and Outline . . . 2

2 Three-Dimensional Simulation of Geologic Carbon Dioxide Sequestration using `MRST` 4
- 2.1 Introduction . . . 4
- 2.2 Generation of PVT Data for Black-oil Models . . . 7
  - 2.2.1 Calculation of phase composition and PVT output . . . 7
  - 2.2.2 `MRST` example . . . 10
- 2.3 Relative Permeability Hysteresis . . . 13
  - 2.3.1 Killough's (1976) model . . . 14
  - 2.3.2 Implementation for use in `ad-blackoil` . . . 14
  - 2.3.3 `MRST` example: validation with the PUNQ-S3 model . . . 17
- 2.4 Molecular Diffusion . . . 19
  - 2.4.1 Mathematical model . . . 19
  - 2.4.2 Implementation for use in `ad-blackoil` . . . 20
  - 2.4.3 `MRST` example: the effect of CO_2 diffusion on convective fingers . . . 21
- 2.5 Discussion . . . 23
- 2.6 Summary . . . 25

3 Direct Comparison of Numerical Simulations and Experiments of CO_2 Injection and Migration in Geologic Media: Value of Local Data and Forecasting Capability 26
- 3.1 Introduction . . . 27
- 3.2 Physical Experiments . . . 28
  - 3.2.1 Sand petrophysical properties . . . 29
  - 3.2.2 Experimental setup . . . 30
  - 3.2.3 Porous media geometries . . . 31

3.2.4 Experimental injection schedule . . . 31
3.3 Numerical Simulations . . . 31
3.3.1 Model setup . . . 31
3.3.2 Simulation model . . . 34
3.3.3 Model calibration . . . 38
3.4 Results . . . 40
3.4.1 Initial model results . . . 40
3.4.2 Manual history matching and value of local data . . . 40
3.4.3 Transferability: model forecasts . . . 46
3.5 Discussion . . . 50
3.6 Conclusions . . . 52

4 Fault Permeability from Stochastic Modeling of Clay Smears 58
4.1 Introduction . . . 58
4.2 Stochastic Computation of Fault Permeability . . . 59
4.3 Results and Discussion . . . 61
4.3.1 Validation with experimental fault-scale permeability . . . 61
4.3.2 Clay smear modeling leads to multimodal fault permeability distributions 61
4.3.3 Stratigraphic controls on fault permeability . . . 62
4.3.4 Fault clay fraction and permeability . . . 62
4.3.5 Fault permeability uncertainty and anisotropy . . . 64
4.4 Application to Fault Permeability Modeling in Real Settings . . . 64
4.5 Conclusions . . . 65

5 Updip Migration of Sequestered CO_2 along Gulf Coast Miocene Growth Faults is Unlikely 66
5.1 Introduction . . . 67
5.2 Fault Hydraulic Properties . . . 69
5.2.1 Fault permeability structure in unlithified siliciclastic sequences . . . 69
5.2.2 Faults in continuum numerical models of multiphase flow . . . 70
5.2.3 Fault multiphase petrophysics from stochastic modeling of clay smears 71
5.2.4 Simulation cases . . . 74
5.3 Numerical Simulations . . . 74
5.3.1 Computational grid and formation properties . . . 74
5.3.2 Fluids and setup . . . 76
5.4 Results . . . 77
5.4.1 Continuous vs discontinuous top seal . . . 77
5.4.2 Stochastic clay smear modeling . . . 78
5.5 Discussion . . . 80
5.6 Summary and Conclusion . . . 83

6 Conclusions and Future Work 85

A Additional Analysis of Numerical Simulation Results (Ch. 3) **88**
A.1 Additional Analysis of Simulation Model Concordance with Experiment B1 . 88
A.1.1 Results with initial model parameters 88
A.1.2 Calibrated models 89
A.2 Nonlinear Solver Number of Iterations 92
A.3 Comparison of Simulation Results with Multiple Grid Resolutions 94

B Detailed description of PREDICT (Ch. 4) **98**
Nomenclature for Appendix B 98
B.1 PREDICT: PeRmEability DIstributions of Clay-smeared faulTs 100
B.1.1 Concept, initial assumptions and validation 100
B.1.2 Intermediate variables 103
B.1.3 Smear dimensions and placement 106
B.1.4 Upscaling 108
B.2 Assessment of PREDICT's Behavior 110
B.2.1 Convergence analysis 110
B.2.2 Uncertainty propagation 111
B.2.3 Sand connectivity 115
B.3 Kettermann et al.'s (2017) Experimental Permeability Calculation 117
B.3.1 Computation hydraulic conductivity from normalized flux measurements 120
B.3.2 Computation of intrinsic permeability from hydraulic conductivity . . 121

C Methods (Ch. 5) **122**
Nomenclature for Ch. 5 and Appendix C 122
C.1 Upscaling of fault multiphase flow properties 124
C.1.1 Relative permeability 124
C.1.2 Capillary pressure 125
C.2 SGR modeling of base cases 127

References **129**

List of Figures

2.1 Supercritical CO_2 trapping mechanisms . . . 6
2.2 Predicted CO_2 coefficients . . . 9
2.3 Predicted mutual solubilities at 30, 60 and 90 °C for 0-4 molal sodium chloride brines . . . 9
2.4 Comparison to results by Hassanzadeh et al. (2008) . . . 10
2.5 CO_2 density and viscosity . . . 10
2.6 Pure water, brine and CO_2-saturated aqueous phase properties . . . 11
2.7 Phase density and viscosity in `MRST` . . . 12
2.8 Illustration of bounding gas relative permeability curves . . . 13
2.9 Comparison to results by Juanes et al. (2006) . . . 18
2.10 FluidFlower porous medium and grid used in the diffusion example . . . 22
2.11 Results of convective mixing with multiple pseudo-diffusivities . . . 23

3.1 Overview of the FluidFlower rigs and porous media used in the experiments 29
3.2 Simulation grids overview . . . 33
3.3 Multiphase flow properties for Model 1 . . . 36
3.4 Multiphase flow properties for Model 2 . . . 38
3.5 Multiphase flow properties for Model 3 . . . 38
3.6 Front panel view of Tank 1, showing quantities and times for history matching of numerical models to Experiment A1 . . . 39
3.7 Comparison between Experiment A1 in Tank 1 and results of initial simulation 41
3.8 Convergence of areal quantities during model calibration with Experiment A1 42
3.9 Convergence of mean absolute error over the six areal quantities . . . 43
3.10 Concordance between successive model iterations and the experiment . . . 43
3.11 Convergence of finger migration times . . . 44
3.12 Comparison between Experiment A1 and simulation results with Model 3 . . . 46
3.13 Comparison between Experiment A2 and simulation results with Model 3 . . . 47
3.14 Comparison of areal quantities for Experiment A2 . . . 48
3.15 Comparison between Experiment B1 and Model 1 (end of injection) . . . 54
3.16 Comparison between Experiment B1 and CO_2 concentration maps for simulation models 1-3 . . . 55
3.17 Comparison of areas occupied by each phase during the first 72h of case B1 . 56
3.18 Wasserstein distances to experiments and forecasts (simulations) . . . 57

4.1 `PREDICT` workflow . . . 60

4.2 Validation with experimental data . . . 61
4.3 Effect of increasing section average clay fraction . . . 62
4.4 Stratigraphic controls on fault permeability . . . 63

5.1 Geology and simulation grid . . . 68
5.2 Fault zone architecture in soft siliciclastic sequences . . . 69
5.3 Application of PREDICT to model fault porosity and permeability . . . 72
5.4 Multiphase fluid properties . . . 73
5.5 Overview of gas saturation for S1C1 . . . 78
5.6 Overview of gas migration within the fault . . . 79
5.7 Overview of gas migration in S2C2 . . . 80
5.8 CO_2 migration summary . . . 81
5.9 Buoyancy pressure and fault permeability, and dependence of fault permeability on effective stress . . . 83

A.1 Comparison between Experiment B1 in Tank 2 and models 1-3 (initial parameters) . . . 89
A.2 Ratios between model (A_{M_i}) and experimental mean (A_E) areas occupied by each phase . . . 90
A.3 Wasserstein distances to experiments and forecasts (simulations) (initial models) 92
A.4 Total mass of CO_2 for our simulations of Experiment B1 presented in sect. 3.4.3 92
A.5 Mass of CO_2 in Boxes A and B defined in Fig. 3.1e, for our simulations of Experiment B1 presented in sect. 3.4.3. . . . 93
A.6 Ratios between calibrated model (A_{M_i}) and experimental mean (A_E) areas occupied by each phase in case B1 . . . 94
A.7 Number of iterations and maximum values for various quantities . . . 95
A.8 Concentration maps from our simulations of Experiment A1 with Model 3 . . . 96
A.9 Concentration maps from simulations of Experiment B1 with Model 3 . . . 97

B.1 Clay smears . . . 101
B.2 Clay smear placement algorithm . . . 107
B.3 Convergence of upscaled permeability with respect to cell size . . . 111
B.4 Convergence of upscaled permeability with respect to cell aspect ratio . . . 112
B.5 Convergence of upscaled permeability with respect to number of realizations 113
B.6 Fault displacement over thickness. . . . 114
B.7 Along-strike smear segment number . . . 114
B.8 Residual friction angle as a function of increasing clay volume fraction. . . . 114
B.9 Clay smear porosity . . . 114
B.10 Critical shale smear factor . . . 115
B.11 Porosity for sand-based materials . . . 116
B.12 Permeability of clay smears . . . 116
B.13 Permeability of sand-based materials . . . 117
B.14 Permeability anisotropy ratio . . . 118
B.15 Correlation between intermediate variables . . . 119
B.16 Relative clay smear dimensions . . . 119

B.17 Sand connectivity 120

C.1 Application of PREDICT to model fault multiphase flow properties 126
C.2 Mapping of fault properties for the base cases 128

List of Tables

3.1 Petrophysical properties of sands used in the experiments 30
3.2 Experimental CO_2 injection schedules 32
3.3 Initial porosity and permeability for Model 1 35
3.4 Petrophysical properties of quartz sands in simulations of Experiment A1 . . 45

5.1 Summary of simulation cases and methods for estimating fault properties . . 75
5.2 Formation pore compressibilities, porosities and permeabilities 76

A.1 Sparse data comparison between Experiment B1 in Tank 2 and simulation results with models 1-3 91

B.1 Mean absolute error of log permeability distributions 112

C.1 Results of capillary pressure and relative permeability upscaling 125

Acknowledgments

As I reflect on my academic journey, I realize that many people have contributed to this work, either directly or indirectly. Although it will certainly not be possible to properly describe their actions in the next few paragraphs, I aspire to at least convey my deep sense of gratitude towards them.

I would like to start by thanking my advisor, Ruben Juanes. He gave me the unusual opportunity to pursue graduate studies at MIT, and patiently but consistently has guided me throughout my PhD journey. He has provided a wonderful group environment, invaluable research opportunities, and infinite knowledge on multiphase flow and geomechanics. Ruben has been an incomparable teacher and compassionate mentor, and given me the tools to foster independent thought. His actions speak loudly about his graciousness and confidence, two character traits that undoubtedly make him a great leader. Without him, I would not be the person that I am today, nor would I be able to enjoy the phenomenal academic opportunities that lie on the road ahead. Muchas gracias, Rubén!

My doctoral committee members have been an important influence and a source of inspiration. I am thankful to Herbert Einstein for his encouragement, mentorship, and unwavering support since I arrived to MIT. I admire Brad Hager for his ability to ask the important questions, and his comments have helped me transmit the key aspects of my research. Jan Nordbotten is always one (or many) steps ahead, and I am much more aware of the limitations of numerical models thanks to him. Jan also opened the doors to his research group and collaborators at the University of Bergen (UiB) and NORCE, and my experience in Norway was truly rewarding. I am grateful for the opportunity to work with all of you, and I hope fruitful collaborations await us ahead!

The members of the Juanes Research Group, past and present, have all been kind colleagues and friends. At the risk of forgetting a name, I want to personally thank those with whom I shared an office, in no specific order: Ruby Fu, Amir Pahlavan, Josimar Silva, Jane Chui, Aziz Beljadid, Ehsan Haghighat, Ke Xu, Rebecca Liyanage, Antoine Jacquey, Wei Li, Hannah Lu, Bauyrzhan Primkulov, Maryam Alghannam, Yu Qiu, Olivia Meng, Ruofei Jia and Yury Alkhimenkov. I have dear memories from all of them, which will make me look fondly on my PhD journey in the future. I would also like to acknowledge Josimar, Bauyrzhan, Maryam, Yu and Ehsan for the last few years—it is not easy to remain close after a pandemic. I am indebted to Josimar and Catherine for their assistance during my time in Houston in the summer of 2022. Thanks for always being there! I am also truly grateful to Roberta Pizzinato for taking care of us.

Other friends and collaborators of JRG have also shaped my experience at MIT. Andrés Soage taught me the importance of knowledge breadth, personal connections and family.

David Santillán was extremely supportive and kind in the initial stages of my research. David Castiñeira showed me the importance of choosing the right approach based on time available, and helped me make the most of my internship in Houston. Mike Fehler has always been generous with his time and willing to help me understand earthquakes. Working with my mentee Runako Gentles has been a joyful experience. I wish I can remain in touch with all of you in the future.

My personal and professional development, as well as the work presented in this Thesis, would not have been possible without close collaboration with stellar individuals and groups. I am grateful for the opportunity to work with Josimar Silva, Ehsan Haghighat and Hannah Lu. I appreciate Ganesh Dasari's confidence in me, support and practical advice; Steve Davis' passion for faults and top seals, which sparked my fascination for the topic; and Lisa Lun's support and insight on multiphase flow properties. Malin Haugen and Kris Eikehaug welcomed me in the lab at UiB in the midst of the FluidFlower international study, and provided continuous support and advice. Those days (and nights) are among my best memories from the last few years. Olav Møyner and Knut-Andreas Lie have provided exceptional support with the `MRST` flow simulator, and I am grateful for their altruism. Watching Olav write code was an incredible experience.

I am indebted to the Carbon Storage Team at ExxonMobil for a fulfilling internship in the summer of 2022. That period helped me grasp the importance of being efficient without compromising the quality of my work. I want to thank Jamie White for the opportunity, my mentors Ganesh Dasari, Steve Morgan, Jon Meissner and Jenny Zhang for their guidance and care, Alana Leahy-Dios and Lisa Lun for always looking out for me, and Christie Rogers for gripping conversations on faults. Their commitment towards making a difference was inspiring to see, and I hope that our interactions continue in the future. I also want to express my gratitude to Alana and Pavel for their hospitality.

I have been fortunate to learn from exceptional faculty, at MIT and elsewhere, who stimulated my intellectual curiosity. I wish to express my gratitude to Antonios Vytiniotis, Andrew Whittle, Anthony Patera, Desirée Plata and Youssef Marzouk (MIT), Brendan Meade and John Shaw (Harvard), and Martin Fernø (UiB).

The people at CEE Headquarters have provided outstanding academic support. I would like to extend my appreciation to Kiley Clapper and Sarah Smith for their tremendous help on navigating MIT, empathy and care, and to Max Martelli for always being ready to answer my questions.

I am grateful to MIT Civil and Environmental Engineering for funding through a "Michael F. Parlamis (1962) and Goldberg-Zoino (1954) Combined Fellowship", the MIT Energy Initiative for an "Eni-MIT Energy Fellowship", The MathWorks, Inc. and the MIT School of Engineering for a "MathWorks Engineering Fellowship", and to "La Caixa" Foundation for a postgraduate fellowship. "La Caixa" Foundation, in particular, has provided invaluable networking opportunities and support, and I am much obliged for the work they do to help students achieve their academic dreams.

My academic advisors in Barcelona played a pivotal role in my ability to pursue graduate studies in the US, and have continued to support me along the way. I will always be grateful to Emma Suriñach for her encouragement and belief in me, to Lluís Pujades for his humanity, mentorship and scientific insight, to Tànit Frontera for her uninterrupted help and wise advice, to Xavier Goula for his scientific passion, and to Jordi Corominas and Nieves

Lantada for giving me the opportunity to work with them and guiding me along the way. I also want to thank Milford Edge for making the process of learning English an enjoyable and simple one. I would not be where I am today without them.

My friends at MIT have enriched my graduate student experience. Ferran Vidal, Àlex Armengol and Ferran Lozano provided me a home away from home; 73 Prince St and its frigid living room will always have a special place in my heart. Ferran Vidal has given me wise advice, and helped me make some important decisions over the last few years. Àlex Armengol has always been there and we have shared many laughs together. Dani Rodan welcomed me to Cambridge and has always ensured that I am connected to the incredible Spanish community in Boston. The members of Spain@MIT and friends of the association have always given me a much appreciated smile. Rafael Villamor, Ignacio Arzuaga, Mariana Rodriguez, Katya Boukin, Sidhant Pai and Nicolas Chanut have provided camaraderie and helped me see the bright side. My friends at home have all been a source of happiness. I would like to name Carlos Torreblanca, Raül Sala, Òscar Roselló and Erola Anglada for checking on me, time and again.

My family has given me unconditional love. I am beholden to my parents, Joan and Camino, for showing me the value of effort and for encouraging me to puruse a PhD in the US. My passion for scientific knowledge, academic rigor and optimism is in no small part thanks to them. My brother Manel has been a pillar in my life and provided a much needed and unmatched sense of humor. To the three of them: This Thesis, and what will come next, is also the result of your perseverance and kindness, and I hope you remember it. I am also thankful for each and every member of my extended family; in particular, I would like to express my gratitude to Lola, Jordi, Anna, Clara, Carmen and Lluís for their affection.

Finally, I want to thank my partner, Riley, for sharing her life with me. Riley has been an endless source of support and has put me first whenever I needed it. Her intelligence and grace are too good for this world, as is her love for cats and our planet. Our time together has brought me a great deal of happiness and helped me find a sense of purpose. Riley, you are the greatest gift of my life, and I hope I can enrich your life as profoundly as you enriched mine. I would like to close by mentioning her parents, Matthew and Jill, for making me feel part of their family since day one. Their care has made a difference in my life.

This is a wonderful day, I have never seen this one before.
Maya Angelou

Chapter 1

Introduction

1.1 Background

CO_2 capture and subsequent geologic carbon dioxide storage (GCS) is a climate-change mitigation technology that can be deployed at the scale necessary to significantly offset current anthropogenic CO_2 emissions, especially in combination with so-called negative emission technologies (IPCC 2005; EASAC 2018; IEA 2021; IPCC 2022). Globally, GCS projects currently store about 30-40 Megatons (Mt) per year (Zhang et al. 2022), which is three orders of magnitude lower than global energy-related CO_2 emissions, which are on the order of 35 Gt/y (IEA 2021). To achieve the climate goals of keeping anthropogenic warming to 1.5°C or less and net-zero CO_2 emissions by mid-century, it has been suggested that GCS capacity needs to increase by about 2 orders of magnitude in the next few decades (IEA 2021; IPCC 2022). Such growth in the GCS industry has been labeled "unprecedented" and "dramatic" (Krevor et al. 2023; Zoback and Smit 2023).

In the past two decades, advances in the field of GCS have been made using theory (e.g., Bachu et al. 1994; Hesse et al. 2008; MacMinn et al. 2010; MacMinn et al. 2011; Hidalgo et al. 2012; Szulczewski et al. 2012; Szulczewski et al. 2014), experiments (e.g., Bennion and Bachu 2008; Pentland et al. 2011; MacMinn and Juanes 2013; Zhao et al. 2016; Qiu et al. 2023), and computer simulation (e.g., Juanes et al. 2006; Hassanzadeh et al. 2007; Birkholzer and Zhou 2009; Cappa and Rutqvist 2011; Hidalgo et al. 2012; Nordbotten et al. 2012; Fu et al. 2015; Wallace et al. 2017; Zhao et al. 2019). This has provided a fundamental understanding of CO_2 behavior in the subsurface, including its interaction with other subsurface fluids and its potential hazards. Importantly, these studies have extended our knowledge of the physics of CO_2 migration and trapping (Bachu et al. 1994; Juanes et al. 2006; MacMinn et al. 2010; MacMinn et al. 2011; Hidalgo et al. 2012; Szulczewski et al. 2013; Krevor et al. 2015) and the storage capacity of geologic formations (Birkholzer and Zhou 2009; Szulczewski et al. 2012; Bachu 2015; Treviño and Meckel 2017). This wealth of knowledge supports the scientific consensus that, under appropriate storage conditions, current understanding of GCS allows for safe deployment of the technology (Bickle 2009; Celia et al. 2015; Bourzac 2017).

Physics-based numerical models, used as either the primary tool to make forecasts (Silva et al. 2023), a development tool for reduced order models (Pawar et al. 2016), or a training/testing tool for machine-learning frameworks (Ju et al. 2019; Lu et al. 2023), remain our

primary means to assess subsurface CO_2 migration. Development of free and open-source software (e.g., Mills et al. 2007; Flemisch et al. 2011; Lie 2019; Keilegavlen et al. 2021; Rasmussen et al. 2021; Cusini et al. 2022) is promoting widespread access and multidisciplinary innovation: Numerical models are increasingly able to incorporate, realistically, complex geologic features such as faults (Karimi-Fard et al. 2004; Fredman et al. 2007; Silva et al. 2023), simulate timescales up to thousands of years (Gasda et al. 2011; Lie et al. 2016; Nilsen et al. 2016), and handle resource-intensive numerical schemes required when considering coupled physics (Cappa and Rutqvist 2011; Jha and Juanes 2014; Landa-Marbán et al. 2021; Meguerdijian et al. 2022; Silva et al. 2023). In recent years, experimental and field observations of subsurface CO_2 migration (Arts et al. 2004; White 2009; Eiken et al. 2011; Trevisan et al. 2014; Krishnamurthy et al. 2022; Flemisch et al. 2023) and the induced geomechanical response (Verdon et al. 2013; Stork et al. 2015; Silva et al. 2021b) have become available, which has built confidence in physics-based predictive models. However, achieving accurate (or concordant; see Oldenburg 2018) forecasts of subsurface CO_2 migration using numerical models continues to be challenging due to uncertainty (Nordbotten et al. 2012; Flemisch et al. 2023).

Predictions of subsurface CO_2 migration are uncertain due to (i.) limitations of the mathematical and numerical models (Nordbotten et al. 2012; Flemisch et al. 2023); (ii.) the absence, more often than not, of a ground truth to assess numerical model concordance; and (iii.) incomplete knowledge of physical property distribution in the subsurface (cf. Einstein and Baecher 1982). The latter is especially true for geologic faults, which offset sedimentary layers and lead to volumes where the host material is altered to varying degrees (Caine et al. 1996; Faulkner et al. 2010; Bense et al. 2013; Fossen and Rotevatn 2016; IEAGHG 2016). Subsurface measurements of fault properties are rare, but faults are common in the subsurface and control flow at the reservoir to basin scales (Smith 1966; Person et al. 1996; Jolley et al. 2007; Myers et al. 2007). Previous experience with subsurface energy technologies has exposed the hazards of induced seismicity (Zoback and Gorelick 2012; Juanes et al. 2012; Vilarrasa and Carrera 2015; Alghannam and Juanes 2020; Silva et al. 2021a; Silva et al. 2021b; Hager et al. 2021) and fault CO_2 migration, which may lead to leakage into overlying units or the seafloor (Caine et al. 1996; Ingram and Urai 1999; Revil and Cathles III 2002; Jung et al. 2014; Bond et al. 2017). It is therefore critical to improve knowledge of fault properties to safely deploy GCS at the Gigaton scale (e.g., IEAGHG 2016; Vrolijk et al. 2016).

1.2 Goals and Outline

Following our discussion above, in this Thesis we address (i.) by extending an existing flow simulator to increase fidelity (ch. 2), (ii.) by evaluating concordance between meter-scale GCS simulations and direct experimental observations (ch. 3), and (iii.) by developing a new methodology to quantify uncertainty in fault permeability (ch. 4), and applying it to evaluate the potential of fault CO_2 migration at the field scale (ch. 5). Our overarching goal is, therefore, to develop computational tools to evaluate uncertainty in GCS, including improved characterization of uncertainty sources and their effect on numerical modeling forecasts of CO_2 migration. Due to important differences in the physical mechanisms governing CO_2

migration in different geologic settings, we limit the scope of our research to siliciclastic basins and two fluid phases (brine and CO_2). The latter is a reasonable choice, given that most of the capacity for large-scale GCS deployment is provided by saline aquifers (Szulczewski et al. 2012; de Coninck and Benson 2014; Ringrose and Meckel 2019).

In chapter 2, we present three extensions to the `ad-blackoil` module of the open-source MATLAB Reservoir Simulator Toolbox (`MRST`; Lie 2019). These include a thermodynamic model for the calculation of phase composition and PVT properties of CO_2-brine mixtures; a saturation-history dependent model for the relative permeability of CO_2; and a diffusion model to describe the transport of dissolved CO_2 in brine due to concentration gradients. These tools increase fidelity in 3D simulation models of GCS using `MRST`, which is the main software used in this Thesis. This chapter is being prepared for publication as a research article (Saló-Salgado et al. 2023c).

In chapter 3, we conduct meter-scale CO_2 injection experiments in the FluidFlower rigs. The FluidFlower concept is a meter-scale laboratory tank with transparent panels that allows recreating realistic basin geometries and CO_2 injection and monitoring protocols, including direct observation of CO_2 migration. First, we use experimental data to history-match or calibrate our numerical model. Next, we apply the calibrated model to different settings, and test the predictions against new experimental results that the model has not seen. This allows us to evaluate, quantitatively, the value of local petrophysical measurements and the forecasting capability of numerical models of GCS. This chapter appeared as a research article in *Transport in Porous Media* (Saló-Salgado et al. 2023b).

In chapter 4, we develop a new methodology (`PREDICT`) to estimate the main directional components (dip-perpendicular, strike-parallel and dip parallel) of the fault permeability tensor. Our methodology is applicable to normally-consolidated siliciclastic sequences, which are common in passive margins worldwide and relevant for large-scale GCS. Due to the probabilistic nature of our methodology, the output is a probability distribution for each directional component of the fault permeability tensor. This work extends previous fault permeability algorithms by considering three-dimensions, accounting for anisotropy and quantifying uncertainty; results were validated with experimental data from cm-scale faults. This chapter appeared as a research article in *Geology* (Saló-Salgado et al. 2023a).

In chapter 5, we study fault CO_2 migration in Miocene-age sediments offshore Texas. This area is a promising candidate for industrial-scale GCS given adequate geology, proximity to CO_2 emission sources, and infrastructure provided by decades of hydrocarbon exploration and production. However, faults are common, and it has been shown that they may limit capacity. We conduct CO_2 storage simulations in a field-scale model representative of the Miocene geology, and assess where the CO_2 migrates to after injection next to a fault zone, which represents a very unfavorable scenario. Our evaluation is based on a sensitivity analysis of CO_2 migration to fault petrophysical properties that are uncertain. This chapter is being prepared for publication as a research article (Saló-Salgado et al. 2023d).

Finally, in chapter 6, we briefly summarize the main findings of this Thesis and research opportunities in the context of GCS in faulted siliciclastic basins. We anticipate that multidisciplinary research will be needed to deploy GCS at the scale proposed by mid-century net-zero pathways.

Chapter 2

Three-Dimensional Simulation of Geologic Carbon Dioxide Sequestration using MRST

This chapter is being prepared for publication as a research article (Saló-Salgado et al. 2023c).

Abstract

Physics-based computational modeling of subsurface CO_2 migration constitutes the primary tool to assess geologic CO_2 storage (GCS). Such models are often required to plan injection operations and assess hazards such as CO_2 migration into units above the storage formation. Here, we present three tools developed to increase accuracy of GCS models in the `ad-blackoil` module of the MATLAB Reservoir Simulation Tooblox (`MRST`). These tools include functionality to (1) calculate and output PVT properties of miscible brine and CO_2 as a function of pressure, temperature and salinity; (2) account for relative permeability hysteresis, necessary to model residual trapping; and (3) model CO_2 transport due to concentration gradients (molecular diffusion). We validate our implementation with published results including experimental observations, present `MRST` examples, and conclude with some remarks on applicability, limitations and potential extensions. Source code and examples are provided.

2.1 Introduction

The MATLAB Reservoir Simulation Toolbox (`MRST`) (Lie et al. 2012; Krogstad et al. 2015; Lie 2019) is an open-source software that includes multiple discretization schemes for simulation of multiphase flow in porous media. MATLAB is well suited for rapid prototyping, and `MRST` has been extensively used to implement novel models of subsurface flow (e.g., Ranaee et al. 2019; Landa-Marbán et al. 2021; Lie and Møyner 2021; Wang et al. 2023). `MRST` currently provides two main methods for simulation of field-scale geologic carbon sequestration (GCS):

- Vertical-equilibrium (VE) models for analysis of structural trapping and long-term,

large-scale migration assuming an instantaneous vertical equilibrium between brine and gas (e.g., Nilsen et al. 2015; Lie et al. 2016; Nilsen et al. 2016; Møyner and Nilsen 2019).

- Full-scale solvers (such as `ad-blackoil` or `compositional`) for a more traditional approach to three-dimensional reservoir simulation (e.g., Ranaee et al. 2019; Landa-Marbán et al. 2021; Silva et al. 2023).

The main advantge of VE models is that they reduce the problem of CO_2 migration to two dimensions. This relaxes the requirements for detailed subsurface data, and can speed computation by multiple orders of magnitude. As a result, VE models are particularly useful for regional-scale studies and preliminary exploration or probabilistic assessments (e.g., Gasda et al. 2011; Szulczewski et al. 2012; Celia et al. 2015; Nilsen et al. 2016). Detailed analysis of well placement and CO_2 migration in a specific trap system, however, often requires dynamic simulations that honor subsurface heterogeneity and complex 3D structure.

The migration of a subsurface CO_2 plume is driven by the interplay of buoyancy and pressure gradients (Benson et al. 2005; Krevor et al. 2023) (Fig. 2.1). While buoyant CO_2 rises within the storage formation (SF), it does not reach the surface due to trap systems including a caprock or top seal, faults bounding the storage system and folds (*structural* and/or *stratigraphic trapping*) (Bachu et al. 1994; Bryant et al. 2008; Hesse and Woods 2010; Li and Benson 2015; Saló-Salgado et al. 2023b). Upon reaching the SF top or interbedded capillary barriers, the CO_2 plume spreads laterally and continues its gravity-driven migration updip the storage formation, a process that can cover several kilometers and last hundreds of years or more, depending on geology (Gasda et al. 2011; Boait et al. 2012; Szulczewski et al. 2013; Jackson and Krevor 2020; Silva et al. 2023). As the plume migrates inside the SF, resident brine re-occupies pores previously filled with CO_2; this process, termed secondary imbibition, leads to CO_2 trapping in the form of blobs and ganglia when CO_2 saturation is low enough. This trapping mechanism is known as *residual* or *capillary trapping* (Juanes et al. 2006; Burnside and Naylor 2014). A fraction of injected CO_2 will dissolve in the brine, leading to *solubility* or *dissolution trapping*. The aqueous mixture of saline water and CO_2 is denser than the resident brine and sinks, thereby increasing storage security (Ennis-King and Paterson 2005; Riaz et al. 2006; Hidalgo and Carrera 2009; MacMinn et al. 2011; Neufeld et al. 2010; Szulczewski et al. 2012; Saló-Salgado et al. 2023b). Finally, CO_2 can react with solid grains in the subsurface, which may precipitate carbonate minerals that permanently trap the CO_2 in solid phase (*mineral trapping*) (Bachu et al. 1994; Snæbjörnsdóttir et al. 2020). The first three mechanisms are active in sedimentary basins during operational timescales; the importance of mineral trapping depends on the composition of the trap system and typically increases with time (Benson et al. 2005; Snæbjörnsdóttir et al. 2020; Krevor et al. 2023)(Fig. 2.1b).

The importance of different physical mechanisms on numerical simulations of CO_2 storage has been the subject of much research over the past two decades, and it is beyond the scope of this paper to summarize the state of the art at large. However, some relevant examples include Juanes et al. (2006), who showed that relative permeability hysteresis plays a major role in the migration of CO_2 in an anticline reservoir; Hidalgo and Carrera (2009) described accelerated CO_2 dissolution due to hydrodynamic dispersion; Saadatpoor et al.

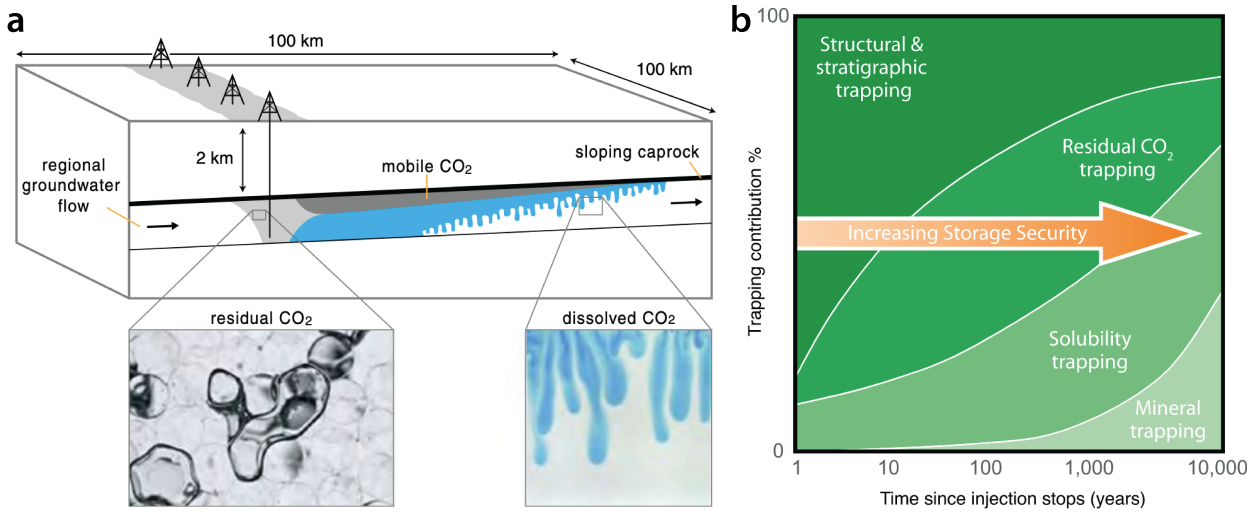

Figure 2.1: Supercritical CO_2 trapping mechanisms. **a**: Schematic of a sloping saline aquifer where CO_2 is injected through an array of wells. As mobile CO_2 migrates updip due to buoyancy (dark grey), brine imbibes at the trailing edge of the plume, immobilizing CO_2 blobs (see inset), and part of the CO_2 dissolves in brine, triggering a Rayleigh-Taylor instability where CO_2-rich brine sinks (see inset). From Szulczewski et al. (2012). **b**: Contribution of different storage mechanisms as a function of time. Post CO_2 injection, the risk of CO_2 leakage decreases due to lower relative contribution of structural and stratigraphic trapping, with respect to the other three mechanisms. From Benson et al. (2005).

(2010) included local capillary heterogeneity within the injection layer, which led to inhomogeneous CO_2 rise and reduced invaded volume; Landa-Marbán et al. (2021) demonstrated that calcite precipitation leads to sealing of migration pathways; Flemisch et al. (2023) and Saló-Salgado et al. (2023b) compared multiple simulation models to experimental observations in a m-scale laboratory setup, and they showed that relatively small changes in PVT and multiphase flow properties can result in significantly different CO_2 migration. Outcomes from these studies and many others strongly suggest that the CO_2-brine system can be very sensitive to variations in subsurface properties and trapping mechanisms. Therefore, developing numerical models of GCS that include all relevant physics for a given geology and spatiotemporal scale is an important research area.

In this paper, we describe three extensions to the `MRST` automatic differentiation (AD) simulators, in particular the `ad-blackoil` module, developed to increase fidelity in simulation of 3D GCS. Specifically, sect. 2.2 describes the implementation of a thermodynamic model to calculate PVT properties of CO_2-brine mixtures for black-oil simulators (see chapters 8.2.3 and 11 in Lie 2019); sect. 2.3 details the modeling of saturation-path dependent relative permeability (hysteresis); and sect. 2.4 provides an implementation of molecular diffusion. Lastly, in sect. 2.5 we discuss the range of applicability and limitations of the models presented. Scripts and input files necessary to reproduce the examples presented in sect. 2.2, 2.3, and 2.4 are available at https://github.com/lsalo/mrst-adblackoil-gcs. The code has been tested with the `MRST` development version as well as the 2023a release.

2.2 Generation of PVT Data for Black-oil Models

Compositional reservoir simulators are widely used to accurately predict complex phase behavior in multicomponent models (Chang et al. 1998). In compositional simulation, equations of state (EOS) are employed to calculate the phase distribution and fluid properties in each grid cell. A black-oil simulator can be viewed as a specific, simple case of a compositional model with two or three pseudo-components, where miscibility properties are modeled as a function of pressure (P) changes only (Aziz and Settari 1979; Møyner 2021). Typically, the gas component can be present in either the oleic or gaseous phase, whereas the oil and water components exist only in their respective phases (Lie 2019, chapter 11). To simulate GCS in CO_2-brine systems, the oleic phase can be modeled as a brine, so that the main component in the gas phase (now CO_2) can dissolve in it. As shown below, it is also possible to consider vaporization of water in the gas phase. Black-oil models often use tabulated input data to speed up calculations, and, due to their simplicity, can be significantly more efficient than general compositional models (Hassanzadeh et al. 2008).

In `MRST`, the `ad-blackoil` module (Bao et al. 2017 and Lie 2019, chapter 11) provides industry-standard reservoir simulation capabilities using black-oil models. For example, the module incorporates functionality for using external, pre-compiled linear solvers such as AMGCL (Demidov and Rossi 2018; Lie 2019) and ECLIPSE-type input decks, and has been used to simulate geologic carbon storage at spatial scales ranging from the laboratory to the field (e.g., Silva et al. 2023; Flemisch et al. 2023; Saló-Salgado et al. 2023b). In this section, we summarize (1) the implementation of a thermodynamic model for calculation of CO_2-brine PVT properties, (2) the preparation of output data in ECLIPSE (SLB 2014a) format, compatible with `MRST`'s `ad-blackoil` module, and (3) usage in `MRST`. Our implementation follows the detailed description by Hassanzadeh et al. (2008), with a few modifications as described below.

2.2.1 Calculation of phase composition and PVT output

The composition of CO_2-brine mixtures is calculated based on the thermodynamic models presented by Duan and Sun (2003), Spycher et al. (2003), and Spycher and Pruess (2005), and it is valid up to $\approx$ 100 °C and $\approx$ 600 bar. Similar to Spycher and Pruess (2005) and Hassanzadeh et al. (2008), equilibrium relationships by Spycher et al. (2003) are used in combination with the activity coefficient formulation of Duan and Sun (2003) to determine the mole fractions of CO_2 and H_2O in the aqueous and gas phases, respectively. With this formulation, we can consider mixing between CO_2 and aqueous solutions of common species such as NaCl, KCl or $CaCl_2$, as well as seawater/brines. Our implementation of the solubility model and calculation of input quantities required for black-oil simulations (brine formation volume factor and gas-oil solution ratio) follows Hassanzadeh et al. (2008); this includes the assumptions of constant salinity and infinite dilution of H_2O in the gas phase to compute fugacity coefficients (Spycher et al. 2003), the Redlich-Kwong equation of state (EoS) (Redlich and Kwong 1949) to compute gas molar volumes, Rowe and Chou (1970) to compute brine density, Garcia (2001) to compute CO_2-saturated aqueous phase density, and Fenghour et al. (1998)'s model for CO_2 viscosity. Therefore, instead of repeating the

lengthy formulation, we provide the code and validation figures below, and note the following aspects of our implementation:

- Given that CO_2 solubility in water is low, Hassanzadeh et al. (2008) considered that the salt mole fraction in the aqueous phase (x_{salt}) remains constant. We default to this option, but, as shown below, an option to include the effect of dissolved CO_2 can be used.

- To calculate the density (ρ) of water-salt solutions (brine), a later correlation by Batzle and Wang (1992) can be used to expand the P, temperature (T) validity range (Rowe and Chou 1970 is for $P < 350$ bar).

- The dynamic viscosity (μ) of the aqueous phase accounts for CO_2 dissolution, in addition to P, T and salinity (S). Similar to the density, we assume that the S effect on aqueous phase viscosity can be modeled by considering a single salt species (NaCl), and use the model presented by Islam and Carlson (2012).

- As mentioned before, the dynamic viscosity of pure CO_2 is calculated using Fenghour et al. (1998) (we neglect the critical enhancement term). The viscosity of the gaseous phase (which may contain vaporized water) is obtained via Davidson (1993)'s model for ideal gas mixtures; differences with respect to pure CO_2 are $\leq 2\%$ at $T, P \in [30, 100]$ °C, $[80 - 400]$ bar. We note, however, that experimental viscosity data for supercritical CO_2-rich mixtures in the P, T range of interest was not found (Munkejord et al. 2016).

Although not our primary goal, vaporization of H_2O in the CO_2-rich phase is considered in the solubility model. Therefore, we can use similar arguments to those presented by Hassanzadeh et al. (2008) for the aqueous phase, and compute the vaporized oil-gas ratio (R_{v}) and gas formation volume factor (B_{g}) as follows:

$$R_{\text{v}} = \frac{V^{\text{s}}_{\text{vH2O}}}{V^{\text{s}}_{\text{CO2}}} = \frac{y_{\text{H2O}}\overline{\rho}^{\text{s}}_{\text{CO2}}}{\overline{\rho}^{\text{s}}_{\text{H2O}} y_{\text{CO2}}} \tag{2.1}$$

$$B_{\text{g}} = \frac{V^{\text{r}}_{\text{g}}}{V^{\text{s}}_{\text{CO2}}} = \frac{\rho^{\text{s}}_{\text{CO2}}}{\rho^{\text{r}}_{\text{g}}(1 - v_{\text{H2O}})} \tag{2.2}$$

where V, y, v, $\overline{\rho}$ and ρ are volume, mole fraction in the gas phase, mass fraction in the gas phase, molar density, and mass density, respectively; subscripts v and g refer to vaporized and gas phase, respectively; and superscripts s and r refer to standard (defined here according to ECLIPSE (SLB 2014a), i.e., 1 atm and 15.56 °C) and reservoir conditions, respectively. Because $y_{\text{H2O}} \leq 1 - 2\%$ at storage P, T, we consider $\rho_{\text{g}} \sim \rho_{\text{CO2}}$ and take ρ_{CO2} from the Redlich-Kwong EoS. This simplification is reasonable based on available experimental data by King et al. (1992) and Hebach et al. (2004), who report changes smaller than experimental uncertainty for P, T up to 300 bar and 60 °C.

Validation plots are provided in Fig. 2.2, 2.3, 2.4, 2.5, and 2.6.

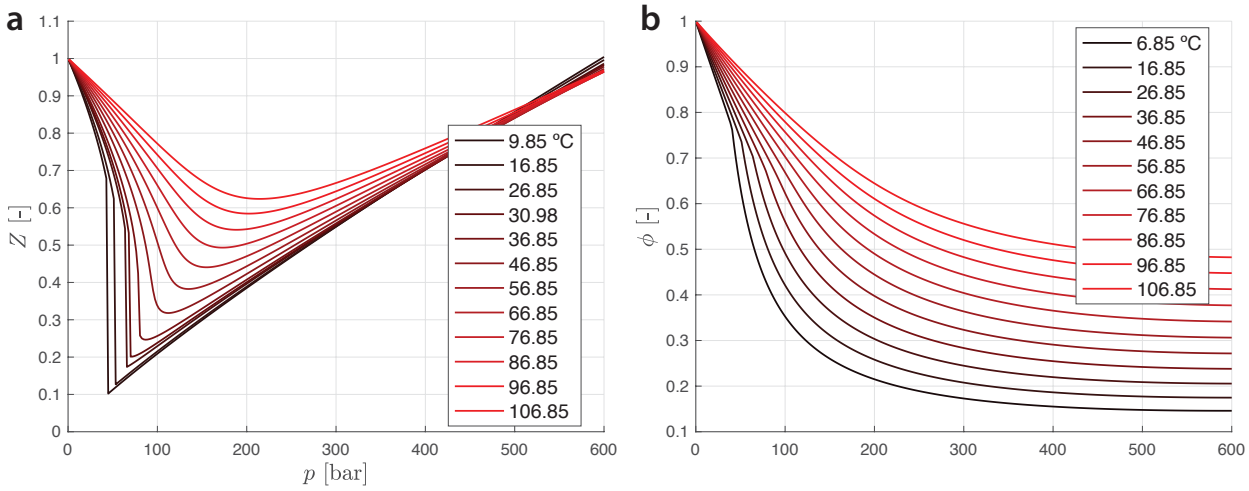

Figure 2.2: Predicted CO_2 coefficients. **a** Compressibility factor (Z; cf. Fig. 8 in Spycher et al. 2003). **b** Fugacity coefficient (ϕ; cf. Fig. 9 in Spycher et al. 2003).

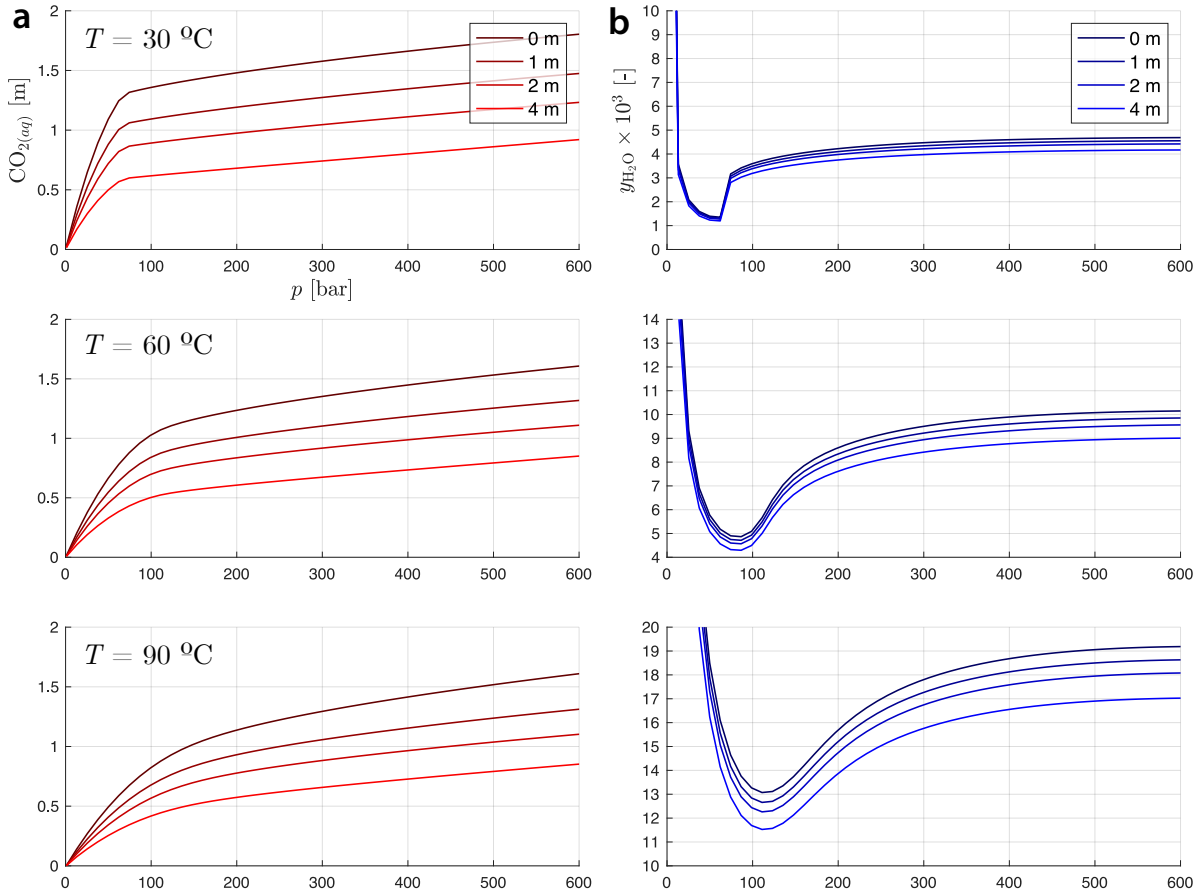

Figure 2.3: Predicted mutual solubilities at 30, 60 and 90 °C for 0-4 molal sodium chloride brines. Solubilities are expressed as molality of CO_2 in the aqueous phase (**a**) and 1000 × mole fraction of H_2O in the gas phase (**b**). Cf. Fig. 2 in Spycher and Pruess (2005).

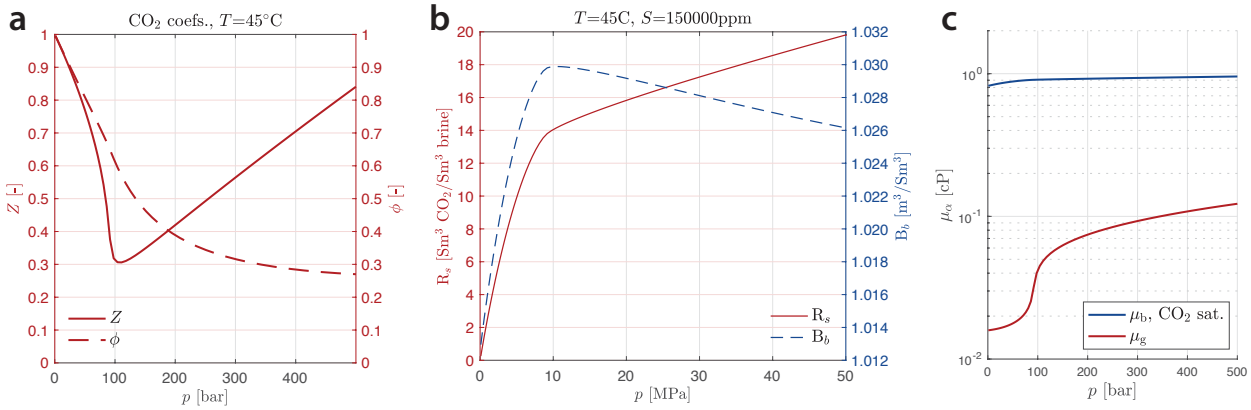

Figure 2.4: Comparison to results by Hassanzadeh et al. (2008). **a** Gas compressibility factor and fugacity coefficient (cf. their Fig. 5c). **b** Gas-oil solution ratio (R_s) and brine formation volume factor (B_b; cf. their Fig. 5a). **c** Dynamic viscosities (μ) neglecting water vaporization (cf. their Fig. 5b,d). There are minor differences in brine viscosity with respect to Fig. 5b in Hassanzadeh et al. (2008), because they neglect the effect of dissolved CO_2.

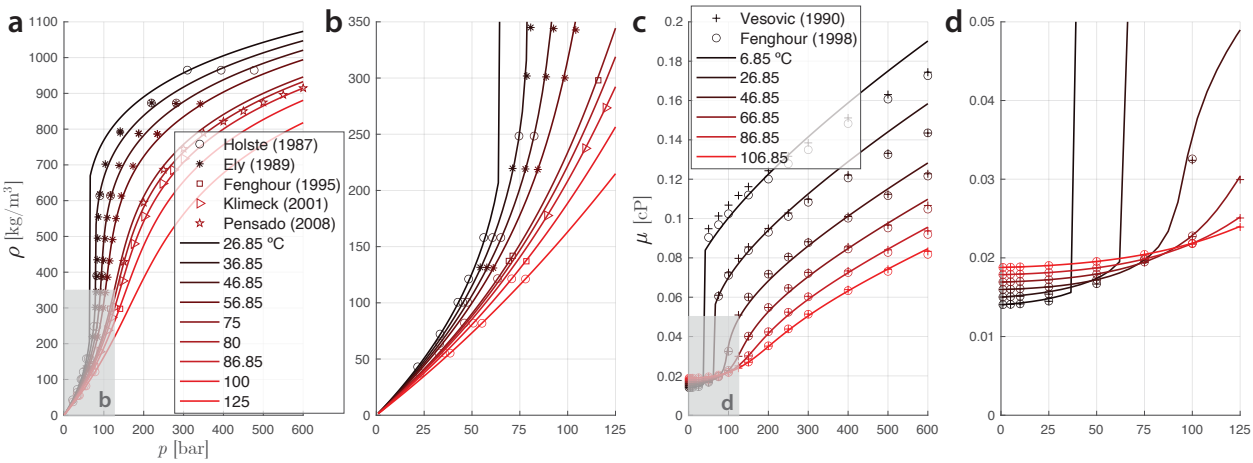

Figure 2.5: CO_2 properties. **a,b** Density compared to measurements by Holste et al. (1987), Ely et al. (1989), Fenghour et al. (1995), Klimeck et al. (2001), and Pensado et al. (2008). **c,d** Viscosity compared to tabulated data by Vesovic et al. (1990) and Fenghour et al. (1998).

2.2.2 `MRST` example

The thermodynamic model described above is implemented in the function `pvtBrineWithCO2BlackOil.m`, which has the following syntax:

```
[t, rho_co2_s, rho_brine_s] = pvtBrineWithCO2BlackOil(T, P, S, saltVar, vapH2O, unsatVals, figs, ↩
    directory);
```

`T`, `P`, and `S` indicate the temperature, pressure range and salinity, respectively. `saltVar`, `vapH2O`, `unsatVals` and `figs` are boolean variables indicating whether the change in salt mole fraction due to CO_2 dissolution into the brine should be accounted for, whether vaporized water should be considered, whether undersaturated values should be provided, and whether

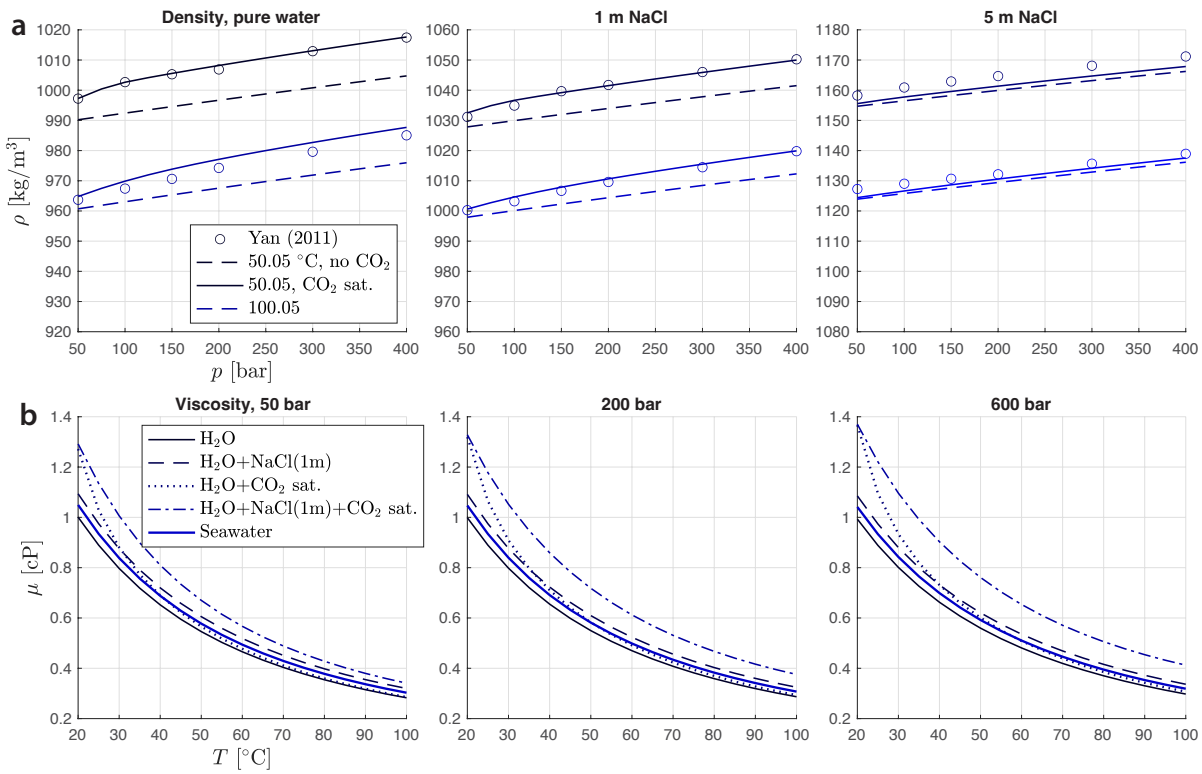

Figure 2.6: Pure water, brine and CO_2-saturated aqueous phase properties. **a** Density as a function of P at $T = 323.2$, 373.2 K compared to experimental measurements by Yan et al. (2011) (see their Fig. 14, 15 and 16). **b** Viscosity as a function of T, shown at $P = 50$, 200 and 600 bar (cf. Fig. 7 by Islam and Carlson 2012).

figures should be plotted, respectively. `directory` is an optional input indicating the path where the output should be saved. Variable outputs include a table with all properties of interest for the gas and brine phase (`t`), and the surface densities of both phases at standard conditions. The function is well documented and interested users should refer to the code for full reference.

In `MRST`, fluid properties are specified by the `fluid` object, which tells the simulator which models should be used. In `ad-blackoil` models, the following properties need to be specified to model fluid PVT behavior (see ch. 11.4 in Lie 2019, for a detailed description): surface densities (ρ_α^{s}), formation volume factors (B_α), and solution gas-oil ratio (R_{s}), where α denotes a generic phase. Optionally, R_{v} (see sect. 2.2.1) may be given if oil vaporization into the gas is accounted for. Viscosities (μ_α) are also specified in the `fluid` object. As noted above, to simulate GCS in saline aquifers we assign brine properties to the oil phase and CO_2 properties to the gas phase. Using these inputs, reservoir densities and viscosities of the oleic and gas phases are computed as (e.g., Lie 2019):

$$\rho_o = b_{\mathrm{o}}(\rho_{\mathrm{o}}^{\mathrm{s}} + R_{\mathrm{s}}\rho_{\mathrm{g}}^{\mathrm{s}}) \tag{2.3}$$

$$\rho_g = b_{\mathrm{g}}(\rho_{\mathrm{g}}^{\mathrm{s}} + R_{\mathrm{v}}\rho_{\mathrm{o}}^{\mathrm{s}}) \tag{2.4}$$

Where, in Eq. 2.3, 2.4, we have introduced the reciprocal factors $b_{\mathrm{o}} = 1/B_{\mathrm{o}}$ and $b_{\mathrm{g}} = 1/B_{\mathrm{g}}$,

which are used by MRST.

The script example_props details how to create a fluid object with all required PVT properties. To this end, we use pvtBrineWithCO2BlackOil to generate tabulated data suitable for an ECLIPSE-type input deck (SLB 2014a). In particular, specifying directory when running pvtBrineWithCO2BlackOil will generate one text file for each phase, which can be copied into the input .DATA file, under the PROPS section, using the appropriate keywords (PVTO and PVDG or PVTG). ECLIPSE .DATA files are the main input system in the ad-blackoil module (see ch. 11.5 in Lie 2019). The fluid structure is then easily obtained:

```
% Read deck: fn is the .DATA file name
deck = convertDeckUnits(readEclipseDeck(fn));
% Generate fluid
fluid = initDeckADIFluid(deck);
```

Following Eq. 2.3, and 2.4, we can recover phase densities as:

```
rho_co2     = fluid.rhoGS*fluid.bG(p_val);   % Dry gas (no water)
rss_val     = fluid.rsSat(p_val);            % Live oil (with CO2)
rho_b_sat   = fluid.bO(p_val,rss_val,true(np,1)) .* (rss_val.*fluid.rhoGS + fluid.rhoOS);
rho_b       = fluid.rhoOS*fluid.bO(p_val,zeros(np,1),false(np,1));
```

Where p_val is a $n \times 1$ vector with the pressure values, and np $= n$. Viscosities are obtained as:

```
mu_co2      = fluid.muG(p_val);
mu_b_sat    = fluid.muO(p_val,rss_val,true(np,1));  % CO2 saturated
mu_b        = fluid.muO(p_val,zeros(np,1),false(np,1));
```

Fig. 7 shows the phase densities and viscosities for the example in example_props, where it can be seen that the values recovered from the fluid object are accurate to the tabulated output given by pvtBrineWithCO2BlackOil.

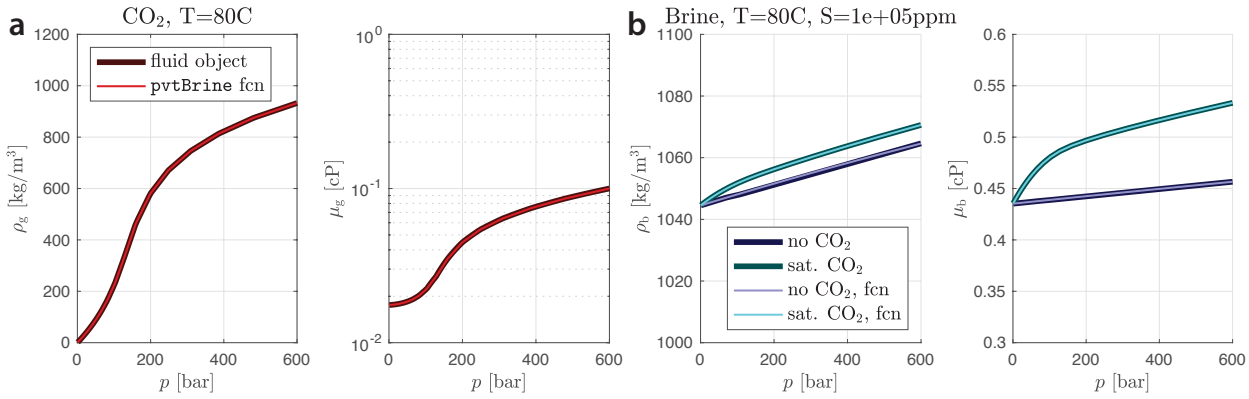

Figure 2.7: Phase density and viscosity as computed from the fluid object (thick solid lines, see main text) and the output of pvtBrineWithCO2BlackOil. Vaporization was not considered in this example. **a** CO_2. **b** brine.

2.3 Relative Permeability Hysteresis

When $n > 1$ fluid phases are present in a porous medium, such as in GCS, the volumetric flux of a given phase ($\underline{u}_\alpha$, [L·T^{-1}]) is given by the multiphase version of Darcy's law (Muskat 1949):

$$\mathbf{u}_\alpha = -\frac{\boldsymbol{k} k_{\mathrm{r}_\alpha}}{\mu_\alpha}(\nabla p_\alpha - \rho_\alpha g \nabla z) \tag{2.5}$$

Where $k_{\mathrm{r}_\alpha}(S_\alpha) \in [0, 1]$ is the relative permeability, a quantity introduced to account for the effect of multiple fluid phases in reducing the flow of a given phase α, depending nonlinearly on the saturation (S_α) (Muskat 1949; Aziz and Settari 1979). Due to pore-scale mechanisms including contact angle hysteresis and disconnection of the non-wetting phase during imbibition, relative permeability depends on the saturation path and saturation history, in addition to the current saturation (see Juanes et al. 2006). In most subsurface aquifers, CO_2 will be the non-wetting phase (Iglauer et al. 2015); therefore, accounting for relative permeability hysteresis is necessary to accurately model CO_2 migration and trapping during GCS, especially during the post-injection stage (Juanes et al. 2006).

Relative permeability hysteresis models use a primary drainage and bounding imbibition curve to compute scanning curves in successive drainage and imbibition cycles, a process illustrated in Fig. 2.8 (Juanes et al. 2006). Several models have been described in the literature (e.g., Killough 1976; Carlson 1981; Lenhard and Parker 1987; Blunt 2000; Spiteri et al. 2008), with reservoir simulators typically using either Killough's (Killough 1976) or Carlson's (Carlson 1981) model for two-phase flow. Because there are two fluid phases during CO_2 storage in saline aquifers, in this work we use the model by Killough (Killough 1976), following the implementation in ECLIPSE (Juanes et al. 2006; SLB 2014b).

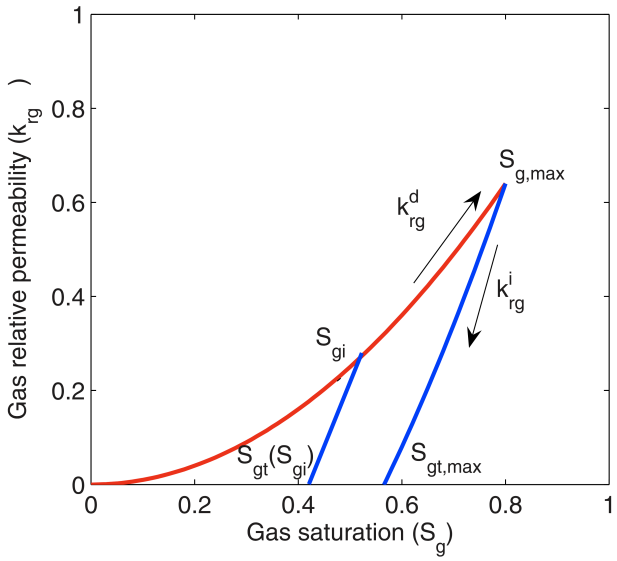

Figure 2.8: Illustration of the primary drainage curve (red), bounding imbibition curve (to the right, blue) and scanning curve (in the middle, blue), as well as the Land's (Land 1968) trapping model parameters. Extracted from (Juanes et al. 2006).

2.3.1 Killough's (1976) model

Consider the relative permeability of the nonwetting phase. Here, this is the CO_2-rich phase, which we refer to as the gas phase (subscript g). While current saturation (S_g) is below the maximum historical saturation (S_{gi}), the relative permeability along a scanning curve is computed as follows (Eq. 2.6, Fig. 2.8):

$$k^{i}_{rg}(S_g) = k^{ib}_{rg}(S^*_g)\frac{k^{d}_{rg}(S_{gi})}{k^{d}_{rg}(S_{g,max})} \tag{2.6}$$

Where k^{ib}_{rg} and k^{d}_{rg} refer to the bounding imbibition and drainage curves, respectively. $S_{g,max}$ is the maximum gas saturation, i.e. one minus the irreducible water saturation. S^*_g is the normalized saturation:

$$S^*_g = S_{gt,max} + \frac{(S_g - S_{gt})(S_{g,max} - S_{gt,max})}{S_{gi} - S_{gt}} \tag{2.7}$$

Where $S_{gt,max}$ is the maximum gas trapped saturation associated with the bounding imbibition curve. The trapped gas saturation for the current scanning curve, S_{gt}, is computed based on Land (1968)'s model:

$$S_{gt} = S_{g,min} + \frac{S_{gi} - S_{g,min}}{1 + C(S_{gi} - S_{g,min})} \tag{2.8}$$

Where $S_{g,min}$ is the minimum gas saturation along the primary drainage curve ($S_{g,min} = 0$ in Fig. 2.8, to be consistent with the reservoir formation being saturated with brine before CO_2 injection). The Land trapping coefficient C is computed as:

$$C = \frac{1}{S_{gt,max} - S_{g,min}} - \frac{1}{S_{g,max} - S_{g,min}} \tag{2.9}$$

This model assumes that scanning curves are reversible, i.e. the same formulation is used during tertiary drainage as long as $S_g < S_{gi}$. As noted by Juanes et al. (2006), the bounding imbibition curve can be obtained from experiments, similar to the primary drainage curve, or following Land (1968) (their Eq. 6). Killough (Killough 1976) also provided a model for the wetting phase relative permeability hysteresis. However, because hysteresis effects in the wetting phase are usually less important (Juanes et al. 2006, and references therein), we limit this work to hysteresis effects in the nonwetting phase.

2.3.2 Implementation for use in `ad-blackoil`

Here, we summarize our implementation. This is provided to facilitate understanding as well as encourage extensions and modifications. Readers planning to use the current implementation via existing `.DATA` input decks can directly skip to sect. 2.3.3. Readers planning to modify `.DATA` input decks or use alternative fluid property input methods should read sect. 2.3.2 before moving to sect. 2.3.3. Note that this implementation uses Killough (1976)'s model (sect. 2.3.1) and is limited to gas phase relative permeability hysteresis (gas is assumed to be the nonwetting phase). Moreover, our implementation is currently limited to two-phase water-gas (immiscible) or oil-gas (miscible) black-oil models.

Input of hysteresis options

Typically, the hysteresis option is specified as part of an input `.DATA` file, which is the main input system in `ad-blackoil` (refer to ch. 11.5 in (Lie 2019) and (SLB 2014a) for details, and the `.DATA` input files on GitHub). This requires adding the following to the `.DATA` file:

1. The item `'HYSTER'` under the keyword `SATOPS` in the `RUNSPEC` section
2. The keyword `EHYSTR` in the `PROPS` section. This keyword should be followed by a line with items `0.1 2 1.0 0.1 KR` terminated by `/`. In ECLIPSE, each of these items is used to specify different options for both capillary pressure and relative permeability hysteresis. In the present implementation, only items two and four are used: Item two indicates the hysteresis model, and therefore must be equal to 2 (Killough's (Killough 1976) model for the nonwetting phase). Item four is used in the implementation of Eq. 2.8 to improve convergence (sect. 2.3.2), and should be 0.1 in most cases (default value).
3. Bounding imbibition relative permeability curves using the appropriate keywords (`SWFN`, `SGFN`, `SGOF`, etc), also in the `PROPS` section. Note that, adding imbibition curves increases the number of saturation tables, so items under the keyword `TABDIMS` in the `RUNSPEC` section may need to be updated.
4. `IMBNUM` keyword, in the `REGIONS` section, followed by a set of lines specifying the cells pertaining to each imbibition region. Optionally, this can be added manually to the `rock` object, as shown below.

The example described in sect. 2.3.3 uses the `CASE2.DATA` input deck, provided by Juanes et al. (2006), where these options are used. The `fluid` object is generated as shown in sect. 2.2.2 and 2.3.3, which will automatically add the flag `fluid.krHyst = 1`. This flag indicates that relative permeability hysteresis is active in all cells (all model regions). If hysteresis is desired in a subset of model regions only, `krHyst` should be modified with an array of size $n \times 1$, where each entry is an imbibition region number (corresponding to the unique values in `rock.regions.imbibition`) where hysteresis is active.

Alternatively, if the `fluid` and `rock` objects (Lie 2019) are generated without an input deck, hysteresis options and flags can be added manually, e.g.:

```
fluid.ehystr = {0.1, 2, 1, 0.1};
fluid.krHyst = 1;   % 1 (all) or subset of imb regions for hysteresis
nreg = max(rock.regions.saturation);
rock.regions.imbibition = rock.regions.saturation + nreg;
```

Hysteresis can also be deactivated in any given run by removing the field `krHyst` or setting it to 0.

Code structure and location

Implemented changes can be subdivided in the following three groups:

1. Input deck processing. This refers to changes needed to read `.DATA` input decks with hysteresis specifications (`EHYSTR` keyword in `PROPS` section).

2. Assignment of the scanning curve model to the fluid object. This refers to adding scanning curve functions to the `fluid` object.

3. Updating the relative permeability state function in `model.FlowPropertyFunctions`, so that the hysteresis model is used during the simulation.

Accordingly, the code is implemented in the corresponding `MRST` modules:

`deckformat`
A new case `'EHYSTR'` is added within the function `readPROPS`. This enables `assignEHYSTR` (in the `ad-props` module) to handle the `EHYSTR` keyword in the input deck.

`ad-props`

- The function `assignEHYSTR`, called under `initDeckADIFluid`, assigns hysteresis options and flags to the `fluid` object (see example in sect. 2.3.3). The flag `fluid.krHyst` will be automatically set to 1 (hysteresis active in all cells) if hysteresis is requested in the input deck. However, as described in sect. 2.3.2, this flag can be modified to use hysteresis in a region subset only.

- The function `addScanKr` adds the scanning curves in the field `fluid.krGi`. As noted above, this currently uses Killough (1976)'s model and is limited to gas phase relative permeability. A slight modification to Killough's model is added to improve convergence, as described in sect. 2.3.2.

`ad-core`
Hysteretic relative permeabilities are handled by the state function `HysthereticRelativePermeability` (see ch. 11 in Lie 2019 and ch. 5 in Lie and Møyner 2021 for `MRST`'s black-oil model structure). This class incorporates the method `evaluatePhaseRelativePermeabilityWithHysteresis`, which checks for the `krHyst` flag in the fluid object, and uses the appropriate relative permeability model where hysteresis is active. This is currently limited to two-phase water-gas (immiscible) or oil-gas (miscible) black-oil models, defined using the `GenericBlackOilModel` class.

Modifications and safeguards

Our implementation within `addScanKr` uses a modification to Eq. 2.8, introduced to improve convergence as done in ECLIPSE (SLB 2014b):

$$S_{\mathrm{gt}} = S_{\mathrm{g,min}} + \frac{S_{\mathrm{gi}} - S_{\mathrm{g,min}}}{A + C(S_{\mathrm{gi}} - S_{\mathrm{g,min}})} \tag{2.10}$$

Where $A = 1 + a(S_{\mathrm{g,max}} - S_{\mathrm{gi}})$. ECLIPSE uses a default value of $a = 0.1$ (SLB 2014b), but the user can specify a different value as described in sect. 2.3.2.
The function `addScanKr` also ensures the following:

- $k_{\mathrm{rg}}^{\mathrm{i}}(S_{\mathrm{g}}) \leq k_{\mathrm{rg}}^{\mathrm{d}}(S_{\mathrm{g}})$
- The minimum tolerance for flow reversal was set to 10^{-3}. This means that unless $S_{\mathrm{g}} + 10^{-3} < S_{\mathrm{gi}}$, the drainage curve is used.
- Unless $S_{\mathrm{gi}} > S_{\mathrm{gh}} + S_{\mathrm{g,min}}$, the drainage curve is always used. S_{gh} is the third input variable in `addScanKr`, which must be provided by the user. Typically, $S_{\mathrm{gh}} = O(10^{-2})$.

2.3.3 MRST example: validation with the PUNQ-S3 model

We validate our implementation using the PUNQ-S3 geologic model example. The PUNQ-S3 represents a three-dimensional reservoir with heterogeneous permeability and anticlinal structure, and has been described in detail by Floris et al. (2001). Juanes et al. (2006) used an adapted version of this model to elucidate the impact of relative permeability hysteresis on GCS, which we reproduce. The model has 1761 active cells, and represents a good compromise between a lightweight setup that can be run quickly on a standard laptop, and a realistic storage aquifer. CO_2 injection is conducted during 10 y using eight wells operating at a reservoir volume rate of 18 rm^3/day each. After the initial 10 y, CO_2 migration continues until $t = 500$ y. In this example, CO_2 and water are considered immiscible. A detailed description of this case is provided by Juanes et al. (2006) (sect. 3).

This example is run using the script `kr_hyst_example`, available on GitHub along with the `CASE2.DATA` input deck. The key statements to run this model with nonwetting phase relative permeability hysteresis are shown below. Note that the statements to add hysteresis in the `fluid` and `model` structures in the following two code listings will be automatically processed in future `MRST` releases. However, we provide them here for consistency with the present implementation, and as a guide to specify the hysteresis model without ECLIPSE input. First, the `fluid` structure is generated using the input deck, and the functionality to compute scanning curves is added:

```
% fn = 'path/to/CASE2.DATA'
deck = convertDeckUnits(readEclipseDeck(fn));
fluid = initDeckADIFluid(deck);
fluid.krHyst = 2;   % imb reg where hysteresis is active (all)
minSat = 0.02;      % saturation threshold for hysteresis activation
fluid = addScanKr(fluid, rock.regions.imbibition, minSat);
```

In this case, there is a single fluid region containing all active cells. Therefore, `rock.regions.saturation = ones(G.cells.num, 1)`. Here, the field `rock.regions.imbibition` is directly assigned to the `rock` object using the input deck. The model and relative permeability state function are defined as:

```
% Use deck to select model
model = selectModelFromDeck(G, rock, fluid, deck);
% Set up the state function groups
model = model.validateModel();
% Update relperm state function
model.FlowPropertyFunctions = ...
model.FlowPropertyFunctions.setStateFunction('RelativePermeability', HystereticRelativePermeability(↩
    model));
```

Once the model setup is complete, we run the simulation using `simulateScheduleAD` or `simulatePackedProblem` (refer to ch. 11 in Lie 2019). We compared our solution with results presented by Juanes et al. (2006), which were obtained with the commercial simulator ECLIPSE 100 (SLB 2014a). Results are shown in Fig. 2.9, which indicates excellent agreement between the two models.

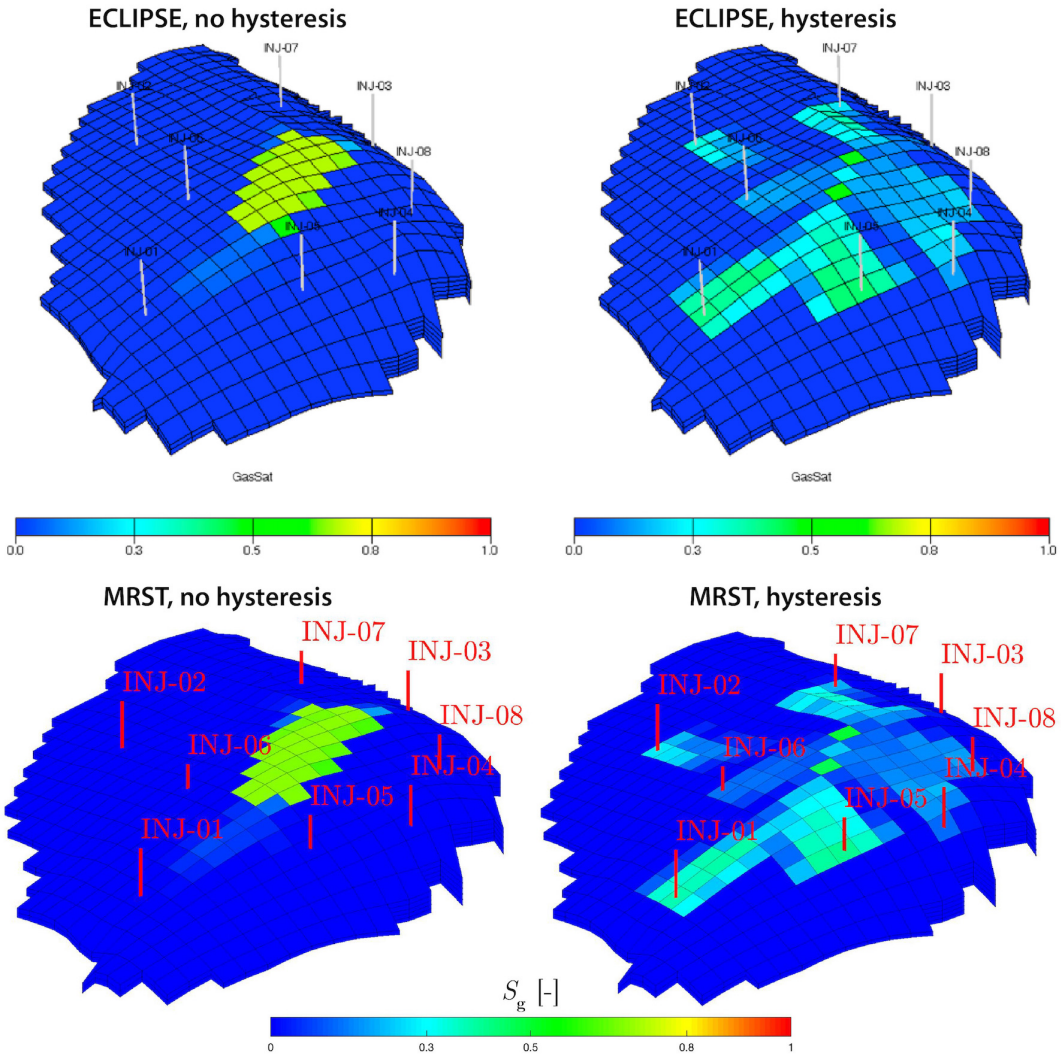

Figure 2.9: CO_2 saturations after 500y. Top row results are from Juanes et al. (2006) (obtained using ECLIPSE 100). Bottom results are with the described implementation in MRST. Left column shows results for case 1 (no hysteresis), while right column shows results for case 2 (hysteresis).

2.4 Molecular Diffusion

When $n > 1$ components are present in a fluid phase, concentration gradients will result in transport of molecules from higher to lower concentration regions. Accordingly, the total macroscopic flux will be given by the advective flux associated with the movement of the fluid phase, as well as the diffusive flux associated with molecular transport within the fluid phase (Bear 1972). Typically, molecular diffusion between components is not accounted for in black-oil models (e.g., Lie 2019); as we show below, this is justified given the magnitude of numerical diffusion, compared to its physical counterpart, in field-scale models. In certain cases, however, it may be necessary to include diffusive fluxes to obtain accurate simulations. An example of this is the validation of numerical models with centimeter- to meter-scale experimental results, which require higher resolution due to smaller spatial scales (Saló-Salgado et al. 2023b).

First, we provide the mathematical model for the diffusive mass flux of a solute in porous media, and briefly discuss the contrasts between physical and numerical diffusion (sect. 2.4.1). Next, we summarize our implementation of molecular diffusion of CO_2 in brine for use in `ad-blackoil` (sect. 2.4.2), and, finally, we present a full `MRST` example (sect. 2.4.3).

2.4.1 Mathematical model

Consider a generic multiphase, multicomponent fluid system. The mass conservation equations for each component $\gamma = 1, ..., M$ can be written as (e.g., Lie 2019):

$$\frac{\partial}{\partial t}\Big(\phi \sum_{\alpha} \rho_\alpha S_\alpha \chi_\alpha^\gamma\Big) + \nabla \cdot \Big(\sum_{\alpha} \mathbf{J}_\alpha^\gamma\Big) = 0 \tag{2.11}$$

where, in Eq. 2.11, ϕ is the porosity, α indicates a generic fluid phase, S is the saturation, χ_α^γ the mass fraction of component γ in phase α, and sources/sinks are 0. $\mathbf{J}$ is the total macroscale flux, which can be decomposed as (Bear 1972; Bear 2018):

$$\mathbf{J}_\alpha^\gamma = \mathbf{J}_{\alpha,\text{adv}}^\gamma + \mathbf{J}_{\alpha,\text{dif}}^\gamma \tag{2.12}$$

i.e., advective and diffusive fluxes, respectively. The advective and diffusive fluxes can be written as (e.g, Bear 1972; Lie 2019):

$$\mathbf{J}_{\alpha,\text{adv}}^\gamma = \rho_\alpha \chi_\alpha^\gamma \mathbf{u}_\alpha \tag{2.13}$$

$$\begin{aligned} \mathbf{J}_{\alpha,\text{dif}}^\gamma &= -\rho_\alpha S_\alpha \mathbf{D}_\alpha^\gamma \nabla \chi_\alpha^\gamma \\ \mathbf{D}_\alpha^\gamma &= \mathbf{D}_{\alpha,\text{m}}^\gamma + \mathbf{D}_{\alpha,\text{h}}^\gamma = \phi \mathcal{D}_{\alpha,\text{m}}^\gamma \mathbf{T}_\alpha + \mathbf{D}_{\alpha,\text{h}}^\gamma \end{aligned} \tag{2.14}$$

where $\mathbf{D}_\alpha^\gamma$ is the total diffusion coefficient (L^2T^{-1}), which is a second-order tensor. $\mathbf{D}_\alpha^\gamma$ can be further decomposed into a coefficient of molecular diffusion ($\mathbf{D}_{\alpha,\text{m}}^\gamma$) given by the porosity, a scalar molecular diffusivity ($\mathcal{D}_{\alpha,\text{m}}^\gamma$, L^2T^{-1}) and dimensionless tortuosity tensor ($\mathbf{T}_\alpha$), and a coefficient of hydrodynamic dispersion ($\mathbf{D}_{\alpha,\text{h}}^\gamma$, L^2T^{-1}).

Note that Eq. 2.14 assumes a Fickian model (Fick 1855) for both the diffusive and dispersive components (i.e., the flux is driven by a concentration gradient). Hydrodynamic dispersion is introduced to explain increased macroscale spreading observed in non-stagnant

fluids in porous media, and multiple models have been proposed (see Bear 2018, and references therein). Tortuosity is a geometrical quantity that accounts for the path length of extensive quantities in porous media being longer than the Euclidean distance, and it is a tensorial quantity in anisotropic media. Because $\mathbf{T}_\alpha$ depends on the specific configuration of the porous medium, it is best determined experimentally (Bear 2018). Hence, for simplicity, we limit the present implementation to a scalar diffusion coefficient, i.e., a pseudo-diffusivity (D_α^γ):

$$\mathbf{J}_{\alpha,\mathrm{dif}}^\gamma = -\phi\rho_\alpha S_\alpha D_\alpha^\gamma \nabla\chi_\alpha^\gamma \tag{2.15}$$

In our two-phase model of CO_2 and brine $D_\alpha^\gamma = D_{\mathrm{o}}^{\mathrm{CO_2}}$, where o is the oleic phase (assigned properties of brine).

In dilute aqueous solutions, $\mathcal{D}_{\alpha,\mathrm{m}}^\gamma \sim \mathcal{O}\ (10^{-9})$ m^2/s, with $\mathcal{D}_{\mathrm{brine}}^{\mathrm{CO_2}} \approx 2 - 3 \times 10^{-9}$ and $\approx 4 - 5 \times 10^{-9}$ at 40 and 80 °C, respectively (Al-Rawajfeh 2004). Numerical diffusion (D_{num}) $\sim uh$, where h is the cell size. For illustration purposes, let us consider a porous formation at storage depth. Taking $k = 100$ mD, $\mu = 0.8$ cP and a modest $\nabla p = 10$ mbar (for $\Delta p = 1$ bar in 100 m), $u \approx 1.2 \times 10^{-7}$ m/s (via Darcy's law). In a typical reservoir-scale model, $h \sim \mathcal{O}(10^2 - 10^3)$ m, which gives $D_{\mathrm{num}} \sim \mathcal{O}(10^{-6} - 10^{-5})$ m^2/s. Therefore, it is evident that physical diffusion is negligible at this scale. If we now consider the FluidFlower rig (Fernø et al. 2023; Haugen et al. 2023) as an example of a laboratory setup at the meter scale, $h \sim 10^{-3}$ m. In this setup, Saló-Salgado et al. (2023b) estimated numerical diffusion to be comparable to or smaller than physical diffusion almost everywhere in their simulations; hence, some degree of diffusivity needs to be introduced.

2.4.2 Implementation for use in `ad-blackoil`

Our implementation is directed towards models that are set up using the `GenericBlackOilModel` class, and simply adds a diffusive component to the total flux term (which, by default, is just the advective flux). Similar to the implementation of relative permeability hysteresis described in sect. 2.3, where we update the relative permeability state function, here we modify the state function for the total CO_2 flux (see ch. 5 in (Lie and Møyner 2021) for an in-depth description of `MRST` state functions). To do this, the user simply needs to specify the pseudo-diffusivity, and update the `ComponentTotalFlux` using `CO2TotalFluxWithDiffusion` (as shown in sect. 2.4.3).

The key statements within the evaluation method in the class `CO2TotalFluxWithDiffusion` are provided below. Note that some of these have been simplified for readability, so interested users should refer to the actual code for full details:

```
% 1. Get quantities
% Model operators;
op = model.operators
% Face diffusivity (analogous to transmissibility)
T = getFaceDiffusivity(model.G, model.rock);
% Get mass fraction of CO2
X_co2 = MassCo2InBrine ./ massBrine;
% Get molecular diffusivity and update T
C = prop.componentDiffusion;
Tc = C(2).*T;
% Mass fraction gradient
grad_xi = op.Grad(X_co2);
% Face density and saturation according to centered or upwind scheme
if faceAvg, ...
else, ...; end

% 2. Get diffusive flux and update total flux
diff_flux = -faceDens.*faceS.*Tc.*grad_xi;   % kg/s/m^2
% Update total CO2 flux
v{2} = v{2} + diff_flux;
```

We emphasize that the `GenericBlackOilModel` class uses mass fluxes instead of surface volumes (used by the earlier, specific black-oil model classes such as `ThreePhaseBlackOilModel`). This ensures consistent units between solvers and facilitates model management. We also note that a code structure similar to the one described here, with a class that incorporates the desired flux model, can be used to extend this implementation (see ch. 5 in Lie and Møyner 2021).

2.4.3 MRST example: the effect of CO_2 diffusion on convective fingers

To illustrate the effect of adding CO_2 diffusion in brine, we present an example inspired by recent work on the FluidFlower project (Eikehaug et al. 2023; Fernø et al. 2023; Flemisch et al. 2023; Haugen et al. 2023; Saló-Salgado et al. 2023b). The FluidFlower is a meter-scale, quasi-2D experimental rig with transparent panels. It can be filled with sands to create realistic cross sections, and multiple ports provide capabilities for multiphase/multicomponent injection and monitoring (Fig. 2.10a). Here, we generated a simple stratigraphic section with dimensions $0.01 \times 1 \times 0.66$ m, including a fault structure, and set it at a depth of 1 km. At this depth, the CO_2 is already in supercritical state, which is the intended state for storage in sedimentary basins. Compared to the FluidFlower, which operates at surface P,T, this facilitates convergence of the nonlinear solver; the main reason is that the CO_2 is much more buoyant at the surface, where it exists in gaseous state (Saló-Salgado et al. 2023b). The reservoir and fault permeability can be seen on top of the grid ($h \approx 2.5$ mm) in Fig. 2.10b. We inject CO_2 in the lower right of the domain at a surface rate of 8 ml/min during one day, and run the simulation for 30 days.

This example is provided in the script `exampleDiffusion`. We specify two phases, oil (with properties of water) and gas. The model can be set up using `GenericBlackOilModel` and `CO2TotalFluxWithDiffusion`:

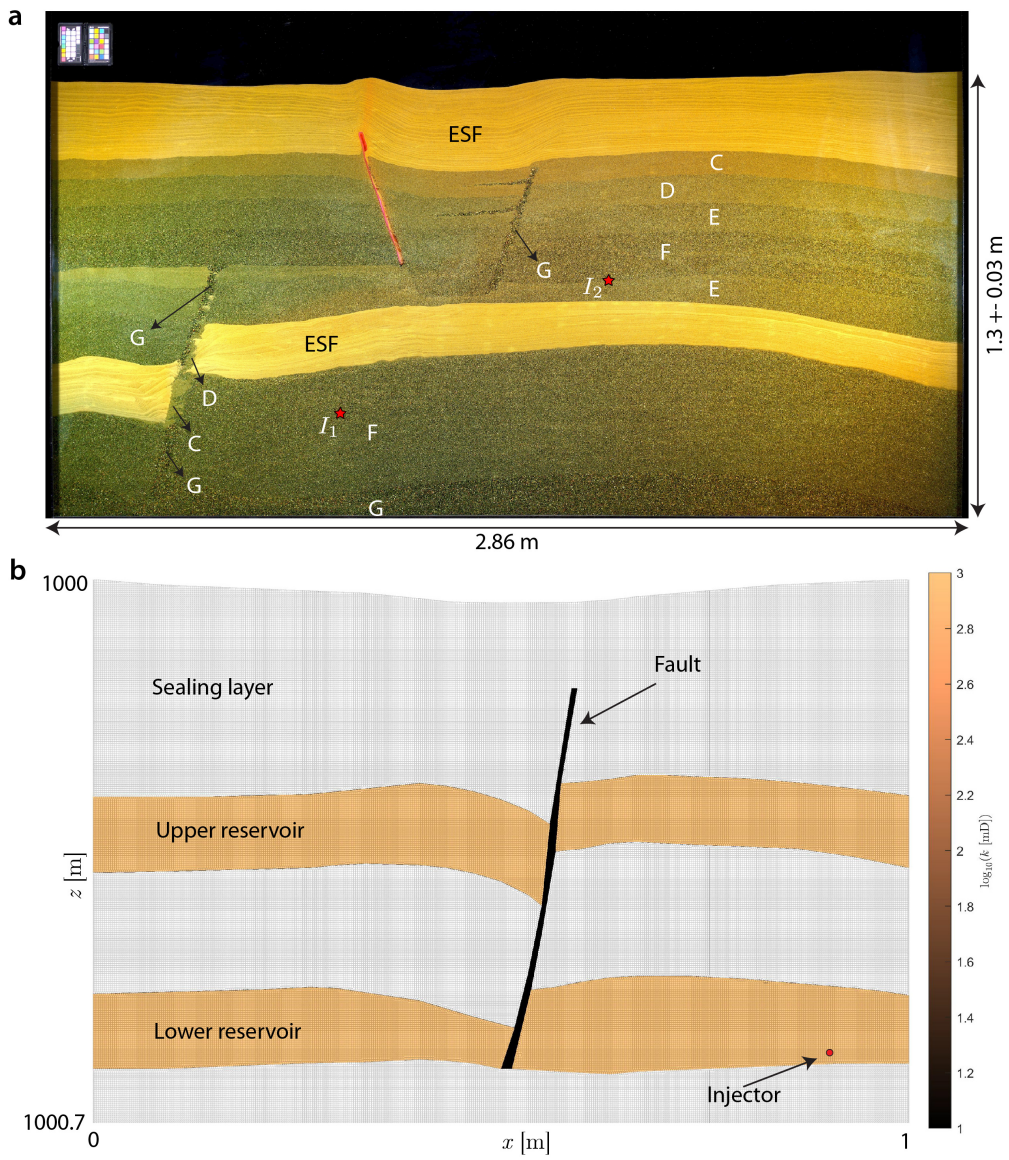

Figure 2.10: **a** Overview of the porous medium used in the FluidFlower international benchmark study (Flemisch et al. 2023). Letters indicate different sand types, and three fault structures are present. Modified from Saló-Salgado et al. (2023b). **b** Setup used in this example, conducted at 1 km depth. $h \approx 2.5$ mm. The colormap shows reservoir and fault permeability (1 D and 10 mD, respectively).

```
% Create model (oil is water)
model = GenericBlackOilModel(G,rock,fluid,'disgas',true,'water',false);
model = model.validateModel();  % Add state function groups
% Specify diffusion
D = 1e-10;  % scalar pseudo-diffusivity for CO2 in water
diff_flux = CO2TotalFluxWithDiffusion(model);
diff_flux.componentDiffusion = [0 D]; % water in gas phase not considered
diff_flux.faceAverage = true;         % Centered scheme
model.FlowDiscretization.ComponentTotalFlux = diff_flux; % Update model
```

Note that the value of $D_o^{CO_2}$ may need to be lower than the molecular diffusivity ($\mathcal{D}_o^{CO_2}$), depending on the magnitude of advective fluxes and grid resolution. Results in Fig. 2.11 show a comparison of convective fingers after CO_2 injection in the lower-right reservoir, using different $D_o^{CO_2}$ values. It is evident that the finger thickness and spacing change as diffusive fluxes are introduced in the system; as noted above, this may be required in m-scale or smaller setups, for example to history-match simulation models to experiments that provide a ground truth (Saló-Salgado et al. 2023b).

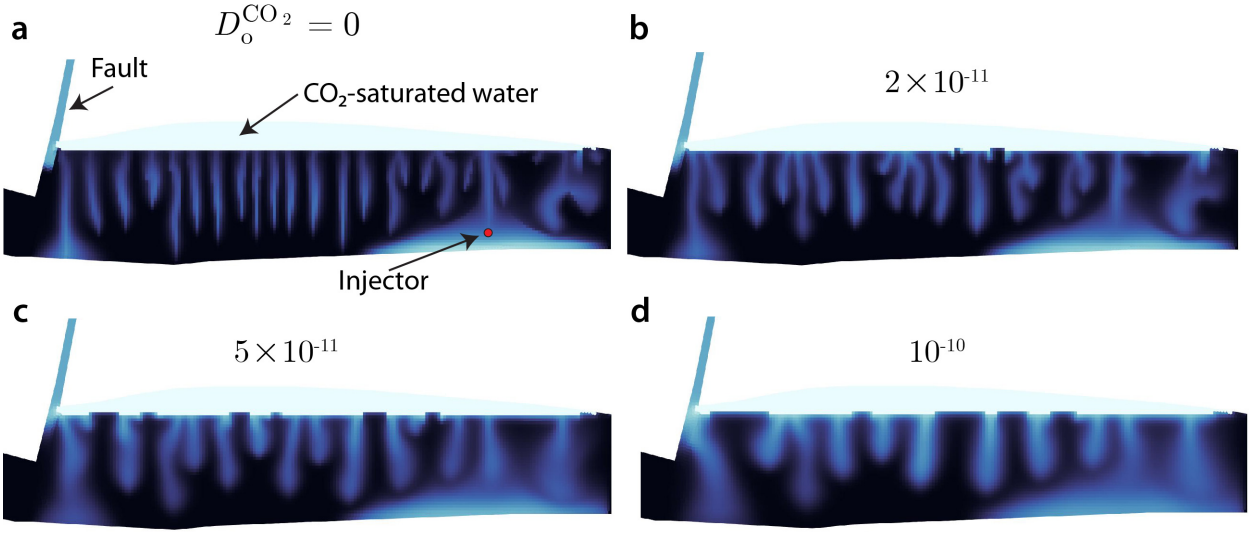

Figure 2.11: Overview of convective mixing in the lower right reservoir using different pseudo-diffusivities. Grid cell size $h \approx 2.5$ mm. Note that the average spacing and finger width increases with the diffusivity. **a** No diffusion. **b** $D = 2\times10^{-11}$ m^2/s. **c** $D = 5\times10^{-11}$ m^2/s. **d** $D = 1\times10^{-10}$ m^2/s.

2.5 Discussion

The three MRST extensions presented in this paper provide a starting point for more specific CO_2 storage models using the `ad-blackoil` or `compositional` modules. As discussed next, new contributions may focus on different equations for PVT properties, application of hysteresis to the wetting phase or three-phase systems, and mechanical dispersion, for example.

The mixing model presented in sect. 2.2 is based on the formulations by Duan and Sun (2003), Spycher et al. (2003), and Spycher and Pruess (2005). It is most accurate at GCS P, T conditions (i.e., $T \in \sim$[30, 90] °C, $P \in \sim$[80, 300] bar), and appropriate above the CO_2 critical point (Hassanzadeh et al. 2008). The main focus of Spycher et al. (2003), Spycher and Pruess (2005), and Hassanzadeh et al. (2008) is in predicting the solubility of CO_2 in the aqueous phase (x_{CO_2}, where x is the mole fraction). This is reasonable given the change in aqueous phase properties with CO_2 dissolution, and that x_{CO_2} is a factor of $\sim$[2, 10] larger than y_{H_2O} at $P \in [80, 300]$ bar, $T < \sim$70 °C. At higher temperatures, $y_{H_2O} \sim x_{CO_2}$ or larger, and the assumption of infinite dilution starts to introduce larger error in the calculation of

water vaporization (Spycher et al. 2003). Similarly, if pressure decreases to the point that CO_2 becomes a gas, y_{H_2O} increases much faster and the assumption no longer applies (still, we note that Fig. 4-7 in Spycher et al. (2003) indicate a good match with experimental data at low pressures). Error in y_{H_2O} is $< 10\%$ for sodium chloride brines up to 6 molal, and $\leq 15\%$ for calcium chloride brines up to 3 molal (Spycher and Pruess 2005). Overall, the implemented PVT model is appropriate for most CO_2 reservoirs in sedimentary basins; however, in higher temperature and/or salinity reservoirs, or where CO_2 phase changes are expected (as P, T decrease), a different model may be needed. In addition to phase composition, this also applies to errors introduced by some of the PVT property models, such as CO_2 viscosity (Fig. 2.5).

In sect. 2.3, we accounted for relative permeability hysteresis in the nonwetting phase (gas in most sediments) due to its importance during secondary imbibition at the trailing edge of the CO_2 plume (Juanes et al. 2006). Hysteresis in the wetting phase is typically less pronounced (Juanes et al. 2006), but depends on the rock type and fluid system (Naar et al. 1962; Bennion and Bachu 2008; Akbarabadi and Piri 2013). It is well known that the relative permeability of a given fluid phase is impacted by a number of factors including flow rates, pore structure, wettability and degree of cementation (e.g., Naar et al. 1962; Bryant and Blunt 1992; Jadhunandan and Morrow 1995; Spiteri et al. 2008; Krevor et al. 2012; Reynolds and Krevor 2015). As a result, we emphasize that the choice of the relative permeability model and its parameters must be evaluated on a case-to-case basis. Additionally, our implementation of relative permeability hysteresis in sect. 2.3 is limited to two-phase water-gas (immiscible) or oil-gas (miscible) systems. Most reservoir simulators model three-phase relative permeability based on the model by Stone (Stone 1970), where $k_{rw}(S_w)$, $k_{rg}(S_g)$ and $k_{ro}(S_w, S_g)$ (see ch. 8.1.4 and 11.3 in Lie 2019). If the two-phase relative permeabilities display hysteresis, the interpolation method for k_{ro} can also accommodate hysteresis (e.g., Killough 1976). However, three-phase relative permeability measurement and modeling remain topics of active research (Blunt 2017), and an in-depth discussion on this topic is beyond the scope of this paper. Therefore, while we note that implementations for three-phase fluid systems would also be of great interest to the MRST community, we do not address this topic further. Interested readers are referred to Baker (1988), Spiteri and Juanes (2006), Alizadeh and Piri (2014), Blunt (2017), and Jia et al. (2018) and references therein.

In sect. 2.4, we presented a model for the diffusive flux based on a scalar diffusion coefficient. Besides practicality, the reasoning behind the choice of Eq. 2.15 is that D_α^γ can be increased to account for mechanical dispersion in relatively homogeneous media (e.g., Riaz et al. 2006). However, in a recent application of this model, Saló-Salgado et al. (2023b) reported that the use of a scalar coefficient may lead to inaccuracies at higher flow velocities. This is consistent with the findings of Liang et al. (2018), who showed that, in homogeneous glass beads, the dominant mechanism can be estimated as $R_d = \mathcal{D}_\alpha^\gamma / \alpha_t u$, where α_t is the transverse dispersivity (L); this leads to dispersion dominating over molecular diffusion for $R_d \ll 1$, which occurs when grain diameters are above 0.4 mm. In natural sediments, heterogeneity increases the effective dispersivity, which in turn increases mechanical dispersion (Gelhar et al. 1992; Liang et al. 2018). Therefore, our model is appropriate for relatively homogeneous sediments where molecular diffusion dominates. In heterogeneous media or where larger flow velocities are expected, a dispersion tensor ($\mathbf{D}_{\alpha,h}^\gamma$) is likely necessary.

2.6 Summary

This work focuses on enhancing the capabilities of the `ad-blackoil` module in `MRST`, with the main goal of simulating 3D geologic carbon sequestration (GCS) in saline aquifers. Our contributions can be divided in three sections:

- Sect. 2.2: thermodynamic model to calculate input PVT properties
- Sect. 2.3: relative permeability hysteresis
- Sect. 2.4: molecular diffusion

We provide the code and examples detailing how to use each of these additions, which are intended for two-phase water-gas (immiscible) or oil-gas (miscible) models obtained with the `GenericBlackOilModel` class. The description provided in this paper, together with the code, should facilitate implementation of alternative models.

Code availability

The code, including examples presented in this paper, can be accessed through https://github.com/lsalo/mrst-adblackoil-gcs. Please note that most of the functionality described will be integrated into `MRST` in the near future; hence, the code (including file names) is still subject to change. Updates will be posted in the `README` file on GitHub.

Chapter 3

Direct Comparison of Numerical Simulations and Experiments of CO_2 Injection and Migration in Geologic Media: Value of Local Data and Forecasting Capability

This chapter has been published in Saló-Salgado et al. (2023b).

Abstract

Purpose: The accuracy and robustness of numerical models of geologic CO_2 sequestration are almost never quantified with respect to direct observations that provide a ground truth. This study presents CO_2 injection experiments in meter-scale, quasi-2D tanks with porous media representing stratigraphic sections of the subsurface, compared to numerical simulations of those experiments.
Goals: Evaluate (1) the value of prior knowledge of the system, expressed in terms of ex-situ measurements of the tank sands' multiphase flow properties (local data), with respect to simulation accuracy; and (2) the forecasting capability of the matched numerical models, when applied to different settings.
Methods: Match three versions of a numerical simulation model—each with access to an increasing level of local data—to a CO_2 injection experiment in Tank 1 (89.7×47×1.05 cm). Matching is based on a quantitative comparison of CO_2 migration at different times from timelapse image analysis. Next, use the matched models to make a forecast of a different injection scenario in Tank 1, and, finally, a different injection scenario in Tank 2 (2.86×1.3×0.019 m), which represents an altogether different stratigraphic section.
Results and conclusion: The simulation model can qualitatively match the observed free-phase and dissolved CO_2 plume migration and convective mixing. Quantitatively, simulations are accurate during the injection phase but their concordance decreases with time. Using local data reduces the time required to history match, although the forecasting ca-

pability of matched models is similar. The sand-water-$CO_{2(g)}$ system is very sensitive to effective permeability and capillary pressure changes; where heterogeneous structures are present, accurate deterministic estimates of CO_2 migration are difficult to obtain.

3.1 Introduction

CO_2 capture and subsequent geologic carbon sequestration (GCS) is a climate-change mitigation technology that can be deployed at scale to offset anthropogenic CO_2 emissions during the energy transition (Marcucci et al. 2017; EASAC 2018; Celia 2021; IPCC 2022). In GCS, reservoir simulation, including coupled flow and geomechanics, is the primary tool used to assess and manage geologic hazards such as fault leakage (e.g., Caine et al. 1996; Ingram and Urai 1999; Nordbotten and Celia 2012; Zoback and Gorelick 2012; Juanes et al. 2012; Jung et al. 2014; Vilarrasa and Carrera 2015; Saló-Salgado et al. 2023a) and induced seismicity (e.g., Cappa and Rutqvist 2011; Zoback and Gorelick 2012; Juanes et al. 2012; Ellsworth 2013; Verdon et al. 2013; Alghannam and Juanes 2020; Hager et al. 2021). In response to the inherent uncertainties associated with modeling and simulation of CO_2 storage (Nordbotten et al. 2012), building confidence in the forecasting capabilities of simulation models requires calibration (or, synonymously, history matching), a process that involves updating the reservoir model to match field observations as they become available (Oliver and Chen 2011; Doughty and Oldenburg 2020).

History matching is an ill-posed inverse problem (Oliver and Chen 2011). This means that multiple solutions (i.e., parameter combinations) exist that approximate the data equally well. Automated techniques such as Markov chain Monte Carlo, randomized maximum likelihood or ensemble-based methods can be used to quantify uncertainty in history-matched models, especially in combination with surrogate models to reduce forward model computational time (see Aanonsen et al. 2009; Oliver and Chen 2011; Jagalur-Mohan et al. 2018; Jin et al. 2019; Liu and Durlofsky 2020; Santoso et al. 2021; Landa-Marbán et al. 2023, forthcoming, and references therein). In practice, however, it may be difficult to ensure that the chosen simulation model provides the best possible forecast. This is due to different subsurface conditions, the inability to include all sources of uncertainty in the models, incomplete field data and limited time for history matching.

In the laboratory, intermediate-scale (∼meter) experiments have been used to study the physics of petroleum displacement (e.g., Gaucher and Lindley 1960; Brock and Orr 1991; Cinar et al. 2006) and contaminant transport (e.g., Silliman and Simpson 1987; Wood et al. 1994; Lenhard et al. 1995; Fernández-García et al. 2004). Similar 2D and 3D flow rigs have recently been applied to CO_2 storage, providing a link between core-scale measurements and field observations:

Kneafsey and Pruess (2010) found the impact of convective dissolution to be significant, using a page-size Hele-Shaw cell and numerical simulations. Neufeld et al. (2010) studied the scaling of convective dissolution and found it to be an important mechanism in the long-term trapping of injected CO_2 in an idealized site. Wang et al. (2010) used a 3D setup to investigate the ability of electrical resistivity tomography to identify localized leaks. Trevisan et al. (2014) and Trevisan et al. (2017) focused on the impact of structural and residual trapping. In homogeneous sands, they found that previous trapping models, such as the Land (1968)

model, can approximate the residually trapped gas saturation ($R^2 > 0.6$). Studying an heterogeneous aquifer characterized by a log-normal distribution of six different sand facies, they report that trapping efficiency increased significantly due to structural trapping. A strong control of sand heterogeneity on upward migration of CO_2 was also found by Lassen et al. (2015). Krishnamurthy et al. (2019) and Krishnamurthy et al. (2022) devised a novel technique to automate the process of beadpack/sandpack deposition and generate realistic depositional fabrics; they concluded that grain-size contrast and bedform architecture significantly impact CO_2 trapping. Subsequently, Ni et al. (2023) presented modified invasion-percolation simulations and reported that bedform architecture can impact CO_2 saturation if enough grain-size contrast is present. Askar et al. (2021) used a ∼8 m-long tank to test a framework for GCS monitoring of CO_2 leakage. These studies employed homogeneous glass beads or sands, or focused on heterogeneities and bedform architectures in the aquifer layer; structural complexity was minimal.

In this paper, we use quasi-2D, intermediate-scale experiments of CO_2 storage to evaluate, quantitatively, the forecasting capability of history-matched simulation models against well-defined spatial data. An attempt was made to recreate realistic basin geometries, including stacking of storage reservoirs, faults, caprock and overburden. We simulate each of the three presented experiments with three versions of a numerical model, each with increasing access to local petrophysical measurements. These different versions are denoted Model 1 (M_1), Model 2 (M_2) and Model 3 (M_3). This allows us to assess (1) the value of local information of the system, expressed in terms of sand petrophysical measurements, during history matching, and (2) transferability or forecasting capability of our matched simulation models, when tested against a different experiment. The term *concordance* is used to evaluate agreement between experiments and observations (Oldenburg 2018).

3.2 Physical Experiments

The physical experiments of CO_2 injection are conducted using the *FluidFlower* rigs. These rigs are meter-scale, quasi-2D tanks with transparent Plexiglass panels designed and built in-house at the University of Bergen (Fig. 3.1). Here, we used two tanks, with dimensions $89.9 \times 47 \times 1.05$ cm and $2.86 \times 1.3 \times 0.019$ m (referred herein to as Tank 1 and Tank 2, respectively). Different geologic settings are constructed by pouring unconsolidated sands with desired grain sizes into the water-saturated rigs. The rigs have multiple ports which allow flushing out fluids after a given CO_2 injection, such that multiple injections can be conducted in the same setting. The location of the ports can be adjusted to accommodate different injection scenarios. A variety of techniques have been developed by UiB engineers in order to build complex structures such as folds and faults.

Below, we summarize the petrophysical measurements, experimental setup, geologic model/porous media construction and experimental schedule. Details on the conceptualization of the FluidFlower rigs and technical information are given in Fernø et al. (2023) and Eikehaug et al. (2023), while the full description of the physical experiment in Tank 1 and ex-situ measurements are provided by Nordbotten et al. (2022) and Haugen et al. (2023). Further details on the experiment in Tank 2, as well as results of the international benchmark study (IBS), are provided by Flemisch et al. (2023).

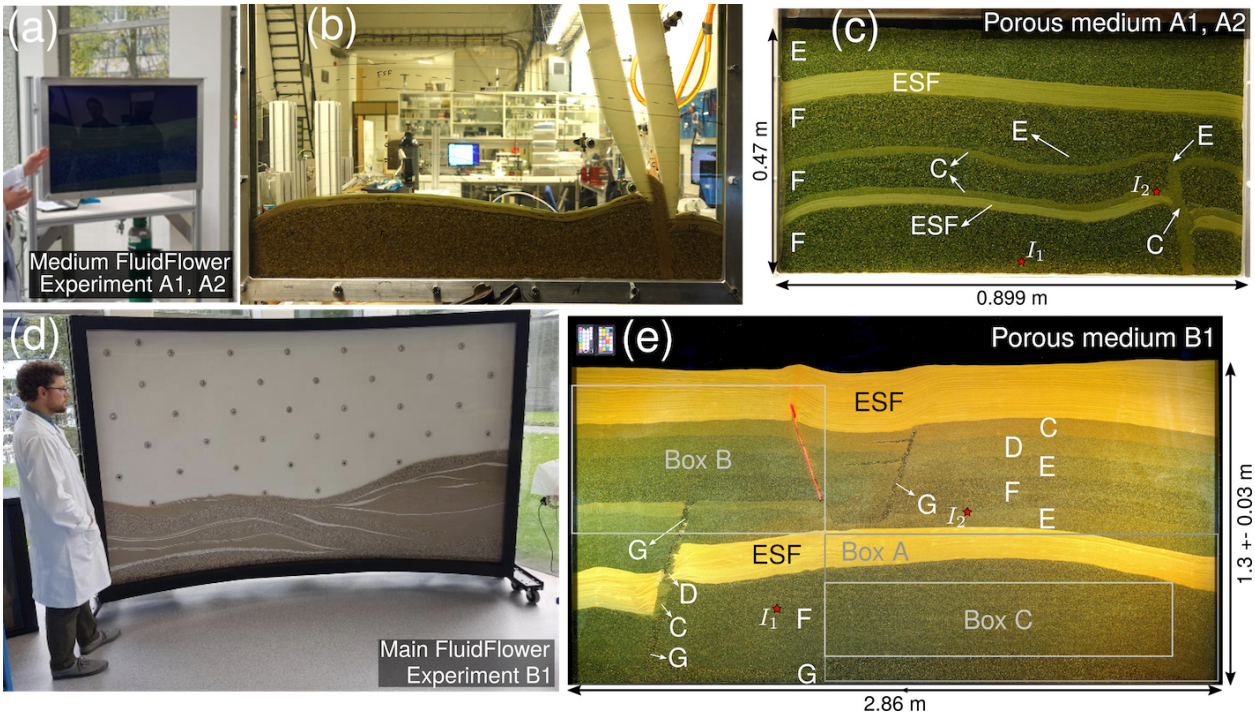

Figure 3.1: Overview of the FluidFlower rigs and porous media used in the physical experiments. **a** Medium FluidFlower rig (Tank 1). **b** Snapshot during sand pouring to build the porous medium used in Experiments A1 and A2 in Tank 1 (Haugen et al. 2023). **c** Front view of porous medium in Tank 1, with lithologies in white and injector location shown with a red star. The length and height correspond to the porous medium. Note the fixed water table at the top. **d** Overview of the main FluidFlower rig (Tank 2), showing the back panel with sensor network. **e** Porous medium in Tank 2, used for Experiment B1, with lithologies in white. Location of injectors and Boxes A, B and C for analysis are shown with a red star and gray boxes, respectively. Length and variable height correspond to the porous medium.

3.2.1 Sand petrophysical properties

Measurements on the employed Danish quartz sands were conducted using specialized equipment to determine average grain size (d), porosity (ϕ), permeability (k), capillary entry pressure (p_e) and drainage and imbibition saturation endpoints (denoted as connate water saturation, S_{wc}, and trapped gas saturation, S_{gt}). The methodology is described by Haugen et al. (2023) and obtained values are provided in Tab. 3.1. Sands C, D, E and F are very well sorted, sand G is well sorted, and sand ESF is moderately sorted (Haugen et al. 2023). We verified that Darcy's law is applicable in our system using the Reynolds number (R_e):

$$R_e = \frac{ud}{\nu} \tag{3.1}$$

where u is the fluid discharge per unit area, d the mean grain diameter, and ν the kinematic viscosity of the fluid. From our simulation results, matched to experimental observations, $\max(R_e) \leq 1$, which ensures the applicability of Darcy's law (e.g., Bear 1972).

Table 3.1: Petrophysical properties for used quartz sands, as obtained from local, ex-situ measurements. Porosity and permeability are the average from two measurements for each sand, with a maximum difference between measurements of 0.02 (ϕ) and estimated 20% uncertainty (k). Measured gas column heights for sands E-G were 0, so p_e could not be directly measured. Experimental error in p_e, S_{wc} and S_{gt} was not quantified. A detailed description of the methodology and petrophysical values is provided by Nordbotten et al. (2022) and Haugen et al. (2023).

Sand type	d (std) [mm]	ϕ [-]	k [D]	p_e [mbar]	S_{wc}	S_{gt}
ESF	0.2 (0.11)	0.435	44	15	0.32	0.14
C	0.66 (0.09)	0.435	473	3	0.14	0.1
D	1.05 (0.14)	0.44	1110	1	0.12	0.08
E	1.45 (0.19)	0.45	2005	-	0.12	0.06
F	1.77 (0.31)	0.44	4259	-	0.12	0.13
G	2.51 (0.63)	0.45	9580	-	0.1	0.06

3.2.2 Experimental setup

The front and back panels of the FluidFlower are mounted on a portable aluminum frame, such that boundaries are closed on the sides and bottom (no flow). The top surface is open and in contact with fluctuating atmospheric pressure (Fig. 3.1). A fixed water table above the top of the porous medium was kept throughout the experiments conducted here. The experimental setup incorporates mass flow controllers to inject gaseous CO_2 at the desired rate, and a high-resolution digital camera with time-lapse function (Haugen et al. 2023).

Experiments were conducted in 2021 and 2022 in Bergen (Norway) at room temperature ($\approx$ 23 °C) and ambient atmospheric pressure. Temperature changes were minimized as much as possible, but maintaining a constant temperature was not possible in the available laboratory space. The fluids and sands were set in the FluidFlowers using the following procedure:

1. The silica sands are cleaned using an acid solution of water and HCl to remove carbonate impurities.

2. The FluidFlower rig is filled with deionized water.

3. Sands are manually poured into the rig using the open top boundary, in order to construct the desired porous medium.

4. A pH-sensitive, deionized-water solution containing bromothymol blue, methyl red, hydroxide and sodium ions is injected through multiple ports until the rig is fully saturated. This enables direct visualization of CO_2 gas (white), dissolved CO_2 (yellowish orange to red), and pure water (dark teal).

5. 5.0 purity (99.999%) CO_2 is injected as gaseous phase at the desired rate. CO_2 is injected through dedicated ports directly into the rig (Fig. 3.1).

6. After the injection phase, injection ports are closed and CO_2 migration continues.

7. Once the experiment is finished, the rig can be flushed with deionized water and the process can start again from step 4.

Full details on the fluids are given in Fernø et al. (2023) and Eikehaug et al. (2023). Below, we refer to the pH-sensitive solution in the rigs as "dyed water".

3.2.3 Porous media geometries

The geometries of the porous media used in this paper aim to recreate the trap systems observed in faulted, siliciclastic, petroleoum-bearing basins around the world, given the geometrical constraints of the FluidFlowers and manual sand pouring (Fernø et al. 2023; Eikehaug et al. 2023). Features such as folds, faults and unconformities were built in both Tanks 1 and 2. The construction of faults, shown in Fig. 3.1b and detailed in Haugen et al. (2023), requires a minimum effective "fault-plane" thickness; hence, our fault structures are thicker than natural faults with the same displacement (Childs et al. 2009). Fine sands ($d \approx 0.2$ mm) are used to represent sealing or caprock formations.

The geometry in Tank 1 (Fig. 3.1c) contains three main high-permeability reservoirs (F sand). The bottom and middle F sand are separated by a seal (ESF sand), while the middle and top are separated by the C sand and connected through a higher permeability fault (refer to sect. 3.2.1 for pertrophysical properties). The fault separates the bottom section into two compartments. The bottom and top F sand provide anticlinal traps for the CO_2 to accumulate in.

The geometry in Tank 2 (Fig. 3.1e) was specifically motivated by the structure of North Sea reservoirs and petroleum basins. From bottom to top, it contains two sections of decreasing-permeability reservoirs capped by two main sealing layers. A fault separates the bottom section into two compartments, while two faults separate the top section into three compartments. Each fault has different petrophysical properties: The bottom fault is a heterogeneous structure containing ESF, C, D, F and G sands, the top-left fault is an impermeable structure made of silicone and the top-right fault is a conduit structure containing G sand.

3.2.4 Experimental injection schedule

The injection schedules for experiments in Tanks 1 and 2 are provided in Tab. 3.2. Injection ports have an inner diameter of 1.8 mm.

3.3 Numerical Simulations

3.3.1 Model setup

The isothermal simulations presented in this work were performed with the MATLAB Reservoir Simulation Toolbox, `MRST` (Krogstad et al. 2015; Lie 2019; Lie and Møyner 2021). Specifically, we used the black-oil module, which is based on fully implicit solvers with automatic differentiation, and assigned properties of water to the oleic phase, such that the gaseous phase (CO_2 only) can dissolve in it. Vaporization of water into the gas phase and chemical

Table 3.2: Schedules for the three CO_2 injection experiments simulated in this work. I_R is injection rate, while I_i denotes injector (port) number. A five-minute ramp-up and ramp-down was applied in Experiments A1 and A2 in Tank 1. Total duration of conducted experiments and simulations is 48h (A1), 5h (A2) and 120h (B1). Location of injection wells is provided in Fig. 3.1.

Experiment A1		A2		B1	
I_R [ml/min]	t [hh:mm:ss]	I_R	t	I_R	t
0.1 (I_1)	00:00:00	0.1 (I_1)	00:00:00	10.0 (I_1)	00:00:00
2.0	00:05:00	2.0	00:05:00	10.0	05:00:00
2.0	00:50:00	2.0	04:43:44	0.0	05:00:01
0.0	00:55:00	0.0	04:48:33	10.0 (I_2)	02:15:00
0.1 (I_2)	01:09:11	0.0	05:00:00	10.0	05:00:00
2.0	01:14:11			0.0	05:00:01
2.0	02:29:11			0.0	120:00:00
0.0	02:34:00				
0.0	48:00:00				

reactions are not considered, because they are not primary controls on fluid migration for our operational setup and analysis time.

In addition to structural and dissolution trapping, we also considered residual trapping (Juanes et al. 2006) to be consistent with local measurements showing nonzero trapped gas saturation (sect. 3.2.1). This is achieved through hysteretic relative permeability curves for the nonwetting (gas) phase (see sect. 3.3.2). Our implementation in `MRST` follows ECLIPSE's technical description (SLB 2014b), and Killough's (1976) model is used to compute the scanning curves (Saló-Salgado et al. 2023c, forthcoming). Physical diffusion was also included through the addition of a diffusive flux term with a scalar, constant coefficient in the computation of the total CO_2 flux (Bear 1972).

The simulator requires very small time-steps (seconds to minutes) due to the buoyancy of CO_2 at atmospheric conditions and high sand permeabilities (Tab. 3.1). Linear solver time was reduced by means of AMGCL (Demidov and Rossi 2018; Lie 2019), an external, pre-compiled linear solver. The greatest challenge was the convergence of the nonlinear solver, which required many iterations and time-step cuts. This is consistent with the groups working in the FluidFlower international benchmark study (Flemisch et al. 2023).

Next, we describe the computational grids for experiments in Tanks 1 and 2, PVT properties and boundary conditions. Petrophysical properties are specific of each model version and are detailed in sect. 3.3.2.

Computational grids

A front panel image of the porous medium was used to obtain layer contact coordinates through a vector graphics software (Fig. 3.2a). These contacts were then imported into MATLAB to generate the computational grids using the UPR module (Berge et al. 2019; Berge et al. 2021)(Fig. 3.2b,d). The grids were generated in 2D and then extruded to 3D (using a single cell layer) to account for thickness and volume. Note that, in Tank 1, where

the porous medium has dimensions of $89.7 \times 47 \times 1.05$ cm, the thickness (space between the front and back panels) is constant (10.5 mm). Tank 2, which is significantly larger (porous medium dimensions $2.86 \times 1.3 \times 0.019$ m), has a thickness of 19 mm at the sides; however, it varies towards the middle due to forces exerted by the sand and water, to a maximum of 28 mm. A thickness map obtained after initial sand filling was used to generate our variable-thickness mesh via 2D interpolation (Fig. 3.2c). Also, the top surface of the porous medium is not flat (height $= 130 \pm 3$ cm).

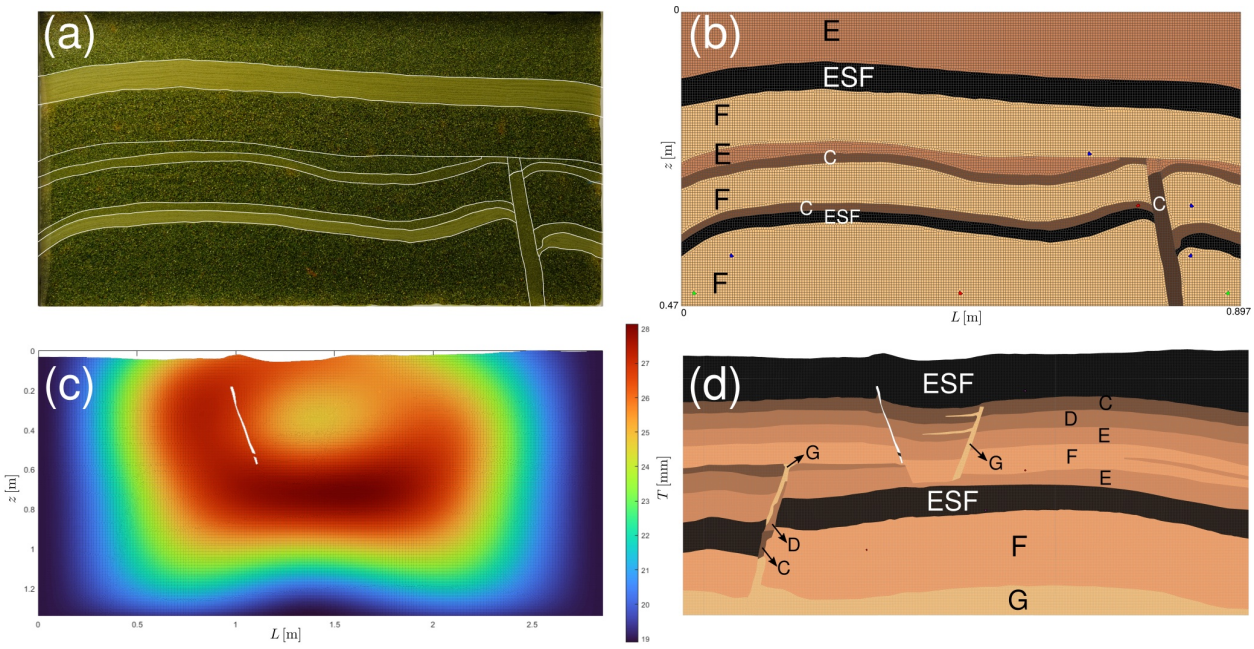

Figure 3.2: Simulation grids overview. **a** front panel view of Tank 1, where the layer contacts have been highlighted in white. **b** front view of simulation grid for experiments in Tank 1, with lithologies indicated and colored based on petrophysical properties (see sect. 3.3.2). Location of injection wells is shown in red. **c** thickness map of simulation grid for experiments in Tank 2. **d** front view of simulation grid for experiments in Tank 2, with lithologies indicated and colored based on petrophysical properties. Location of injection wells is shown in red.

Our composite Pebi grids (Heinemann et al. 1991) have a Cartesian background and are refined around face constraints (contacts and faults) as well as cell constraints (injection wells) (Berge et al. 2019; Berge et al. 2021). We generated multiple grids to test the finest grid we could afford to simulate Experiment B1 in Tank 2 with. Our grid has a cell size $h \approx 5$ mm and 151,402 cells (Fig. 3.2d). The grid used for Tank 1 has a similar cell size ($h \approx 4$ mm and 27,200 cells), which was chosen to reduce grid-size dependencies when applying our matched models to Experiment B1.

PVT properties

Consistent with experimental conditions, our simulations are conducted at atmospheric conditions ($T = 25$ C), where the CO_2 is in gaseous state. We employed a thermodynamic model based on the formulations by Duan and Sun (2003) and Spycher et al. (2003) and Spycher

and Pruess (2005) to calculate the composition of each phase as a function of p, T. The implementation for a black-oil setup is described in Hassanzadeh et al. (2008) and references therein. Given the boundary conditions (sect. 3.3.1) and dimensions of our experimental porous media, pore pressure changes (Δp) are very small in our simulations (max $\Delta p \ll 1$ bar). Hence, the fluid properties remain similar to surface conditions, where the water and CO_2 have, respectively, a density of 997 and 1.78 kg/m^3, and a viscosity of 0.9 and 0.015 cP. The maximum concentration of CO_2 in water is ≈ 1.5 kg/m^3.

Initial, boundary and operational conditions

Our porous media are fully saturated in water at the beginning of CO_2 injection. No-flow boundary conditions were applied everywhere except at the top boundary, which is at constant pressure and includes a fixed water table a few cm above the top of the porous medium. Injection is carried out via wells completed in a single cell at the corresponding coordinates. The diameter of injection wells is 1.8 mm in both Tank 1 and Tank 2, which operate at a constant flow rate (see sect. 3.2). The simulation injection schedule follows the experimental protocol, provided in Tab. 3.2. Note that injection rates in our simulations of Experiment A1 and A2 were slightly adjusted during the calibration procedure, as explained in sect. 3.3.3 and 3.4.

3.3.2 Simulation model

Three different model versions, denoted Model 1 (M_1), Model 2 (M_2) and Model 3 (M_3), are used throughout this study to evaluate the value of local data in forecasting subsurface CO_2 migration. Each successive model was constructed based on access to an increasing level of local data, with M_1 having access to the least data and M_3 having access to the most data. The model-specific parameters are limited to the following:

- Petrophysical properties (porosity, permeability, capillary pressure and relative permeability), which depend on available local data and are described in this section.
- The molecular diffusion coefficient (D). Models 1-3 were calibrated using the same value, $D = 10^{-9}$ m^2/s. Additionally, Model 3 was also calibrated with $D = 3 \times 10^{-9}$ m^2/s. Accordingly, where required we denote Model 3 as $M_{3,1}$ and $M_{3,3}$.
- Injection rate. Experiments in Tank 1 were conducted at a very low injection rate ($I_R = 2$ ml/min, see Tab. 3.2). Given that the mass flow controllers used in Tank 1 may be inaccurate for this rate, the injection rate was also modeled as an uncertain parameter. Model calibration was achieved with $I_R \in [1.6, 1.8]$ ml/min for all three models.

All other model characteristics, including the grid and numerical discretization, remain unchanged. Below, we describe the starting petrophysical values for each of our three simulation models. Note that the experimental geometry in Tank 1, used for matching, only contained sands ESF, C, E and F. Properties for sands D and G are also provided because they were required to simulate the experiment in Tank 2 (Fig. 3.1).

Model 1 (M_1)

For this model, local petrophysical data were limited to a measure of the average grain size (d; see sect. 3.2.1 and Tab. 3.1). Hence, petrophysical properties were estimated from published data in similar silica sands. Porosity was selected from data in Beard and Weyl (1973) and Smits et al. (2010) for moderately to well-sorted sands. Permeability was obtained from fitting a Kozeny-Carman model to data in Beard and Weyl (1973) and Trevisan et al. (2014). The resulting equation has the form $k = \beta d^2 \phi^3$, where β equals 12,250 in our fit with d in mm and k in D. Obtained porosity and permeability values are provided in Table 3.3.

Table 3.3: Initial porosity and permeability for Model 1. See main text for estimation details.

Sand type	d [mm]	ϕ [-]	k [D]
ESF	0.2	0.37	25
C	0.66	0.38	290
D	1.05	0.40	930
E	1.45	0.39	1530
F	1.77	0.39	2280
G	2.51	0.42	5720

Capillary pressure curves were computed as described below:

1. Capillary pressure measurements in a similar system were obtained from the literature. In this case, Plug and Bruining (2007) measured capillary pressure curves on the unconsolidated quartz sand-CO_2-distilled water system at atmospheric conditions. We used their measurements on sand packs with an average particle size between 0.36 and 0.41 mm, which are closest to the C sand in our experiments (Fig. 3.3a).

2. A Brooks and Corey (1964) model of the form $p_c = p_e (S_w^*)^{-\frac{1}{\lambda}}$ was fitted to these data, where p_e is the nonwetting phase entry pressure at $S_w = 1$, $\lambda = 2.6$ and $S_w^* = \frac{S_w - S_{wc}}{1 - S_{wc}}$ is the normalized water saturation with irreducible or connate water saturation S_{wc}. This fit led to our reference curve, p_{cr} (Fig. 3.3a).

3. The capillary pressure depends on the pore structure of each material, such that sands with different grain sizes require different p_c curves. The capillary pressure variation can be modeled by means of the dimensionless J-function proposed by Leverett (Leverett 1941; Saadatpoor et al. 2010): $J(S_w) = \frac{p_c}{\sigma \cos\theta} \sqrt{\frac{k}{\phi}}$, where σ is the surface tension and θ the contact angle. Assuming the same wettability and surface tension for different sand regions, and the same shape of the p_c curve, the capillary pressure for any given sand (p_{cs}) can be obtained from the reference curve as $p_{cs}(S_w) = p_{cr}(S_w) \sqrt{\frac{k_r \phi_s}{k_s \phi_r}}$ (Fig. 3.3b).

Drainage relative permeabilities were obtained from CO_2-water measurements by DiCarlo et al. (2000), who used water-wet sandpacks with 0.25 mm grain size. Specifically, we used the data reported in their Fig. 4 and 5, and fitted Corey-type functions (Corey 1954;

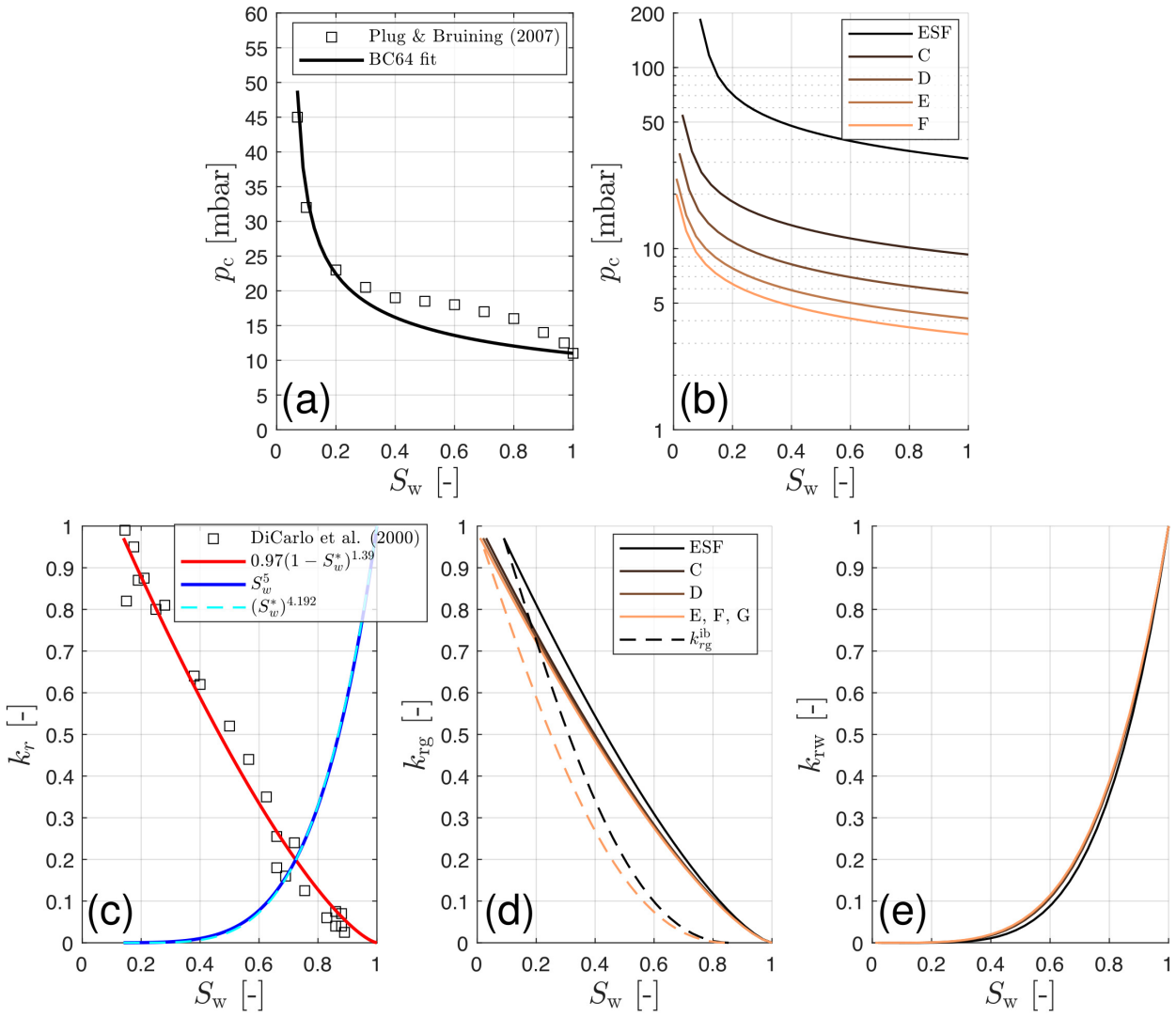

Figure 3.3: Multiphase flow properties for Model 1. **a** Capillary pressure measurements and reference curve using a Brooks and Corey (1964) function. **b** Initial capillary pressure curves, computed from the reference curve using Leverett scaling (see main text). **c** Relative permeability data (squares and S_w^5 model) and our fitted Corey model. **d,e** Relative permeability of gas and water, respectively. The drainage curve is shown as a solid line, while the bounding imbibition curve is shown for sands ESF and G as a discontinuous line. No relative permeability hysteresis was considered for the water phase.

Brooks and Corey 1964) of the form $k_{rw} = (S_w^*)^a$ and $k_{rg} = c(1 - S_w^*)^b$ (Fig. 3.3c). The fitted exponents a and b are 4.2 and 1.4, respectively, while c is 0.97. We assumed that the difference in relative permeability of different sands is the result of different irreducible water saturation only (see Fig. 3.3d,e). For each of our sands, S_{wc} was obtained from Timur (1968) as $S_{wc} = 0.01 \times 3.5\frac{\phi^{1.26}}{k^{0.35}} - 1$, where ϕ is in percent and k in mD. This model was used to compute S_{wc} for both the p_c and k_r curves.

In CO_2 storage, secondary imbibition occurs where the water displaces buoyant gas at the trailing edge of the CO_2 plume, disconnecting part of the CO_2 body into blobs and

ganglia and rendering them immobile (Juanes et al. 2006, and references therein). This means that the maximum water saturation that can be achieved during imbibition equals 1 - S_{gt} (the trapped gas saturation). Here, we used measurements in sandpacks from Pentland et al. (2010) to determine S_{gt}. In particular, we fitted Land (1968)'s model with the form $S^*_{gt} = \frac{S^*_{gi}}{1+CS^*_{gi}}$, where $S^*_g = \frac{S_g}{1-S_{wc}} = 1 - S^*_w$, S_{gi} is the gas saturation at flow reversal, and C is Land's trapping coefficient with a value of 5.2 in our fit. Although Pentland et al. (2010) report that the best fit is achieved with the Aissaoui (1983) and Spiteri et al. (2008) models (cf. their Fig. 5), Land's model was chosen here given that most relative permeability hysteresis models build on this one (see next paragraph).

Nonwetting phase trapping contributes to irreversibility of the relative permeability and capillary pressure curves (hysteresis). Here, we accounted for this mechanism in the gas relative permeability due to its importance in subsurface CO_2 migration (Juanes et al. 2006, and references therein). In particular, we used Land's (1968) model to compute the bounding imbibition curve (see Fig. 3.3d), where S_{gt} is obtained as described above, and Killough's (1976) model to characterize the scanning curves. In Killough's model, the scanning curves are reversible, such that the relative permeability at $S_g < S_{gi}$ no longer depends on the displacement type.

Model 2 (M_2)

This model had access to local, ex-situ measurements of single-phase petrophysical properties, i.e., porosity and intrinsic permeability (see sect. 3.2.1 and Tab. 3.1). Comparing with Tab. 3.3, it can be seen that our estimation for Model 1 above was correct to the order of magnitude, but resulted in smaller values: porosity $\in$ [85, 93]% and permeability $\in$ [53, 84]% of the local measurements.

Capillary pressures and relative permeabilities were obtained using the same procedure described above for Model 1. The slight differences with respect to the curves shown in Fig. 3.3b,d,e come from the porosity and permeability values used in the Leverett scaling and to determine S_{wc}, which were taken from Tab. 3.1 instead. The obtained curves for Model 2 are provided in Fig 3.4.

Model 3 (M_3)

This model was allowed access to all local, ex-situ measurements (see Tab. 3.1). Initial porosity and permeability remain unchangded with respect to Model 2. Capillary pressure curves were obtained by scaling the reference curve described in sect. 3.3.2 and shown in Fig. 3.3a using the measured entry pressure (sect. 3.2.1). The scaling followed the model $p_{cs}(S_w) = p_{cr}(S_w)\frac{p_e}{p_{er}}$, where p_e is the measured entry pressure for each sand, and p_{er} is the reference curve entry pressure. The obtained curves are shown in Fig. 3.5a.

Relative permeabilities were computed following the same procedure described for Model 1 above. In this case, however, each sand type was assigned the measured S_{wc} and S_{gt} values (see Tab. 3.1). This led to differences in both the drainage and imbibition curves, as shown in Fig. 3.5.

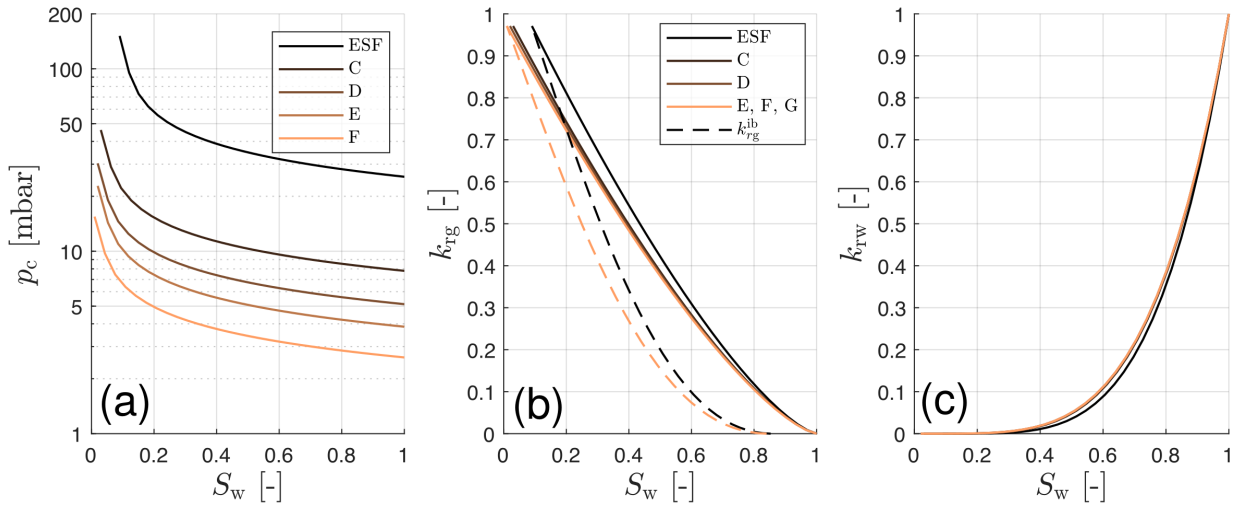

Figure 3.4: Multiphase flow properties for Model 2. **b** Initial capillary pressure curves, computed from the reference curve using Leverett scaling (see main text). **b,c** Relative permeability of gas and water, respectively. The drainage curve is solid, while the bounding imbibition curve is shown for sands ESF and G as a discontinuous line. No relative permeability hysteresis was considered for the water phase.

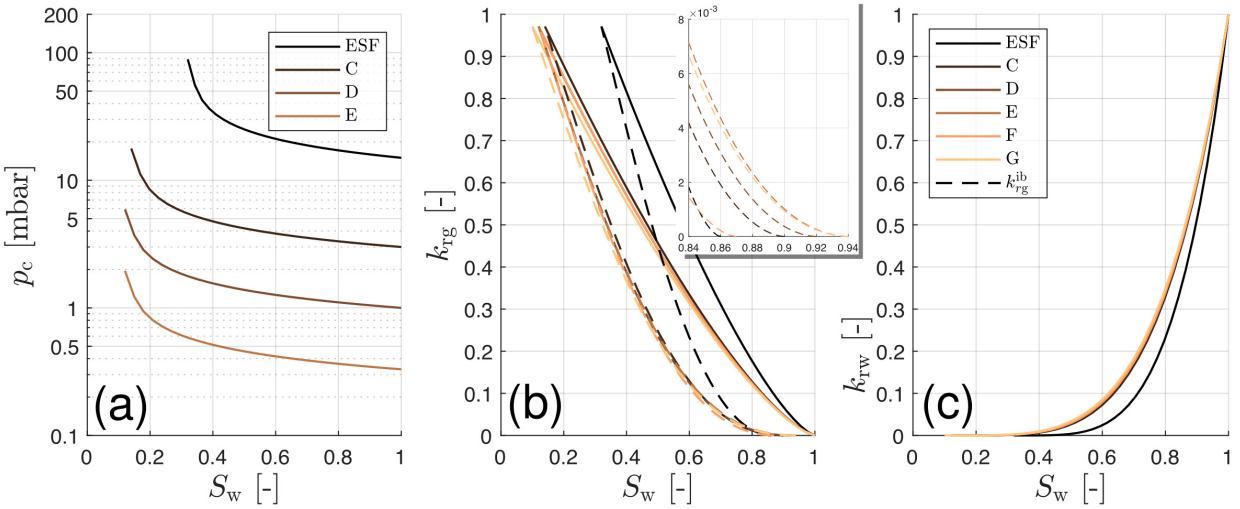

Figure 3.5: Multiphase flow properties for Model 3. **b** Initial capillary pressure curves, computed according to the entry pressure determined experimentally (see sect. 3.2.1). **b,c** Relative permeability of gas and water, respectively, according to the endpoints determined experimentally (sect. 3.2.1). The drainage curves are solid, while the bounding imbibition curves are shown as a discontinuous line. The inset in **b** is a zoom view around the trapped gas saturation. No relative permeability hysteresis was considered for the water phase.

3.3.3 Model calibration

Concordance between results obtained with each simulation model (1 to 3) and the validation experiment in Tank 1 (A1, see sect. 3.2.4) is quantitatively assessed by comparing the following quantities (see Fig. 3.6):

1. At $t = 55$ min (end of injection in port I_1): Areas occupied by free-phase CO_2, and dyed water with dissolved CO_2 in the bottom F reservoir.

2. At $t = 154$ min (end of injection in port I_2): Areas occupied by free-phase CO_2, and dyed water with dissolved CO_2, in the middle and top F reservoirs.

3. Time at which the first finger touches the tank bottom.

4. Time at which the first finger (sinking from the top F reservoir) touches the middle C sand.

Experimental values for points 1-2 were obtained by computing areas from time-lapse images using a vector-graphics software. Careful visual inspection of color-enhanced images was used to distinguish between free-phase CO_2 (white) and dyed water with dissolved CO_2 (yellowish orange to red), and to identify the times for points 3-4 above. Error in experimental values was estimated to be $\leq 5\%$, based on repeated measurements (points 1-2), and ~ 5 min, based on timelapse image comparison (points 3-4). In the simulation models, the threshold gas saturation and CO_2 concentration in water used to compute areas were $S_g > 10^{-3}$ and $C_{CO_2} > 15\%(C^{max}_{CO_2}) \approx 0.2$ [kg/m^3], respectively. The C value was chosen after a shape comparison of the region with dissolved CO_2. A smaller value of $C_{CO_2} > 0.05$ [kg/m^3] was selected to determine finger times for points 3 and 4 above. Fig. 3.6 shows an overview of the experimental values for points 2 and 3, while Fig. 3.12 in Sect. 3.4.2 shows the full comparison with the history-matched/calibrated simulation models.

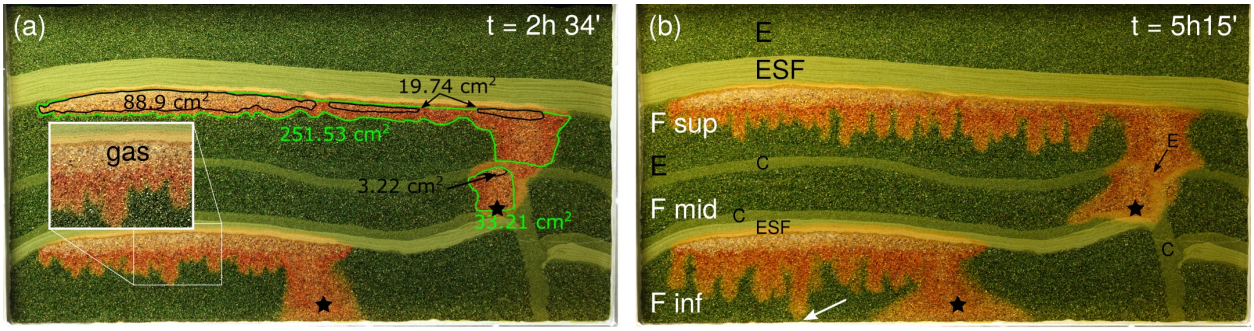

Figure 3.6: Front panel view of Tank 1, showing quantities and times for history matching of numerical models to Experiment A1. **a** shows areas with gaseous CO_2 (free-phase, black contours) and dyed water with dissolved CO_2 (green contours) at the end of injection. Location of injection ports is shown with a star. **b** shows the time and location where the first finger touches the bottom of the tank (white arrow), as well as the different lithological units. Note the three F reservoirs labeled 'inf', 'mid' and 'sup', mentioned in the text and other figures.

The experiment was conducted first. Afterwards, the process consisted of running simulation models 1 to 3, in parallel, starting with the petrophysical properties described in sect. 3.3.2. Given the number of uncertain variables (four petrophysical properties for each lithological unit, the diffusion coefficient and the injection rate) and the time required to complete a single simulation, a manual history matching method was employed. At the end of each run, quantities 1-4 above were compared and one or more properties were manually changed based on observed concordance and domain knowledge. During the first few runs,

only quantities 1 and 2 above were compared. After obtaining a satisfactory areal match, petrophysical properties were further adjusted to match quantities 3 and 4.

3.4 Results

In sect. 3.4.1, we present the results of the first simulation of Experiment A1 with each model and property values detailed in sect. 3.3.2. Then, we detail the calibration of simulation models using Experiment A1, and assess the value of local data to history-match CO_2 storage simulation models (sect. 3.4.2). Finally, we apply these matched models to Experiment A2, analog for a longer injection in the same geology (sect. 3.4.3), and to Experiment B1, analog for a larger-scale injection in a different geologic setting (sect. 3.4.3). We use simulations of Experiments A2 and B1 to assess the forecasting ability of simulation models in different conditions.

3.4.1 Initial model results

Fig. 3.7 shows the comparison between Experiment A1 and the first run with each model, at times indicated in sect. 3.3.3. Numerous differences are evident between the experiment and models 1 and 2, while Model 3 is much closer to the experiment. In particular, models 1 and 2 overestimate the extent of CO_2-rich brine and underestimate the amount of gaseous CO_2 in all F reservoirs (refer to Fig. 3.6 for location). Model 3 approximates much better the areal extent of gaseous CO_2 in all regions, as well as the CO_2-rich brine in the middle and upper F reservoirs. Model 2 provides the closest finger migration times (points 3 and 4 in sect. 3.3.3), although this was not evaluated in the first run, as discussed below.

Petrophysical properties for models 1 and 2 were obtained from references in sect. 3.3.2, which also used silica sands with similar grain sizes. However, despite the relatively homogeneous nature of our quartz sands, Model 3 is significantly more concordant. This result stems from natural sand variability and highlights the difficulty in establishing general, representative elementary volume-scale properties for porous media (see, for instance, Hommel et al. 2018; Schulz et al. 2019, for a discussion on intrinsic permeability). Additionally, results in Fig. 3.7 highlight the need for conducting sand/rock-specific measurements, even in the case of well-sorted, homogeneous sediments.

3.4.2 Manual history matching and value of local data

Fig. 3.8 shows convergence of areas occupied by free gas (A_g) and water with dissolved CO_2 (A_d), according to sect. 3.3.3. Each iteration corresponds to a successive model with manually updated parameters, and the different F sand regions evaluated in each panel (a) to (f) are provided in Fig. 3.6. With the exception of A_d in the upper compartment, Model 3 is accurate since the beginning, and all areas were satisfactorily matched after four iterations. Conversely, Model 1 and 2 were significantly off the experimental reference during the first few iterations. Model 2, however, was accurate after five iterations, while Model 1 required seven iterations to give satisfactory areal estimates. The mean absolute error (MAE) over the six areal quantities presented in Fig. 3.8 is evaluated in Fig. 3.9, where it can be seen that,

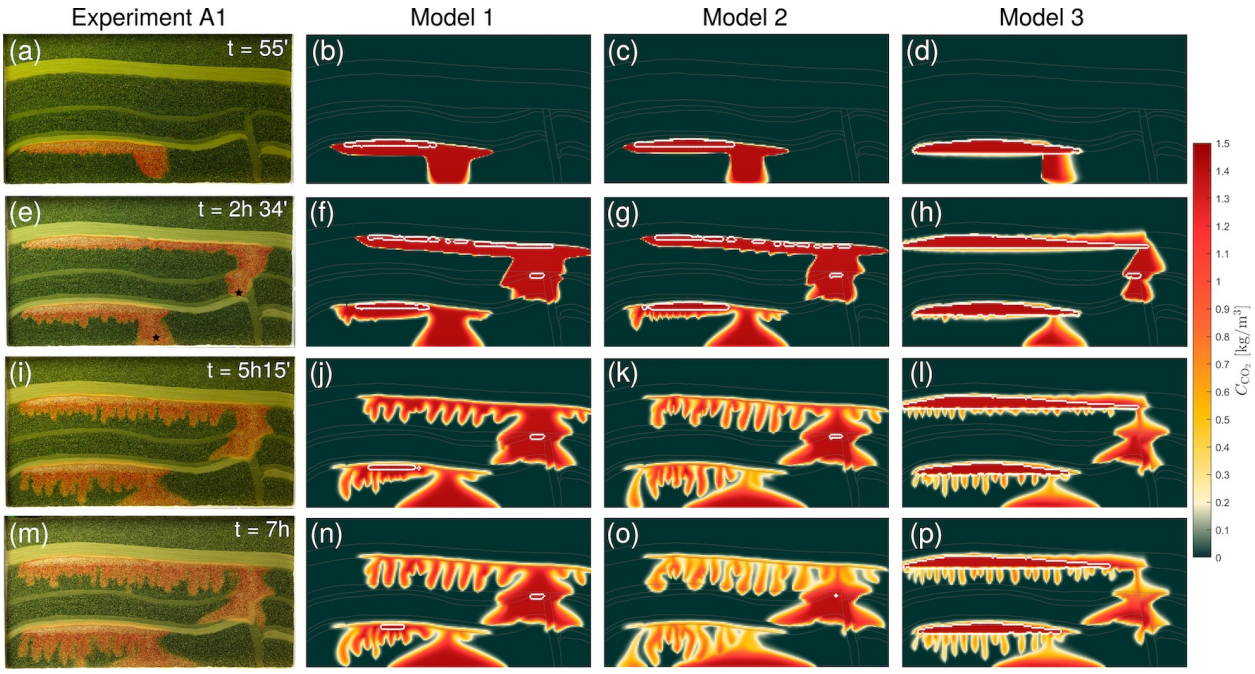

Figure 3.7: Comparison between Experiment A1 in Tank 1 (left column) and first run simulation results with models 1-3. Color map in simulation plots refers to CO_2 concentration in water, according to color bar. The white contours in simulation plots indicate $S_g = 10^{-3}$. **a-d**: end of injection in port 1. **e-h**: end of injection in port 2. **i-l**: time at which the first finger touches the tank bottom. **m-p**: time at which the first finger touches the middle C sand.

while all models are accurate towards the end (MAE $\in [5-10]$ cm^2), that required a six-fold improvement in models 1 and 2, but only two-fold in Model 3. As mentioned in sect. 3.3.3, $C_{CO_2} > 15\%(C^{max}_{CO_2}) \approx 0.2$ [kg/m^3] was used as threshold to determine areas. While the absolute values and error would change with a different C_{CO_2} threshold, we checked that the relative accuracy of our calibrated models does not with both $C_{CO_2} > 0.01$ and 0.1 [kg/m^3].

Agreement between simulations and experimental observations is readily seen in Fig. 3.10, where the 1:1 line indicates perfect concordance. The degree of concordance can be quantified by means of Lin's concordance correlation coefficient (CCC) (Lin 1989; Oldenburg 2018), which, for N-valued observation (x) and model (y) vectors (the six areal quantities) is computed as:

$$\mathrm{CCC} = \frac{2\sigma_{xy}}{\sigma_x^2 + \sigma_y^2 + (\overline{x} - \overline{y})^2} \tag{3.2}$$

Where $\overline{x}$ and $\overline{y}$ are the means, σ_x^2 and σ_y^2 the variances, and σ_{xy} the covariance, all calculated using $1/N$ normalization. Results in Fig. 3.10 show that model calibration results in very good concordance for all models (CCC ≥ 0.99).

Convergence of quantities 3 and 4 in sect. 3.3.3, the times at which the first finger touches the rig bottom and the middle C sand, respectively, are provided in Fig. 3.11. These times were only evaluated after a satisfactory areal match for quantities in Fig. 3.8 was achieved. Therefore, areas no longer change much in the last few iterations in Fig. 3.8. In Fig. 3.11, it can be seen that Model 2 and 3, which incorporated local intrinsic permeability

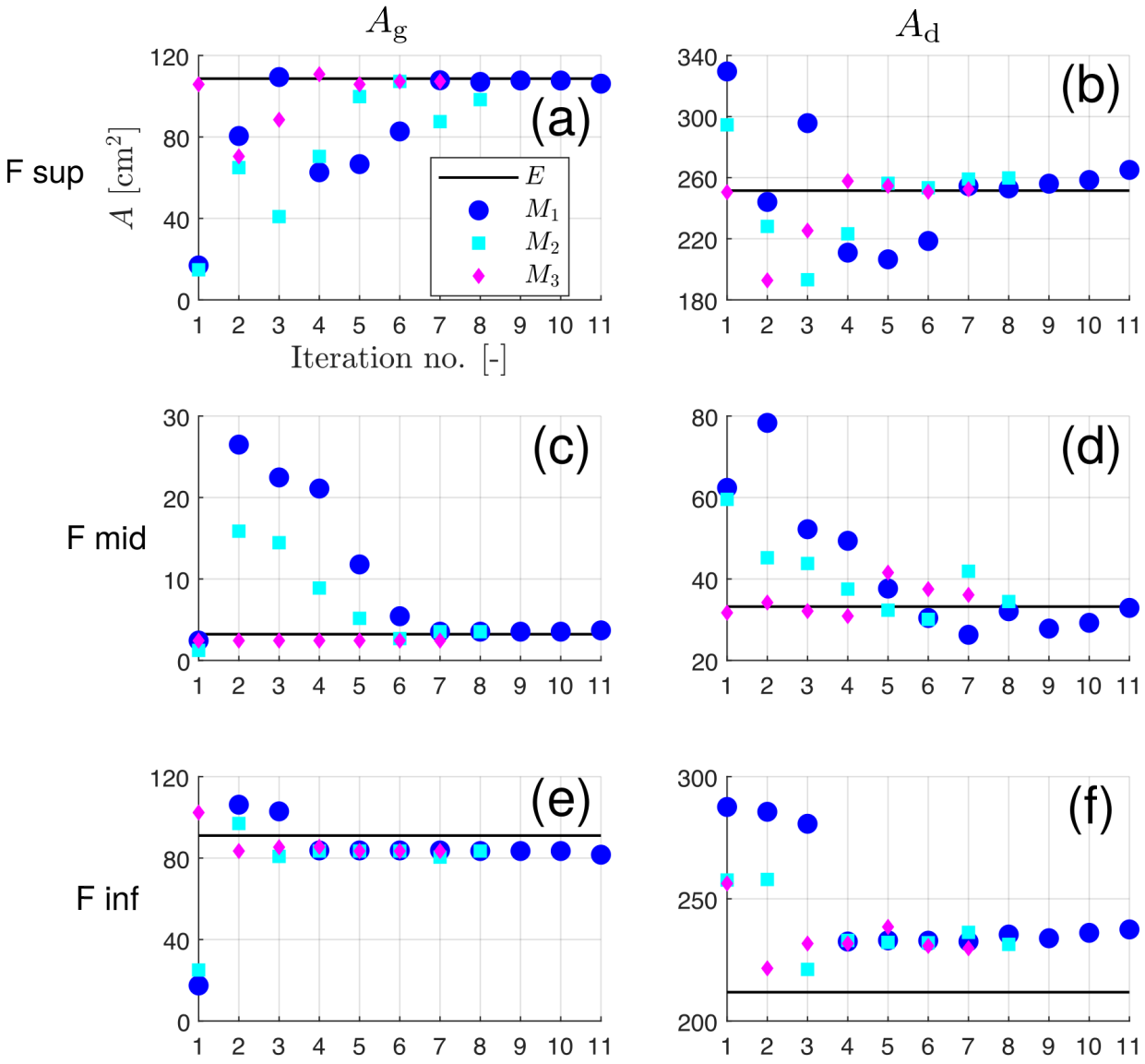

Figure 3.8: Convergence of areas occupied by free gas (A_g, left column) and water with dissolved CO_2 (A_d, right column), during the calibration of models 1-3 with Experiment A1. A_d includes area with gaseous CO_2 (see Fig. 3.6). Each iteration represents a new simulation run, and the experimental reference (E) is shown as a black line. Refer to Fig. 3.6 for region location, and to sect. 3.3.3 for calibration procedure. **a,b**: upper F sand. **c,d**: middle F sand. **e,f**: lower F sand.

measurements, were significantly closer to our experimental reference than Model 1. Initially, however, we observed that sinking of gravity fingers in the experiment was faster than our model values by a factor of ≈ 2. A satisfactory match of all quantities evaluated was achieved after 11, 8, and 7 iterations for models 1-3, respectively.

Overall, we find that Model 3, with access to local single-phase and multiphase flow properties, is closer to the experimental reference (i.e., more concordant) from the start. Model 1 started farthest, and required significantly more effort for calibration. After the calibration process, all models achieve very good concordance (CCC $\geq$ 0.99), based on

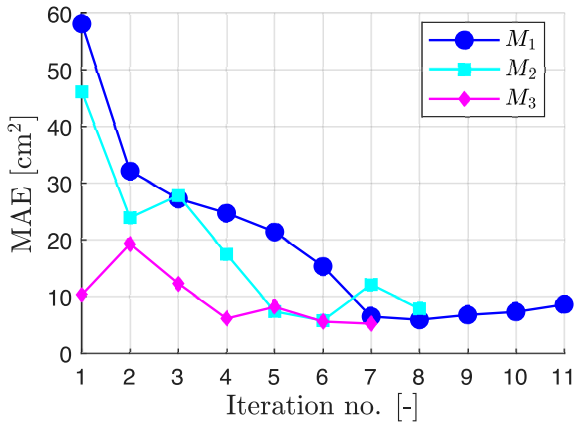

Figure 3.9: Convergence of mean absolute error over the six areal quantities measured during the calibration process. The error is computed with respect to experimental values. See Fig. 3.8 for areas measured, and refer to sect. 3.3.3 for calibration procedure.

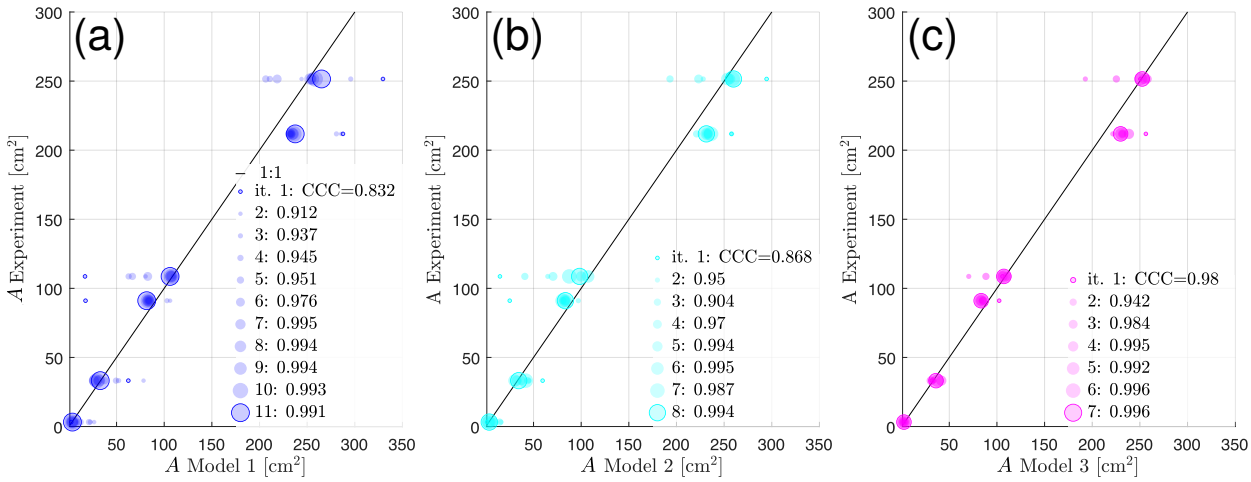

Figure 3.10: Concordance between successive model iterations and the experiment, based on six areal measures evaluated during the calibration. Lin's CCC (Lin 1989) is shown in the key of each subplot, computed according to Eq. 3.2. **a**: Model 1. **b**: Model 2. **c**: Model 3.

evaluated quantities (Fig. 3.10). The calibration shown in Fig. 3.8, 3.9, 3.10, 3.11 employs $D = 10^{-9}$ m^2/s in all model versions (M_1 to M_3). Injection rates (I_R) started at 2.0 ml/min for all three models, and were 1.6 ml/min, 1.8 ml/min and 1.75 ml/min, respectively, at the end of the calibration. I_R is slightly different because the goal was to obtain the best match with each model, considering I_R to be an uncertain variable. In sect. 3.4.3 below, the same I_R is used to make forecasts with all three models.

Tab. 3.4 compares the starting and final (matched) key petrophysical variables for each model. The models were successfully calibrated by adjusting intrinsic permeability and the capillary pressure curves (same shape, but scaled to higher or lower p_e) only. It was found that CO_2 migration was most sensitive to the properties of the F sand, were most of the CO_2 migration occurs, as well as the ESF seal, which structurally traps the CO_2

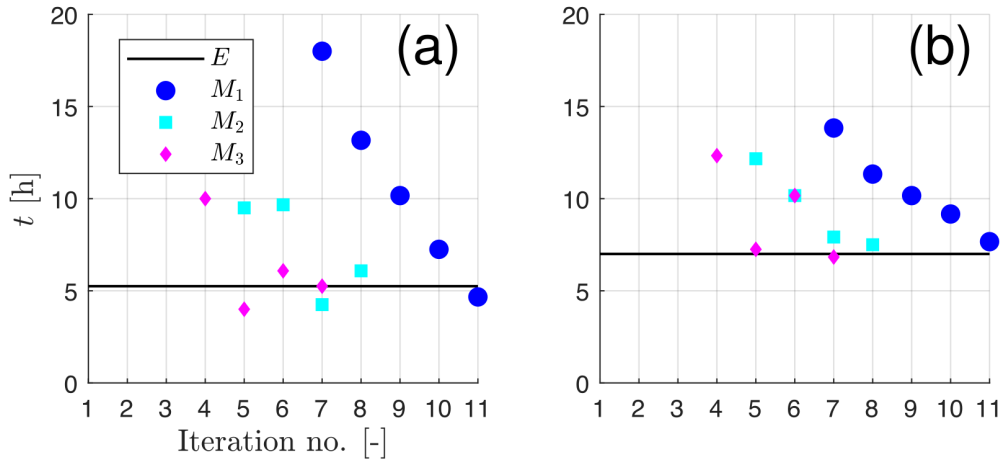

Figure 3.11: Convergence of times at which the first finger touches the bottom of the rig (**a**) and the middle C sand (**b**), during the calibration of models 1-3 with Experiment A1. Refer to sect. 3.3.3 for calibration procedure.

plume. In our matched models, p_e of ESF is about twice the measured value; this was required because the minimum saturation at which we can define p_e and ensure numerical convergence is $S_g \approx 10^{-4}$. Reality, however, is closer to a jump in p_c from 0 to p_e at an infinitesimally small S_g. Additionally, we found that concordance improved when using different values for the C and F sands in different model regions. In the case of the C sand, the explanation lies in the fault construction process, which may reduce porosity with respect to "natural" sedimentation of stratigraphic layers (Haugen et al. 2023). The increase in F sand permeability was required to match finger migration times, and is possibly compensating the absence of mechanical dispersion in the simulations. This is discussed in sect. 3.5. Our calibrated values are within the same order of magnitude of the ex-situ measurements (Tab. 3.4) and history-matched values for the porous medium in Tank 2 (Landa-Marbán et al. 2023, forthcoming).

Fig. 3.12 shows gas saturation (S_g) and CO_2 concentration (C_{CO_2}) maps at times at which quantities 1-4 described in sect. 3.3.3 are evaluated. Snapshots are provided for Model 3 only, since all three calibrated models were qualitatively very similar. It can be seen that CO_2 migration is successfully approximated by our numerical model. In detail, however, some differences are apparent: Firstly, sinking of CO_2-rich water from the bottom injector and horizontal migration along the bottom of the rig is faster in the model. This is due to the higher permeability that our numerical model requires in order to match the gravity fingering advance (cf. Tab. 3.4). Secondly, the experiment shows that denser, CO_2-rich water sinks with a rather compact front and closely spaced, wide fingers. Our model with constant $D = 10^{-9}$ m^2/s approximates all gravity-driven migration of the CO_2-rich water through thinner fingers, with the CO_2-saturated region receding with S_g. To better represent fingering widths, we also matched Model 3 with $D = 3 \times 10^{-9}$ m^2/s, used in sect. 3.4.3.

Table 3.4: Petrophysical properties for used quartz sands in Experiment A1. Methodology for local measurements is provided by Haugen et al. (2023), while starting property modeling is described in sect. 3.3.2. For each sand, measured (first row), initial (superscript i) and final (superscript f) values for each of our models is shown. For sand C, the second permeability value refers to the fault, if different from the rest. For sand F, the second permeability value refers to the middle F layer, if different from the rest. For Model 3, where property values are different, $M_{3,1}$ refers to the calibration with $D = 10^{-9}$ m^2/s and $M_{3,3}$ refers to $D = 3 \times 10^{-9}$ m^2/s.

Sand type / model	ϕ [-]	k [D]	p_e [mbar]	S_{wc} [-]	S_{gt} [-]
ESF	0.435	44	15	0.32	0.14
M_1^i	0.37	25	31.4	0.09	0.1468
M_1^f	0.37	6	31.4	0.09	0.1468
M_2^i	0.435	44	25.6	0.09	0.1468
M_2^f	0.435	44	25.6	0.09	0.1468
M_3^i	0.435	44	15	0.32	0.14
M_3^f	0.435	15	30	0.32	0.14
C	0.435	473	3	0.14	0.1
M_1^i	0.38	293	9.3	0.03	0.1565
M_1^f	0.38	293, 27	4.6	0.03	0.1565
M_2^i	0.435	473	7.8	0.03	0.1565
M_2^f	0.435	473, 158	2.6	0.03	0.1565
M_3^i	0.435	473	3	0.14	0.1
M_3^f	0.435	473, 118	4.5	0.14	0.1
E	0.45	2005	-	0.12	0.06
M_1^i	0.39	1528	4.1	0.01	0.16
M_1^f	0.39	1528	0.5	0.01	0.16
M_2^i	0.45	2005	3.86	0.01	0.16
M_2^f	0.45	3008	0.58	0.01	0.16
M_3^i	0.45	2005	0.33	0.12	0.06
$M_{3,1}^f$	0.45	2406	0.33	0.12	0.06
$M_{3,3}^f$	0.45	3208	0.33	0.12	0.06
F	0.44	4259	-	0.12	0.13
M_1^i	0.39	2277	3.3	0.01	0.16
M_1^f	0.39	6540, 2907	0	0.01	0.16
M_2^i	0.44	4259	2.62	0.01	0.16
M_2^f	0.44	6814, 4259	0	0.01	0.16
M_3^i	0.44	4259	0	0.12	0.13
$M_{3,1}^f$	0.44	7240, 4685	0	0.12	0.13
$M_{3,3}^f$	0.44	9796, 4259	0	0.12	0.13

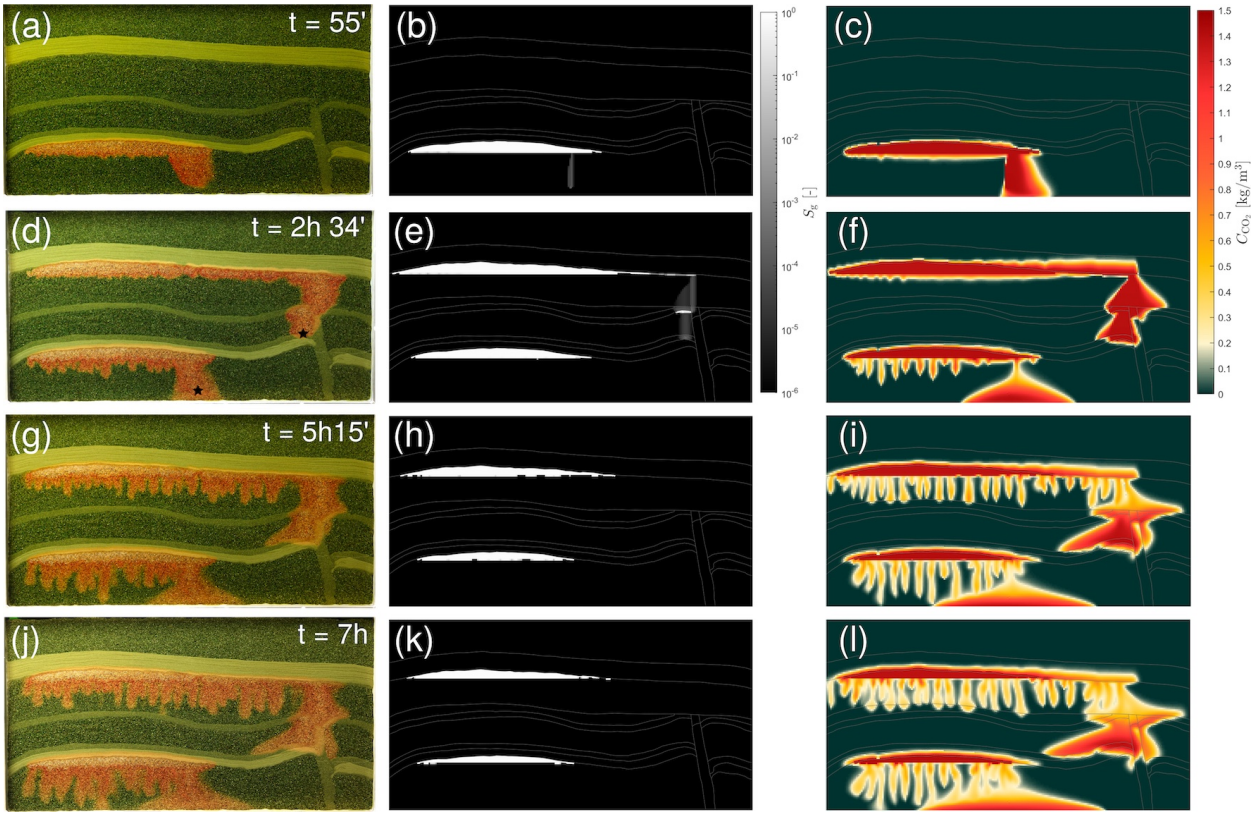

Figure 3.12: Comparison between Experiment A1 in Tank 1 (left column) and simulation results with Model 3 after calibration (gas saturation shown in middle column, and CO_2 concentration shown in right column). Location of injection ports shown by black stars in **d**. $D = 10^{-9}$ m^2/s. **a-c**: End of injection in lower port. **d-f**: End of injection in upper port. **g-i**: Time at which the first finger touches the rig bottom. **j-l**: Time at which the first finger touches the middle C layer.

3.4.3 Transferability: model forecasts

A key question after history matching a flow simulation model is whether the physical description has actually been improved, or whether parameters have been modified to match a set of specific observations only. By applying the history-matched models to a different injection protocol (Experiment A2 in Tank 1; refer to Tab. 3.2), and subsequently to a different geometry (Experiment B1 in Tank 2), this can be assessed to some extent.

Analog for a longer CO_2 injection in the same geologic setting

This case illustrates concordance of our history matched models in a much longer injection in the same geology (Experiment A2). Before simulating this case, we observed that the trapped gas column against the fault in the experiment was different than what could be achieved with our previous p_e for models 1-3 (Tab. 3.4). Because the capillary properties of the C sand in the fault were not directly involved in Experiment A1, we increased p_e in our calibrated models for that specific region (p_e = 5 mbar against the lower F sand, and 3.5 mbar against the middle F sand). All other parameters were taken from the values calibrated to match Experiment A1.

Evaluation was performed at the end of injection, at $t = 4$ h 48 min, with a single run with models 1-3. I_R and D were set to the same value in all three models: 1.7 ml/min and 10^{-9} m/s^2, respectively. The experimental result is shown in Fig. 3.13a, while the simulation with Model 3 is depicted in Fig. 3.13b,c. We observe that the general distribution of CO_2 is close to the experimental truth. However, the experiment shows a compact sinking front of the CO_2-rich water without fingers; in our model, gravity fingering is apparent at this stage and fingers are close to the bottom of the rig. Additionally, CO_2-saturated brine touches the right boundary in the upper F reservoir, which does not occur in the experiment. This is due to capillary breach of the C sand above the middle F reservoir, as shown in Fig. 3.13b, and can be avoided by reducing the gas saturation value at which p_e is defined, or by increasing p_e.

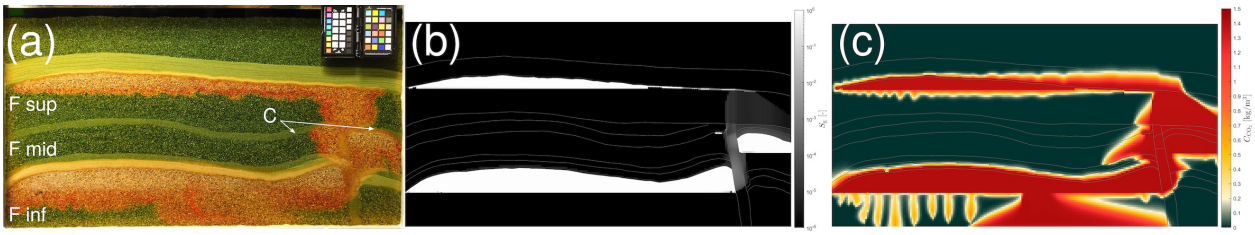

Figure 3.13: Comparison between Experiment A2 in Tank 1 (**a**) and simulation results with Model 3 (**b,c**) at the end of the injection phase ($t = 4$h 48 min).

The comparison of areal quantities is provided in Fig. 3.14, and demonstrates good to very good concordance. Model 2 (MAE = 16 cm^2, CCC = 0.996) and 3 (MAE = 14.54 cm^2, CCC = 0.996) are similarly accurate and slightly better than Model 1 (MAE = 20.18 cm^2, CCC = 0.988), but there are no marked differences.

Analog for a larger-scale CO_2 injection in a different geologic setting

Finally, we compare the forecasting ability of our calibrated models against Experiment B1, conducted in a larger-scale, more complex geology (Fig. 3.1e) (Flemisch et al. 2023). Similar to sect. 3.4.3, our goal is to assess the forecasting ability of our calibrated models—without changing their properties. However, given that sand D controls migration in the lower fault (see Fig. 3.2e) and it was not present in our calibrated models, we allowed one change for models 1 and 2, which did not have access to local p_c measurements. This means that we ran an initial simulation of this experiment with Model 1 and 2, and then adjusted the p_c curve of the D sand. The selected curve lies at $\approx \frac{1}{3}$ of the $p_c(S_w)$ shown in Fig. 3.3 and Fig. 3.4, respectively.

Next, we evaluate concordance of models 1-3 by comparing them to the experimental truth after a single run. Evaluation is performed over the total duration of the experiment (120 h), which is simulated with the same I_R (10 ml/min) and D (10^{-9} m^2/s) in all three models (M_1, M_2, $M_{3,1}$). Additionally, a run with $D = 3 \times 10^{-9}$ m^2/s was completed with Model 3 ($M_{3,3}$) to better approximate finger widths, as noted in sect. 3.4.2.

Gas saturation and CO_2 concentration maps at the end of injection with Model 1 are shown in Fig. 3.15a and Fig. 3.15b, respectively. The full visual comparison is provided in Fig. 3.16. We make the following observations:

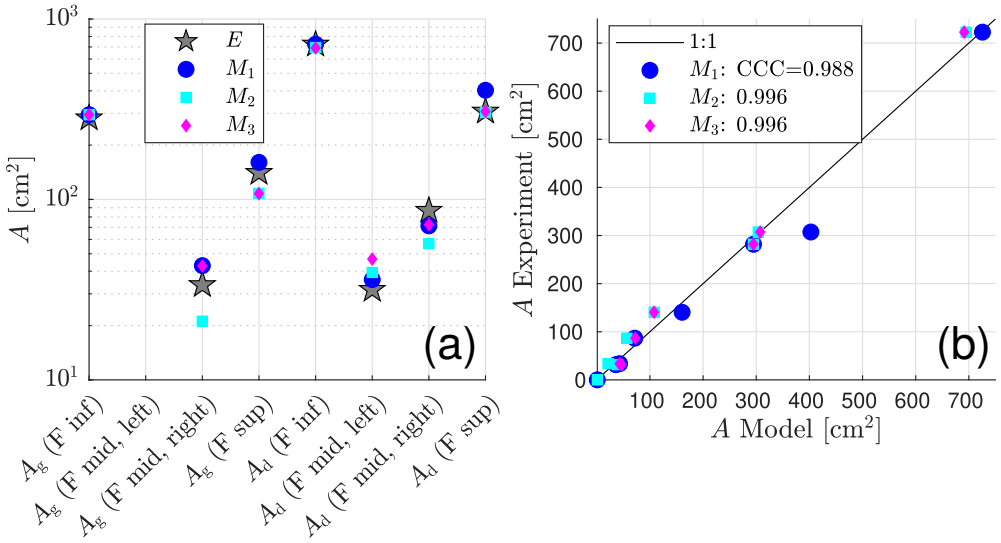

Figure 3.14: **a**: Comparison of areas occupied by free gas (A_g) and water with dissolved CO_2 (A_d) for Experiment A2 in Tank 1. Experimental reference shown with a star (E). A_g (F mid, left) not shown because values are very close to 0. Refer to Fig. 3.6 or Fig. 3.13a for region location. **b**: Concordance plot for each of the three models, using the same areal quantities as in **a**. Lin's CCC (Lin 1989) is shown in the key, according to Eq. 3.2.

- At the end of injection (t = 5 h), all three models forecast some migration of CO_2 into Box B. Model 2 (Fig. 3.16c) and 3 (Fig. 3.16d) underestimate the amount of CO_2, while Model 1 (Fig. 3.16b) overestimates the amount of CO_2 in the top C sand.
- Also at the end of injection, all models forecast faster sinking of the CO_2-charged water tongue arising from the lower injector. This is due to the higher F sand permeability required to match finger advance (see sect. 3.4.2), particularly in Model 3 with $D = 3 \times 10^{-9}$ m^2/s.
- The speed at which CO_2-rich fingers sink is slightly faster in our models, compared to the experiment. As expected, Model 3, with a higher diffusion coefficient, displays thicker fingers, with closer widths to the experiment. Similar to our previous observations, the numerical models cannot approximate the compact, CO_2-rich water front closely trailing the fingers.
- Dissolution of CO_2 is underestimated by models 1 and 2, while it is closer, but overestimated, by Model 3.

Consistent with our approach described in sect. 3.3.3, quantitative analysis is provided by means of areal quantities over time in Fig. 3.17. Experimental values were obtained via segmentation of timelapse images, and the data was reported on a 1×1 cm grid where 0 is pure water, 1 is water with dissolved CO_2, and 2 is gaseous CO_2. The segmentation procedure is explained in Nordbotten et al. (2023), this issue. We then obtained the areas of each phase within Box A and B to generate Fig. 3.17 (refer to Fig. 3.15a for box location).

In Box A, which contains the main F reservoir and ESF seal, we observe very good concordance (accurate areas) during injection. Afterwards, Model 3 with $D = 3 \times 10^{-9}$ m^2/s

continues to follow the experiment closely, whereas the others overestimate gaseous CO_2. Note that the PVT properties of our fluids are the same in all models; differences arise due to (1) higher sand F S_{wc} in Model 3, and higher sand F k in Model 2 and especially Model 3 ($D = 3 \times 10^{-9}$ m^2/s), compared to Model 1, which allow greater convective mixing (Ennis-King and Paterson 2005)(Tab. 3.4); and (2) lower p_e and higher k of sand ESF in Model 2 (Tab. 3.4), which allows some CO_2 migration into the seal (Fig. 3.16). In Box B (Fig. 3.17d-f), Model 1 and Model 3 with $D = 10^{-9}$ m^2/s are able to approximately track the experimental truth during injection. However, our models without dispersion cannot capture the areal increase of CO_2-rich water that occurs afterwards (cf. Fig. 3.16).

To put these results in perspective, Fig. 3.18 provides a comparison with results submitted by the international benchmark study (IBS) participants, as well as Experiment B1 (Flemisch et al. 2023). Fig. 3.18 presents, for each datapoint, mean Wasserstein distances to experiments and forecasts (simulations by IBS participants). Specifically, the Wasserstein metric (W) measures "the minimal effort required to reconfigure the probability mass of one distribution in order to recover the other distribution" (Panaretos and Zemel 2019). We expect $W \to 0$ for two samples from the same distribution, given enough values, and two samples to be more similar or concordant the closer W is to 0. To calculate distances shown in Fig. 3.18, the cell mass density in a 1×1 cm grid was estimated for all simulations and experiments, and then normalized. Therefore, this metric provides a measure of the overall degree of agreement (i.e., in the whole domain). Resulting distances were dimensionalized using the total CO_2 mass in the system, such that the units are grams × centimeter, with values < 100 gr·cm and < 50 gr·cm representing good concordance and very good concordance, respectively. Details and code are provided by Flemisch et al. (2023). In Fig. 3.18, it can be seen that M_1-M_3 are comparable to or better than the best forecasts by IBS participants. M_1 and $M_{3,1}$, in particular, achieved very good concordance.

Further evaluation of simulation model concordance, including comparison with model results before calibration, mass quantities and error measures, is provided in Appendix A.1. From this analysis (sect. 3.4.3 and Appendix A.1), we find that:

- All matched models approximate well CO_2 migration and distribution in the domain, seal capacity, and onset of convective mixing. M_1 and $M_{3,1}$ are most concordant to experiments (Fig. 3.18).
- Calibrated models are able to accurately estimate specific quantities during the injection phase, yet they accumulate higher errors later on (Fig. 3.17 and Appendix A.1.2).
- Similar to Experiment A1, the calibration procedure significantly improved the concordance of M_1 and M_2 with the experiment (Fig. A.1 and Fig. 3.16). In Box A, calibration also improved concordance for M_3 (Fig. A.2 and Fig. A.6). Overall, however, matched $M_{3,1}$ and $M_{3,3}$ are less concordant than their initial versions, which were already in very good agreement with the experiment (Fig. A.3 and Fig. 3.18).

In summary, calibrated models are transferable to a different operational setting or geologic structure, as long as sediments and trap systems remain the same (Experiment A2 and Box A in Experiment B1). Where reservoir connectivity is provided by heterogeneous structures with uncertain properties, accurate deterministic estimates of CO_2 migration are

unlikely; models calibrated elsewhere (Experiment A1) were not accurate in our test (Box B in Experiment B1). Given unlimited computational time, the forecasting capability of numerical models calibrated with published data appears similar to those having access to local measurements; the main value of local data lies in reducing the time required for history matching. Obtained results suggest that history matching worsened M_3 forecasts in a different setting (Experiment B1). Therefore, forecasts in a given geologic setting may benefit more from local measurements and accurate physics, rather than history matching, unless historical data of the same setting is available. This is because CO_2-brine flow is very sensitive to variations in petrophysical properties such as capillary pressure, which will change in different areas, even if the geology is similar.

3.5 Discussion

In the FluidFlower, strong buoyancy and high permeability lead to persistent appearance and disappearance of fluid phases, as the gas migrates upward and dissolves in the water; coupled with other two-phase flow nonlinearities, these aspects make this problem difficult to solve numerically (e.g., Lie 2019). Comparison between the number of nonlinear iterations and the strength of different physical mechanisms (flow rates, buoyancy, capillarity and dissolution) are presented in Appendix A.2. A clear correlation can be seen between flow rates and number of iterations. However, buoyancy, capillarity and dissolution all appear to be playing a role, and it is not straightforward to discern which effect dominates; hence, this is a topic that requires further study. We note that difficulties with the convergence of the nonlinear solver have been reported by all participants in the international benchmark study (Flemisch et al. 2023). As hinted in sect. 3.3.1, we addressed this by optimizing linear solver time, reducing the time-step length, increasing the number of time-step cuts and relaxing `MRST`'s maximum normalized residual where required.

In a 2D isotropic medium and assuming uniform flow, the hydrodynamic dispersion coefficient ($\underline{\underline{D}}_{\mathrm{h}}$) can be modeled as $\underline{\underline{D}}_{\mathrm{h}} = \left[\begin{smallmatrix} \alpha_{\mathrm{L}}\overline{u} & 0 \\ 0 & \alpha_{\mathrm{T}}\overline{u} \end{smallmatrix}\right]$, where α_{L} and α_{T} are the longitudinal and transverse dispersivity, respectively, and $\overline{u}$ is the average Darcy velocity (Bear 1972). Assuming dispersivities $\geq 10^{-3}-10^{-2}$ m (Garabedian et al. 1991; Gelhar et al. 1992; Schulze-Makuch 2005) and $\overline{u} \approx 3\times10^{-6}$ m/s (from our simulations), we get $\underline{\underline{D}}_{\mathrm{h}} \in [3\times10^{-9},\, 3\times10^{-8}]$ m^2/s or larger; this means that $\underline{\underline{D}}_{\mathrm{h}} \geq D$ for the timescales considered (Riaz et al. 2004; Rezk et al. 2022). We also note that numerical dispersivity is on the order of the cell size ($h \approx 4$ mm in Tank 1, and ≈ 5 mm in Tank 2), so it is likely smaller than hydrodynamic dispersion. Numerical diffusion can be approximated as uh, which yields maximum values $\sim O(10^{-7}\,\mathrm{m}^2/\mathrm{s})$ (water phase). However, using the mean of the 75$^{\mathrm{th}}$ percentile flow velocity over all time-steps, we obtain $\sim O(10^{-9}\,\mathrm{m}^2/\mathrm{s})$. Therefore, we estimate that numerical diffusion is lower than physical diffusion almost everywhere in our simulations. Previous work suggested that hydrodynamic dispersion in homogeneous sediments can be accounted for by increasing D (Riaz et al. 2004; Riaz et al. 2006), as done here. However, our analysis shows that the spreading of CO_2-rich water during convective mixing can be loosely, but not accurately, represented by molecular diffusion. Given (1) the dominance of convective mixing on solubility trapping (Ennis-King and Paterson 2005; Neufeld et al. 2010; MacMinn and Juanes 2013); (2) heterogeneity of many natural reservoirs, which increases the importance

of dispersion (Riaz et al. 2006; Bear 2018); and (3) the acceleration of CO_2 dissolution due to dispersion, as observed here and by others (e.g., Hidalgo and Carrera 2009), it is important to quantify the balance between diffusion and dispersion to estimate CO_2 trapping.

Our study of CO_2 injection and migration in unconsolidated sands at atmospheric p, T conditions captures the CO_2-water system dynamics at short to intermediate timescales: buoyancy-driven flow and structural trapping (Bachu et al. 1994; Bryant et al. 2008; Hesse and Woods 2010; Szulczewski et al. 2013), residual trapping (Juanes et al. 2006; Burnside and Naylor 2014) and convective mixing and dissolution trapping (Weir et al. 1996; Ennis-King and Paterson 2005; Riaz et al. 2006; Neufeld et al. 2010; Hidalgo et al. 2012; MacMinn and Juanes 2013; Szulczewski et al. 2013). Due to the very large sand permeability ($10^2 - 10^4$ D), convective mixing and dissolution dominate CO_2 trapping. With respect to values at ~ 1 km depth ($p \sim 100$ bar, $T \sim 40$ C), the dynamic viscosity and density of CO_2 are $\approx 1/3$ and 3×10^{-3}. Conversely, previous studies with similar setups used analogous fluids with density and viscosity ratios similar to supercritical CO_2-brine (Trevisan et al. 2017; Krishnamurthy et al. 2022). Dynamics observed in these systems are similar to ours, with vertical migration of CO_2 dominated by buoyancy and lateral spreading of CO_2 plumes with a main tongue at the top of the aquifer or high permeability layer. A quantitative scaling analysis of the FluidFlower (Tank 2) was performed by Kovscek et al. (2023), who showed that scaling of physical mechanisms to the field scale is possible. Compared to three CO_2 storage projects (Northern Lights, Sleipner and In Salah) the vertical dimension of the storage reservoir is exaggerated 2 to 3 times. Temporally, 1 h in the FluidFlower is equivalent to $\sim 100 - 400$ y in the field; thus, the experiment in Tank 2 (120 h) covers well the injection and post-injection periods. Similar to the FluidFlower, Kovscek et al. (2023) estimate the onset of convective mixing to occur during injection in high-permeability formations like the Utsira Sand (Sleipner). This analysis demonstrates that observations made in the FluidFlower can be used to describe field-scale fluid dynamics and quantify forecasting accuracy.

Our models retained some error at the end of the calibration phase, which is a known problem of manual history matching (Oliver and Chen 2011). Consistent with previous findings (e.g., Fisher and Jolley 2007), results show that model 2 and 3, which had access to local data, achieved faster match to the experimental truth than model 1 (sect. 3.4.2). However, all models seem to have similar forecasting capability (sect. 3.4.3). Subsurface heterogeneity and time constraints may explain why, in practice, it is critical to include local data to achieve history matching, and, especially, concordant forecasting (e.g., Gosselin et al. 2003; Fisher and Jolley 2007; Myers et al. 2007; Kam et al. 2015; Avansi et al. 2016). Calibration with Experiment A1 decreased overall concordance of model 3 to Experiment B1 (but improved concordance in Box A), compared to forecasts with initial (measured) parameter values. We interpret this to be the result of fluid migration in Experiment A1 being controlled by different units than in Box B in Experiment B1. Therefore, local measurements are paramount, especially if historical data in the trap system of interest are not available.

Additionally, we did not quantify uncertainty in history-matched models due to the availability of a ground truth. In general, however, this is necessary to manage reservoir operations (e.g., Aanonsen et al. 2009; Oliver and Chen 2011; Jagalur-Mohan et al. 2018; Jin et al. 2019; Liu and Durlofsky 2020; Santoso et al. 2021, and references therein). It is also important to note that history-matched models may have grid-size dependencies (see Appendix A.3), which may require that the grid used to make forecasts, if different or en-

compassing additional regions, maintain a similar resolution. Finally, multiphase flow in poorly-lithified sediments is non-unique (Haugen et al. 2023), which also contributes to uncertainty. Therefore, it seems prudent to adopt a probabilistic perspective when estimating subsurface CO_2 migration. This is consistent with results in Fig. 3.18 and Flemisch et al. (2023): in the highly-resolved and geologically simple FluidFlower (compared to the subsurface), forecasts by different simulation groups show large spread.

3.6 Conclusions

We performed experiments (sect. 3.2) and numerical simulations (sect. 3.3) of CO_2 migration in poorly-lithified, siliciclastic sediments at the meter scale. Three simulation model versions, with access to different levels of local data, were manually history-matched to the experiments (sect. 3.4.1, 3.4.2), and then used to make forecasts (sect. 3.4.3). The main findings are:

1. The time required to history match model 3 (access to both single-phase and multiphase measurements) is lower than model 2 (access to local single-phase measurements), which is lower than model 1 (no access to local petrophysical measurements).

2. All simulation models achieve a satisfactory qualitative match throughout the experiments. Quantitatively, forecasting capability of models 1-3 appears similar: in specific domain regions, models were close to the experimental truth during CO_2 injection, and accumulated larger errors afterwards, especially where heterogeneous structures control CO_2 migration.

3. Overall forecasts with model 3 after calibration in a similar, but not identical, geologic setting were less accurate than forecasts made with measured values. This emphasizes the importance of local measurements and history matching in the same geologic setting.

4. The addition of a constant molecular diffusion coefficient allows matching convective finger widths to experimental observations. However, simulations without dispersion cannot approximate the compact, CO_2-rich sinking front closely trailing convective fingers in our experiments.

Simulation models were not always accurate. Given the degree of control in our study, it seems prudent to quantify uncertainty when assessing subsurface CO_2 migration in the field using numerical models. Results presented in sect. 3.4 suggest that confidence can be increased by:

- Obtaining local data. Because numerical models are computationally expensive to run, acquiring local data facilitates history matching.

- Quantifying petrophysical parameter uncertainty, because CO_2 migration in the subsurface can be very sensitive to changes in petrophysical parameters.

- Testing sensitivity to petrophysical parameters in different model regions. Again, due to computational time and difficulty of assessing parameter uncertainty throughout

the computational domain, model regions or structures controlling migration should be identified, so that modeling efforts can focused appropriately.

- Using historical data from the same setting where forecasts are to be made, given that significant petrophysical property differences can exist between similar settings.
- Including post-injection data when history matching, because forecasts' accuracy in specific model areas decreased with time for models calibrated with little post-injection data.
- Incorporating multiple scenarios of CO_2 migration, given the difficulty of achieving quantitatively accurate deterministic forecasts where heterogeneous structures are at play.

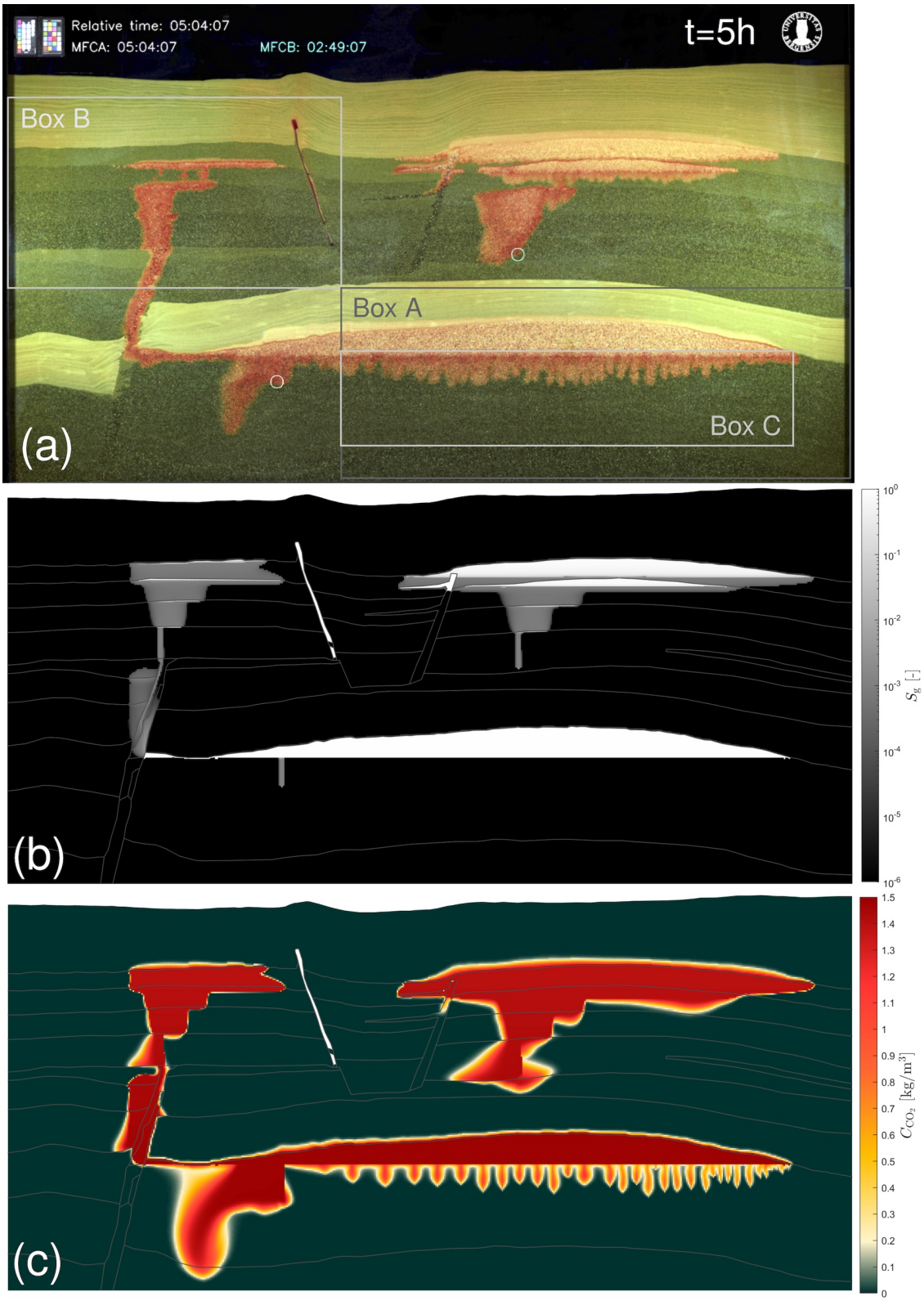

Figure 3.15: Comparison between Experiment B1 in Tank 2 (**a**) and simulation Model 1 (**b,c**) at the end of injection ($t = 5$h). Circles in **a** denote the location of injection ports.

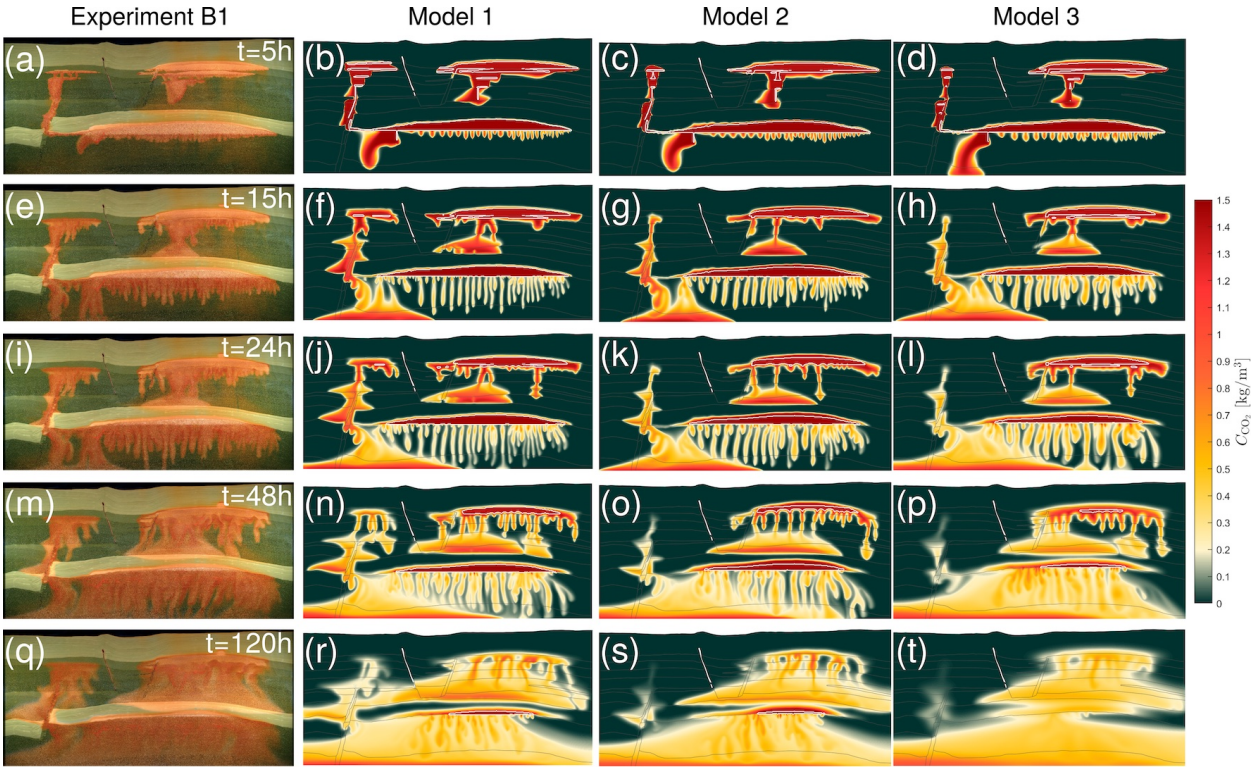

Figure 3.16: Comparison between Experiment B1 in Tank 2 (leftmost column) and CO_2 concentration maps for simulation models 1-3 (middle-left, middle-right and rightmost, respectively). $D = 10^{-9}$ m^2/s (Model 1 and 2), $D = 3 \times 10^{-9}$ m^2/s (Model 3). The white contours in simulation plots indicate $S_g = 10^{-3}$. **a-d** end of injection. **e-h** t = 15h. **i-l** t = 24h. **m-p** t = 48h. **q-t** t = 120h.

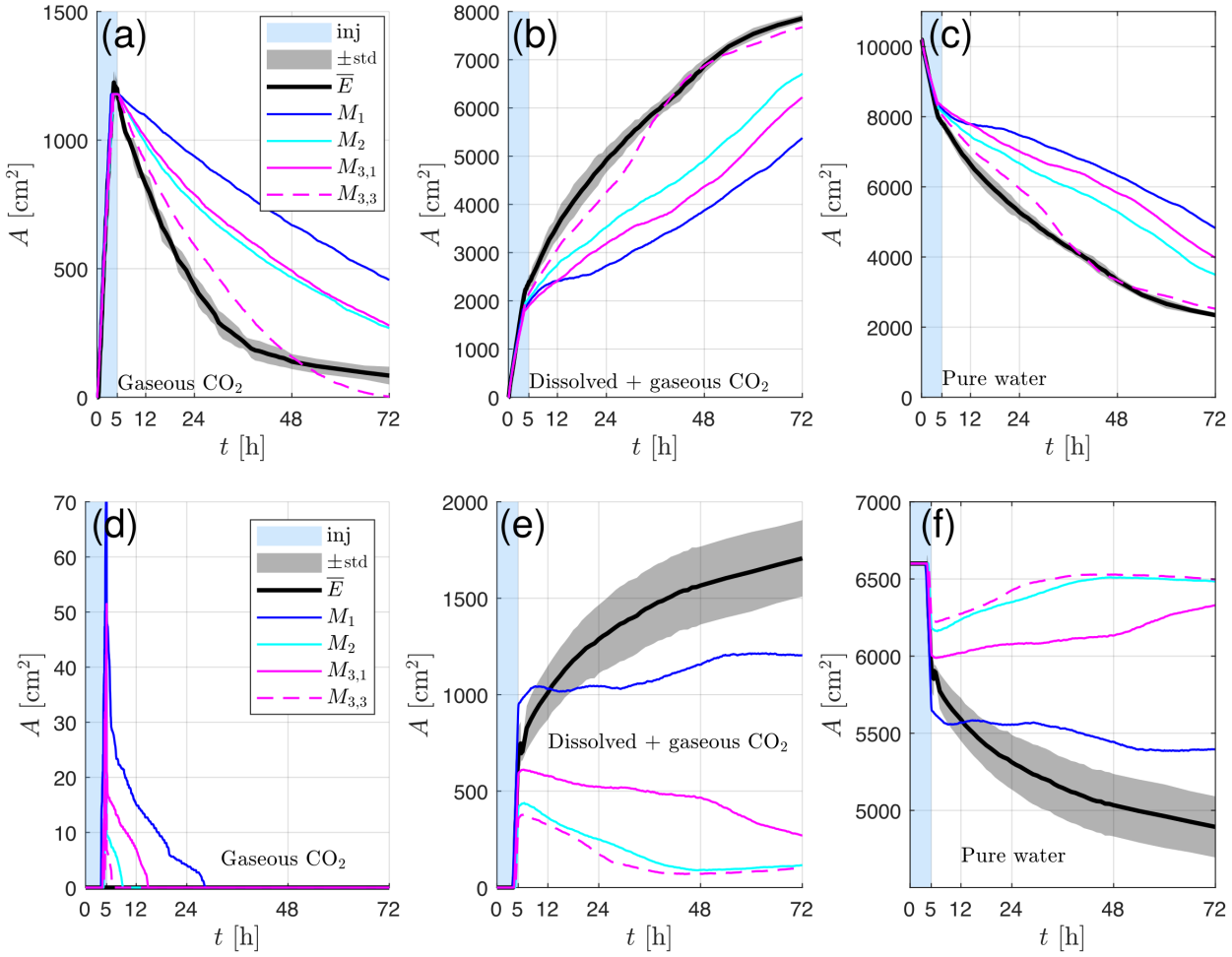

Figure 3.17: Comparison of areas occupied by each phase during the first 72h of case B1. Experimental mean ($\overline{E}$) and standard deviation (std) obtained from four experimental runs with identical protocol, while the results for models 1-3 are for a single run with each matched model. For M_3, two cases are shown: $D = 10^{-9}$ m^2/s ($M_{3,1}$) and $D = 3 \times 10^{-9}$ m^2/s ($M_{3,3}$). Top row shows areas in Box A, and bottom row shows areas in Box B. **a,d** gaseous CO_2. **b,e** dissolved CO_2 (includes area with gaseous CO_2). **c,f** pure water.

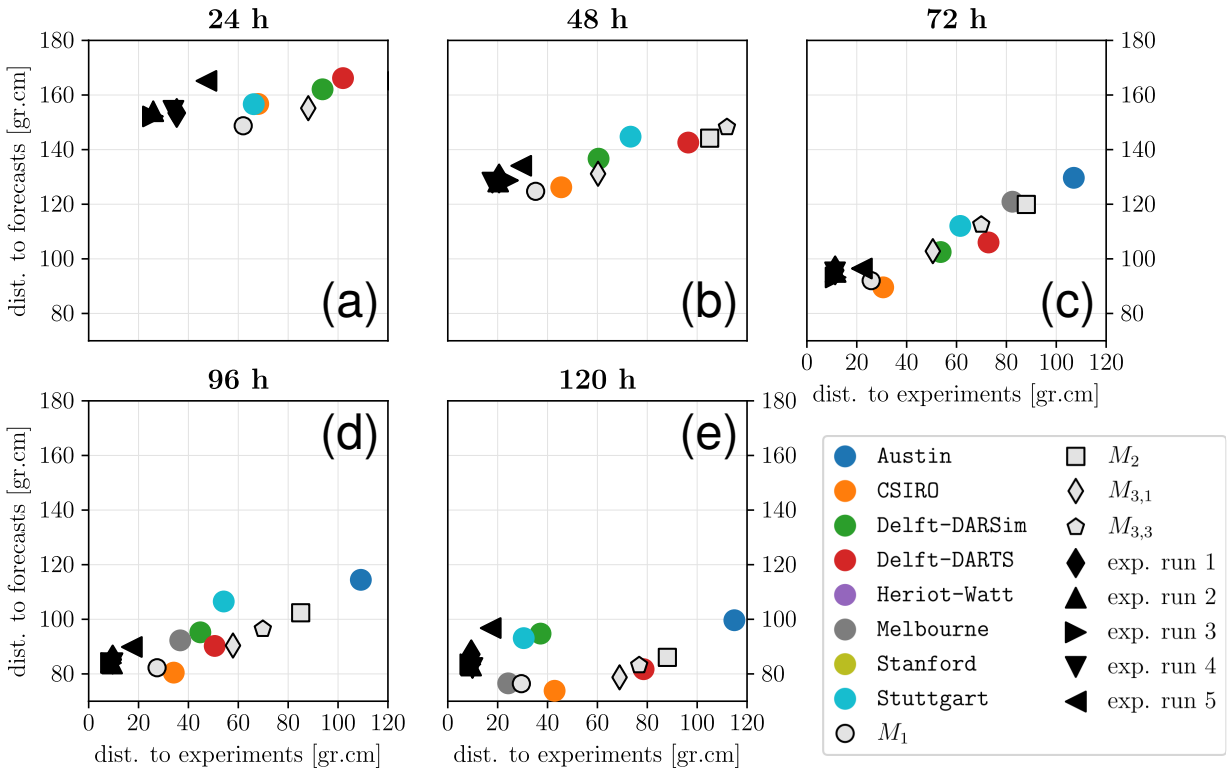

Figure 3.18: Wasserstein distances to experiments and forecasts (simulations). Colored circles show forecasts by IBS groups, and results with calibrated models 1-3 are presented with light gray markers. In each subplot, the vertical axis shows the mean distance between a given datapoint and the forecasts (considering the IBS participants only), while the horizontal axis shows the mean distance between a given datapoint and the experiments. Markers not present fall outside of the axes limits. **a**: 24h. **b**: 48h. **c**: 72h. **d**: 96h. **e**: 120h.

Chapter 4

Fault Permeability from Stochastic Modeling of Clay Smears

This chapter has been published in Saló-Salgado et al. (2023a).

Abstract

In normally-consolidated, shallow (depth $<$ 3 km) siliciclastic sequences, faults develop clay smears. Existing models include the dependence of permeability on the clay fraction, but improved predictions of fault permeability should account for uncertainty and anisotropy. We introduce `PREDICT`, a methodology that computes probability distributions for the directional components (dip-normal, strike-parallel and dip-parallel) of the fault permeability tensor from statistical samples for a set of geological variables. These variables, which include geometrical, compositional, and mechanical properties, allow populating multiple discretizations of the fault core with sand and clay smears to upscale the permeability to a coarser scale (e.g., suitable for reservoir modeling). We validated our implementation with experimental data, and apply `PREDICT` to several stratigraphic sequences. We show that fault permeability is controlled by the clay smear configuration and, crucially, that it typically exhibits multimodal probability distributions due to the existence of holes. The latter is a unique feature of our algorithm, which can be used to build fault permeability scenarios to manage and mitigate risk in subsurface applications.

4.1 Introduction

As observed by Weber et al. (1978) and Lehner and Pilaar (1997), faults in normally-consolidated, shallow (depth $<$ $\sim$3 km) sand-clay sequences develop ductile clay smears (see comprehensive review by Vrolijk et al. 2016). The influence of clay has been recognized in pioneering models of fault permeability, which were derived from laboratory measurements (Manzocchi et al. 1999; Sperrevik et al. 2002). These models depend on an estimate of the fault clay fraction, which is included through a proxy such as the shale gouge ratio (SGR; Yielding et al. 1997). Subsequent algorithms and models founded on a similar

premise have been developed (Jolley et al. 2007; Myers et al. 2014), but require extensive local datasets. Key shortcomings of this type of model are: scale-independent, averaged upscaling of lithological diversity, which contrasts with the strongly heterogeneous materials in shallow faults (Rawling et al. 2001; Childs et al. 2007; Vrolijk et al. 2016); limited insight on the geologic elements or properties controlling permeability; and the computation of cross-fault permeability only.

To increase generality and better represent outcrop observations, Tveranger et al. (2005) developed the fault facies concept, and Bense and Person (2006) presented an algorithm that includes permeability anisotropy due to vertical layering in the fault zone. Childs et al. (2007) described a probabilistic shale smear predictor; they computed the average smear gap length between a given smearing layer at each side of the fault to calculate the permeability perpendicular to the fault via arithmetic averaging. Grant (2020) focused on fault core sealing and developed a stochastic, facies-based fault permeability algorithm. In Grant (2020)'s algorithm, the proportions of different fault rocks and number of material layers in the core are defined by the user; the output permeability, perpendicular to the fault, is computed via harmonic averaging.

The algorithms outlined above are difficult to generalize because a quantitative description of the controls on fault material distribution is lacking, representing a key area to improve fluid-flow predictions in smear-dominated faults (Vrolijk et al. 2016). In addition, previous algorithms do not quantify uncertainty or anisotropy in the directional components (dip-normal, k_{xx}; strike-parallel, k_{yy}; and dip-parallel, k_{zz}) of the fault permeability tensor, which arises from material heterogeneity. This is required to manage and mitigate risk subsurface applications like geological CO_2 storage (GCS) where flows along faults can be critical (IEAGHG 2016).

To bridge this gap, we develop `PREDICT`, a methodology to quantify fault permeability in normally-consolidated (NC), shallow ($<\sim$3 km) siliciclastic sequences. For example, these conditions are found in Cenozoic sediments in passive margins, and they are relevant for large-scale GCS projects (Ringrose and Meckel 2019).

4.2 Stochastic Computation of Fault Permeability

`PREDICT` (full algorithm description in Appendix B and the code is available at https://github.com/lsalo/predict) computes the directional components of the fault permeability tensor in an upscaling (coarse) grid defined by the user; flexible upscaling is useful to assign fault permeability in subsequent flow simulations. The computation is performed in a given throw window, in which `PREDICT` represents the fault core (Fig. 4.1). Consistent with offset of clay layers across a finite-thickness shear zone, smears are placed at an angle $\alpha > 0$ to the fault plane (e.g., Fig. 3 in Lindsay et al. 1993). Constant throw along strike is assumed. A summary of `PREDICT` follows.

The algorithm requires a set of input parameters that describe the faulted stratigraphy: the layer thickness (T), clay volume fraction (V_{cl}), and dip angle (β), plus the fault dip (f_β), maximum burial depth (z_{max}), and faulting depth (z_f). By combining these inputs as described in § B.1.2 in Appendix B, `PREDICT` generates marginal probability distributions (P_x) for another set of numerical quantities: fault thickness (f_T), residual friction angle

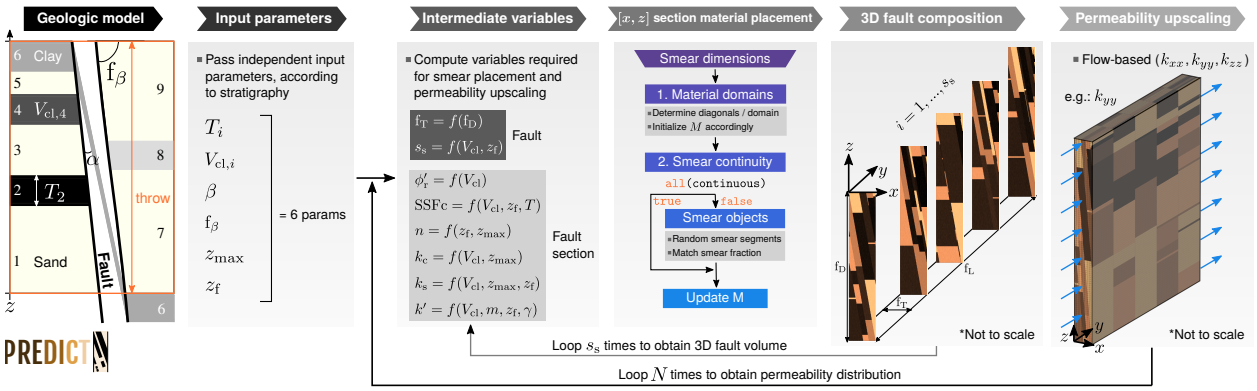

Figure 4.1: PREDICT workflow (left to right). Stratigraphic section is described by the input parameters, which PREDICT uses to compute the ranges and probability distributions for the intermediate variables. Each 3D fault realization is obtained by generating $i = s_s$ fault sections with constant thickness and arranging them along strike. For each fault section, resdiual friction angle (ϕ'_r), critical shale smear factor (SSFc), porosity (n), permeability (k) and permeability anisotropy ratio (k') are sampled and used to place fault materials and assign their properties. Subscript "c" refers to clay smear, and "s" refers to sand-based. Permeability is upscaled using the 3D fault volume. See the main text for notation, and Appendix B for details.

(ϕ'_r), critical shale smear factor (SSFc) (Færseth 2006; Childs et al. 2007), porosity (n), permeability (k), permeability anisotropy ratio (k'), and a parameter describing along-strike smear segmentation (s_s). The P_x are used to sample each intermediate variable accounting for dependency, and to populate the fault with clay smears ($V_{cl} \geq 0.4$) and sand smears ($V_{cl} < 0.4$), according to § B.1.2 and § B.1.3 in Appendix B (also see Fig. 4.1).

To populate the fault, PREDICT first generates a set of strike-perpendicular fault sections (FSs), each discretized with 10^4 cells (§ B.1.4 in Appendix B). Each FS is generated independently and is first subdivided into different domains according to the contributed materials and their thickness. The clay smear thicknesses are computed via Egholm et al. (2008)'s equation 5, which is valid for failure of granular materials with varying friction (see § B.1.3 in Appendix B), while sand smears fill the remaining f_T. Next, downdip smear continuity is assessed, and object-based simulation is used to place the discontinuous smears in the corresponding domains. After assigning fault materials and their properties to each FS, a three-dimensional (3-D) fault volume is obtained by arranging them along-strike (fine grid). The number of unique FSs in a given 3-D realization is equal to s_s. The 3-D volume has dimensions $f_T \times f_D \times f_L$, where f_D is the fault displacement, and f_L is the length (along-strike), which is set equal to f_D.

Finally, the permeability for the studied throw window is computed in the coarse grid by flow-based upscaling of the fine grid permeability using the MATLAB Reservoir Simulation Toolbox (MRST; Lie 2019). Multiple realizations of this process result in probability distributions for k_{xx}, k_{yy}, and k_{zz} (see Fig. 4.1; see Appendix B).

4.3 Results and Discussion

4.3.1 Validation with experimental fault-scale permeability

We validated our implementation by comparing PREDICT's k_{xx} values to experimental cross-fault permeabilities estimated from flux measurements by Kettermann et al. (2017) (their Figure 14). Kettermann et al. (2017) presented a set of experiments in a water-saturated sandbox, where sediment faulting was driven by a rigid basement fault, and flow across the sheared clay was induced by lowering the hydraulic head in the bottom reservoir (Fig. 4.2A). They also presented smear/hole maps (Fig. 4.2B), which we used to define s_s (Fig. 4.1; § B.1.2 in Appendix B). A view of the discontinuous clay smear in PREDICT is shown for one realization (single clay layer) in Fig. 4.2C. The permeability comparison is shown in Fig. 4.2D, where we used a coarse grid with a single cell to obtain our bulk fault permeability. It is apparent that most of PREDICT's probability distribution matches the range defined by the experimentally derived permeabilities (calculation details are given in § B.3 in Appendix B).

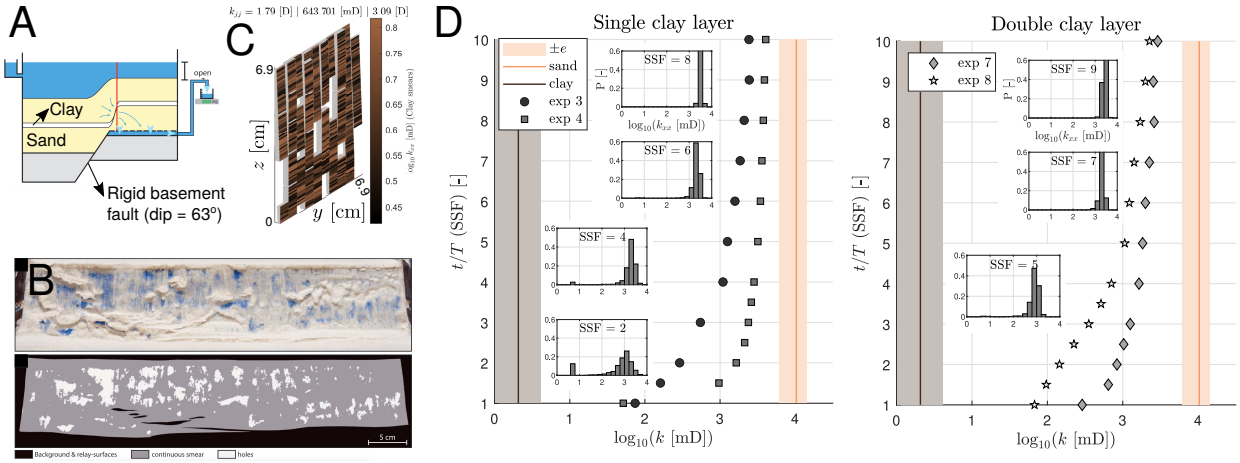

Figure 4.2: Validation with experimental data from Kettermann et al. (2017). (**A**) Experimental diagram. (**B**) Frontal view of excavated fault surface showing discontinuous smear (top) and smear hole mapping (bottom). Both A and B are from Kettermann et al. (2017). (**C**) PREDICT realization for shale smear factor (SSF) = 6, showing segmented clay smear. Fault dip was set to 60°. (**D**) Main plots show experimental cross-fault permeabilities (markers) and end-member permeabilities (vertical lines), computed from data in Kettermann et al. (2017) (see § B.3 in Appendix B). Inset plots show PREDICT's predictions for several SSF values.

4.3.2 Clay smear modeling leads to multimodal fault permeability distributions

The effect of increasing the average section clay fraction ($\overline{V}_{cl}$) is illustrated in Fig. 4.3, where multimodal or wider distributions arise when some material configurations lead to unobstructed sand pathways, and others do not (Fig. 4.3B and 4.3C). The presence of holes in 3-D clay smears is consistent with previous observations (e.g., Noorsalehi-Garakani et al.

2013). Overall, we found that the main factor determining whether most of the probability is at lower or higher permeability is the frequency of continuous sand pathways (cf. Fig. B.17 in Appendix B). This frequency is inversely related to the stratigraphic clay fraction, which agrees with previous stochastic models of clay smear (Childs et al. 2007; Yielding 2012; Grant 2020) and field evidence (Bense et al. 2013; Vrolijk et al. 2016, and references therein).

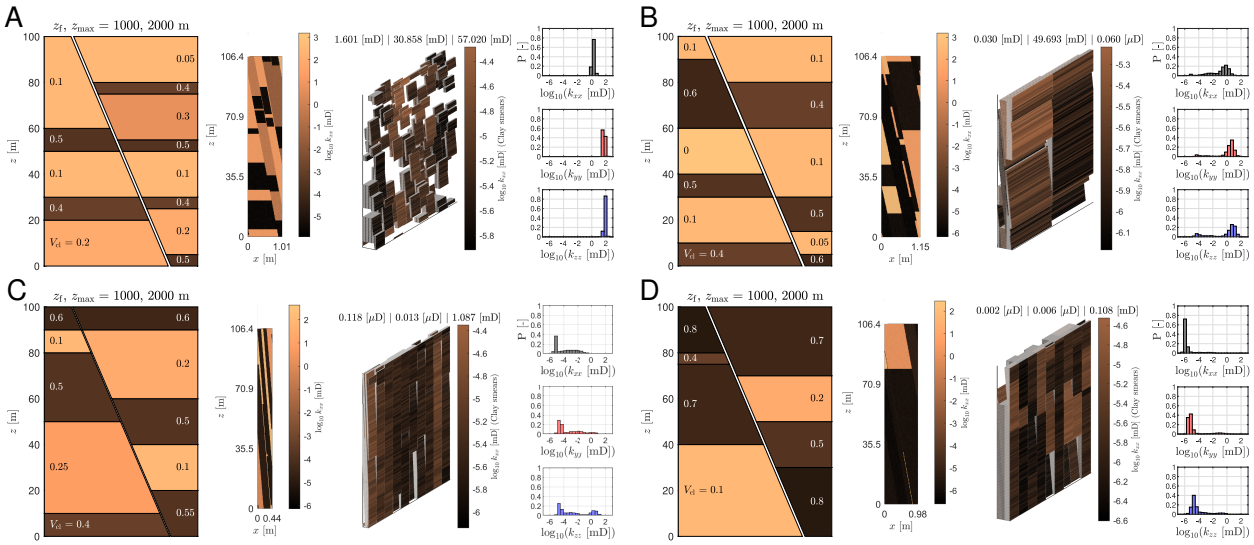

Figure 4.3: Effect of increasing section average clay fraction ($\overline{V}_{\mathrm{cl}}$). Each panel depicts: faulted stratigraphic interval (left); example fault material realization (center), showing frontal (x, z) cross section on left and clay smear distribution on right (upscaled permeability result shown at the top); and probability (P) distributions of fault permeability using single cell for upscaling (right). Throw is 100 m in all four cases, and stratigraphy is colored by $\overline{V}_{\mathrm{cl}}$. (**A**) $\overline{V}_{\mathrm{cl}} = 0.21$. (**B**) $\overline{V}_{\mathrm{cl}} = 0.27$. (**C**) $\overline{V}_{\mathrm{cl}} = 0.36$. (**D**) $\overline{V}_{\mathrm{cl}} = 0.53$.

4.3.3 Stratigraphic controls on fault permeability

Next, we modeled sequences with the same $\overline{V}_{\mathrm{cl}}$ but different layering and burial history. We considered three intervals with $\overline{V}_{\mathrm{cl}} = 0.3$, inspired by the Lower Miocene section offshore Texas (Treviño and Meckel 2017) (Fig. 4.4A), the Statfjord Formation in the North Sea (Myers et al. 2007) (Fig. 4.4B), and the Mount Messenger Formation in New Zealand (Childs et al. 2007) (Fig. 4.4C). As the clay layer thickness decreased (Figs. 4.4A–C), we observed (1) a decrease in the average fault clay fraction ($\mathrm{f}_{V_{\mathrm{cl}}}$), which typically led to higher permeability; and (2) a notable increase in k_{yy} and k_{zz} because of thinner smears. Hence, in agreement with long-standing observations (Weber et al. 1978; Lindsay et al. 1993), the macroscale fault permeability is primarily dependent on the derived smear configurations. This demonstrates the importance of accounting for material heterogeneity.

4.3.4 Fault clay fraction and permeability

Because all three sections in Fig. 4.4 had equal $\overline{V}_{\mathrm{cl}}$ and were relatively shallow, the permeability calculation according to Sperrevik et al. (2002) (using the SGR) yielded very similar

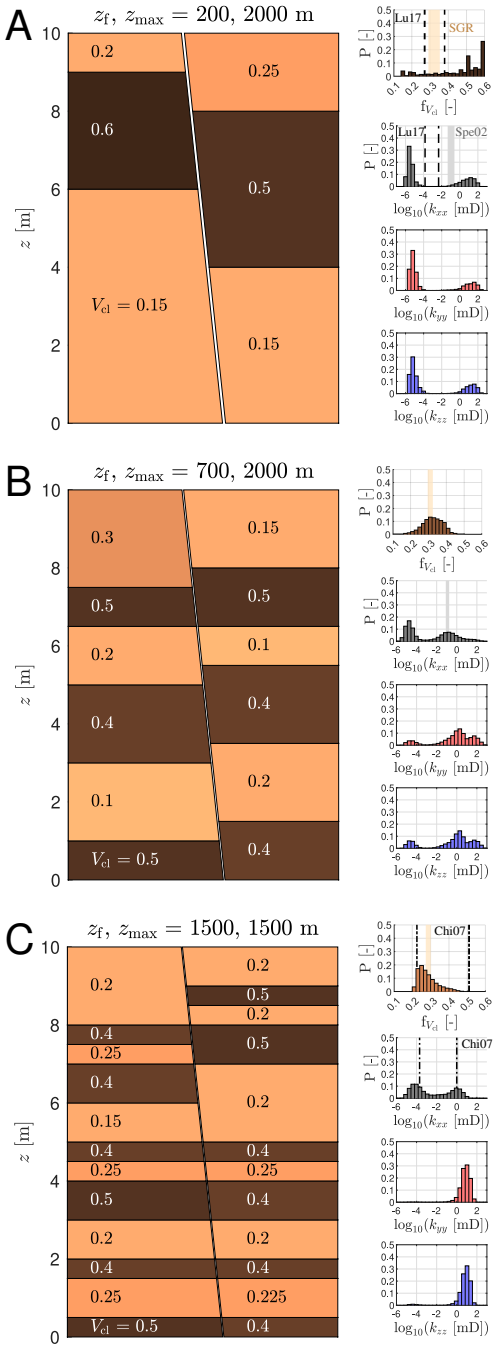

Figure 4.4: Fault permeability for three sequences with average clay fraction $\overline{V}_{\mathrm{cl}} = 0.3$ and throw = 10 m. Fault thickness in each stratigraphic section is from arbitrary realization. At right: Upscaled probability (P) distributions of average fault clay fraction ($\mathrm{f}_{\mathrm{V_{cl}}}$) and fault permeability. Upscaling grid with $2 \times 10 \times 10$ equal cells (x, y, z) was used to make results comparable (in scale) to reported measurements, and all upscaled cell values were collapsed into single distributions. Shale gouge ratio (SGR; orange fill) and resulting permeability range (gray fill) from Sperrevik et al. (2002) (Spe02) is also shown. Ranges obtained by Lu et al. (2017) (Lu17) and Childs et al. (2007) (Chi07) (within 20%–60% phyllosilicate) are plotted with dashed and dash-dotted lines, respectively.

values. This contrasts with PREDICT's output, which showed diminishing $f_{V_{cl}}$ and different permeability distributions. Our results agree with results by Childs et al. (2007), who showed that their smear-based permeability is lower than the SGR-based permeability where only a few beds are displaced, but they are likely closer as the shale layer thicknesses decrease (cf. Fig. 4.4). In Fig. 4.4A, estimated values from Lu et al. (2017) for Miocene mudstone cores from the Gulf of Mexico fall above PREDICT's main mode, which seems to be compatible with their lower V_{cl}. Zheng and Espinoza (2021) reported 10^{-5}–10^{-4} mD for synthetic mixtures of Frio sand and Anahuac shale at 20 MPa effective stress, which is very close to our main mode. Faults in the Mount Messenger Formation were studied by Childs et al. (2007), who reported ranges similar to PREDICT's output (Fig. 4.4C).

4.3.5 Fault permeability uncertainty and anisotropy

For a given stratigraphy, our analysis showed that multiple smear configurations (and upscaled permeability values) are possible. This reflects (1) the fact that knowledge of the subsurface is insufficient to model faults deterministically (Lunn et al. 2008; Bense et al. 2013; IEAGHG 2016; Vrolijk et al. 2016), and (2) PREDICT's quantification of this uncertainty. In PREDICT, permeability anisotropy of fault materials is typically within one order of magnitude. Higher anisotropy, as observed in some realizations in Figs. 4.3 and 4.4, is the result of material arrangement in the fault. This agrees with previous studies, which show that the maximum anisotropy of sheared clay-rich material is typically ∼10 (Dewhurst et al. 1996; Daigle and Dugan 2011).

4.4 Application to Fault Permeability Modeling in Real Settings

PREDICT models the fault as a shear zone and ignores the occurrence of other smearing mechanisms such as abrasion (Lindsay et al. 1993) and injection (Lehner and Pilaar 1997). Shear-dominated smear formation is supported by observations in shallow siliciclastic sequences, where the clay layers are dragged into the fault (Weber et al. 1978; Kettermann et al. 2016). Recently, Vrolijk et al. (2016, their Fig. 27) proposed a framework to characterize the smearing processes, which suggests that our algorithm is most applicable to sequences in which the clay, compared to the sand, is weaker to similarly strong. Considering typical cohesion and friction angles, this is expected in most shallow sequences at hydrostatic pressure and depths below a few tens of meters.

Each 3-D fault core realization was obtained by concatenating serial, equal-length two-dimensional (2-D) sections along-strike, which led to all clay smears being truncated at the same along-strike coordinates (Fig. 4.1). Additionally, each 3-D fault core realization had a constant thickness. While these geometric choices are a simplification of reality (Lunn et al. 2008; Kettermann et al. 2016; Sosio de Rosa et al. 2018), PREDICT balances this by considering thousands of realizations; in each realization, both fault thickness and the number of concatenated sections change. Clay smears are modeled as tabular bodies, which is a reasonable approximation (Çiftçi et al. 2013; Kettermann et al. 2016; Kettermann et al. 2017).

Along-strike throw variations cannot be explicitly accounted for, but the algorithm can be quickly run multiple times with varying inputs (e.g., fault displacement). PREDICT has matched experimental bulk fault permeabilities (Fig. 4.2) and is consistent with local measurements (Fig. 4.4). PREDICT's quantification of uncertainty and permeability anisotropy unlocks the ability to quantify, manage, and communicate hazards associated with subsurface technologies such as GCS (Bjørnarå et al. 2021; Snippe et al. 2022), natural gas storage, and nuclear waste disposal.

4.5 Conclusions

PREDICT includes a description of smearing in granular materials that is consistent with observations in shallow (depth $<\sim$ 3 km) siliciclastic sequences and incorporates uncertainty in the physical quantities controlling the fault and material dimensions and their properties. The output probability distributions, which characterize the directional components of the fault permeability tensor (dip-normal, strike-parallel, and dip-parallel) in a coarse grid defined by the user, can be multimodal. Our algorithm provides (1) a parameter-based link among the stratigraphy, the heterogeneous fault core materials, and the macroscale permeability; and (2) the likelihood of different fault permeability scenarios, which is required to assess hazard in subsurface technologies.

Chapter 5

Updip Migration of Sequestered CO_2 along Gulf Coast Miocene Growth Faults is Unlikely

This chapter is being prepared for publication as a research article (Saló-Salgado et al. 2023d).

Abstract

Recent studies indicate that Miocene-age reservoirs offshore Texas are promising candidates for industrial-scale geologic carbon sequestration. It has been shown, however, that faults are less competent seals than the low-permeability sediments overlying the reservoirs; this means that faults may limit the amount of CO_2 that can be permanently sequestered. Here, we conduct flow simulations of megaton-scale CO_2 injection next to a major reservoir-bounding fault in the Miocene, and evaluate (1) where fault sealing capacity is exceeded, and (2) where the CO_2 migrates after it enters the fault zone. We use a geologic model that includes the key structural features of fault-bounded systems near-offshore Texas, and consider both a continuous and discontinuous top seal. To model fault petrophysics, we apply a new methodology for faults in soft sediments that populates three-dimensional realizations of the fault core with sand and clay smears. We quantify uncertainty in the directional components of the fault permeability tensor and multiphase flow fault properties. We evaluate the sensitivity of fault CO_2 migration to these properties, and show that the capillary entry pressure is exceeded in the lower portion of the fault. This leads to fault CO_2 migration being controlled by effective fault permeability. We demonstrate that, even in this unfavorable scenario, the amount of sequestered CO_2 remaining in the injection formation after 1000 y exceeds 93% in all cases, and that CO_2 never migrates above the top seal. Considering pore pressure increase from injection, CO_2 is unlikely to migrate updip Miocene growth faults.

5.1 Introduction

Geologic CO_2 storage or carbon sequestration (GCS), where CO_2 previously captured from point sources or the atmosphere is injected in deep subsurface formations for permanent storage, is considered necessary to limit anthropogenic warming to < 2 °C and achieve net-zero by 2050 (IEA 2021; IPCC 2022). In 2022, global CO_2 emissions were between 35 and 40 Gigatons (Gt) from energy-related sources alone, which account for roughly 3/4 of greenhouse gas emissions. GCS, currently abating 30-40 Mt/y, needs to be scaled up two orders of magnitude to achieve our mid-century climate goals. This requires extensive growth in the GCS industry in the next three decades, and will require international collaboration between academia, industry, governments and the public (Krevor et al. 2023).

In the US, the Gulf of Mexico (GoM) is an important asset to deploy GCS at scale. Key aspects include conducive geology, extensive subsurface knowledge and infrastructure provided by decades of hydrocarbon exploration and production, and proximity to significant CO_2 emission sources, particularly along the Gulf Coast. Indeed, industrial projects such as the Houston CCS Alliance[1], which aims to cature and store ∼100 Mt/y by 2040, are already under way to increase capacity. In near-offshore Texas State Waters (OTSW), siliciclastic sediments of Miocene age have recently been the subject of an extensive study by the Bureau of Economic Geology at UT Austin (Treviño and Meckel 2017). The Miocene sequence is characterized by poorly to semi-lithified sands and shales; growth fault zones, laterally-sealing in many intervals; and rollover anticlines with increased sedimentary thickness in the hangingwall (Fig. 5.1a). Analysis of Miocene petroleum systems has identified fault-anticline settings to be suitable for GCS (Meckel and Rhatigan 2017).

In the GoM, Meckel et al. (2017) and Zheng and Espinoza (2022) report that capillary fault seal is variable and typically limits capacity before the top seal. One question that naturally arises concerns the fate of CO_2 after capillary breach, which requires dynamic flow modeling to quantify CO_2 migration within faults. This is one key aspect separating this study from most of the literature on fault leakage, where fluid migration results from fault reactivation and where multiphase flow properties of fault zones are largely ignored (e.g., Rinaldi et al. 2014; Meguerdijian and Jha 2021). In the GoM, recent studies have incorporated multiphase fault petrophysics: Zulqarnain et al. (2018) and Zulqarnain et al. (2020) used a geologic model from the Bayou Sorrel field in southern Louisiana and investigated the effect of trapping mechanisms, hydromechanical coupling and damage zone fractures on CO_2 migration in a fault zone. They discretized the fault with relatively high-permeability damage zone facies, and employed a quasi-2D geometry leading to extreme reservoir overpressurization driving CO_2 migration ($\Delta p > 10 - 20$ MPa at ∼2 km depth). Silva et al. (2023) studied the viability of Megaton-scale GCS using coupled flow-geomechanics and a geologic model based on the South Timbalier block, offshore Louisana. In their model, stratigraphy is dominated by clay-rich sediments, which led to best-estimate fault zone petrophysics preventing updip CO_2 migration.

Here, we extend these studies by conducting a stochastic analysis of fault CO_2 migration that incorporates uncertainty in multiphase fault properties. To model these properties (sect. 5.2), we employ a new methodology that honors fault architecture in soft siliciclastic se-

[1] https://houstonccs.com/

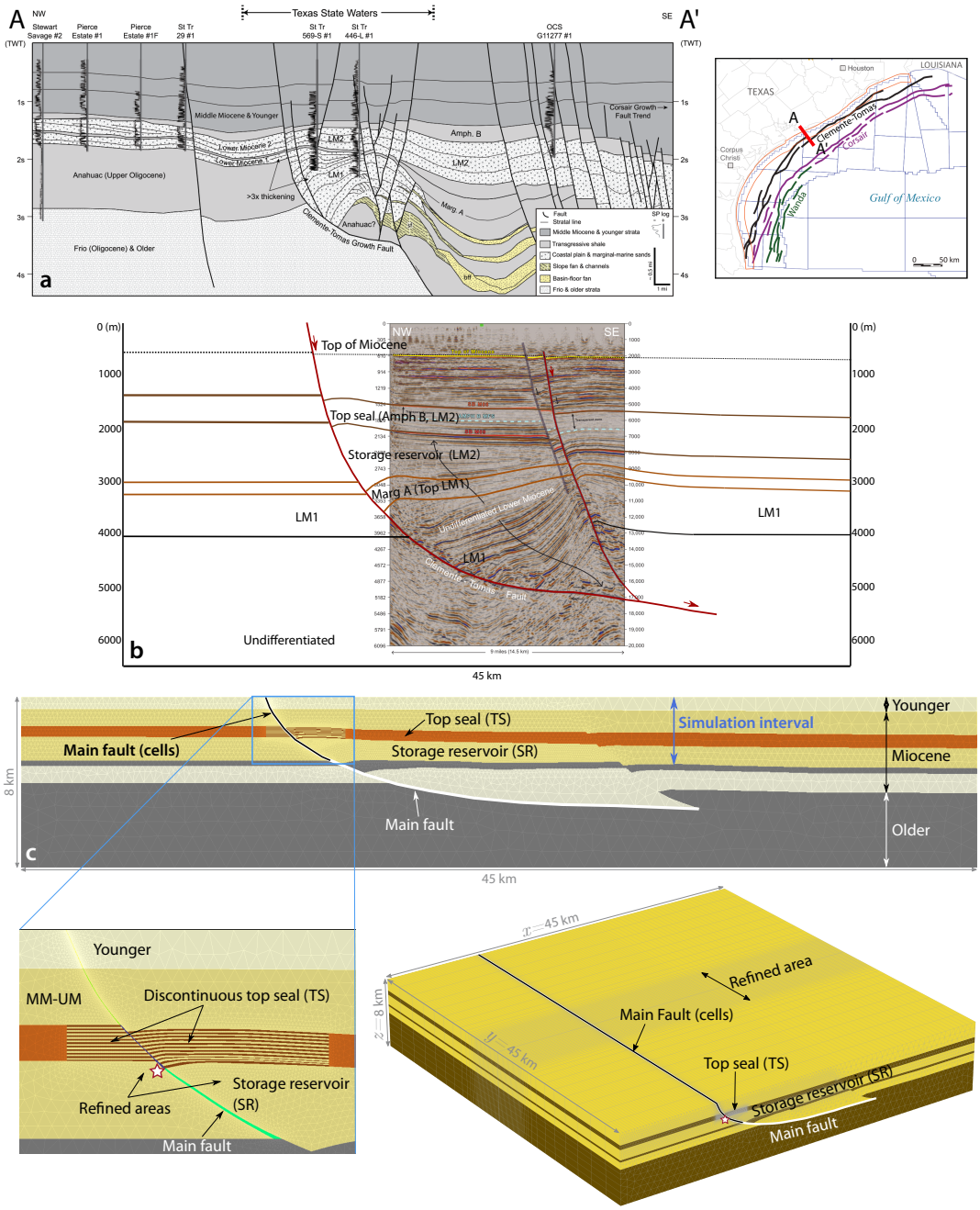

Figure 5.1: Geology and simulation grid. **a** Cross section of the Miocene in Offshore Texas State Waters (Nicholson 2012). The map to the right shows the cross section location, as well as Miocene-aged main faults along the Texas Gulf Coast. Modified from Treviño and Rhatigan (2017) (original in Ajiboye and Nagihara (2012)). **b** Synthetic geologic profile perpendicular to the coastline, displaying typical features of Miocene-age sediments in OTSW (cf. **a**). The background sesimic profile is from Lu et al. (2017, originally provided by Seismic Exchange, Inc.). **c** Meshed profile. The zoomed area around the injector (star) details the fault explicit thickness (cells), as well as the ∼25 m-thick layers within the top seal (TS) allowing control of seal continuity. The 3D grid used in the simulations (lower right) was obtained by extruding the 2D profile.

quences (Saló-Salgado et al. 2023a), compatible with the Miocene section offshore Texas, and quantifies uncertainty. Both improved fault property characterization and uncertainty quantification have been identified as research gaps hindering GCS deployment at scale (IEAGHG 2016; Vrolijk et al. 2016). Using a geologic model representative of the Miocene (Fig. 5.1b,c and sect. 5.3), we show that CO_2 migration updip a growth fault partially offsetting the top seal is unlikely, even when the fault capillary entry pressure is exceeded during injection (sect. 5.4, 5.5).

5.2 Fault Hydraulic Properties

5.2.1 Fault permeability structure in unlithified siliciclastic sequences

Following Caine et al. (1996)'s seminal paper, the conceptual model for faults in lithified rocks includes a central low-permeability volume (the core zone, CZ) and a surrounding volume of fractured rock that is hydraulically well connected (the damage zone, DZ) (Faulkner et al. 2010; IEAGHG 2016). Faults that grow in sediments, i.e., granular materials with low cohesion, typically develop a permeability structure that does not adhere to this description (Rawling et al. 2001; Bense et al. 2013, and references therein). Fundamentally, this is due to shear-driven sediment deformation behavior, where ductile deformation and granular flow dominate over brittle structures and cataclasis (Fig. 5.2).

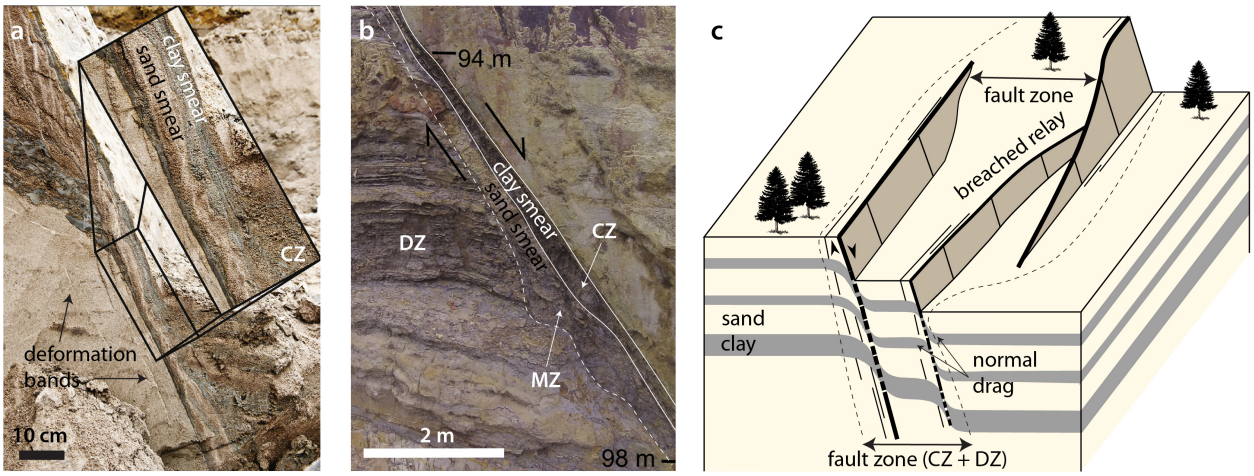

Figure 5.2: Fault zone architecture in soft siliciclastic sequences. **a** Photograph from the Hambach lignite mine (Germany) by Vrolijk et al. (2016), showing a layered fault core with both sand and clay smear. **b** Photograph from Miri (Malaysia) by Sosio de Rosa et al. (2018) showing a footwall zone of mixing with clay and sand smears, and a core dominated by clay smear with smaller sand lenses. **c** Schematic of a segmented normal fault, depicting key structural terms. In the frontal cross section, the fault cores (main fault segments) are discontinuous across the clay to emphasize distributed deformation, rather than localization. The external envelope (discontinuous line) delineates the fault zone. Figure inspired by Childs et al. (2009).

Faults in soft siliciclastic sediments can develop three main architectural domains (Rawling et al. 2001; Rawling and Goodwin 2006; Loveless et al. 2011; Bense et al. 2013): DZ,

CZ and mixed zone (MZ). The DZ is the outer element and characterized by dragging of sedimentary beds as well as the presence of defromation bands close to the boundary with the MZ/CZ (Fig. 5.2b,c). An important difference with respect to lithified DZs is the absence of macroscopic open fractures, thus limiting the potential of the DZ as a flow conduit. Consistent with its name, the MZ is a strongly heterogeneous domain incorporating relatively intact as well as deformed sediments, and grain-scale mixing. A MZ may not develop or, alternatively, may be the main element (Balsamo et al. 2010; Loveless et al. 2011; Bense et al. 2013); where developed, it will typically impede flow due to layering as well as reduced porosity and grain size as a result of penetrative particulate flow and cataclasis, complementing the CZ (Rawling and Goodwin 2006) (Fig. 5.2b). Therefore, the MZ acts as a transition zone between a weakly developed DZ and the CZ, which accommodates most of the shear deformation. In the CZ, both clay and sand smearing lead to a layered and heterogeneous domain, with potentially strong permeability anisotropy (Zee and Urai 2005; Saló-Salgado et al. 2023a, and references therein) (Fig. 5.2a).

The evolution of a fault's internal structure depends on a number of factors including stratigraphy, stress state, displacement and burial history, which lead to thermo-hydro-chemo-mechanical couplings rarely quantifiable. As a result, models of fault architecture evolution are difficult to generalize. Still, two key aspects are (1) the progressive linkage of fault segments that initiate on competent layers (Peacock and Sanderson 1992; Childs et al. 1996), and (2) evolution from normally consolidated conditions during (synsedimentary) faulting at shallow depths to overconsolidated states and increased localization as a result of overpressure, shear strain, diagenesis and/or exhumation (Rawling and Goodwin 2006). Mechanical contrast may promote the incorporation of wall material as fault bends are sheared off, which may lead to a distinct MZ as displacement increases. However, sand-clay mechanical heterogeneity is typically low near the surface, which promotes shear-type smears and layered fault materials (Vrolijk et al. 2016). Necessarily, this is an oversimplified picture, but these studies strongly suggest that faults in soft sediments mainly control fluid flow due to layering and heterogeneity in and around the main shear zone.

5.2.2 Faults in continuum numerical models of multiphase flow

Modeling fault architecture and petrophysics in field-scale numerical models is challenging. First, this is due to multiple order of magnitude differences in the relevant spatial and time scales (e.g., sect. 5.2.1). Accordingly, fault zones are typically included in the simulation model as $(D-1)$-dimensional entities, i.e., surfaces in 3D (Juanes et al. 2002; Manzocchi et al. 2008). This approach hinders representation of directional and saturation-based quantities, but remains an area of research given its applicability to commercial reservoir simulators and computational efficiency (Islam and Manzocchi 2021). Alternatively, faults are treated as D-dimensional objects in the computational domain (Fredman et al. 2007; Silva et al. 2023). This approach, followed here, may significantly increase computational time, but allows for direct consideration of multiphase flow properties.

Second, this is due to limited knowledge of fault properties, i.e., porosity (ϕ), absolute permeability ($\mathbf{k}$), relative permeability (k_r), and capillary pressure (P_c). In siliciclastics, several $\mathbf{k}$ models have been proposed that relate permeability to the stratigraphy (Saló-Salgado et al. 2023a, and references therein). Multiphase flow properties are rarely considered, but

their importance in applications like GCS is motivating efforts in this direction (e.g., Gasda et al. 2022; Snippe et al. 2022). However, validation of field-scale models remains elusive, and inclusion of physics-based dynamic properties is not yet attainable. Therefore, sensitivity analysis of quantities of interest to fault properties derived from consistent geology is required to enable decision-making. To address this, we propose a framework to quantify the effects of uncertain multiphase petrophysics on fault CO_2 migration, and apply it to the GoM. Our approach, described in sect. 5.2.3, builds on a method developed to estimate permeability of normal faults in soft, normally consolidated siliciclastic sequences (Saló-Salgado et al. 2023a). Consistent with fault anatomy (sect. 5.2.1), we disregard the DZ and focus on the main shear zone or CZ.

5.2.3 Fault multiphase petrophysics from stochastic modeling of clay smears

Here, we use `PREDICT` (Saló-Salgado et al. 2023a) to model clay smearing in the fault core and estimate bulk fault hydraulic properties. This methodology generates probability (P) distributions of fault core porosity and the diagonal components of the intrinsic permeability tensor (dip-perpendicular, k_{xx}; strike-parallel, k_{yy}; and dip-parallel, k_{zz}). To achieve this, `PREDICT` uses a description of the stratigraphy to populate multiple realizations of the main shear zone with sand and clay smears, and then computes the bulk fault permeability in a given throw window using single-phase flow-based upscaling. Each fault core realization has dimensions of $\mathrm{f_T} \times \mathrm{f_L} \times \mathrm{f}_D$, where f_T is the thickness (treated as a random variable), f_D is the fault displacement (determined by the stratigraphy) and f_L is the length, set equal to f_D.

To assign fault porosity and permeability in our simulation model, we first subdivide the main fault in the six throw windows (W_1 to W_6) covering the TS thickness (Fig. 5.3a). The P distributions for W_5 are shown in Fig. 5.3b. In our simulation model, all cells in W_i are assigned the same ϕ and k_{jj} at a given y (along-strike) coordinate; stochastic variability along the fault strike is assigned by randomly sampling from the P distributions at each y coordinate (Fig. 5.3c). Random sampling is supported by available data on spatial variation in fault core and clay smear thickness, as well as smear hole presence, which suggests that $\lambda_y < \mathrm{f}_D$, where λ_y is the correlation length of k_{yy} (Kettermann et al. 2016; Kettermann et al. 2017; Sosio de Rosa et al. 2018). This is because here, $h_y \geq \mathrm{f}_D$, where h_y is the cell size along the y axis.

The highly-resolved fault core material realizations from `PREDICT` can be also be used to upscale relative permeability (k_r) and capillary pressure (P_c) in each throw window W_1 to W_6. To achieve this, we assign core-scale curves to sand and clay smears in a given 3D fault core, and use simulations to obtain representative values at the throw window scale. k_r is upscaled via CO_2-brine dynamic simulations where CO_2 circulates in the 3D fault core parallel to the dip (z axis). Depth-averaged saturation profiles are computed as a function of time, and then compared with multiple 1D solutions with a single relative permeability curve. The 1D model with the lowest error is the best upscaled curve. P_c is upscaled via macroscopic invasion-percolation (MIP) simulations in the 3D fault core, also in the z direction. A detailed account of this methodology is provided in Appendix C.1, and upscaled curves are shown in Fig. 5.4b,c (see sect. 5.2.4 for cases considered). Variations along strike

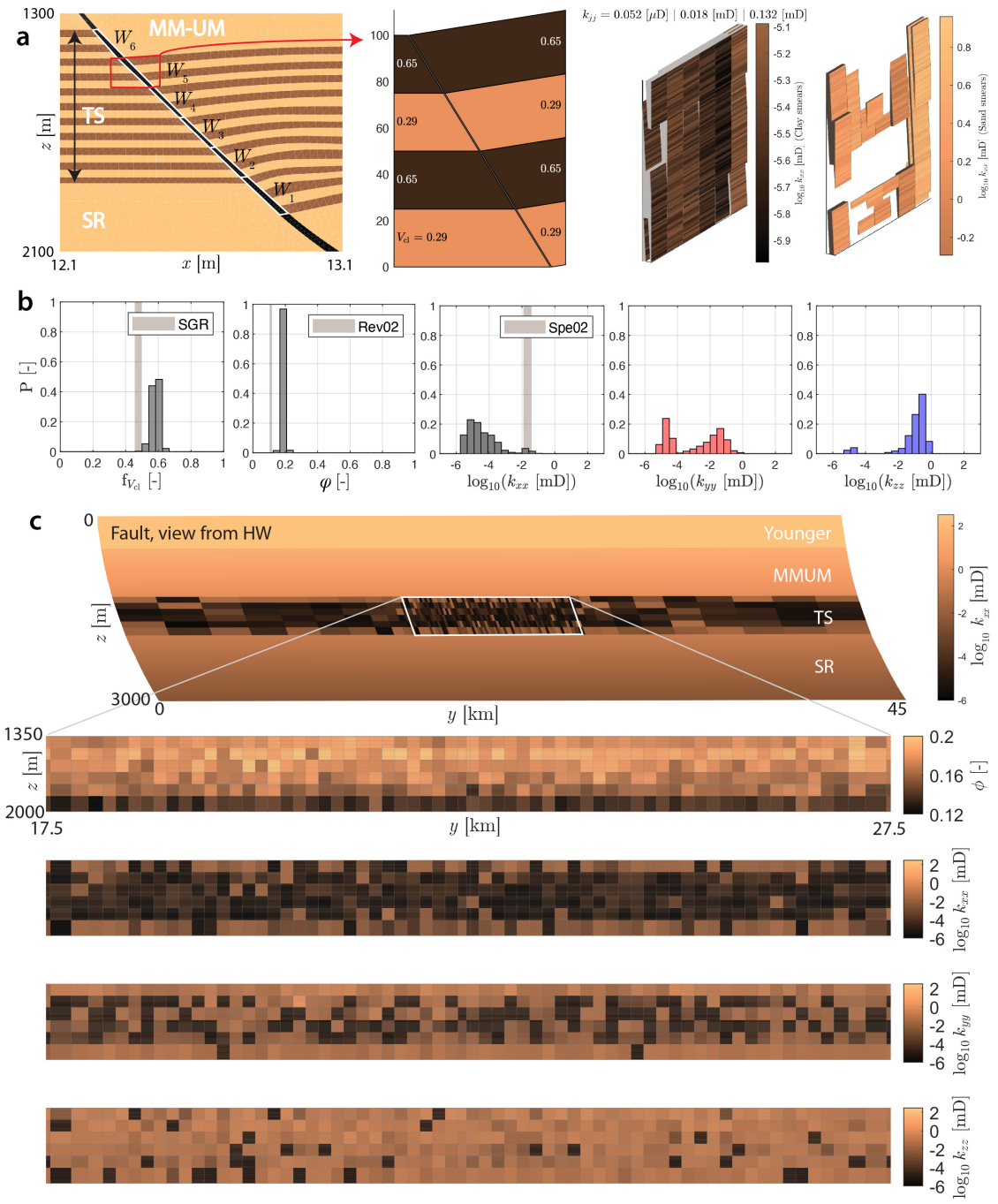

Figure 5.3: Application of `PREDICT` to model fault porosity and permeability. **a** Left: Vertical cross section of the TS in our computational model, showing the six fault throw windows. Right: Representation of W_5 and fault core materials for a given realization, showing clay smears and sand smears, respectively. **b** Outputs for W_5. From left to right: probability (P) distributions of clay volume fraction ($f_{V_{cl}}$), porosity (ϕ), and dip-perpendicular (k_{xx}), strike-parallel (k_{yy}), and dip-parallel (k_{zz}) permeability, respectively. **c**: A realization of fault porosity and permeability in our simulation model after stochastic assignment (see main text for details). The top image is a perspective of the full fault. `PREDICT` is used in the TS depth interval (see detailed panels), while the SGR is applied elsewhere.

in natural faults advocate for a different curve for each cell along y, similar to ϕ and $\mathbf{k}$; however, this is impractical due to computationally expensive upscaling and 3D reservoir simulation with hundreds of fluid regions. Therefore, we select two bounding curves for each throw window (sect. 5.2.4).

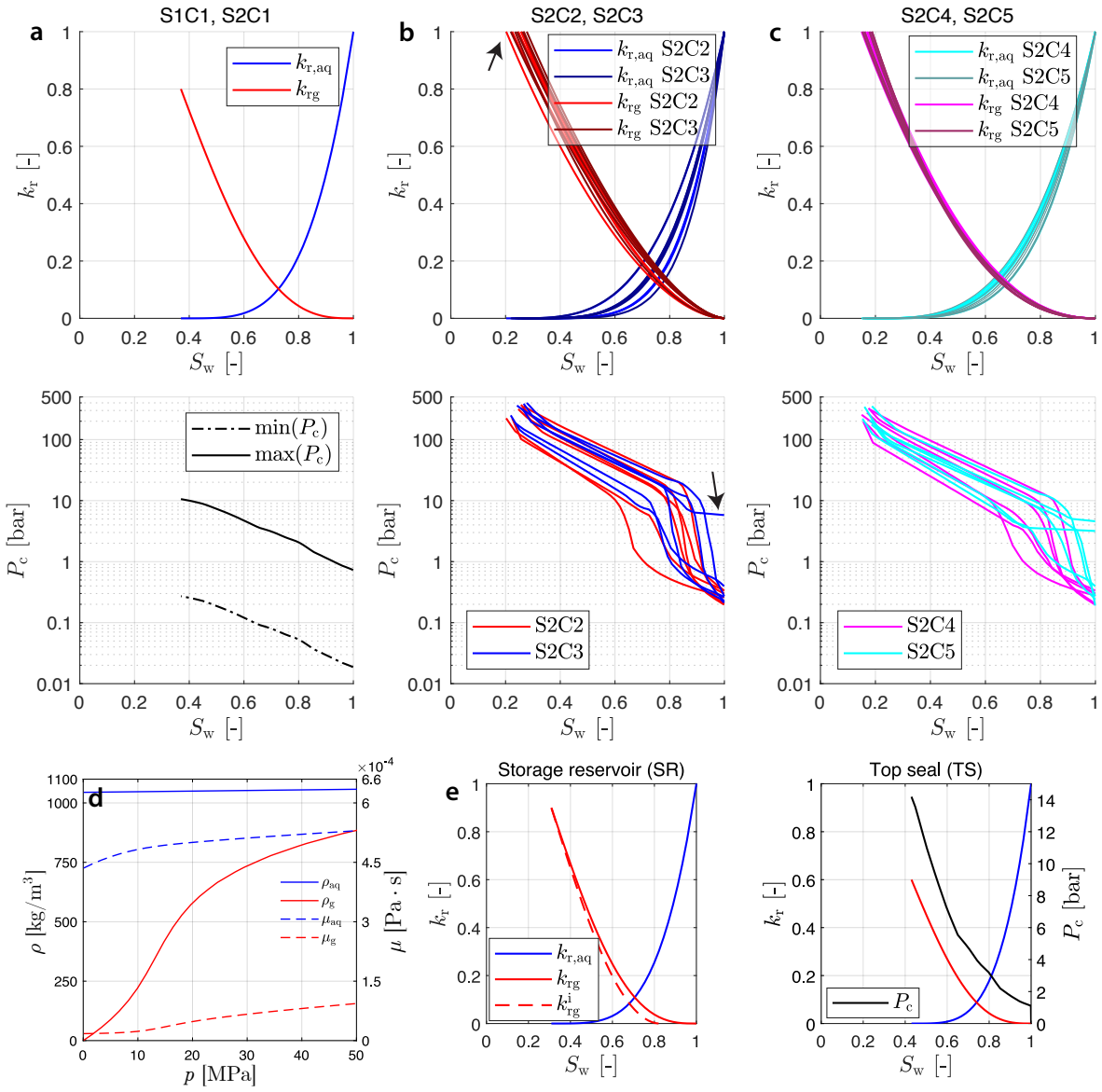

Figure 5.4: Multiphase fluid properties. **a** Top: Relative permeability for any fault cell in S1C1 and S2C1. Bottom: Lowest and highest fault capillary pressure curves in the TS depth interval (blue cells in Fig. 5.1c) in S1C1 and S2C1. **(b)**: Upscaled fault relative permeability curves (top) and capillary pressures for S2C2 and S2C3. Note the difference in residual water saturation and maximum entry pressure with respect to **c** (arrows). **c** Same as **b**, but for S2C4 and S2C5. **d**: Density (ρ) and dynamic viscosity (μ) of the aqueous and gas phases. **e**: Gas and water drainage relative permeabilities (solid lines) and gas bounding imbibition curve (dashed line) for the storage reservoir and other sand units (left). Right: Gas and water drainage relative permeability and capillary pressure curve for clay layers in the top seal interval.

5.2.4 Simulation cases

As shown in Fig. 5.1c, the top seal (TS) is meshed with a set of fine (∼25 m-thick) sublayers around the fault to model scenarios with varying clay proportions. Here, we consider two TS possibilities: continuous seal, where the ≈ 500 m-thick TS interval has a constant, high clay-fraction (scenario 1, S1), and discontinuous seal (scenario 2, S2). S1 is the default choice in km-scale simulation models, where the caprock interval is often assumed homogeneous and impermeable (e.g., Birkholzer et al. 2011; Newell and Martinez 2020; Gasda et al. 2022; Silva et al. 2023). However, detailed well-log analysis by Lu et al. (2017) shows that thin, coarser-grained strata may be present within the Amph B confining zone. Additionally, a reduction in seal quality and lateral extension is expected towards the coastline (e.g., Jonk et al. 2022). This can reduce CO_2 trapping capacity and impact fault properties (sect. 5.2.1); therefore, we dedicate most of our effort to evaluating fault-related CO_2 migration when the TS contains interbedded sands (S2). In particular, in S2 we consider 50% clay and 50% sand, which represents a conservative scenario (Fig. 5.1c).

For comparison purposes, we model a base case for each of the two scenarios (S1C1 and S2C1) using the well-established shale gouge ratio method (SGR; Yielding et al. 1997). A description of fault properties for the base cases is provided in Appendix C.2. We then apply the methodology described in sect. 5.2.3 to S2, where we consider two possibilities for the wettability (θ) of clay material (Iglauer et al. 2015): $\theta = 30$ and 60°. For each θ value, we select a high permeability and a low permeability realization (in each throw window) for k_r and P_c upscaling. In particular, we evaluate the joint probability of k_{ii} and select a range for the high permeability and low permeability modes; we then choose a random fault core realization within these modes for upscaling. This leads to four cases (S2C2 to S2C5), which are summarized in Table 5.1. Note that, to assess the sensitivity of CO_2 migration to uncertain fault ϕ and $\mathbf{k}$, we run three simulations for each case S2C2 to S2C5. In a given case, k_r and P_c remain unchanged, while fault ϕ and $\mathbf{k}$ change in each simulation due to stochastic assignment (Fig. 5.3). This adds up to the 14 simulations in Table 5.1.

5.3 Numerical Simulations

We conducted numerical simulations of isothermal CO_2-brine flow using the `ad-blackoil` module of the MATLAB Reservoir Simulation Toolbox, MRST (Lie et al. 2012; Krogstad et al. 2015; Lie 2019). We account for (1) structural/stratigraphic trapping via capillary pressure; (2) solubility trapping via dissolution of CO_2 in the brine phase; and (3) residual trapping in the sand formations via gas relative permeability hysteresis, owing to its control on CO_2 migration (Juanes et al. 2006). The thermodynamic model for fluid PVT properties and relative permeability hysteresis model follow Hassanzadeh et al. (2008) and Killough (1976), respectively, and are described in detail in a forthcoming paper.

5.3.1 Computational grid and formation properties

We first generated a geologically representative section of the Miocene sequence in OTSW, including the key structural features of fault-bounded trap systems (Fig. 5.1b): Major growth

Table 5.1: Summary of simulation cases and methods for estimating fault properties, according to the description in sect. 5.2. Columns refer to mesh scenario (Sc.), simulation number(s) (No.), simulation case code (Id), and methodologies used to estimate materials, porosity (ϕ), intrinsic permeability ($\mathbf{k}$), relative permeability (k_r) and capillary pressure (P_c).

Sc.	No.	Id	Materials	ϕ	$\mathbf{k}$	k_r	P_c
1	1	S1C1	SGR	Revil et al. (2002)	Sperrevik et al. (2002)	Based on literature (Appendix C.2)	Leverett scaling using reference curve from Lu et al. (2017, sect. 5.3.2)
2	2	S2C1	SGR	Same as S1C1	Same as S1C1	Same as S1C1	Same as S1C1
2	3-5	S2C2	PREDICT	Random sampling from PREDICT's output P (Fig. 5.3)	Random sampling from PREDICT's output P	Dynamic upscaling in high $\mathbf{k}$ fault core realizations from PREDICT. Sand rock curves from coreflood experiments on unconsolidated sandstones, clay rock curves from literature (see Appendix C.1)	Upscaled from MIP simulations in fault cores from PREDICT (high $\mathbf{k}$ mode). Sand rock curves from porous plate experiments on unconsolidated sandstones, clay rock curves from Lu et al. (2017) (see Appendix C.1)
2	6-8	S2C3	PREDICT	Same as S2C2	Same as S2C2	Same as S2C2 (low $\mathbf{k}$ mode)	Same as S2C2 (low $\mathbf{k}$ mode)
2	9-11	S2C4	PREDICT	Same as S2C2	Same as S2C2	Same as S2C2, but consider intermediate wetting for clay ($\theta = 60°$)	Same as S2C2 ($\theta = 60°$ for clay)
2	12-14	S2C5	PREDICT	Same as S2C2	Same as S2C2	Same as S2C3 ($\theta = 60°$ for clay)	Same as S2C3 ($\theta = 60°$ for clay)

faults with listric geometries displacing most of the Miocene section, secondary synthetic faults and rollover anticlines, increased thickness of the Lower Miocene (LM) interval in the hangingwall, and thick sand-dominated intervals capped by clay-rich intervals. This profile was meshed using unstructured triangular elements that conform to faults and horizons (Fig. 5.1c). The main fault was meshed with elements of size ∼10 m (increasing downwards with fault displacement), while the top seal (TS) was subdivided using a set of fine (∼25 m-thick) layers around the fault. These two aspects allow us to readily assign fault multiphase flow properties and to control the proportion of clay in the TS, respectively. Finally, the 3D computational grid was obtained by extruding the meshed profile in the horizontal direction (dimensions 45×45×8 km; Fig. 5.1c). In the simulations presented here, only the cells pertaining to the storage reservoir (SR) and above are active (≈ 2 M cells).

Given our primary goal, formation properties were kept relatively simple (Table 5.2). Data from Miocene gas reservoirs was used to define representative $\mathbf{k}$ values for the SR and other sand-dominated intervals (Wallace 2013). The correlation between permeability and porosity (ϕ) in Miocene reservoirs can be modeled as $\phi = \ln(k\,[\text{mD}]/0.7385)/20.011$ (Wallace 2013). Uniaxial pore volume compressibilities of poorly lithified sands from Crawford et al. (2011) were used to define the formation compressibility (C_f); chosen values are representative of unloading conditions, consistent with fluid injection (Zheng and Espinoza 2021). The petrophysical properties of Miocene mudrocks are based on core tests by Lu et al. (2017), who reported $\phi \in [3,\ 11]\%$, and permeability mostly $\in [10^{-4},\ 10^{-2}]$ mD. Clay compressibility is roughly one order of magnitude larger than the sand compressibility (e.g., Merrell et al. 2014).

Table 5.2: Formation pore compressibilities (C_f), porosities (ϕ) and permeabilities (k_{xx} and k_{zz}) for units in the simulation interval (Fig. 5.1c).

Mesh unit	C_f [bar^{-1}]	ϕ [-]	k_{xx} [mD]	k_{zz} [mD]
SR (LM2)	1.45×10^{-4}	0.265	150	$0.2k_{xx}$
TS (clay)	1.28×10^{-3}	0.15	5×10^{-3}	$0.2k_{xx}$
TS (sand)	1.45×10^{-4}	0.27	175	$\frac{1}{3}k_{xx}$
MM-UM	1.45×10^{-4}	0.28	200	$\frac{1}{3}k_{xx}$
Younger	1.45×10^{-4}	0.35	500	500

5.3.2 Fluids and setup

The composition, density and viscosity of the gas (CO_2 only) and aqueous (brine and dissolved CO_2) phases was computed at $T = 80$ °C and salinity $= 10^5$ ppm (Christie and Nagihara 2016; Kraemer and Reid 1984) (Fig. 5.4d). The simulation domain is divided in three main fluid regions for assignment of relative permeability (k_r) and capillary pressure (P_c). The curves for sand (SR, sand layers in TS, MM-UM and Younger; see Fig 5.1 and Table 5.2) and clay-rich (TS) regions are shown in Fig. 5.4e (fault properties are described in sect. 5.2). In Fig. 5.4e, the drainage relative permeability curves are Corey-type (Brooks and Corey 1964) curves consistent with previous work (Ghomian et al. 2008; Wallace 2013), while

Land (1968)'s model was used to compute the bounding imbibition curve, consistent with Killough (1976)'s hysteretic model. The reference P_c curve for clay rich layers (Fig. 5.4e) is from mercury intrusion capillary pressure (MICP) measurements by Lu et al. (2017). Their MICP curve (P_c^{MICP}) was converted to CO_2-brine (P_c^{CB}) as:

$$P_c^{CB} = P_c^{MICP} \times \frac{\gamma^{CB} \cos\theta^{CB}}{\gamma^{MICP} \cos\theta^{MICP}} = P_c^{MICP} \times \frac{25 \cos 70°}{480 \cos 140°} \tag{5.1}$$

where γ is the interfacial tension and θ the contact angle. The values in Eq. 5.1 are those suggested by Lu et al. (2017); the use of $\theta^{CB} = 70°$ is consistent with intermediate wetting conditions and represents a conservative estimate.

Our computational domain is initially fully saturated in brine, and we assumed a constant water table with height = 50 m. Similar to previous studies (Juanes et al. 2006; Silva et al. 2023), we recreate a strong aquifer support by multiplying the pore volumes of the cells in the perimeter of the SR layer by 10^4. We inject CO_2 at a rate of 1 Megaton (Mt) per year during 50 years, and run all simulations for a total of 1000 y. The injector is placed in the SR layer at ≈2 km depth, with the goal of achieving quick contact of the CO_2 plume against the fault (Fig. 5.1c).

5.4 Results

In this study, CO_2 exists either as a supercritical fluid in its own phase, or dissolved in brine. For correspondence with phase definition in the numerical model, we refer to supercritical CO_2 as gas or free-phase CO_2.

5.4.1 Continuous vs discontinuous top seal

We first evaluate the effect of seal continuity by comparing the two base cases (S1C1 and S2C1, see sect. 5.2.4). An overview of gas migration around the injector is provided in Fig. 5.5. In both cases, we observe that most of the CO_2 that migrates outside of the injection compartment crosses the fault at the SR-SR juxtaposition and accumulates in the hangingwall (HW) compartment below the TS. After 1000 y, the remaining gas is located at the highest elevations in both SR compartments, due to its lower density (Fig. 5.5b,d). In S1C1, there is no CO_2 at any point where the TS is self-juxtaposed (Fig. 5.5a,c). Conversely, in S2C1 (discontinuous TS) CO_2 is able to migrate updip ≈25 m more and reach up to the third sand-rich layer within the TS (OR_3; Fig. 5.5e); interbedded sands act as secondary reservoirs, and prevent further gas migration updip.

The dynamics of CO_2 migration within the fault are summarized in Fig. 5.6. In our simulations, $p_g = p + P_c(S_g)$, where p_g and p are the dynamic gas and brine pressures, respectively. Fig. 5.6a shows that, during injection, $p_g - p > P_e$, where P_e is the entry capillary pressure (defined at $S_g = 10^{-3}$). This renders the fault *open* to migration of the nonwetting CO_2. However, CO_2 does not saturate much of the fault updip, because the flow path of less resistance is into the high-permeability sands within the TS and along the fault strike (Fig. 5.6b). Therefore, after P_e is exceeded, CO_2 migration is a dynamic process controled by $\mathbf{k}_{eg}(S_g) = \mathbf{k}k_{rg}(S_g)$, where $\mathbf{k}_{eg}$ is the effective gas permeability, and

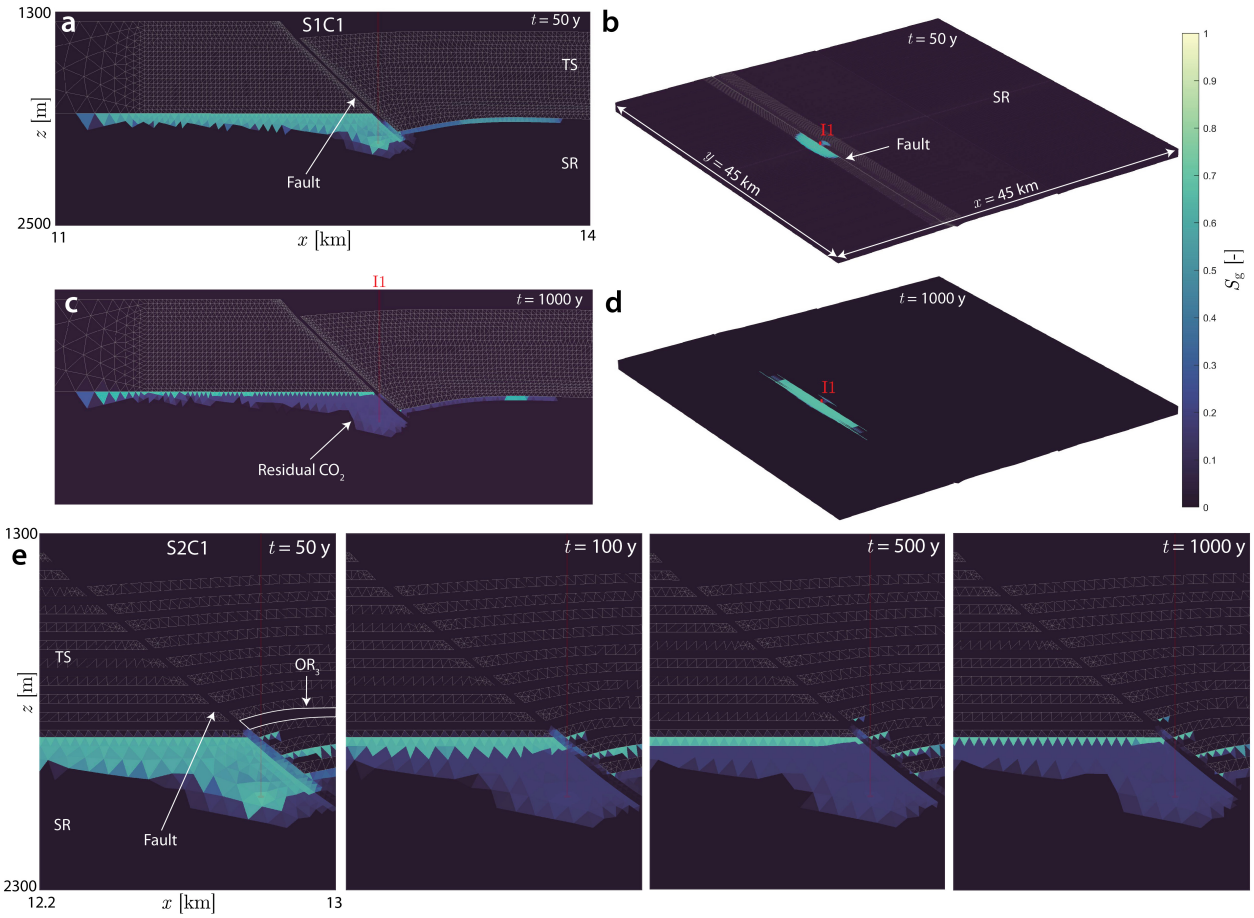

Figure 5.5: Overview of gas (free-phase CO_2) saturation for S1C1 (**a-d**) and S2C1 (**e**). **a**, **c** Vertical cross sections, perpendicular to the fault strike, showing CO_2 migration around the injection location and fault. Both the storage reservoir (SR) and top seal (TS) are visible, and the injector, completed in a single cell, is shown with a thin red line. **b**, **d** Top view of the storage reservoir (SR). Gas migration is evident across the fault and parallel to the fault strike. **e** Zoomed view of gas saturation around the injector and fault for S2C1.

CO_2 leakage above the caprock does not necessarily occur. Maximum fault p and S_g are shown in Fig. 5.6c,d. The maximum Δp is < 1 MPa, which represents a moderate increase at this depth, and reaches higher values in S1C1 due to the buffering effect of the TS sand layers in S2. As noted above, no gas is present above W_1 in S1C1 due to the low fault permeability. CO_2 saturation within the fault is nonlinearly decreasing with time, consistent with reduced CO_2 migration hazard at later times.

5.4.2 Stochastic clay smear modeling

A comparison of S2C2 ($\theta = 30°$, high-permeability) and S2C3 ($\theta = 30°$, low-permeability) is provided in Fig. 5.7. We observe that gas migration across and along the fault is much more irregular due to the varying permeability along the fault strike (Fig. 5.7a,b). However, the overall picture in S2C2 is similar to S2C1, with free-phase CO_2 reaching up to the lower

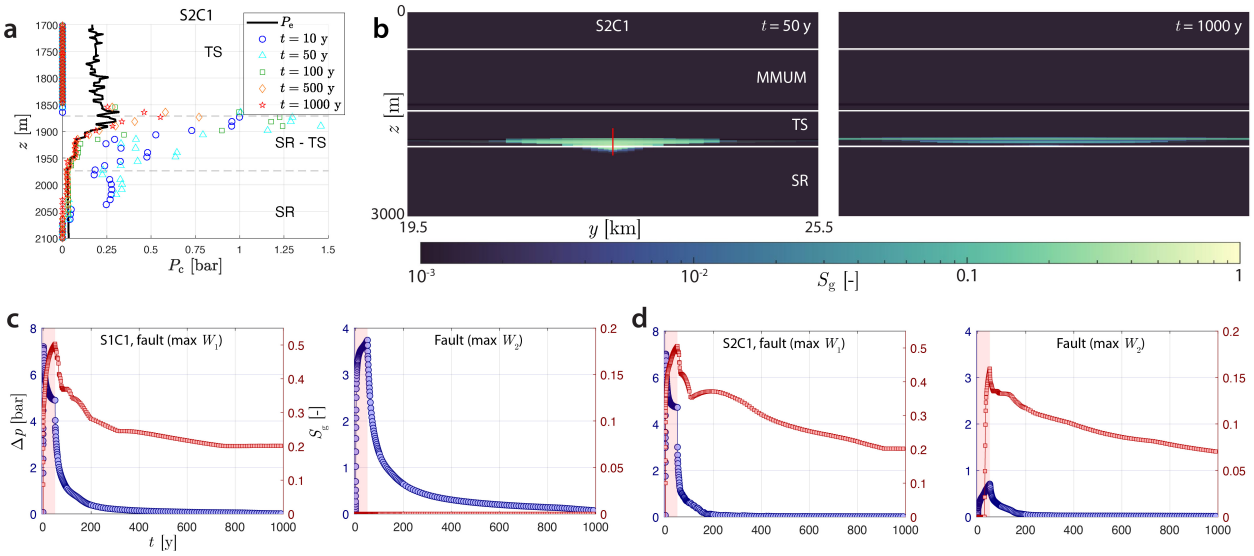

Figure 5.6: Overview of gas (free-phase CO_2) migration within the fault. **a** Capillary entry pressure (solid black line), defined at $S_g = 10^{-3}$, compared to actual capillary pressure at select times. Plotted values correspond to fault cells at the center of the domain ($y = 22.5$ km, closest to the injector), on the hangingwall (HW) side (see red line in **b**). **b** Gas saturation on the fault from the HW, spanning ± 3 km from the center of the y axis. Note that most of the gas migration within the fault volume is dip-perpendicular and strike-parallel, rather than updip. **c** Maximum pore pressure change (left axis, blue) and gas saturation (right axis, red) within W_1 (left) and W_2 (right) for S1C1. **d** Same as **c**, now for S2C1. Refer to Fig. 5.3a for W_i location.

portion of W_2 and migrating into OR_3, which is more permeable than the fault. Also in agreement with our observations from the base cases, maximum gas saturation within the fault decreases with time after the end of injection (Fig. 5.7c); however, here this occurs later in W_2 due to strong permeability variations that hinder fluid movement (note that we extended the run in Fig. 5.7c to $t = 2000$ y). Maximum values within W_1 and W_2 are presented in Fig. 5.7d for S2C3. Maximum Δp remains similar given the same stratigraphy, but in this case we do not observe gas in W_2. This is because the low-permeability fault core realization for P_c upscaling in W_2 is dominated by clay smearing, which leads to an order of magnitude higher P_c compared to S2C2 (see arrow in Fig. 5.4b).

A summary of the simulation results from all cases is provided in Fig. 5.8, which shows the percentage of the total mass of injected CO_2 (50 Mt) in different units. We separate free-phase CO_2 (Fig. 5.8b) from dissolved CO_2 (Fig. 5.8c). As noted above, most of the CO_2 leaving the injection compartment crosses the fault at the SR-SR juxtaposition and gets stored in the HW. The continuous seal case (S1C1) shows the lowest amount of CO_2 within the fault, and no migration into the TS. The discontinuous seal base case (S2C1) estimates the highest amount of CO_2 into OR_1, because P_c is lower and **k** higher at the SR-TS juxtaposition, compared to the smear modeling cases (S2C2 to S2C5). It is also evident that, for a given θ value, the low-permeability cases (S2C3 and S2C5) estimate less CO_2 within the fault and TS sands than their high-permeability counterparts.

Interestingly, S2C4 and S2C5 ($\theta = 60°$) show lower CO_2 migration into OR_1 and OR_2 than S2C2 and S2C3. This is counter-intuitive at first, given that the clay smear P_e is

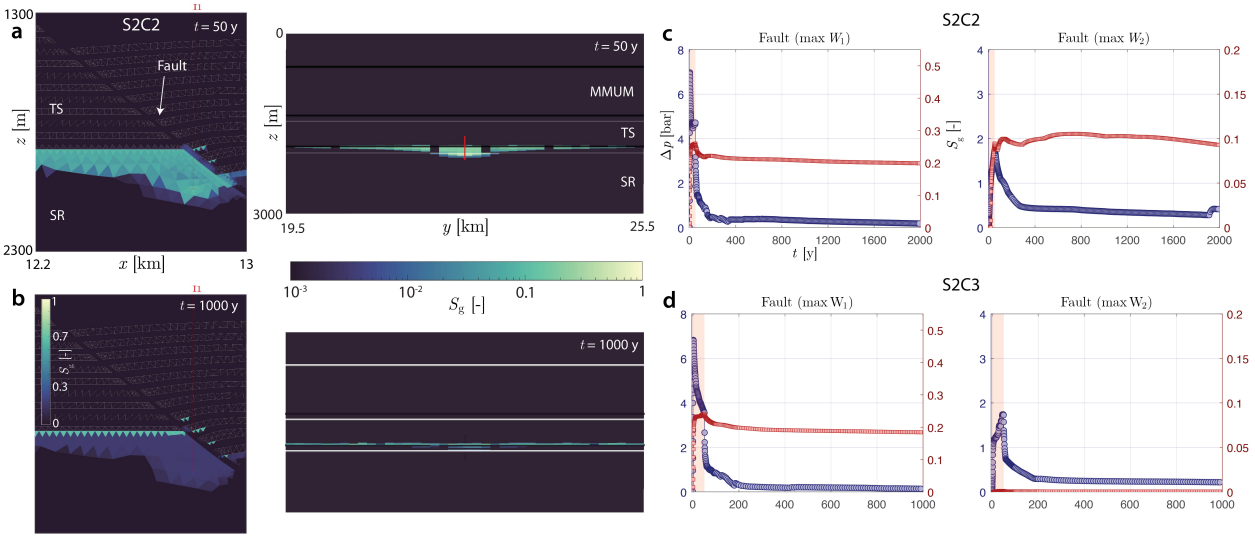

Figure 5.7: Overview of gas (free-phase CO_2) migration in S2C2 (**a-c**) and S2C3 (**d**). **a** Gas saturation in a cross section around the injector (left) and within the fault (right) at the end of CO_2 injection. **b** Same as **a**, now at $t = 1000$ y. **c** Maximum pore pressure change (left axis, blue) and gas saturation (right axis, red) within W_1 (left) and W_2 (right) for S2C2. Note that this run was extended to $t = 2000$ y (see main text). **d** Same as **c**, now for S2C3.

lower (Appendix C.1), which in turn results in lower upscaled P_e in W_1 and W_2 (Fig. 5.4b,c). However, since $P_c > P_e$ during injection, CO_2 migration is governed by effective permeability; k_{rg} for $\theta = 60°$ (Fig. 5.4c) is lower than k_{rg} for $\theta = 30°$ (Fig. 5.4b), which explains this result. We have checked that this is the main control, and not $\mathbf{k}$, by running a simulation for each θ with the same $\mathbf{k}$. In OR_3, free-phase CO_2 is only present in the high-permeability cases (S2C2 and S2C4), given that $p_g - p < P_e$ otherwise. The amount of CO_2 in OR_3 is still increasing after 1000 y, but we have checked that the rate continues to decrease by extending one of the S2C2 runs to $t = 2000$ y. As noted previously (Krevor et al. 2023, and references therein), we observe that free-phase CO_2 migration hazard decreases with time, given the p decrease and increase in immobile and dissolved CO_2. The mass of CO_2 remaining in the storage unit after 1000 y is ≥ 46.5 Mt or $\geq 93\%$. Overall, our results suggest that, in the Miocene section, CO_2 is unlikely to bypass a top seal via updip migration in a listric growth fault.

5.5 Discussion

Due to pore pressure increase from CO_2 injection, free-phase CO_2 overcomes the fault capillary barrier, leading to fault CO_2 migration that is controled by effective fault permeability. Results assuming a discontinuous TS show that CO_2 migration is predominantly into the TS sand-rich layers and along the fault, rather than updip, and no updip fault migration occurs if the TS is continuous (sect. 5.4). Central aspects of this work that are subject to uncertainty include the choice of fault rock curves and upscaling methods (Appendix C), as well as limiting the dependence of fault intrinsic permeability to stratigraphy and burial history

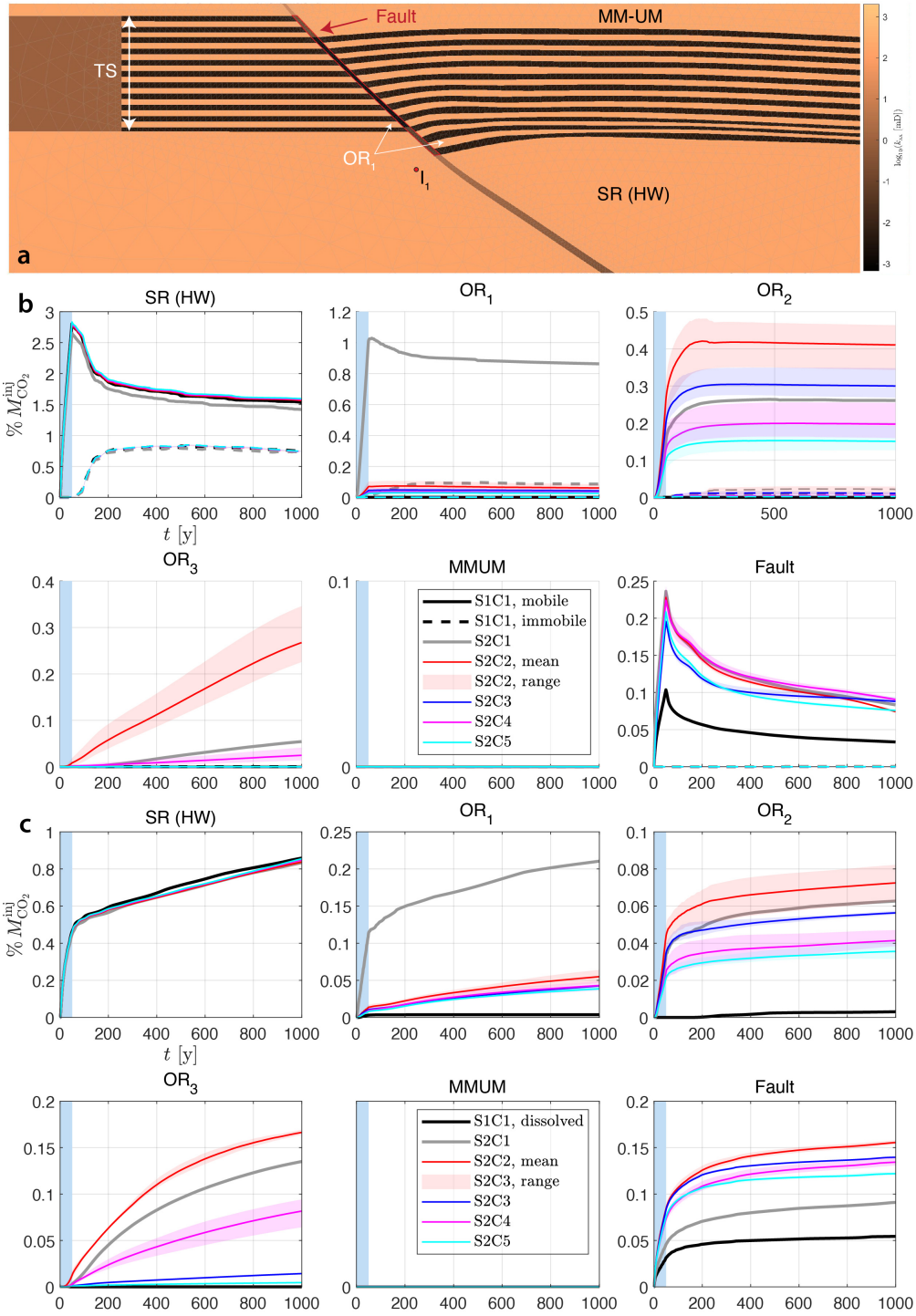

Figure 5.8: CO_2 migration summary, expressed as a percentage of the total mass of injected CO_2 ($\% M^{inj}_{CO_2}$). **a** Grid cross section showing the main geologic units. The sand layers within the TS are numbered OR_i, starting from the bottom. **b** Mobile (solid lines) and residual or immobile (discontinuous lines) free-phase CO_2. For each case S2C2 to S2C5, we plot the mean and range obtained from the three runs (see sect. 5.2.4). **c** Same as **b**, but now for dissolved CO_2.

(sect. 5.2.3). As we argue below, however, our main findings are unlikely to be impacted by these choices.

Relative permeability rock curves are based on measurements at high flow rates (Appendix C.1). This is consistent with viscous-dominated flow during injection, but buoyancy and capillarity control fluid migration at later times. Reducing the capillary number (Ca) typically lowers the nonwetting phase relative permeability by increasing the exponents (Bryant and Blunt 1992; Krevor et al. 2012), which hampers CO_2 migration. This trend is analogous to a θ increase (Morrow et al. 1973). In practice, however, the direction of change is variable and depends on heterogeneities (Krause and Benson 2015; Reynolds and Krevor 2015; Blunt 2017, and references therein), but, given our low gas exponent (1.7 for $\theta = 30°$), we do not expect a significant k_{rg} increase. We also disregarded P_c to upscale k_r, and obtained curves between those of end-members (Fig. 5.4). Dynamic upscaling with full physics, where k_r depends on Ca, is potentially most accurate (e.g., Durlofsky and Chen 2012). Nevertheless, in our model, CO_2 migration is dominated by $\mathbf{k}_{eg}$ differences. $\mathbf{k}_{eg}$ will remain higher in the sands, because sand $\mathbf{k}$ (Table 5.2) is multiple orders of magnitude larger than fault $\mathbf{k}$ (Fig. 5.3). This suggests that dynamics observed in our simulations are robust, even if we cannot capture all k_r variations.

Capillary pressures were upscaled in the fault core using macroscopic invasion-percolation (MIP) simulations (Ioannidis et al. 1996) (Appendix C.1). Here, we imposed the constraint that $S_g = 0$ until percolation occurs, which is necessary to separate fault core realizations with continuous updip sand pathways and those where clay smear impedes flow (see arrow in Fig. 5.4b). MIP assumes that the domain is in capillary equilibrium, and therefore it is only strictly applicable during the post-injection phase. This is reasonable given that fault P_e is clearly exceeded during injection (e.g., Fig. 5.6a) and most of the CO_2 migration occurs in the remaining 950 y. Additionally, stratigraphic studies show that the Amph B shale is a regionally-extensive, very consistent seal (Treviño and Meckel 2017). The effect of increasing the clay proportion in the TS is shown on Fig. 5.9a for W_5 (cf. Fig. 5.3b). For the two cases shown, the buoyancy pressure envelope and most $\mathbf{k}$ values are on the order of maximum P_e and lowest $\mathbf{k}$ values for S2C3 and S2C5, where we did not observe CO_2 above W_1. Hence, our analysis with 50% clay material in the TS is a conservative estimate of fault CO_2 migration.

It is well known that fault permeability is a function of effective stress ($\boldsymbol{\sigma}_{eff}$). At ~2 km depth, a representative value for the effective normal stress acting on a fault, assuming hydrostatic pressure, is 200 bar. The maximum W_1 Δp in our simulations was ≈7 bar, while Silva et al. (2023) obtained 14 and 57 bar for max fault Δp in open and closed aquifer scenarios, respectively. Fig. 5.9b shows a model for faults and crystalline rocks in the seismogenic crust (Rice 1992), a model from siliciclastic faulted cores from the North Sea (Sperrevik et al. 2002), and experimental data for quartz-kaolinite gouge (Crawford et al. 2008). For simplicity, we assume here that $\Delta\sigma_{eff} = \Delta p$. It can be seen that clay-rich mixtures are relatively insensitive to $\Delta\sigma_{eff}$, and even for 40% weight fraction the variation is smaller than one order of magnitude based on aforementioned Δp. Similarly, Sperrevik et al.'s model predicts about one order of magnitude variation for $\Delta\sigma_{eff} = 50$ bar in clay-rich shear zones. At the field scale, Rice's model has been used to explain pressure distributions in mechanically weak faults and episodicity of flow along faults. One example in the Gulf of Mexico where this model fits in-situ measurements is the Red Fault (Revil and Cathles III 2002) (Fig. 5.9b). Importantly, this is a strongly overpressured fault system where $\sigma_{eff} \to 0$. It is

currently active, and dilatancy, fluidization and hydrofracturing are hypothesized to occur during pressure pulses driving flow updip the fault. Another field example from shale faults where injection results in shear slip and strong permeability increase at low σ_{eff} has been presented by Cappa et al. (2022). Clearly, our study cannot address fault behavior changes with reactivation and $\sigma_{\text{eff}} \to 0$. However, since the permeability of clay-rich material in the fault core is steadily sensitive to $\Delta\sigma_{\text{eff}}$, our results are reliable for faults without open fracture networks subject to moderate Δp, as obtained from this study and previous coupled flow-geomechanics modeling in a similar setting (Silva et al. 2023).

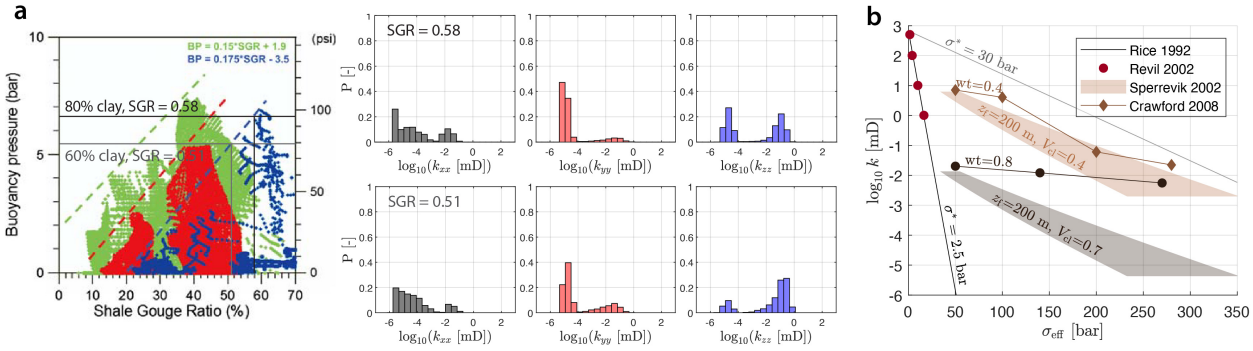

Figure 5.9: **a** (Left) Global dataset of hydrocarbon buoyancy pressure as a function of the shale gouge ratio (SGR), colored by maximum burial depth (from Yielding et al. 2010). The dashed lines are maximum pressure envelopes, and the solid lines are for W_5, where the thickness of the clay layers is increased to 60% and 80% of the throw (instead of 50% used in the simulations). (Right) Permeability distributions from `PREDICT` for W_5 with 60% and 80% clay. **b** Dependence of fault permeability on σ_{eff}. Lines show $k = k_0 \exp(-\sigma_{\text{eff}}/\sigma^*)$ (Rice 1992), red markers are in-situ measurements in the Red Fault System by Revil and Cathles III (2002), markers with trend lines are for 40 and 80% weight fraction quartz-kaolinite gouges under hydrostatic compression (Crawford et al. 2008), and shaded areas are for Sperrevik et al.'s 2002 model. For the latter, we roughly estimated σ_{eff} from the maximum burial depth ($z_{\max}$), with the shaded area showing $\sigma^z_{\text{eff}} \in [0.8\sigma^z - p,\ \ \sigma^z - p]$, where $\sigma^z(z_{\max})$ is the overburden stress and $p(z_{\max})$ the hydrostatic pore pressure.

5.6 Summary and Conclusion

We used a geologic model representative of the Miocene section offshore Texas State waters (Gulf of Mexico) and evaluated CO_2 migration through a listric fault partially offsetting the top seal (TS). Our analysis is based on multiphase flow modeling, incorporating stochastic modeling of clay and sand smears in the main shear zone and their effect on multiphase flow properties (sect. 5.2 and 5.3). Results presented here are applicable to soft siliciclastic settings with approximately hydrostatic pore pressures and faults that are not reactivated during injection. In these conditions, we have shown that CO_2 migration updip a listric growth fault is prevented by capillary and low-permeability barriers and mitigated by secondary sand reservoirs within the top seal interval (sect. 5.4). Although we injected CO_2 next to the fault, $\geq$ 93 % of the total injected mass remains in the storage unit after 1000 y. Our results address the question of CO_2 migration within faults after capillary breach,

which limits capacity in GoM fault-bounded traps (Meckel et al. 2017). We conclude that CO_2 leakage above the top seal is unlikely, even if the capillary entry pressure is briefly exceeded during injection.

In addition to flow models, GCS planning in similar settings will benefit from hydrogeologic studies at the basin, reservoir and core scales; geomechanical studies to avoid fault reactivation (e.g., Silva et al. 2023); and risk analyses that incorporate uncertainty sources beyond faults (e.g., Pawar et al. 2016). Research continues to be needed on evolutionary models of fault zone architecture (e.g., how can we confidently predict a fault's internal structure), as well as the spatial variability of fault attributes (e.g., correlation length of strike-parallel fault permeability). Quantitative knowledge in these areas would reduce uncertainty on fault-related flows and reactivation potential, which are also of interest in other subsurface technologies like hydrogen storage or geothermal energy.

Chapter 6

Conclusions and Future Work

In this Thesis, we have extended the `ad-blackoil` module of `MRST` to increase fidelity in numerical simulations of geologic carbon dioxide sequestration (GCS) in saline aquifers (ch. 2), evaluated–quantitatively–the degree of concordance between numerical simulations and experiments of CO_2 injection and migration at the meter scale (ch. 3), developed a probabilistic methodology to estimate the directional components of the fault permeability tensor (ch. 4), and applied this methodology to assess fault CO_2 migration in Miocene sediments offshore Texas (ch. 5). The key findings from this work are:

1. Concerning numerical models of GCS: calibration requires less time if local data are available, models are less accurate when applied to geologic settings different from those used to calibrate them (even if governing physics remain the same), and models are unlikely to achieve quantitatively accurate deterministic estimates of CO_2 migration, especially in contexts with heterogeneous structures like faults.

2. With regard to fault zone permeability in soft siliciclastic sequences: it is dominated by the configuration of clay smears, it is difficult to constrain (probabilistic estimates are multimodal and span several orders of magnitude), and it can be highly anisotropic due to material layering.

3. In terms of fault CO_2 migration: if the fault seal is breached, migration is controlled by effective permeability. In the Miocene section offshore Texas, updip CO_2 migration in listric growth faults is unlikely due to clay-rich caprocks and stacking of multiple sand intervals, which are more permeable than the fault.

We have provided evidence on: (1) the limits of numerical models and our ability to make quantitative forecasts based on simulation results; (2) what is the impact of uncertainty on permeability estimates in layered fault cores, typical of faults in soft siliciclastic sequences; and (3) the interplay between structural geology and petrophysics on fault CO_2 migration. Our findings strongly suggest that numerical models can adequately describe CO_2-brine migration, but also that accurate deterministic forecasts of subsurface CO_2 migration are difficult to obtain. This is not necessarily surprising given uncertainties inherent in subsurface engineering, but emphasizes the need to describe the effect of uncertainty sources on quantitative estimates of CO_2 migration (cf. Einstein and Baecher 1982; Einstein

and Baecher 1983). In the field, the main uncertainty source is typically the distribution of physical properties; additionally, simulating GCS in km-scale models requires modeling choices which also impact the quality of numerical solutions. We therefore conclude, first, that uncertainty quantification in petrophysical properties and probabilistic assessments of CO_2 migration are necessary. Second, in agreement with previous work (e.g., Nordbotten et al. 2012), that flow simulation models should be history-matched and updated as field data become available.

Our work also points to the need for further research in the following areas:

- Uncertainty quantification of CO_2 migration: Numerical models are computationally expensive, and development of more efficient solvers continues to be needed. It is typically impossible to fully quantify uncertainty in forecasts using physics-based models. Hence, surrogate modeling frameworks using physics-based or data-driven reduced order models (ROMs) are required. A question that arises from our results concerns the choice of geologic models, petrophysical properties and numerical simulator(s), since CO_2 migration is sensitive to all of these aspects; thus, the forecasting capability of subsequent models trained on physics-based data will be influenced by these choices.

- Fault permeability structure: Structural geology and hydrogeologic studies have provided evidence of architectural styles, local and bulk fault zone hydraulic behavior. Quantitative bulk measurements, however, are rare, with a recent exhaustive review reporting 3 and 14 values for fault zones in unlithified siliciclastics and mudrocks, respectively (Scibek 2020); this renders statistical modeling unfeasible. It is also difficult to confidently predict a fault's 3D permeability structure, including segmentation, mesoscale structures and distribution of fault materials, which leads to uncertainty of several orders of magnitude in properties like permeability. The characterization of fault relative permeability and capillary pressure is even more uncertain, especially considering the absence of measurements. The oil and gas industry has traditionally used juxtaposition analysis and local calibrations based on across-fault pressure differences and laboratory measurements to determine fault sealing and permeability. Because extrapolation based on empirical models is difficult, work is needed to improve predictions of fault behavior, in particular regarding fault-parallel flow and in settings without previous hydrocarbon history.

- Characterization of subsurface settings: Site-specific evaluations are needed to increase GCS capacity. Our analysis of fault zone CO_2 migration suggests that local, reservoir and basin-scale hydrogeologic studies are important to determine local petrophysics, background pressures and large-scale flow regimes, all of which influence CO_2 migration. Geomechanics assessments are also critical to constrain the pore pressure increase that can be safely accommodated during CO_2 injection to avoid fault reactivation.

Our discussion is centered around megaton-scale GCS in faulted siliciclastic settings, expected to play a significant role as CO_2 storage increases two orders of magnitude to meet mid-century climate goals (IEA 2021; IPCC 2022). It should be noted, however, that significant storage space exists in reservoirs that have already been extensively studied (e.g., depleted petroleum fields) and, also, that CO_2 can be stored in laterally-extensive formations

and hydraulically open reservoirs to limit intersection of the CO_2 plume with major faults and pore pressure increase (e.g., Chadwick et al. 2004; Silva et al. 2023). These types of settings should arguably be utilized first; in parallel, research to address the points above should be conducted to access further reservoirs later on.

It is our view that increasing GCS capacity by two orders of magnitude requires close collaboration among researchers in geological sciences, hydrology, geomechanics and seismology, and numerical, data-driven and uncertainty modeling. Collaboration between academia, industry and government will also be required to plan operations with high probability of success and establish conducive policies to achieve our mid-century climate goals. Finally, we note that, while this Thesis is framed around GCS in faulted siliciclastic sequences, our conclusions and future work should be useful in other settings, as well as in other applications in groundwater hydrology, subsurface energy storage and production, or waste disposal.

Appendix A

Additional Analysis of Numerical Simulation Results (Ch. 3)

A.1 Additional Analysis of Simulation Model Concordance with Experiment B1

A.1.1 Results with initial model parameters

Fig. A.1 compares Experiment B1 and concentration maps from simulations with initial parameters, for each of the three model versions considered. Qualitatively, all models estimate the location of the two main gas plumes correctly, but it is clear that Model 1 and 2 are less concordant to the experiment than Model 3. This is particularly true in the upper left of the domain, where CO_2 migration is controlled by the heterogeneous fault. Similar to results presented in sect. 3.4.1, Model 3 is already very close to the experiment, although the advance of convective fingers is slower.

Concordance between our initial models and the simulation is shown in Fig. A.2 by means of the ratio between the model and experimental areas for different quantities in Box A and B (see Fig. 3.15 for box location). Values below 1 indicate that the model underestimates the areal extent of a given quantity, while values above 1 indicate that the model overestimates it. During the first 48-72h, all models except $M_{3,1}$ are reasonably close to the experiment in Box A. Afterwards, M_1, M_2 and $M_{3,3}$ forecast earlier dissolution of the CO_2 plume, while $M_{3,1}$ forecasts later dissolution. In Box B, concordance is relatively good for M_3 during the first 48h, but model accuracy diminishes with time for all model versions.

Further comparison between our initial model results and experimental values are provided in Fig. A.3, where we evaluate mean Wasserstein distances to the international benchmark study (IBS) participants' forecasts and experiments (Flemisch et al. 2023). Fig. A.3 is consistent with Fig. A.1, where it can be seen that M_3 is already very close to the experiment, and is similarly concordant or more concordant than the best of the IBS participants.

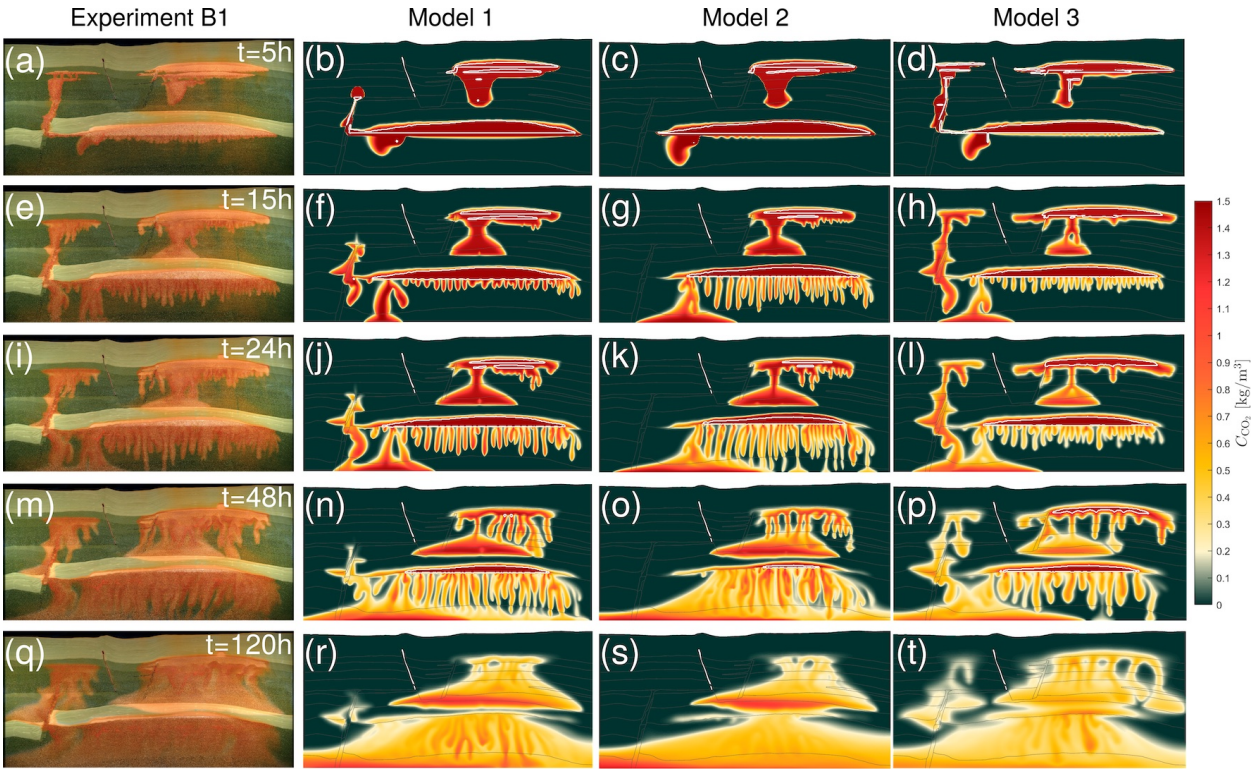

Figure A.1: Comparison between Experiment B1 in Tank 2 (leftmost column) and CO_2 concentration maps for simulation models 1-3 (middle-left, middle-right and rightmost, respectively) with initial parameters. $D = 10^{-9}$ m^2/s (Model 1 and 2), $D = 3 \times 10^{-9}$ m^2/s (Model 3). **a-d** end of injection. **e-h** $t = 15$h. **i-l** $t = 24$h. **m-p** $t = 48$h. **q-t** $t = 120$h.

A.1.2 Calibrated models

First, we provide the total mass of CO_2 in the computational domain in Fig. A.4, and the mass in Boxes A and B in Fig. A.5.

Next, in Tab. A.1, the following measures are compared with quantities estimated from the experiment via segmentation of timelapse images (Nordbotten et al. 2023). These measures correspond to the sparse data requested to participants of the FluidFlower IBS (Flemisch et al. 2023):

1. time of maximum mobile free phase in Box A
2. mass of mobile $CO_{2(g)}$, immobile $CO_{2(g)}$, dissolved CO_2, and CO_2 in the seal (in any phase), in Box A, 72 h after injection start (2a-d)
3. the same quantities as 2. for Box B (3a-d)
4. time at which m (defined below) exceeds 110% of the width of Box C
5. total mass of CO_2 in the ESF seal, in Box A, at $t = 120$ h

Convective mixing in Box C (see Fig. 3.1e) is reported as the integral of the magnitude of the gradient in relative concentration of dissolved CO_2 (Flemisch et al. 2023):

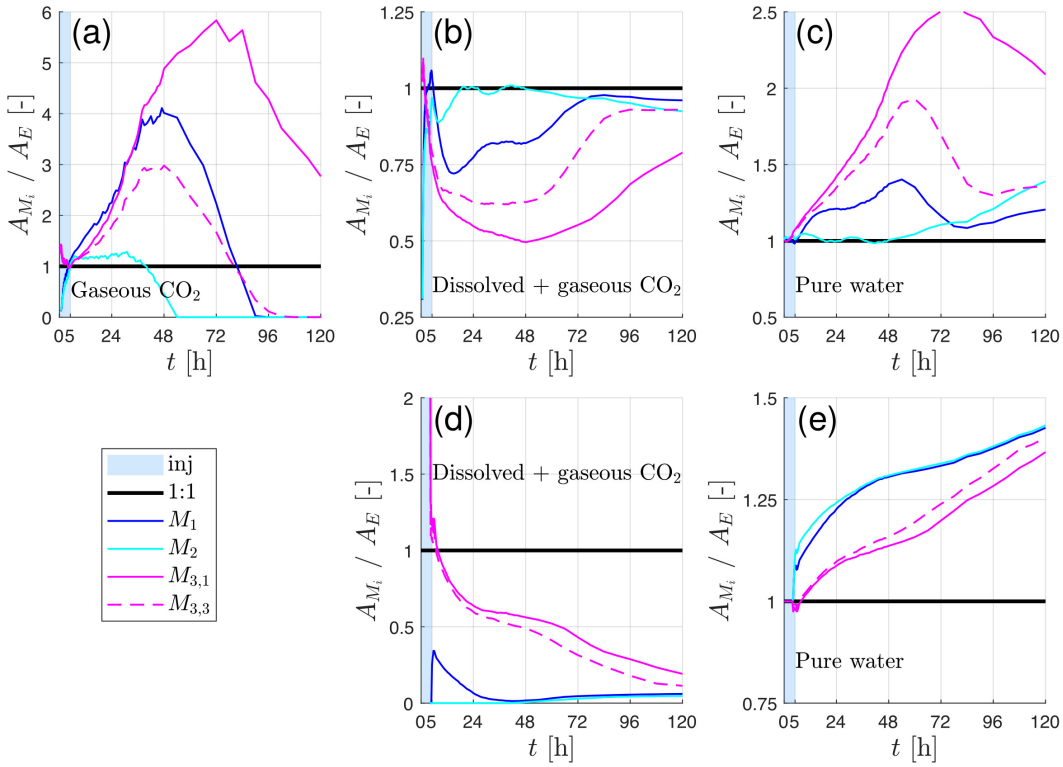

Figure A.2: Ratios between model (A_{M_i}) and experimental mean (A_E) areas occupied by each phase. Experimental mean was obtained from four experimental runs with identical protocol, while the results for models 1-3 are for a single run. For M_3, two cases are shown: $D = 10^{-9}$ m^2/s ($M_{3,1}$) and $D = 3 \times 10^{-9}$ m^2/s ($M_{3,3}$). Top row shows Box A, and bottom row shows Box B. Ratios for gaseous CO_2 in Box B are not computed because experimental values are 0. **a** gaseous CO_2. **b,d** dissolved CO_2 (includes area with gaseous CO_2). **c,e** pure water.

$$m(t) = \int_C \left| \nabla \left(\frac{\chi^{w}_{CO_2}}{\chi^{w,max}_{CO_2}} \right) \right| d\mathbf{x} \tag{A.1}$$

where $\chi^{w}_{CO_2}$ is the mass fraction of CO_2 in water, and the dissolution limit is $\chi^{w,max}_{CO_2}$. Note that quantity 4, based on m, cannot be provided with full accuracy based on experimental data, so an uncertain lower and upper bound is provided instead. Therefore, error is not computed in Tab. A.1.

Relative error is evaluated with respect to the experimental mean ($\overline{E}$) as $\varepsilon_i(\%) = 100 \times \frac{|\overline{E_i} - M_{J,i}|}{\overline{E_i}}$, where i is a given measure and J refers to any of the models 1-3. In Tab. A.1, it can be seen that all models accumulate some error in most of the quantities reported. The maximum errors are $\approx 140\%$ for models 1-2 and $< 100\%$ for Model 3. Model 1 is more concordant in the uncertain region (Box B; see sect. 3.4.3 as well), while models 2 and 3 are more accurate in Box A, the region where the calibration performed with Experiment A1 is more meaningful. Overall, $M_{3,1}$ does marginally better.

We provide additional analysis in Fig. A.6, which shows ratios between model and experimental areas, similar to Fig. A.2. As shown in sect. 3.4.3, $M_{3,3}$ is most concordant in Box A, while M_1 and $M_{3,1}$ do better in Box B. Compared to Fig. A.2, the maximum ratio

Table A.1: Sparse data comparison between Experiment B1 in Tank 2 and simulation results with models 1-3. Experimental mean and standard deviation were obtained from six experimental runs with identical protocol, while the results for models 1-3 are for a single run with each matched model. For m_3, two cases are shown: $D = 10^{-9}$ m^2/s ($m_{3,1}$) and $D = 3 \times 10^{-9}$ m^2/s ($m_{3,3}$). Experimental quantity 4 is reported using a lower and upper bound due to high uncertainty, so errors are not computed. See main text for measure description.

Measure	$\overline{E}$	$\sigma(E)$	M_1	ε_1 [%]	M_2	ε_2 [%]	$M_{3,1}$	$\varepsilon_{3,1}$ [%]	$M_{3,3}$	$\varepsilon_{3,3}$ [%]
1 [s]	14880	720	17700	19	17160	15.3	17280	16.1	18000	21
2a [g]	0.36	0.13	0.87	140.7	0.57	59.7	0.54	48.7	0.005	98.8
2b [g]	0	0	0	0	0	0	0	0	0	0
2c [g]	3.5	0.08	2.11	39.7	3.1	11.3	2.8	19	3.6	3.5
2d [g]	-	-	0.43	n/a	0.97	n/a	0.74	n/a	0.7	n/a
3a [g]	0	0	0	0	0	0	0	0	0	0
3b [g]	0	0	0	0	0	0	0	0	0	0
3c [g]	0.55	0.32	0.52	4.7	0.1	80.7	0.23	58.4	0.1	82.4
3d [g]	n/a	n/a	0.002	n/a	0.006	n/a	0.002	n/a	0.004	n/a
4 [s]	[12180, 17990]	[438, 2261]	15000	n/a	15000	n/a	18600	n/a	15600	n/a
5 [g]	0.38	0.047	0.52	37.1	0.94	148.5	0.73	91.6	0.62	63.1
$\overline{\varepsilon}$ [%]	n/a	n/a	n/a	30.1	n/a	39.4	n/a	29.2	n/a	33.6

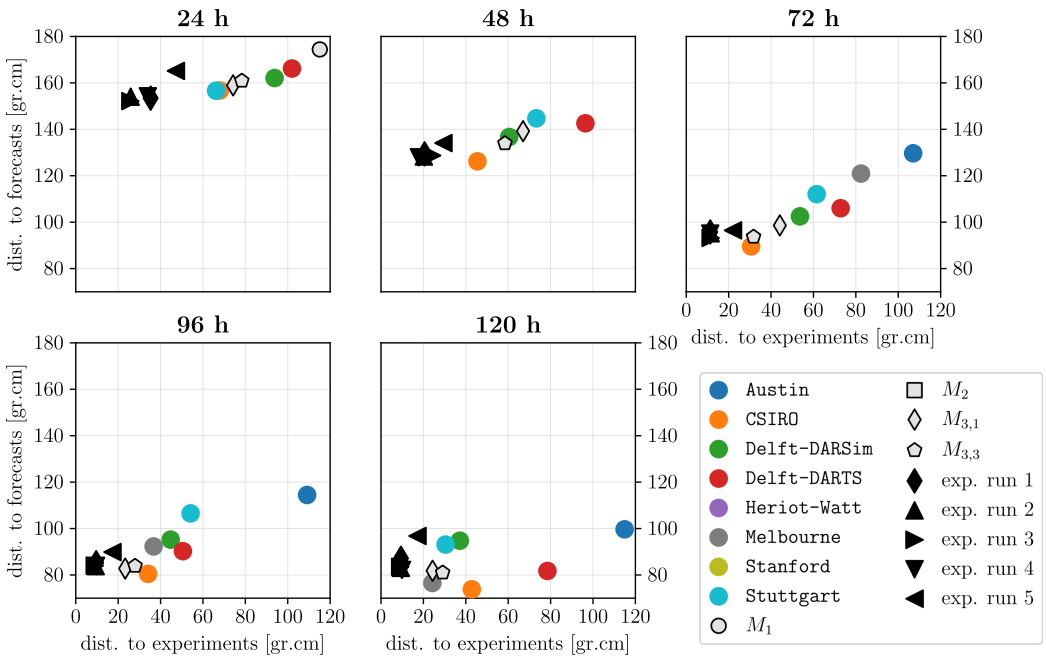

Figure A.3: Wasserstein distances to experiments and forecasts (simulations). Colored circles show forecasts by IBS groups, and results with initial models 1-3 are presented with light gray markers. In each subplot, the vertical axis shows the mean distance between a given datapoint and the forecasts (considering the IBS participants only), while the horizontal axis shows the mean distance between a given datapoint and the experiments. Markers not present fall outside of the axes limits. See sect. 3.4.3 for details.

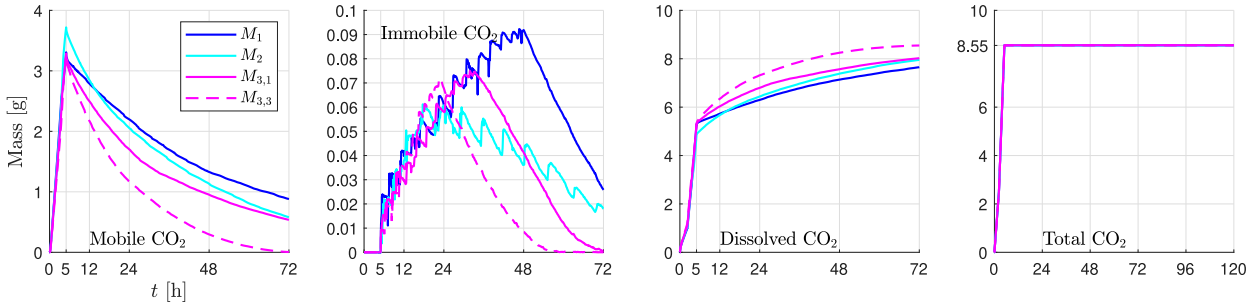

Figure A.4: Total mass of CO_2 for our simulations of Experiment B1 presented in sect. 3.4.3. Results are provided for models 1 to 3. For M_3, two cases are shown: $D = 10^{-9}$ m^2/s ($M_{3,1}$) and $D = 3 \times 10^{-9}$ m^2/s ($M_{3,3}$).

is reduced. In Box A ($t < 72$h), Model 1 and 2 are less accurate than in Fig. A.2, but this is not representative of their concordance in the whole domain (sect. 3.4.3).

A.2 Nonlinear Solver Number of Iterations

According to fluid migration in the FluidFlower, flow dynamics are initially dominated by injection rates, then by buoyancy of the gas phase, and finally by capillarity and dissolution.

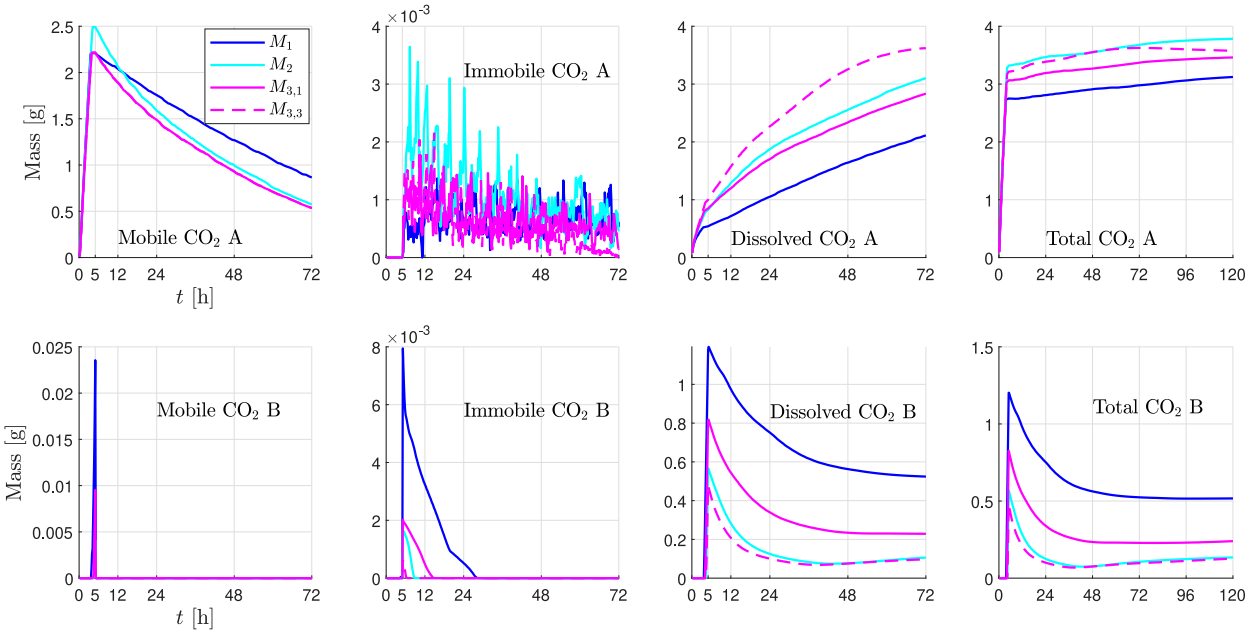

Figure A.5: Mass of CO_2 in Boxes A and B defined in Fig. 3.1e, for our simulations of Experiment B1 presented in sect. 3.4.3. Results are provided for models 1 to 3. For M_3, two cases are shown: $D = 10^{-9}$ m^2/s ($M_{3,1}$) and $D = 3 \times 10^{-9}$ m^2/s ($M_{3,3}$).

In Fig. A.7, we present, for the experiment in Tank 2, the relationship between the number of iterations, the maximum Darcy velocity (u) and the maximum concentration rate ($\dot{C}$), evaluated as dC/dt, as a function of time. Additionally, we estimated the maximum values of the dimensionless Reynolds (R_e, see Eq. 3.1), Capillary (C_a) and Bond (B_o) numbers during and after injection (e.g., Bear 1972):

$$C_a = \frac{\mu_\alpha u_\alpha}{\sigma} \tag{A.2}$$

$$B_o = \frac{\Delta\rho g k}{\sigma} \tag{A.3}$$

Where μ is the dynamic viscosity, u the Darcy velocity, σ the interfacial tension, $\Delta\rho$ the density difference, g the gravity, k the permeability, and subscript α denotes a generic fluid phase. Max $B_o \sim O(10^{-3})$ and remains constant in our system. Max $C_a \sim O(10^{-6})$, $\sim O(10^{-7})$ for water and $\sim O(10^{-6})$, $\sim O(10^{-8})$ for gas (during and after injection, respectively), while max $R_e \sim O(10^{-2})$ for water and $\sim O(10^{-1})$, $\sim O(10^{-2})$ for gas (during and after injection, respectively).

From Fig. A.7, a correlation between max $|u_{\mathrm{h,g}}|$ is apparent during injection. The number of iterations increases significantly after an injection port becomes active, and also when CO_2 spills out of the lower reservoir and starts migrating along the lower fault (see Fig. 3.15); this occurs at $t \approx 215$ min and $t \approx 250$ for M_1 and $M_{3,3}$, respectively. Peaks in $\dot{C}$ appear at the onset of injection, but we do not observe significant variations otherwise. Values from the dimensionless groups are indicative of high flow rates (R_e close to 1), relatively strong capillary forces, compared to viscous forces ($C_a \sim O(10^{-6})$ or smaller), and appreciable buoyancy. We identify that high flow rates and sudden appearance/disappearance of fluid

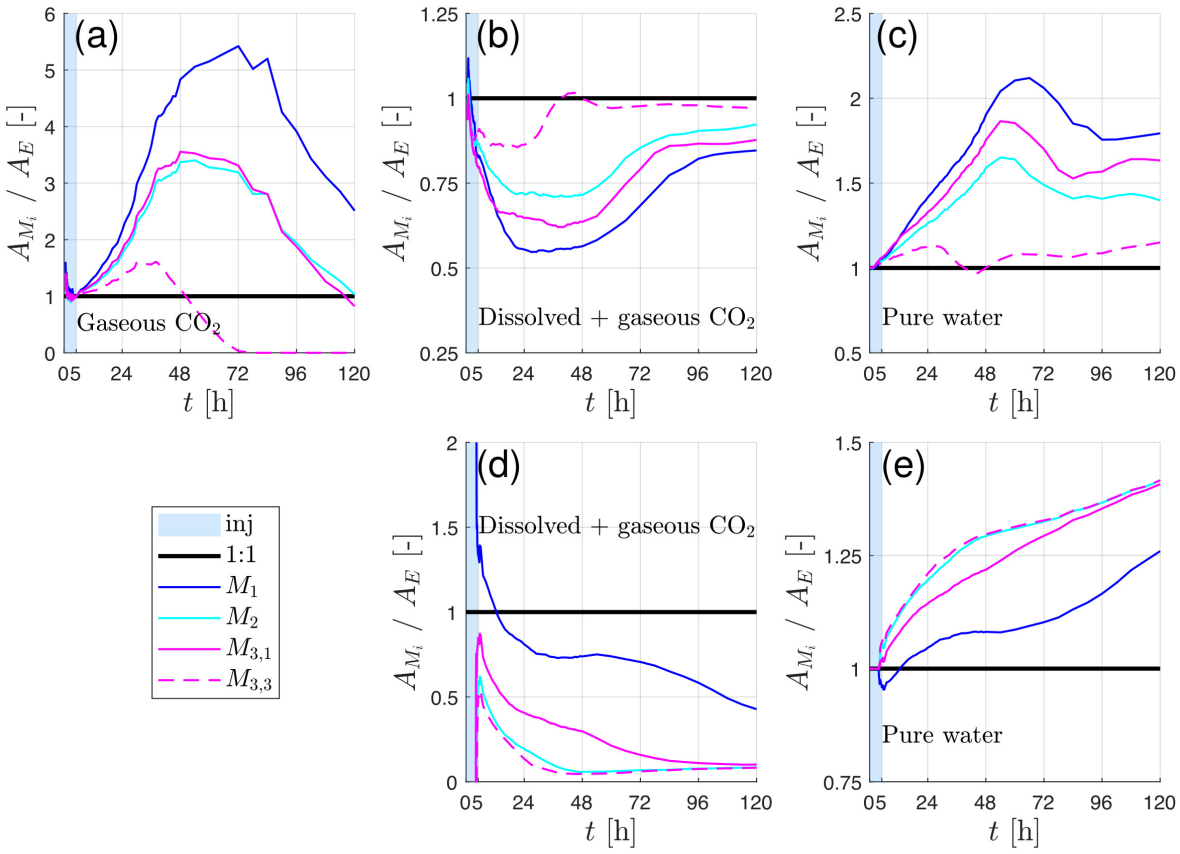

Figure A.6: Ratios between calibrated model (A_{M_i}) and experimental mean (A_E) areas occupied by each phase in case B1. Experimental mean was obtained from four experimental runs with identical protocol, while the results for models 1-3 are for a single run with each model. For M_3, two cases are shown: $D = 10^{-9}$ m^2/s ($M_{3,1}$) and $D = 3 \times 10^{-9}$ m^2/s ($M_{3,3}$). Top row shows Box A, and bottom row shows Box B. Ratios for gaseous CO_2 in Box B are not computed because experimental values are 0. **a** gaseous CO_2. **b,d** dissolved CO_2 (includes area with gaseous CO_2). **c,e** pure water.

phases challenge the nonlinear solver during injection. Buoyancy and capillarity forces, which are active throughout the simulation, also impact convergence, but it is not straightforward to identify if one exerts a greater control on the number of iterations. After injection, we observe difficulties between $t \approx 315$ and 1440 min in M_1, and $t \approx 720$ and 1440 in $M_{3,3}$. Our analysis does not reveal why, so this is a topic that warrants further study.

A.3 Comparison of Simulation Results with Multiple Grid Resolutions

This section provides two comparisons of concentration maps obtained with Model 3 after the calibration presented in sect. 3.4.2:

1. For Experiment A1, we compare two grid sizes: $h = 4$ mm, as shown in the paper, and

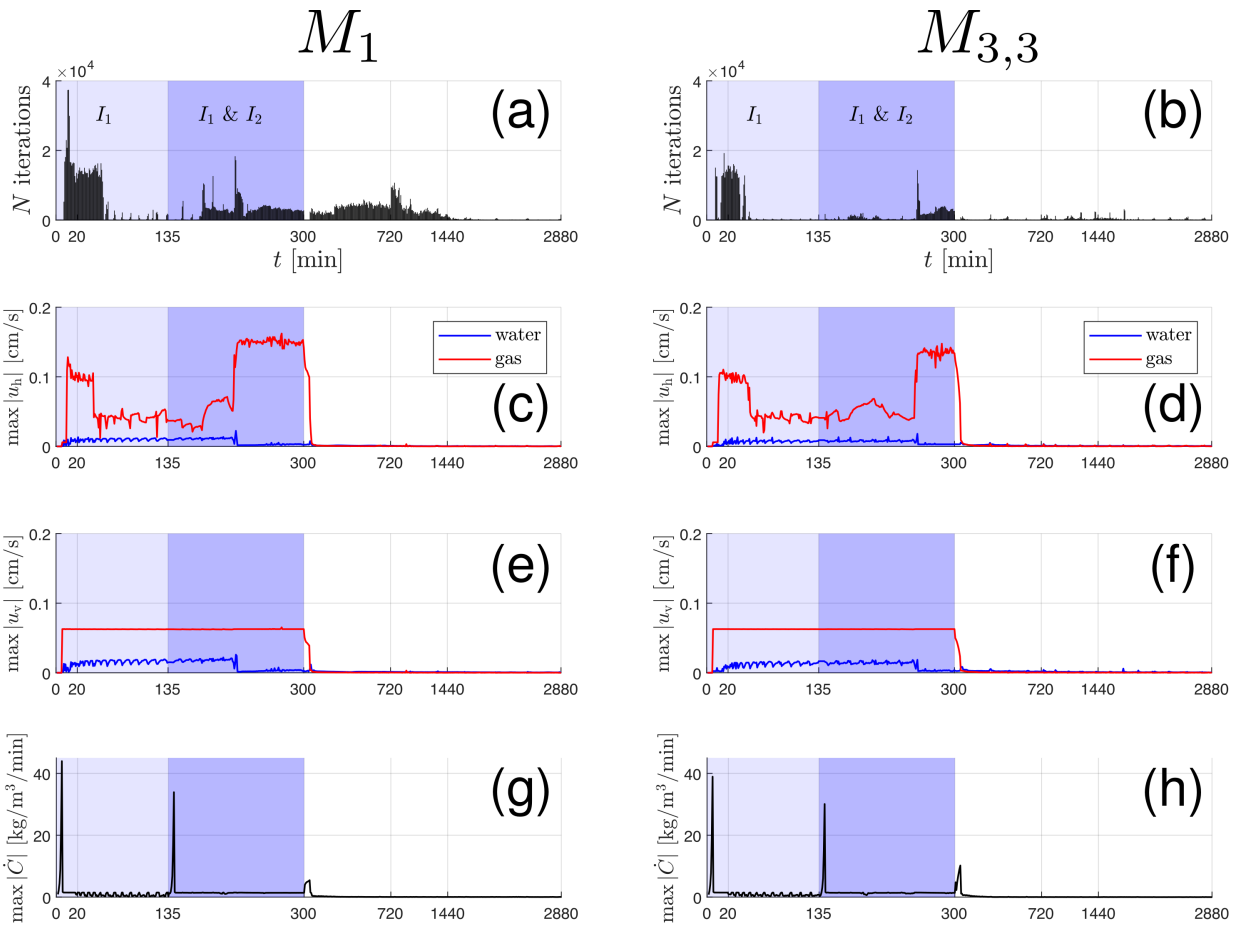

Figure A.7: Number of iterations and maximum values in the simulation domain for various quantities, as a function of time. Results are provided for M_1 (left column) and $M_{3,3}$ (right column). **a,b** Number of nonlinear solver iterations. **c,d** Horizontal Darcy velocity. **e,f** Vertical Darcy velocity. **g,h** Concentration rate ($\dot{C}$).

a coarser grid with $h = 8$ mm (Fig. A.8).

2. For Experiment B1, we compare three grid sizes: $h = 5$ mm, used throughout the paper, and two coarser grids with $h = 10$ mm and $h = 20$ mm, respectively (Fig. A.9). Note that, in the three simulations in Fig. A.9, a total of 8.13 g of CO_2 were injected; this is slightly smaller than the 8.55 g actually injected in the experiment and in our simulations in the rest of the paper.

It can be seen that, for the calibrated parameter set (Tab. 3.4), the coarser models maintain a general agreement with the finer ones (and the experimental solution). However, some differences are clear even in this qualitative comparison, including (1) smaller extent of the CO_2 plume, (2) lower dissolution, (3) lower number of fingers and finger widths, and (4) different CO_2-rich finger sinking speed. Therefore, the calibration process is somewhat cell-size dependent, which has implications for applying history matched models from e.g., pilot tests to field-scale CO_2 storage projects.

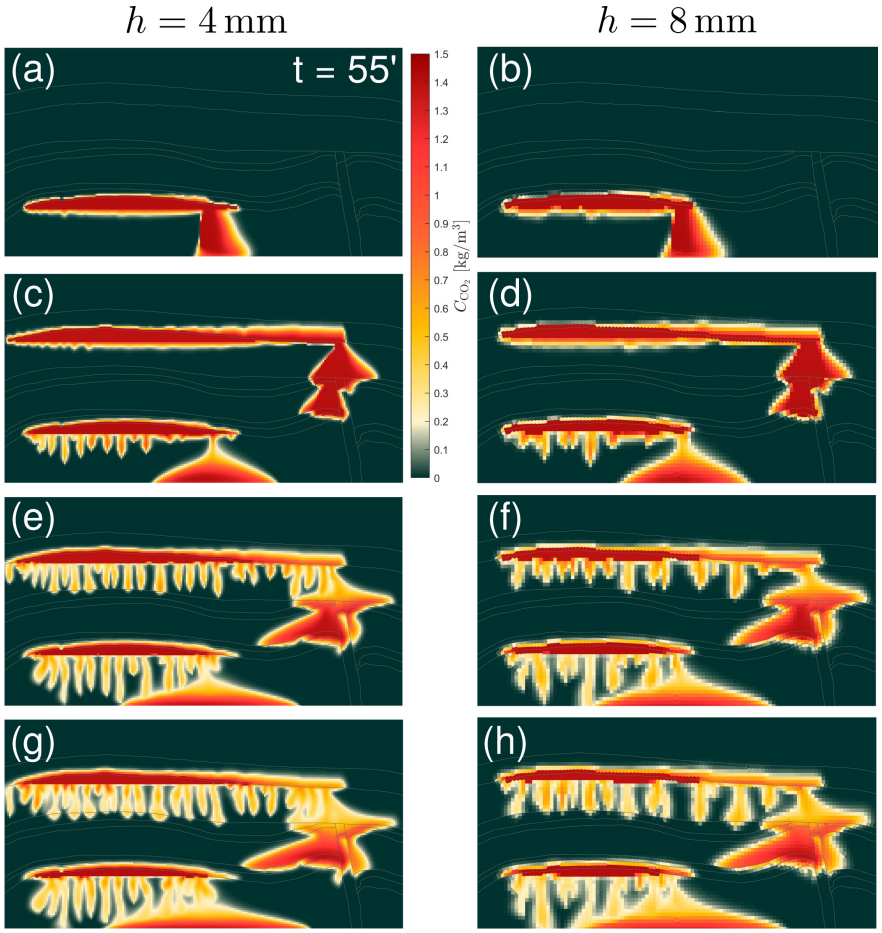

Figure A.8: Concentration maps from our simulations of Experiment A1 with Model 3. Results with two grids are shown: $h = 4$ mm (**a**, **c**, **e**, **g**) and $h = 8$ mm (**b**, **d**, **f**, **h**).

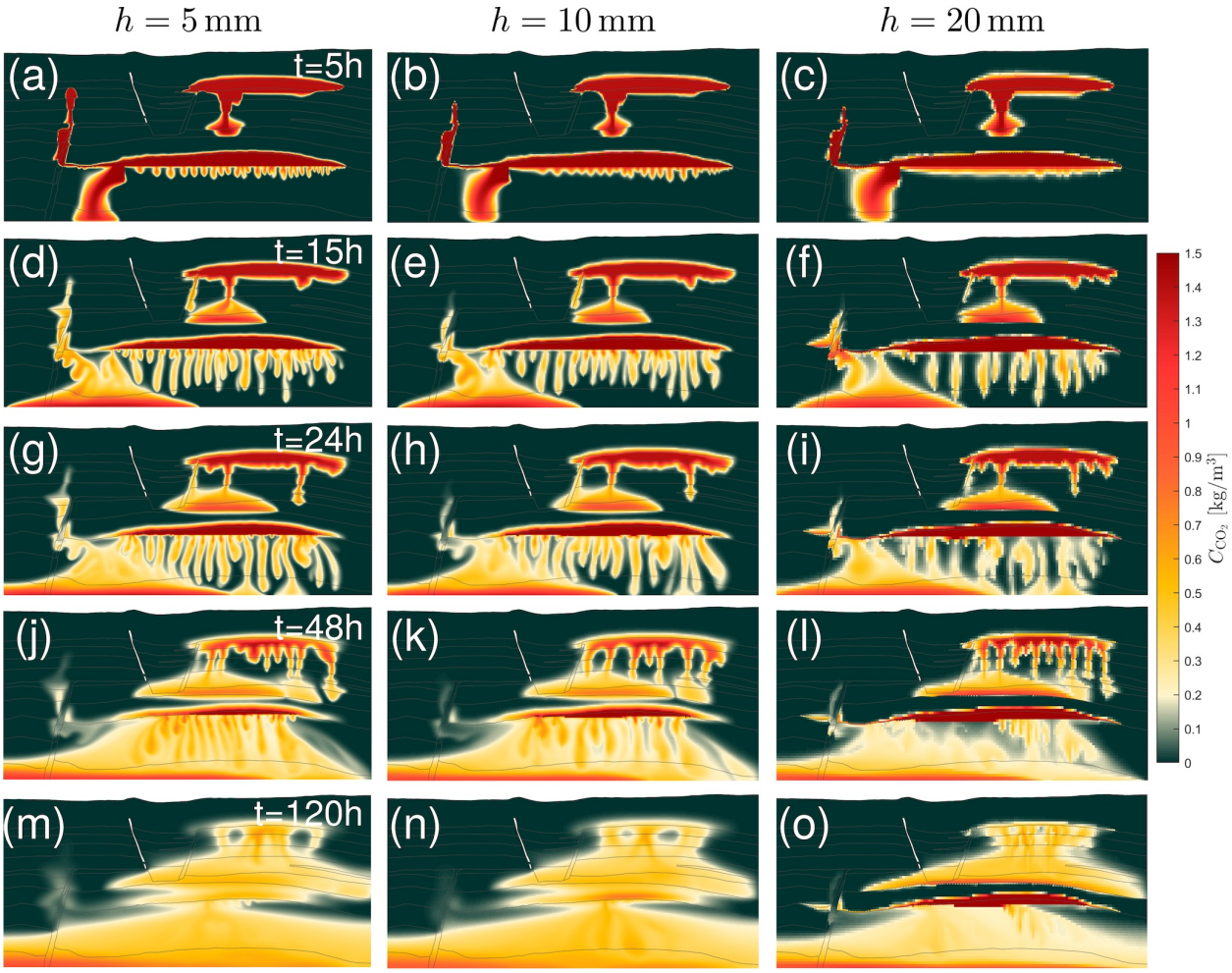

Figure A.9: Concentration maps from simulations of Experiment B1 with Model 3. Results with three grids are shown: $h = 5$ mm (**a**, **d**, **g**, **j**, **m**), $h = 10$ mm (**b**, **e**, **h**, **k**, **n**) and $h = 20$ mm (**c**, **f**, **i**, **l**, **o**).

Appendix B

Detailed description of PREDICT (Ch. 4)

Nomenclature for Appendix B

Input parameters

β	Dip angle of the FW and HW stratigraphy
f_β	Fault dip angle
m	Predominant clay mineral in the FW and HW stratigraphy (optional)
T	Layer thickness
V_{cl}	Layer clay volume fraction
z_{f}	Faulting depth
$z_{\max}$	Maximum burial depth

Intermediate variables

f_{T}	Fault thickness
$k' = \frac{\hat{k}zz}{\hat{k}xx}$	Permeability anisotropy ratio of each fault material
$\hat{k}_{xx}$	(local) permeability across each fault material
n	Porosity of each fault material
s_{s}	Along-strike smear segment number, i.e., the number of unique strike-parallel fault sections in a 3D fault realization
SSFc	Critical shale smear factor (defined for each layer with $V_{\mathrm{cl}} \geq 0.4$)
ρ	Linear correlation coefficient between intermediate variables
ϕ_{r}	Residual friction angle (defined for each stratigraphic layer)

Outputs

f_n	Upscaled fault porosity
$\mathrm{f}_{V_{\mathrm{cl}}}$	Upscaled fault clay volume fraction
$\underline{\underline{k}}$	Permeability tensor
k_{xx}	Upscaled permeability, fault dip-perpendicular
k_{yy}	Upscaled permeability, fault strike-parallel
k_{zz}	Upscaled permeability, fault dip-parallel
N	Number of simulations/realizations employed to compute the output quantitites
P	Probability

Other fault variables

$\mathrm{f_D}$ Fault displacement
$\mathrm{f_L}$ Fault length (strike-parallel)
$\mathrm{f_{LE}}$ Fault "longitude" (see B.1.3)
$\gamma = \frac{\mathrm{f_D}}{\mathrm{f_T}}$ Shear strain

Clay smear attributes

$\mathrm{s_D}$ Smear domain length (line connecting the parent layer cutoffs through the fault)
s_L Smear length (strike-parallel)
$\mathrm{s_{LD}}$ Down-dip smear length (adding all segments if discontinuous)
$\mathrm{s_l^{max}}$ Maximum down-dip smear segment length
s_T Smear thickness
$\mathrm{s_{T^*},}_i$ Smear thickness-in-fault (see Fig. B.2)
$\mathrm{s}_\chi = \frac{\mathrm{s_{LD}}}{\mathrm{s_D}}$ Smear fraction

Acronyms

AR Aspect ratio of grid cells
FW Footwall
HW Hangingwall
MAE Mean absolute error
MPFA Multi-point flux approximation
`MRST` MATLAB Reservoir Simulation Toolbox (Lie 2019)
PFFR Phyllosilicate fault framework rock
`PREDICT` PeRmEability DIstributions of Clay-smeared faulTs (this algorithm)
TPFA Two-point flux approximation

Other symbols

A Area
G 2D computational grid or mesh used for flow-based upscaling of permeability
h_y Grid cell length along the y axis
h_z Grid cell length along the z axis
m_eq Equivalent grain aspect ratio of a sand-clay mixture (Daigle and Dugan 2011)
M Mapping matrix (square matrix with the same dimensions as G)
p Fluid pressure
R Parameter uncertainty range
$\underline{u}$ Darcy velocity or flux
$\overline{V_\mathrm{cl}}$ Average stratigraphic clay volume fraction computed as $\frac{\sum_i V_{\mathrm{cl},i} T_i}{\sum_i T_i}$, including HW and FW
α Angle between the fault dip and the fault materials
ϵ Tolerance during smear placement
θ Average grain orientation of Daigle and Dugan (2011)
ν Absolute frequency
Ω Computational domain, i.e. the physical dimensions of G

B.1 PREDICT: PeRmEability DIstributions of Clay-smeared faulTs

B.1.1 Concept, initial assumptions and validation

In siliciclastic sequences (those characterized by alternating sand-dominated and clay-dominated sediments), fault materials are typically classified according to the proportion of clay (Fisher and Knipe 1998). Fault materials predominantly composed of sand (referred to as sand-based here) can be divided into sand-lenses (< 15 % clay, minimal grain comminution), phyllosilicate fault framework rocks (PFFRs; 15 % $\leq$ clay $\leq$ 40 %, lower permeability), and cataclasites (intense sand grain comminution) (Fisher and Knipe 1998; Braathen et al. 2009). Clay-based fault materials are typically referred to as clay smears (Vrolijk et al. 2016) (> 40 % clay), and, in the absence of extreme cataclasis, they are the lowest permeability component of the fault, with values in the micro- to nano-Darcy range or lower (Sperrevik et al. 2002; Fisher and Knipe 1998; Childs et al. 2007). In a fault volume, these materials are accompanied by other structures, such as segmented slip surfaces, deformation bands, or fractures (Caine et al. 1996; Braathen et al. 2009; Childs et al. 2009; Faulkner et al. 2010). However, faults in soft sediments (our focus here) typically display an architecture without macroscopic (open) fractures, the result of predominantly ductile deformation and granular flow (Heynekamp et al. 1999; Rawling et al. 2001; Caine and Minor 2009; Bense et al. 2013; Kettermann et al. 2016; Delogkos et al. 2020). Because of that, it is the main shear zone (fault core) that exerts a dominant control on fluid flow. Therefore, we focused on obtaining a realistic representation of material heterogeneity in the fault core only (Fig. B.1).

To develop PREDICT, the following choices were made to compromise between data availability, importance in sedimentary sequences under analysis, and practicality in a fully probabilistic framework:

1. Fault zone materials are placed at a constant angle $\alpha \neq 0$ with respect to the fault dip (Fig. B.1b). α is determined by the amount of throw and fault thickness, and a constant value implies that fault zone materials stay parallel to the line connecting the footwall and hangingwall source layer cut-offs through the fault. This assumption is consistent with shear-type smears, typically dominant in relatively shallow sand-clay sequences (Weber et al. 1978; Lindsay et al. 1993; Kettermann et al. 2016). Other smearing mechanisms such as abrasion (Lindsay et al. 1993) and injection (Lehner and Pilaar 1997) are not considered.

2. A given 3D fault volume used for permeability upscaling is obtained by arranging multiple, constant-thickness fault cross sections along-strike (see Fig. 1 in the main text). First, this means that all smears placed in each 2D cross-section will be projected parallel to strike and truncated at the same along-strike coordinates where they meet the projected smears from the adjoining 2D cross-sections. Second, PREDICT currently assigns the same along-strike length to all segments (i.e., to each fault section), the sum of which equals the fault length (f_L). Although this is a simplification of reality, data on along-strike smear segmentation is too limited to justify a more complex approach here. Finally, while natural and experimental fault core thickness varies along-strike (e.g.,

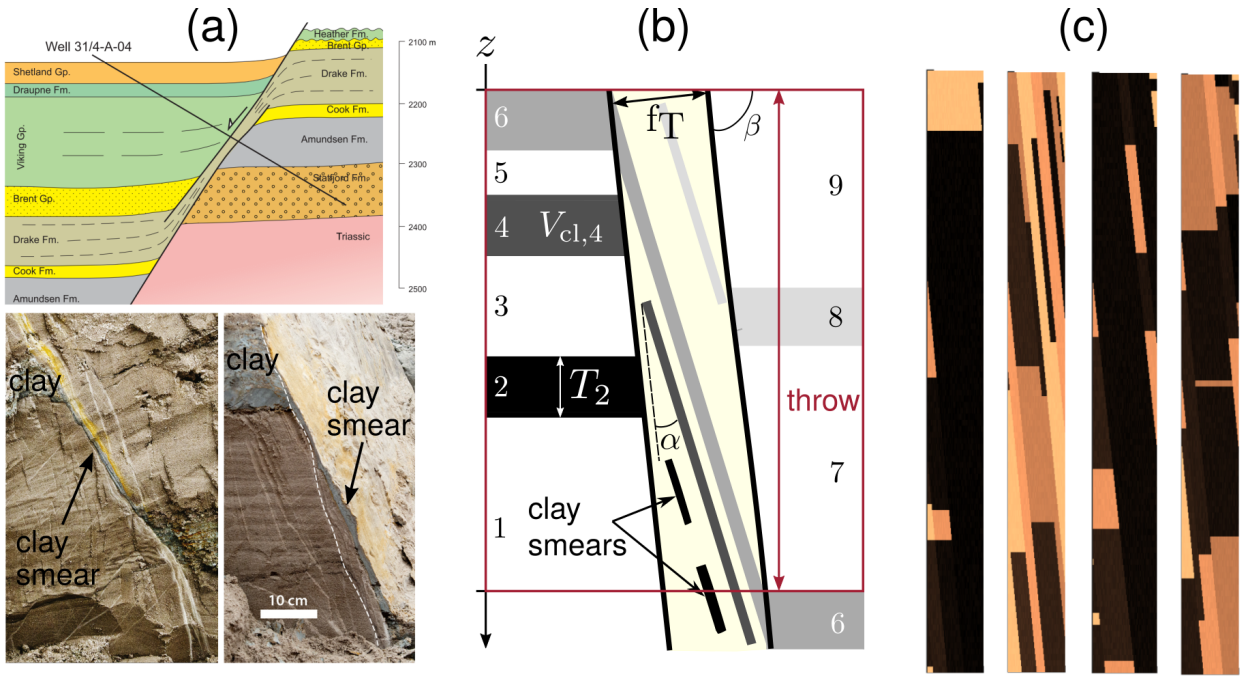

Figure B.1: **(a)**: Top plot shows a cross section of a clay smear-filled fault in the North Sea (Brage East Fault, throw ~200-250m) by Færseth et al. (2007). Bottom left and bottom right plots are direct observations of faulted sand-clay sequences, showing heterogeneous sand and clay layering within the fault core. Pictures are from Vrolijk et al. (2016) and Kettermann et al. (2016), respectively. **(b)**: Conceptual scheme of the clay smear distribution within a fault section, as treated by PREDICT. Each layer in the stratigraphy with $V_{cl} \geq 0.4$ can contribute smear into the fault. **(c)**: PREDICT snapshots of four fault sections consistent with a given stratigraphy. Fault materials, which can be continuous or discontinuous, are colored according to permeability. PREDICT arranges fault sections along-strike to form 3D fault volumes for permeability upscaling.

Kettermann et al. 2016; Sosio de Rosa et al. 2018), PREDICT models each realization with constant thickness. This is reasonable given that each realization considers a relatively short f_L (equal to the fault displacement), and that, by running multiple realizations, the effect of varying fault core thickness is accounted for.

3. PREDICT does not handle along-strike variations of fault throw, which means that a given 3D fault realization has constant throw. In order to account for varying throw, which is observed in natural faults, PREDICT can be run multiple times changing the inputs. This allows understanding the impact of varying throw windows on fault permeability, but the effects of varying throw cannot be combined in a single permeability prediction (i.e., for a unique realization).

4. All layers with clay volume fraction (V_{cl}) ≥ 0.4 are smear sources, but observations indicate that this is not always the case (Zee and Urai 2005; Vrolijk et al. 2016). However, the limited available data makes it difficult to relax this assumption.

5. The algorithm is intended for normal faults in normally-consolidated (NC) siliciclastic sequences. PREDICT considers that the faulted stratigraphy is at, or close to, maximum

historical burial depth. It does not model reverse or strike slip faults, poroelasticity (e.g. enhanced permeability due to unloading associated with uplift), or fracturing.

6. The material properties and distribution in the fault can be predicted based on the following set of inputs (see § B.1.2): thickness (T) and V_{cl} of each layer in the footwall and hangingwall, faulting and maximum burial depths (z_{f} and z_{max}, respectively), and dip angle of both the stratigraphy (β) and the fault (f_{β}). Inputs were kept to a minimum to limit data requirements.

7. Mixing of parent materials is not considered, i.e., any given cell in the upscaling fault grid has properties derived from a single stratigraphic layer. PREDICT's goal is to honor macroscale observations of the main shear zone, which is typically heterogeneous with distinct sand-based and clay-based fault zone materials (Childs et al. 2007; Giger et al. 2013; Kettermann et al. 2016). Composite smears (where a clay-rich body in the fault results from amalgamation and/or grain-scale mixing of multiple sources) were not considered here (§ B.1.3). Quantitative data on this topic are scarce, which would make it difficult to validate an implementation.

8. Gaps in a given smear are equally likely at all locations on the down-dip smearing path (§ B.1.3). Although ideal shear-zone smears lose continuity due to thinning towards the midpoint between the footwall and hangingwall cutoffs (Lindsay et al. 1993), outcrop studies show that gaps can occur at any location (Childs et al. 2007). Additionally, Grant (2017) showed that randomly placed smears have the greatest statistical variation, which supports this choice for generality purposes. We also assume that the smear contributed by a given clay source maintains constant thickness in the fault, in contrast to natural smears, which taper.

9. PREDICT uses MRST (Lie 2019) to perform flow-based upscaling with sealing boundaries (Durlofsky 1991), similar to permeability measurements on cores. By default, PREDICT uses the traditional two-point flux approximation (TPFA) to discretize the single-phase flow equation, which ensures maximum computing speed. We validated that PREDICT's output is accurate by comparing differences with upscaled permeabilities obtained using a multi-point flux approximation (MPFA). Additionally, physically-sound and converged upscaling results were ensured via convergence analysis of the grid cell size, cell aspect ratio, and the number of performed realizations (§ B.2.1).

The main goal of this work is providing new insight on the impact of stratigraphically-consistent fault material arrangements with clay smears on fault permeability. In § 3 in the main text we validate PREDICT with cm-scale experiments by Kettermann et al. (2017), and we also compare our results to those from Sperrevik et al. (2002)'s permeability predictor and other laboratory and field measurements in similar geology. A multi-scale, 3-component validation of PREDICT's output requires quantifying the mismatch between the permeability distributions and measurements of the macroscale fault permeability in m- to km-scale faults. This requires comprehensive field data and analysis, and is beyond the scope of this paper, where the main goal is to introduce PREDICT and its capabilities.

B.1.2 Intermediate variables

Given a set of input parameters, PREDICT generates the corresponding marginal probability distributions for the intermediate variables (see Fig. 1 in the main text). These variables are treated as continuous random variables, and are required to compute the dimensions of the clay smears contributed by each source (§ B.1.3), their placement in the fault zone (§ B.1.3), and the upscaled permeability (§ B.1.4). Each variable depends differently on the input parameters characterizing the stratigraphy, as described next.

Marginal distributions

For each 3D fault:

- **Fault thickness** ($\mathrm{f_T}$): Fault rock (or core) thickness is known to depend primarily on displacement (Childs et al. 2007; Childs et al. 2009). Although other controls exist, such as clay content (i.e. rheology) and juxtapositions in the deformed section (Sperrevik et al. 2002), it is difficult to include them rigorously due to lack of data. Hence, we only consider the dependency of fault thickness on fault displacement ($\mathrm{f_D}$). In accordance with published data, we consider that $\mathrm{f_D/f_T}$ is between 10 and 1000, with most of the data around $\mathrm{D/T} = 100$. We further assume that $\log_{10}(\frac{\mathrm{f_D}}{\mathrm{f_T}}) \sim \mathrm{Beta}(a, b)$ with $a = b = 5$, which gives a bounded symmetric distribution, and with few data in the upper and lower 20%.

- **Along-strike smear segment number** ($\mathrm{s_s}$): This parameter defines the segmentation of smears in the strike-parallel direction, and is based on the hole mappings in excavated fault surfaces by Noorsalehi-Garakani et al. (2013), Kettermann et al. (2016), and Kettermann et al. (2017). We counted the number of holes along strike-parallel, horizontal lines of length equal to $\mathrm{f_D}$ to define the maximum and minimum number of holes (N_h). Because each hole must be surrounded by smear, we set $\mathrm{s_s} = 2N_\mathrm{h}$. This led to $\mathrm{s_s} \in [1, 16]$, which, given the experimental conditions in the studies above, is the range for near-surface faulting; the upper bound is reduced with increasing faulting depth. A triangular distribution is assumed to sample $\mathrm{s_s}$, whose mode depends on V_cl: as the average clay fraction of the smear sources increases, the mode moves closer to the lower bound. This follows similar logic to the SSFc (see below) in that larger z_f and/or V_cl lead to more continuous smears.

For each fault section:

- **Residual friction angle** (ϕ_r): The residual friction angle of clays is well correlated with the clay-sized fraction of a granular material. We fit an exponential function to data in Skempton (1964) and Mesri and Cepeda-Diaz (1986) (for $V_\mathrm{cl} \in [0.2, 1]$), and determine an interval of confidence around that fit, which is a function of the clay fraction. Then, a stochastic term is incorporated such that $\phi_\mathrm{r}(V_\mathrm{cl} \geq 0.2) \sim \mathrm{Beta}(a, b)$. We use $a = 3$ and $b = 5$ to avoid many values near the extremes, and a distribution somewhat skewed to the smaller values (more datapoints). For $V_\mathrm{cl} < 0.2$, we define $\phi_\mathrm{r}(V_\mathrm{cl} < 0.2) \sim \mathrm{U}(28, 38)$.

- **Critical shale smear factor** (SSFc): The SSFc defines the ratio between the fault displacement and source layer thickness at which clay smears become discontinuous (Lindsay et al. 1993; Færseth 2006; Childs et al. 2007). We impose a minimum V_{cl} of 0.4 for a stratigraphic layer to contribute smear into the fault zone, so the SSFc is undefined for clean and shaly sands. For source clays, the initial SSFc endpoints are determined based on V_{cl} following Fig. 4a in Grant (2017), which is most representative of shallow faulting at about 500m of depth. Next, the endpoints are modified according to the faulting depth of the sequence under analysis, with greater depth, i.e. greater effective stress, leading to higher SSFc (Sperrevik et al. 2000; Clausen and Gabrielsen 2002; Çiftçi et al. 2013; Giger et al. 2013). The endpoints can be further modified to account for hybrid failure in very shallow faults (e.g., Kettermann et al. 2017), such that discontinuous smears may appear at any value of f_D. Finally, the endpoints are adjusted to account for the scale factor, which leads to smaller faults displaying larger SSFc (Færseth 2006). These revised endpoints correspond to the bounds of the triangular distribution used to sample SSFc values, while the mode moves closer to the upper bound as layer thickness increases, and viceversa. This is introduced to agree with observations that thicker clay layers generate longer smears, which could be related to increased water content in the clay, documented to favor continuity in the laboratory (Sperrevik et al. 2000).

- **Porosity** (n): Although porosity is not the quantity we are focused on, it is also required in flow simulation and used in several mathematical models of permeability, including the one employed here to estimate clay permeability. To determine sand porosity ($V_{cl} < 0.4$), PREDICT uses the ideal packing model of Revil et al. (2002). First, the end-member porosities of pure sand and pure clay are determined using generic values provided in Revil et al. (2002). A modification is introduced for the residual sand porosity to account for increased grain comminution with faulting depth. The porosity of the pseudo-ideal sand-clay mixture (n_1) is calculated following equations 11 and 12 in Revil et al. (2002), and a 4% porosity variation is introduced such that $n(V_{cl} < 0.4) \sim \mathrm{U}(n_1 - 0.02, n_1 + 0.02)$. Clay porosity is estimated using the Baldwin and Butler (1985) $\pm$ 5 % limits (n_l, n_u), which cover most of the expected range for normally compacted clays. A uniform distribution is used to sample from that range, i.e. $n(V_{cl} \geq 0.4) \sim \mathrm{U}(n_l, n_u)$, hence clay porosity is determined based on maximum burial depth only.

- **Permeability** ($\hat{k}_{xx}$): Permeability across sand-based fault materials is estimated according to Sperrevik et al. (2002)'s fault permeability model. This is an empirical relationship obtained from a consistent dataset of siliciclastic reservoirs in the North Sea and is based on the clay content, faulting depth and maximum burial depth. An uncertainty range (R) of one order of magnitude around the value from the empirical relationship is assumed, and a stochastic term is introduced such that $\hat{k}_{xx}(V_{cl} < 0.4) \sim \mathrm{U}(\min(R), \max(R))$. Permeability across clay smears is modeled following the approach described in Grant (2020): the maximum burial depth is associated with a porosity range (estimated as described above), which in turn can be used to determine the permeability bounds using a porosity-permeability relationship.

PREDICT uses Yang and Aplin (2010)'s empirical model, which was obtained from a total of 303 samples from mostly marine sediments, and is a function of the material clay fraction and porosity. All values are assumed equally likely within a given permeability range, i.e. $\hat{k}_{xx}(V_{\mathrm{cl}} \geq 0.4) \sim \mathrm{U}(\min(R), \max(R))$.

- **Permeability anisotropy** ($k' = \frac{\hat{k}_{zz}}{\hat{k}_{xx}}$): The permeability anisotropy ratio of fault zone materials is calculated following the model by Daigle and Dugan (2011) (Eq. 19), which depends on the porosity (n), the equivalent grain aspect ratio (m_{eq}), and the average grain orientation (θ). n is approximated following the model outlined above. m_{eq} is obtained from V_{cl} and the predominant clay mineral (PREDICT assumes Kaolinite/Illite by default), and θ is estimated assuming compaction up to faulting depth and shear strain (γ) equal to $\mathrm{f_D}/\mathrm{f_T}$; in both cases, we follow the approach in Daigle and Dugan (2011). Since k' depends on n and γ, which in our case change at each model realization, a deterministic model (Eq. 19 in the paper) is directly used to sample values.

§ B.2.2 provides an overview of the marginal distributions for different inputs.

Sampling

For each unique fault section in a 3D fault realization, PREDICT draws i samples for each intermediate variable, where i is the total number of layers in the studied throw interval. Each of these i samples is obtained using the previously defined distributions, which are constrained according to the input parameters of each stratigraphic layer (parent material). Dependency is introduced between intermediate variables in the following groups:

1. ϕ_{r} and SSFc: Both variables control the total smear volume in the fault, with smear thickness increasing with decreasing clay ϕ_{r}, and total smear length increasing with increasing SSFc (see sect. B.1.3). Hence, although length and thickness are modeled separately, it seems reasonable to expect that both quantities would increase as the clay volume entrained in the fault increases, and viceversa. This supports introducing a negative correlation between ϕ_{r} and SSFc.

2. n and k. PREDICT accounts for the positive correlation between n and k in siliciclastic sediments and sheared gouges (Crawford et al. 2008; Yang and Aplin 2010).

Dependency is modeled via Gaussian copulas (Nelsen 2006; The MathWorks, Inc. 2021, Chap. 2). A transformation, which uses the inverse cumulative distribution function (CDF) of the involved random variables (RVs), can be applied so that the marginals maintain the desired probability distributions. PREDICT uses the inverse CDF of the marginal distributions detailed in § B.1.2 and a moderate $\rho = 0.6$ to handle correlation between all RV pairs in groups 1 and 2.

Finally, k' (at the fault section level) and $\mathrm{f_T}$ and $\mathrm{s_s}$ (at the fault level, i.e., sampled only once for each 3D fault realization) are treated independently, and samples are drawn directly from their marginal distributions. This means that all fault sections used to generate a given 3D fault realization are assigned the same $\mathrm{f_T}$ (see Fig. 1 in the main text). § B.2.2 illustrates the correlation between intermediate variables, as well as the resulting smear dimensions, for a given clay source.

B.1.3 Smear dimensions and placement

Dimensions of clay smears resulting from each source layer with $V_{cl} \geq 0.4$ in a studied throw interval are computed according to the following:

- **Thickness** (s_T): We follow Eq. 5 in Egholm et al. (2008) to obtain an average clay smear thickness for each source ($s_{T,i}$) from the residual friction angle of the involved clay ($\phi_{r,i}$) and sands (ϕ_s), the true layer thickness (T_i), and the corresponding fault longitude ($f_{LE,i}$). ϕ_s is a thickness-weighted average of the residual friction angle of all sands in the faulted section, and $f_{LE,i} = f_D + T_i^*$, where T_i^* is the apparent layer thickness of the corresponding source on the fault. We take a value of 1 for the proportionality constant in Egholm et al. (2008), which means that all clay material in the zone of instability is incorporated into the fault. We used the smear thickness measurements by Kettermann et al. (2016) (surface 2), and estimations from larger faults by Færseth (2006), to validate that a choice of 1 is reasonable.

- **Down-dip length** (s_{LD}): The total clay smear length for a given source is computed as $s_{LD,i} = \frac{T_i^*}{\cos\alpha} SSFc_i$, where $SSFc_i$ is the corresponding critical shale smear factor as defined above.

- **Maximum down-dip segment length** (s_l^{max}): Similar to the fragmented mode in Grant (2017), we assume that the smear produced by a given source will be more fragmented the longer it is displaced, i.e., the higher the $SSFc_i$. Hence, for a given random sample, the closer the $SSFc_i$ is to the upper endpoint for that source ($SSFc_i^{max}$), the shorter the maximum segment length: $s_{l,i}^{max} = \frac{SSFc_i^{max} - SSFc_i}{SSFc_i^{max} - SSFc_i^{min}} s_{LD,i}$. To prevent extreme fragmentation, which complicates convergence of the smear placement module, it is also imposed that $s_l^{max} \geq \max(\{0.1 s_{L,i}, 3h_L\})$, where h_L is the grid resolution along the z axis (cell length).

- **Along-strike length** (s_L): Since each fault section in a given 3D fault realization is generated independently, clay smear segmentation generally occurs at the coordinates where two sections meet. Therefore, the length of each of these fault sections is equivalent to the strike-parallel clay smear length (s_L). This length is computed as $s_L = \frac{f_L}{s_s}$, where s_s is defined as described in § B.1.2 for $f_L = f_D$.

Additionally, a smear fraction ($s_\chi \in [0, 1]$) is calculated for each smear such that $s_{\chi_i} = s_{LD,i}/s_D$, where s_D is the domain length or the length of the line connecting the footwall and hangingwall smear source cutoffs through the fault. Hence, s_{χ_i} also represents the probability of finding a clay smear-filled cell in the corresponding domain, and is conceptually equivalent to the complement of Childs et al. (2007)'s individual gap probability in their probabilistic shale smear factor (PSSF). As described below, these quantities are used to model the thickness, length and continuity of the materials populating the fault in each realization.

To generate a fault section, PREDICT places clay- and sand-based materials in the fault following a two-step process (Fig. 1 in the main text, Fig. B.2). First, a material mapping matrix (M) is initialized. M is square and provides a direct mapping to the grid used for flow-based permeability upscaling (see § B.1.4). M is subdivided into a discrete number of domains according to the parent layer contributing material to each one. A domain is

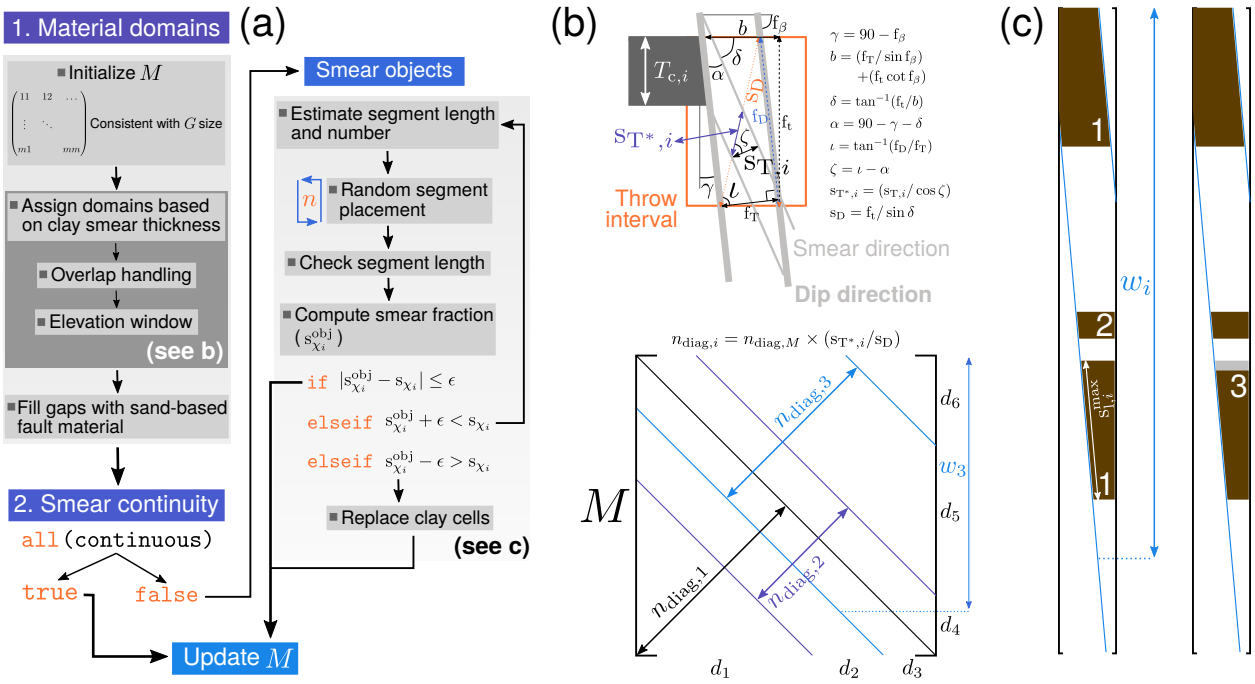

Figure B.2: Clay smear placement algorithm (refer to the main text for details). **(a)**: Workflow for (1) material domain assignment and (2) smear continuity assessment and object simulation **(b)**: (top) Illustration of fault and clay smear dimensional quantities required to compute the initial number of M diagonals assigned to each smear. (bottom) Illustration of three overlapping smears and the resulting number of unique domains (d_1 to d_6, of which d_1 to d_5 are clay smear domains and d_6 is sand-based material only). Each domain is assigned one single parent and the corresponding elevation window (w_1 to w_3 in this case). **(c)**: Illustration of smear object (segment) placement in a given domain. Here, the first main iteration places two segments of length $s_{l,i}^{\max}$. The second places an additional, shorter segment, which leads to a smear fraction slightly above the calculated one. Finally, the third shortens the longest segment until the smear fraction matches the calculated value to a pre-defined tolerance.

defined as a group of diagonals in M with the same parent material, and maintains constant thickness (number of diagonals) along the modeled throw interval. The material mapping module assigns clay smear domains first, and fills the gaps with sand-based materials next. Each potential clay smear is initially distributed around the diagonal in M that meets the center of each source, and has a number of diagonals derived from the thickness-in-fault ($s_{T^*,i}$; see Fig. B.2b). The mapping module keeps track of overlaps in any diagonals, and divides M in a discrete number of domains based on diagonal groups with the same potential parent source(s) (Fig. B.2a,b). Domains with two or more potential sources are assigned a single one based on a uniform probability law. An elevation window is also assigned to each domain, to ensure that the contributed smear is always located between its source top in the FW and its source base in the HW. This stage is completed by assigning sand-based materials in (1) any unassigned diagonal groups between smear domains, and (2) any diagonal entries in smear domains with elevation beyond the smear windows. Sand-based material properties are derived from the closest material in the faulted stratigraphy with $V_{\mathrm{cl}} < 0.4$ in both cases.

Smear continuity is handled by a second module that evaluates, for each domain whose

parent material is a clay smear source ($V_{cl} \geq 0.4$), whether the generated clay smear is continuous along the smear window ($s_{\chi_i} = 1$) or discontinuous ($s_{\chi_i} < 1$). If the smear is discontinuous, object-based simulation (Pyrcz and Deutsch 2014) is performed to randomly place q clay smear segments with length $s_{l,j}$ for each source i such that $\max(\{s_{l,1}, ..., s_{l,q}\}) \leq s_{l,i}^{max}$ and $(\sum_{j=1}^{q} A_{c,j})/A_i \simeq s_{\chi_i} < 1$, where $A_{c,j}$ is the domain area filled by a clay smear segment and A_i is the total domain area. This process, which finalizes M, is completed by successive iterative blocks (Fig. B.2c). First, the initial number of smear segments is estimated using $s_{l,i}^{max}$ and the domain length within the modeled fault. These segments are placed one at a time, each within the longest existing gap after the previous iteration. Placement of each segment in the corresponding gap is random, according to a uniform probability law. $A_{c,i}$ and A_i can be evaluated by counting the number of M entries with clay smear and the total number of entries in the domain, which leads to the resulting smear fraction ($s_{\chi_i}^{obj}$). If this value is within a tolerance (ϵ) of s_{χ_i}, the process for that domain is complete. Otherwise, two options are possible: either $s_{\chi_i}^{obj} + \epsilon < s_{\chi_i}$, in which case another main iteration is performed that places new smear segment(s) in a similar fashion; or, $s_{\chi_i}^{obj} - \epsilon > s_{\chi_i}$, in which case clay smear cells are replaced by sand-based material one cell row at a time until $s_{\chi_i}^{obj}$ is within tolerance of s_{χ_i}.

In order to construct a 3D fault realization, PREDICT repeats this process and generates s_s fault sections (see § B.1.2). Each of these fault sections is assigned a length equal to s_L (see above), and they are arranged one after another (along-strike) to obtain a 3D fault volume with x, y, z dimensions equal to $f_T \times f_L \times f_D$ (refer to Fig. 1 in the main text).

B.1.4 Upscaling

For each fault section, clay fraction, porosity and permeability are assigned to each entry ij in M based on the stratigraphic unit contributing material (the parent unit). This is completed as follows, one domain at a time:

1. Determine whether a single unit (continuous clay smear with window filling the whole domain, or only sand-based material) or two units (discontinuous clay smear and sand) are present.

2. Assign clay volume fraction, porosity and permeability across each entry in the domain ($\hat{k}_{xx}^{ij}$) based on the parent unit. At this point, all intermediate variables have been sampled following sect. B.1.2; additionally, a small randomness is introduced to account for the high variation frequency of these properties, expected to change within the same object (Grant 2020). Permeability is allowed to vary a $\log_{10}$ value of ± 0.2, while porosity is allowed ± 0.015. The resulting ranges are small enough that they barely impact the correlation introduced during sampling (sect. B.1.2).

3. Assign the permeability along the material ($\hat{k}_{yy}^{ij} = \hat{k}_{zz}^{ij}$), which is equal to the product of $\hat{k}_{xx}^{ij}$ and the sampled permeability anisotropy ratio for the contributing parent. This completes the local, diagonal permeability tensor for each entry in M ($\underline{\underline{\hat{k}}}^{ij}$).

4. Fault materials are at an angle α with respect to the fault dip (see sect. B.1.1 and Fig. B.1), so $\underline{\underline{\hat{k}}}^{ij}$ needs to be transformed to the fault coordinate system (aligned with

the grid), before performing flow-based upscaling. Conversely, fault materials are assumed to be roughly parallel to the fault strike, so $\underline{\underline{k}}^{ij}$ is obtained via tensor-rotation about the y-axis and $k^{ij}_{yy} = \hat{k}^{ij}_{yy}\ \forall i, j$. Since the off-diagonal terms involving y are 0, this is equivalent to transforming the 2D permeability tensor involving the x and z components only.

Steps 1-4 are repeated for each fault section in a given 3D fault volume, such that we have $\{M\} = \{M_1, ..., M_{\mathrm{s_s}}\}$ and their corresponding $\underline{\underline{k}}^{ij}$. The only remaining step is to obtain the equivalent or upscaled clay fraction, porosity and fault permeability for the studied throw interval. Given that the focus is on understanding permeability in the main fault directions, PREDICT simply computes the main-diagonal components, i.e. k_{xx}, k_{yy} and k_{zz}. Upscaling is performed using the MATLAB Reservoir Simulation Toolbox (MRST) (Lie 2019) as described next:

i. The user defines a coarse, upscaling grid (G_{C}) onto which the output macroscale permeability will be mapped. G_{C} is defined as the number of cells, in x, y, z, for which the upscaled permeability is to be computed. The total number of cells in G_{C} is the product of each dimension, and all cells in G_{C} are uniform rectangular cuboids. For example, if $[1, 1, 1]$ is passed, PREDICT outputs a single permeability value corresponding to the full throw window; $[2, 10, 10]$ upscales the permeability in a G_{C} with 200 cells. The definition of G_{C} depends on the user end-goal.

ii. The fine, 3D computational grid (G) matching the studied fault throw interval dimensions (thickness, length, displacement) and with equal-size, rectangular cuboid cells is created. By default, the cell dimensions are $[0.01\mathrm{f_T},\ \mathrm{s_L},\ 0.01\mathrm{f_D}]$ in the x, y, z dimensions, so that G has the same number of cells in x, z and $\mathrm{s_s}$ cells along y. This ensures a 1 to 1 correspondence with $\{M\}$, including each ij entry in $M_1, ..., M_{\mathrm{s_s}}$. When G_{C} has several cells along y, PREDICT can generate G with $[0.01\mathrm{f_T},\ \approx 0.01\mathrm{f_L},\ 0.01\mathrm{f_D}]$ resolution, which ensures compatibility between the fine and coarse grids. In this case, each unique fault section, and, therefore, each element in $\{M\}$ and its assigned properties, are repeated $\frac{\mathrm{s_L}}{h_y}$ times, where $h_y \approx 0.01\mathrm{f_L}$ is G's y cell size. A convergence analysis of various aspects related to grid resolution is provided in § B.2.

iii. Each G cell is assigned the clay fraction, porosity and permeability of its reciprocal in $\{M\}$.

iv. Additive properties (clay volume fraction and porosity) are upscaled first. Since all grid cells have the same volume, the upscaled fault clay volume fraction ($\mathrm{f}_{V_{\mathrm{cl}}}$) and porosity ($\mathrm{f}_n$) are simply the average of all cell values in G that fall inside each cell in G_{C}.

v. k_{xx}, k_{yy} and k_{zz} are obtained using flow-based upscaling with sealed boundaries. This translates to imposing a pressure drop (Δp_i) in each axial direction i, while no-flow is imposed on the other four boundaries, and computing the net flux (u_i) at the outflow boundary. The equivalent or upscaled permeability is obtained from Darcy's law (Darcy 1856) as $k_{ii} = -u_i L_i / \Delta p_i$, where L_i is the length (see chapter 15 in Lie (2019) for details). Since we are interested in the intrinsic permeability, the volumetric flux $\underline{u}$ is obtained by solving, on each subset of G within each cell in G_{C}, the equation

describing single-phase, incompressible flow thrice (once for each pressure drop):

$$\nabla \cdot \underline{u} = 0 \quad \in \Omega \subset \mathbb{R}^3 \tag{B.1}$$

Where $\underline{u} = -\underline{\underline{k}}\nabla p$. As is common practice in reservoir simulation, MRST employs a finite-volume method to discretize Eq. B.1. As noted in sect. B.1.1, interface fluxes are obtained with a TPFA to minimize computing time, but we ensured that PREDICT's output is accurate by comparing the result for several configurations against the output using a MPFA. This is because the angle α (refer to sect. B.1.1 and Fig. B.2) is typically very small, so the off-diagonal terms in $\underline{\underline{k}}^{ij}$ are not significant. Parallelization and C-acceleration allow PREDICT to clock up to several realizations per second, although this is highly variable as it depends on G resolution, choice of G_{C}, available computing cores and processor speed. In most cases, we estimate a speed of several realizations per minute.

B.2 Assessment of PREDICT's Behavior

B.2.1 Convergence analysis

Convergence of PREDICT's upscaled permeability distributions is quantitatively assessed with respect to the grid cell size and the cell aspect ratio (2D), and the number of performed realizations (3D). Note that, although all results presented in this paper are obtained with the 3D version of PREDICT, the algorithm can also run in 2D. In the 2D case, permeability is directly upscaled for each $[x, z]$ fault section, which constitutes one realization. Flow-based upscaling (k_{xx}, k_{zz}) using a MPFA to compute fluxes is used, and the algorithm considers a single cell in G_{C} for the modeled throw window.

Grid/Mesh degree of refinement

The impact of the grid's cell size on the upscaled permeability is quantified by running a single 2D realization with multiple cell sizes. The random seed is fixed at the beginning of each iteration, to ensure that differences are only the result of different grid resolution. The process is completed for five stratigraphic sections with varying inputs (A to E). Results are shown in Fig. B.3, where it can be seen that, beyond $h_z \approx 0.01\mathrm{f_D}$, refinement no longer leads to significant changes in the upscaled permeability (i.e., larger than ∼1 order of magnitude). Since M must be square (see sect. B.1.3 and B.1.4), cell refinement can only be accomplished by reducing both the x and z dimensions. These results allow setting PREDICT's default $[x, z]$ cell size for each fault section to $[0.01\mathrm{f_T}, 0.01\mathrm{f_D}]$.

Cell aspect ratio

Since G has the same number of cells in the x and z dimensions, the $[x, z]$ cell-dimension aspect ratio (AR) is equal to $\mathrm{f_D}/\mathrm{f}_T$, i.e. between 10 and 1000 (see § B.1.2). The impact of the AR on the upscaled permeability is quantified as follows: First, a single 2D realization is run with the cell size defaults (see § B.2.1). Next, a set of iterations is completed, in which each

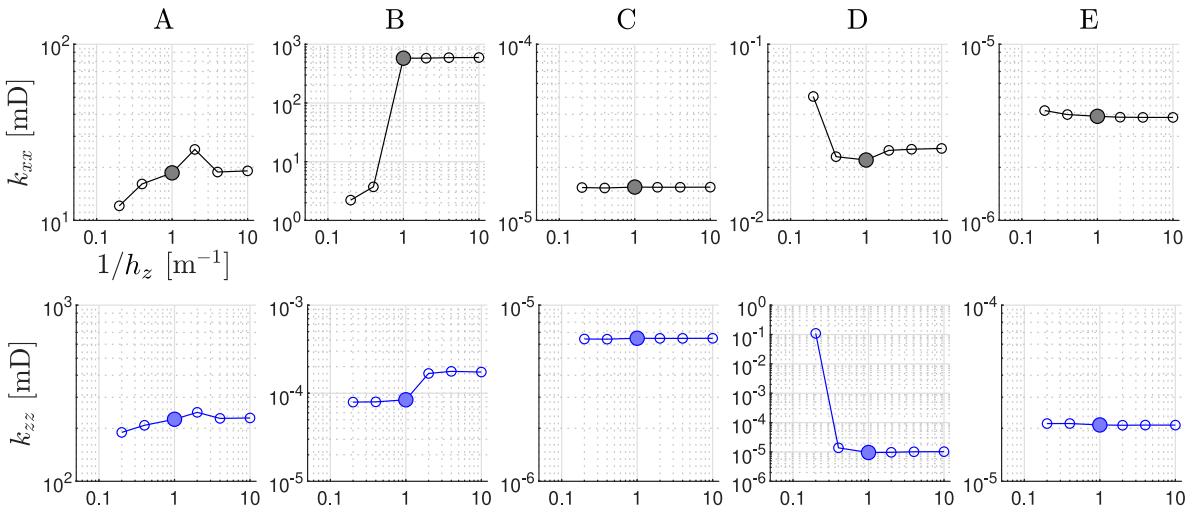

Figure B.3: Upscaled permeability (rows) for five faulted stratigraphic intervals A to E (columns) as a function of cell length (h_z). Fault displacement is 100m in all cases. Filled markers correspond to PREDICT's default cell size.

grid's AR is successively decreased by increasing the number of cells along the z dimension. Cell permeability is assigned based on proximity to the original (default) grid cells, which have permeabilities from the mapping described in § B.1.3. Finally, the permeability is upscaled, and compared to that obtained using the default grid.

Results in Fig. B.4 show a maximum upscaled permeability ratio below 1.5, suggesting that, even for thin faults, the grid's AR does not significantly diminish the upscaling accuracy. For the 3D version of PREDICT, we also tested the differences in k_{xx}, k_{yy}, k_{zz} when using G's default relatively low resolution along y (s_s cells, each with length s_L) as opposed to a similar resolution to that of x, z with about 100 cells along y (see sect.B.1.4). We found that differences were not significant in any case.

Number of simulations

Finally, we assess convergence of the upscaled permeability distribution with respect to the number of performed realizations/simulations in 3D. The analysis uses 2×10^4 realizations to obtain the reference result, and, similar to above, five different stratigraphies are evaluated (A to E). Snapshots of some probability distributions are shown in Fig. B.5, and the differences were quantified by means of the mean absolute error (MAE) of the probability in each log-bin (Table B.1). A MAE of $\approx 0.5\%$ or below with respect to the reference distribution suggests that 1000-2000 realizations are enough for an accurate upscaled distribution. Results were obtained using a single cell in the coarse, upscaling grid.

B.2.2 Uncertainty propagation

This section shows the marginal distributions for the intermediate variables described in § B.1.2, for several input combinations. Then, it uses an example section to illustrate the

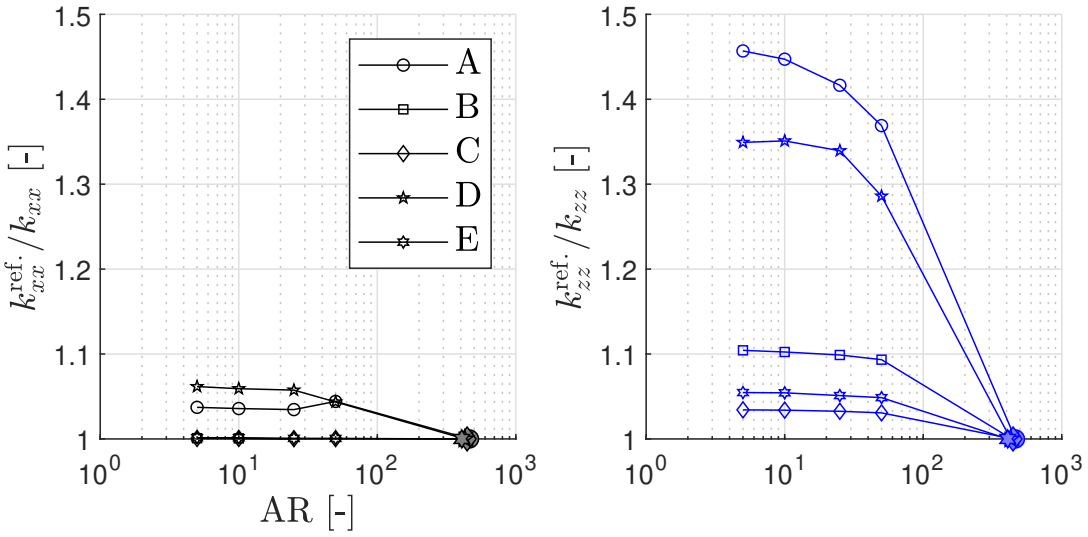

Figure B.4: Upscaled permeability ratios (with respect to the value obtained with the default grid, k_{jj}) down to an AR of 5, and for five stratigraphic sections with varying inputs (A to E). Thin faults with default AR > 400 were used.

Table B.1: Mean absolute error (MAE) of the log permeability distribution obtained with N realizations, compared to the result with $N = 2 \times 10^4$. In each table cell, the top value refers to k_{xx}, the middle one to k_{yy}, and the bottom one to k_{zz}. For each stratigraphic case, the $\log_{10}(k_{jj}$ [mD]) distribution is obtained by binning N values (the output) and computing the probability in each bin. 50 equal-width bins between -7 and 4 were used. Only the bins with $P > 0$ in the reference result ($N = 2 \times 10^4$) are considered when calculating the MAE.

Stratigraphy	$N = 10$	100	200	500	1000	2000	5000	10^4
A	0.0492	0.0130	0.0107	0.0213	0.0024	0.0045	0.0028	0.0008
	0.0312	0.0127	0.0262	0.0146	0.0051	0.0077	0.0022	0.0011
	0.0153	0.0130	0.0038	0.0076	0.0042	0.0033	0.0023	0.0010
B	0.0251	0.0078	0.0070	0.0038	0.0036	0.0023	0.0013	0.0013
	0.0303	0.0098	0.0071	0.0048	0.0043	0.0015	0.0021	0.0014
	0.0154	0.0074	0.0042	0.0040	0.0033	0.0022	0.0012	0.0010
C	0.0322	0.0202	0.0206	0.0082	0.0082	0.0011	0.0038	0.0038
	0.0219	0.0070	0.0086	0.0023	0.0026	0.0020	0.0015	0.0013
	0.0040	0.0047	0.0032	0.0015	0.0011	0.0010	0.0009	0.0007
D	0.0299	0.0065	0.0081	0.0046	0.0038	0.0017	0.0016	0.0008
	0.0513	0.0129	0.0083	0.0072	0.0041	0.0028	0.0020	0.0014
	0.0137	0.0046	0.0053	0.0016	0.0014	0.0005	0.0010	0.0010
E	0.0476	0.0135	0.0073	0.0066	0.0057	0.0040	0.0019	0.0020
	0.0331	0.0130	0.0080	0.0054	0.0033	0.0033	0.0021	0.0017
	0.0536	0.0174	0.0108	0.0072	0.0047	0.0031	0.0023	0.0022

values and correlations for a given clay source, as well as the resulting dimensions of the

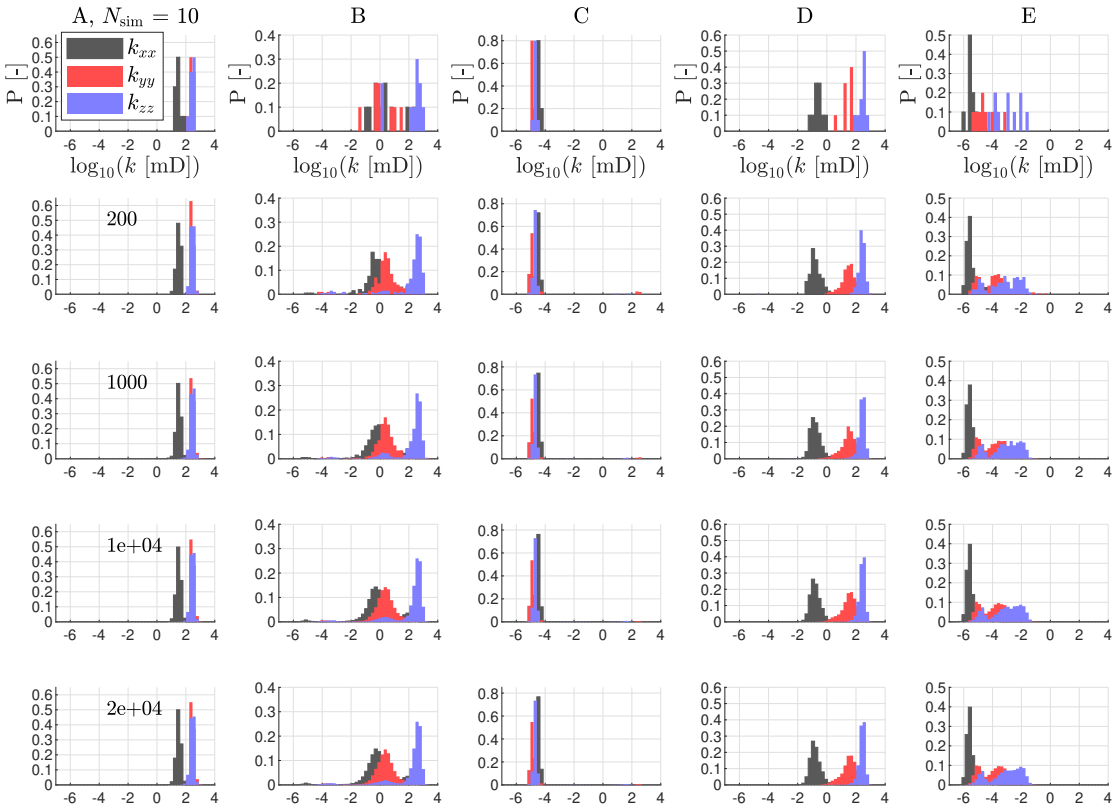

Figure B.5: Permeability distributions obtained using $N = 10$, 200, 1000, 10^4 and 2×10^4 realizations (rows), for five different stratigraphic cases (columns). 50 equal-width bins between -7 and 4 were used.

smear contributed into the fault by that source.

Marginal distributions

The marginal distributions are provided for varying inputs in Fig. B.6-B.14. 5000 realizations were used.

Correlation and smear dimensions

The correlation (input $\rho = 0.6$) between intermediate variable samples for a given fault section is shown in Fig. B.15 for a source layer with $V_{cl} = 0.6$ and $T = 10$ m. z_f and z_{max} are 1000 and 2000 m, respectively (Fig. B.16a). As described in § B.1.2, ϕ_r and SSFc are correlated, and n and k are also correlated.

The relative dimensions of the smear contributed by this example source layer in a total of 1000 fault sections are shown in Fig. B.16b. It can be seen that the relative thickness does not change change much, since ϕ_r is fairly constant (Fig. B.15). The smear fraction oscillates between ~ 0.5 and ~ 0.8, with a distribution shape inherited from the SSFc. For this source, the SSFc ranges between 5 and 9, with the mode at around 5.3 (Fig. B.15). Hence, since most of the values are close to the lower bound of 5, fragmentation is usually

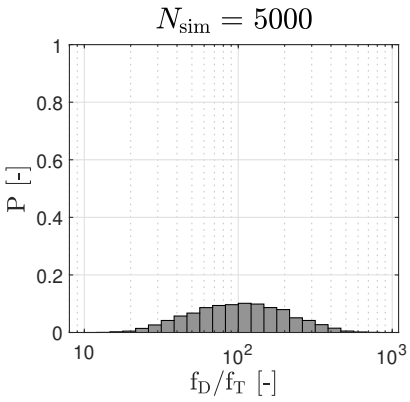

Figure B.6: Fault displacement over thickness.

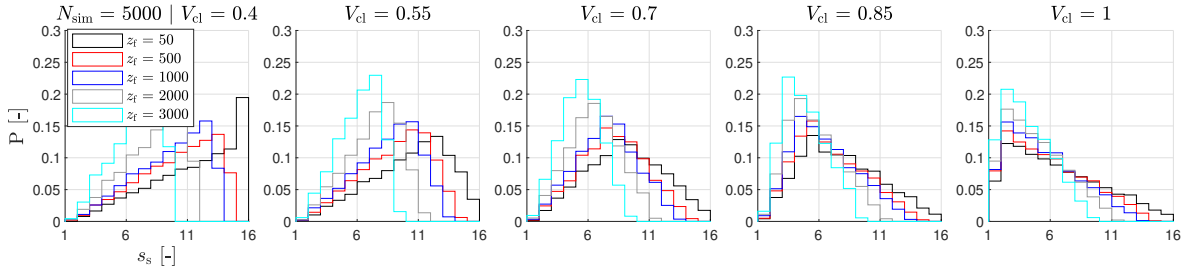

Figure B.7: Along-strike smear segment number as a function of z_f and V_{cl}.

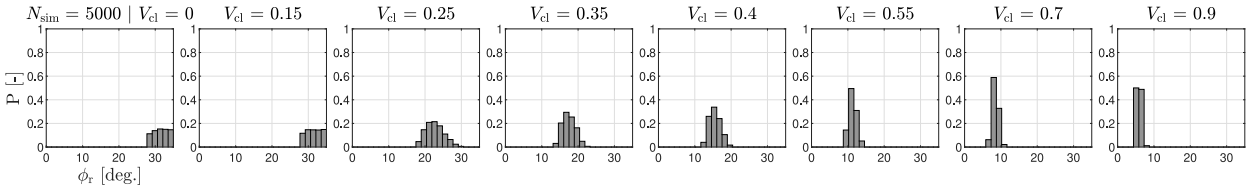

Figure B.8: Residual friction angle as a function of increasing clay volume fraction.

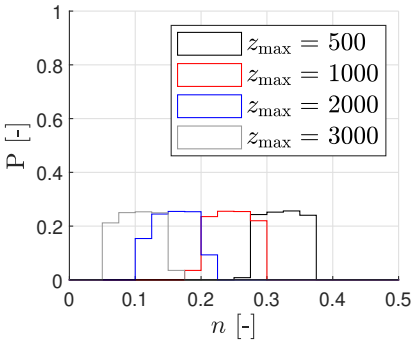

Figure B.9: Clay smear porosity ($V_{cl} \geq 0.4$).

low (s_l^{max} is mostly close to s_{LD}). Note that these reference dimensions are computed before fault material placement (§ B.1.3). In any given fault section, if there is overlap with other

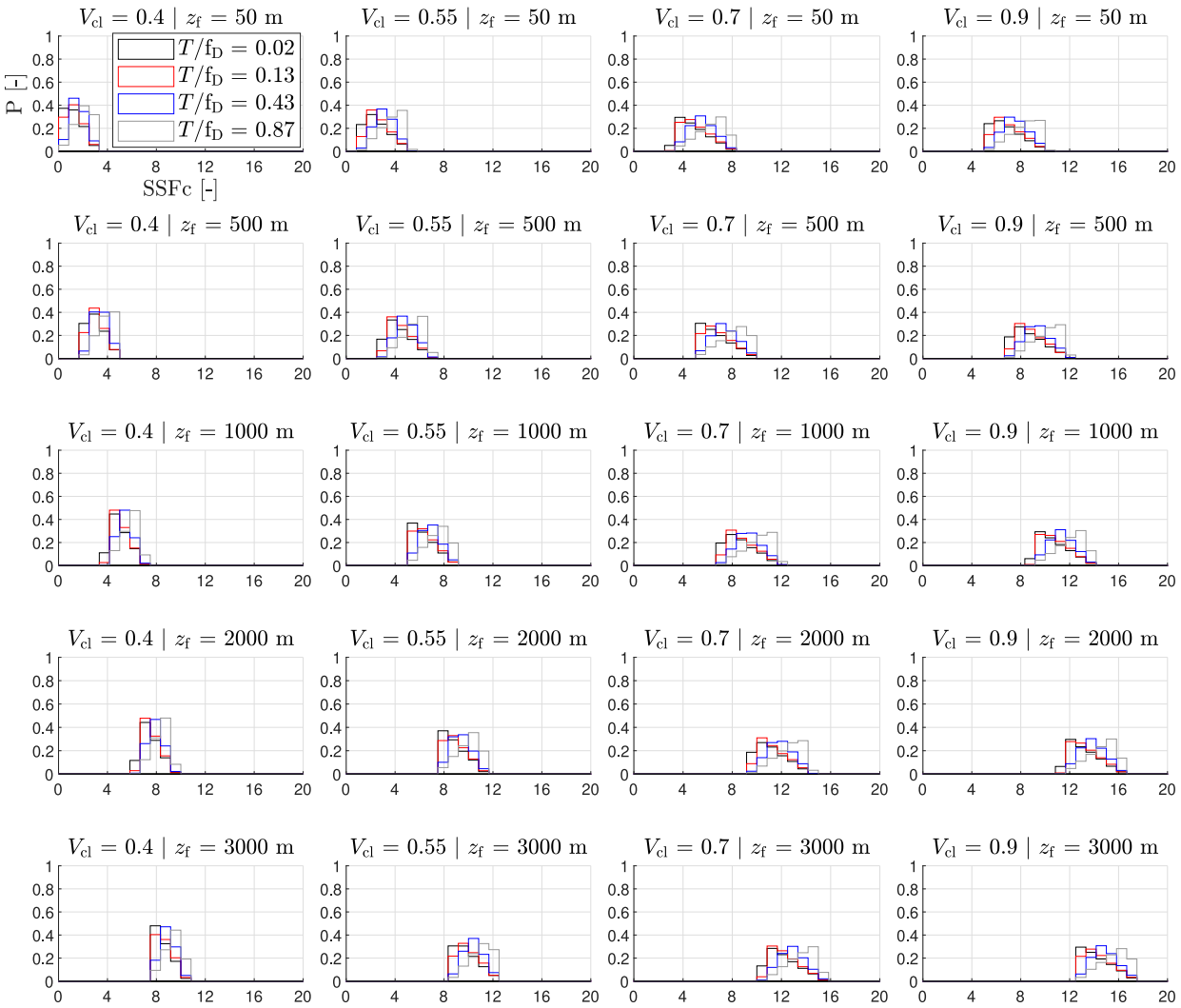

Figure B.10: Critical shale smear factor as V_{cl}, z_f and T change.

smears, the smear resulting from this source may or may not be present in the fault.

B.2.3 Sand connectivity

Fig. B.17b,c (in 2D and 3D, respectively) show the relative frequencies of continuous sand pathways for the four sequences with increasing $\overline{V_{cl}}$ shown in Fig. 3 in the main text. A continuous sand pathway is defined as a sand object that extends from boundary to boundary along one or more of the main axes x, y, z (Fig. B.17a). In this definition, a sand object is a group of connected cells in G with sand-based fault material (different sand-based materials may be present).

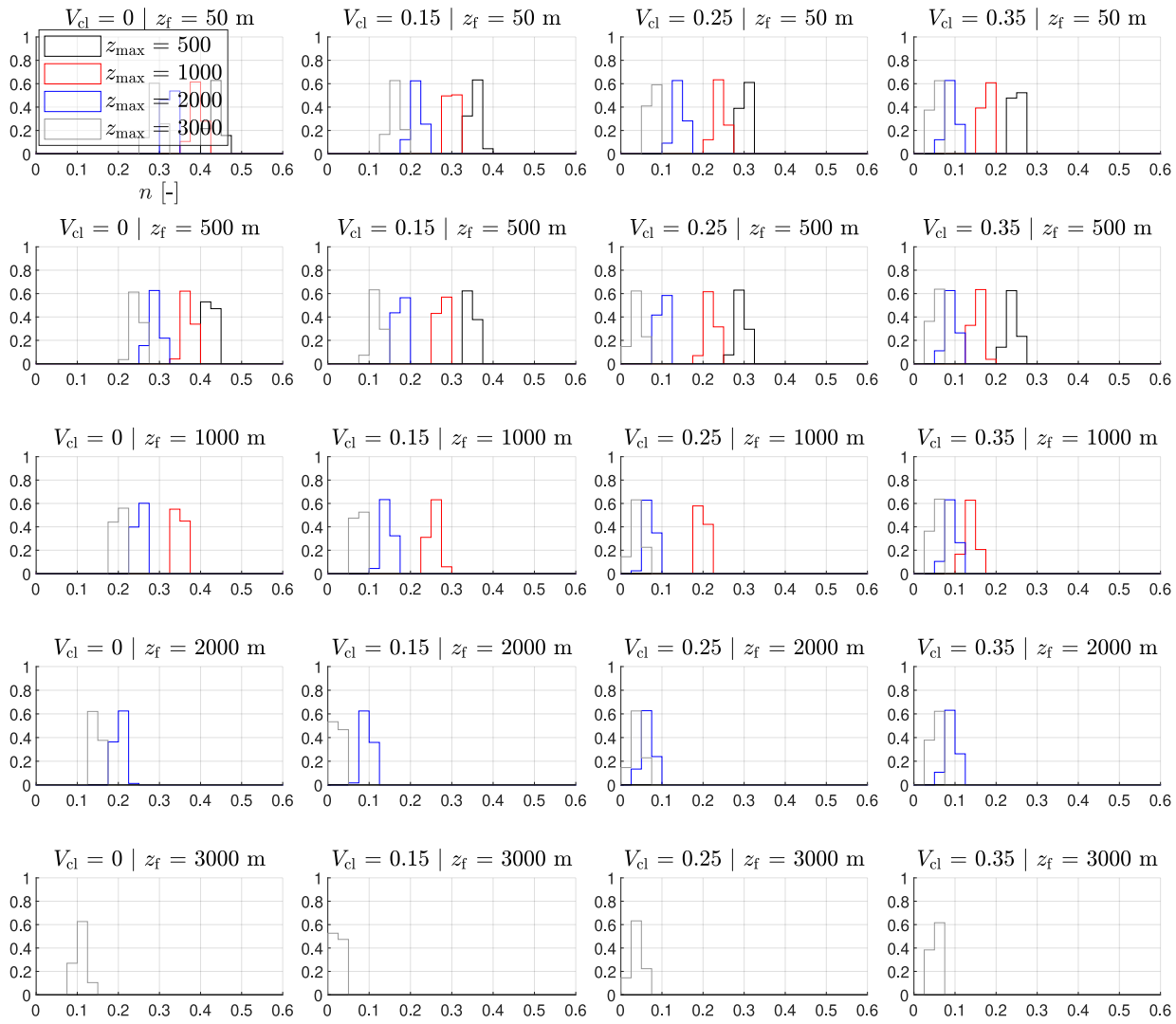

Figure B.11: Porosity for sand-based materials ($V_{cl} < 0.4$).

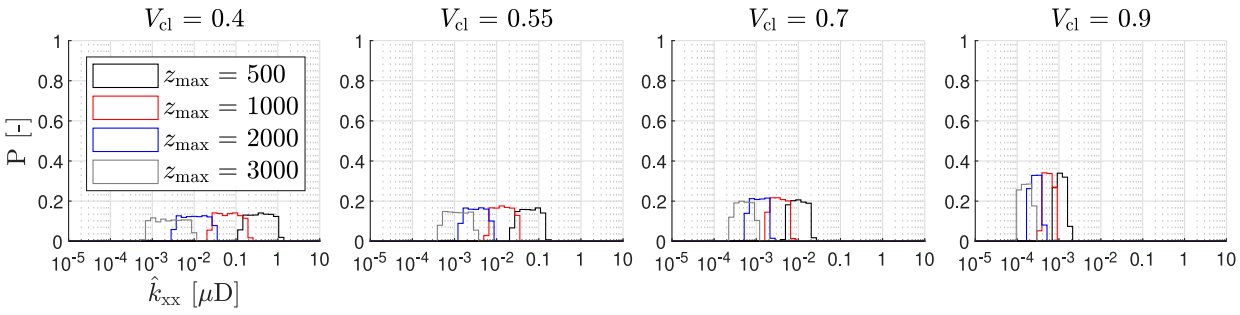

Figure B.12: Permeability of clay smears ($V_{cl} \geq 0.4$).

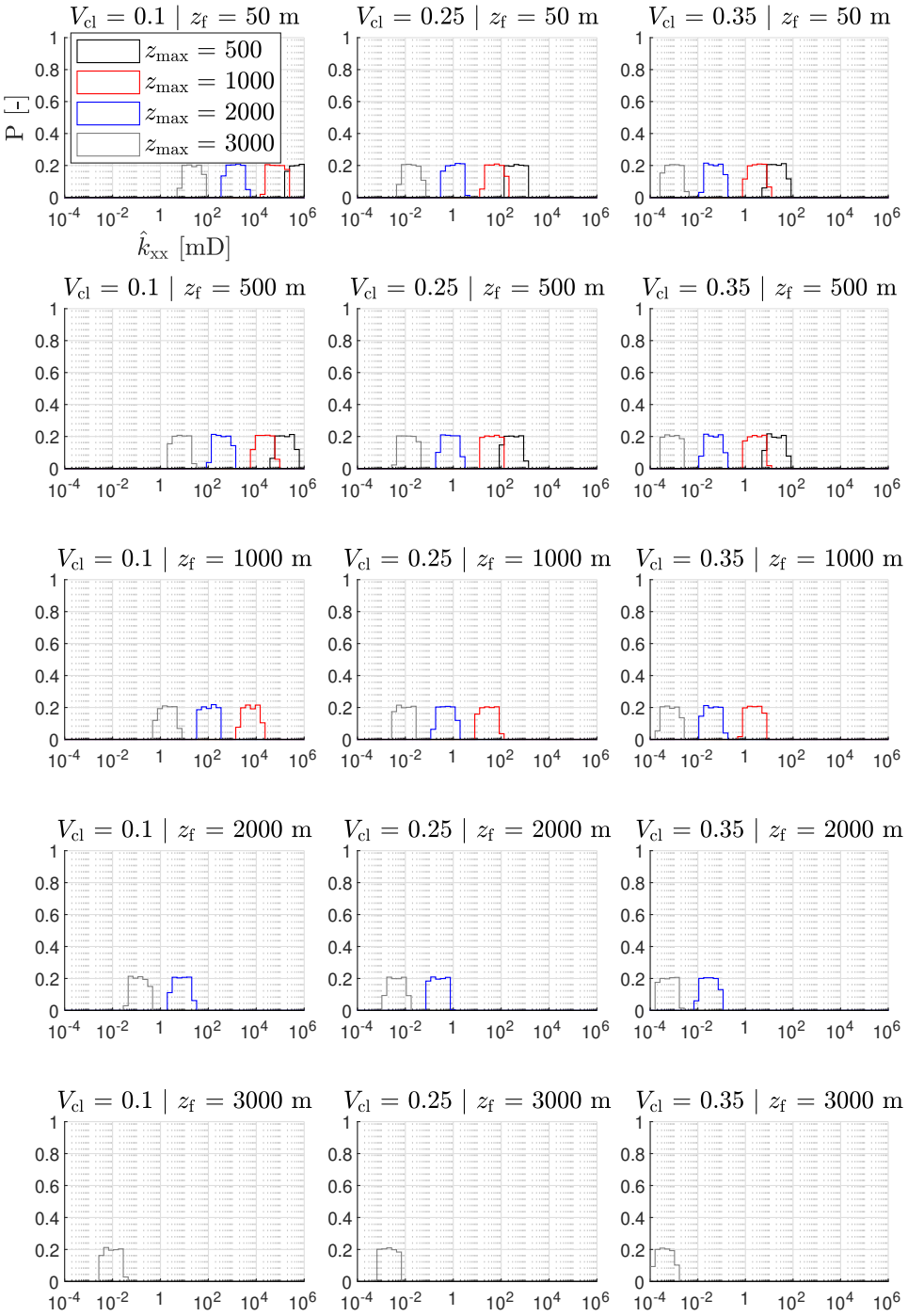

Figure B.13: Permeability of sand-based materials ($V_{cl} < 0.4$).

B.3 Kettermann et al.'s (2017) Experimental Permeability Calculation

In Fig. 2 in the main text, we report the comparison between PREDICT's output and experimental permeabilities estimated from measurements in a water-saturated sandbox by Ket-

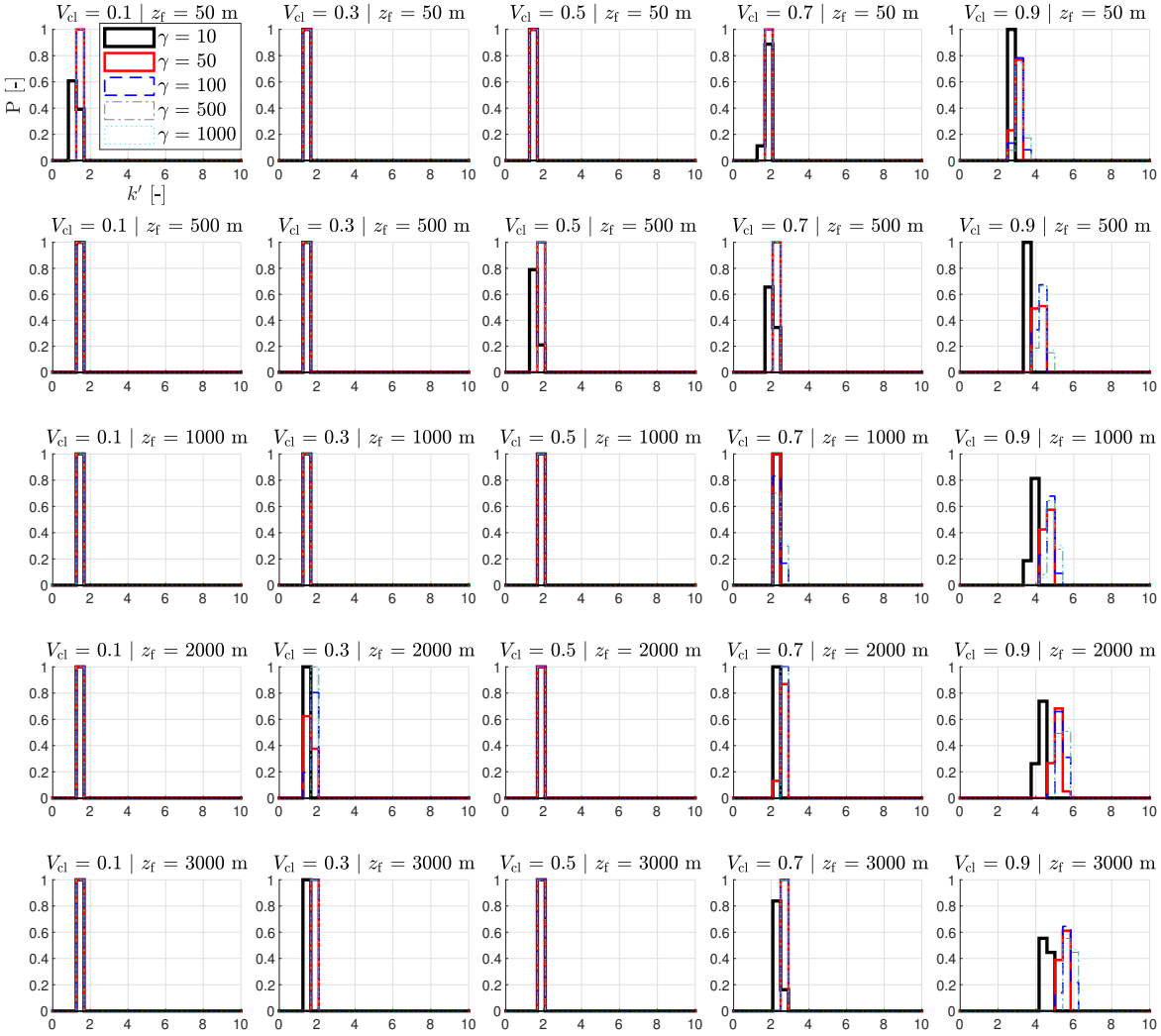

Figure B.14: Permeability anisotropy ratio ($k' = \hat{k}_{zz}/\hat{k}_{xx}$) for materials with kaolinite or illite as predominant clay mineral.

termann et al. (2017), as a way to validate PREDICT's output at the fault-scale (i.e., beyond the mini-permeameter or core measurements reported in Fig. 4 in the main text). Kettermann et al. (2017) measured the outflow for different values of fault displacement, with a bottom-to-top layering of 15 cm sand, 1 cm clay and 12 cm sand. Flow across the (displaced) clay layer is induced by lowering the hydraulic head in the lower sand reservoir by 2 cm (see Fig. 2A in the main text, and Fig. 2 in Kettermann et al. 2017). The outflow, and hence the estimated permeability, is dominated by the thickness and continuity of the displaced clay, i.e., the fault permeability.

In order to obtain the experimental fault permeabilities reported in Fig. 2 in the main text, we followed the steps below using data in Kettermann et al. (2017).

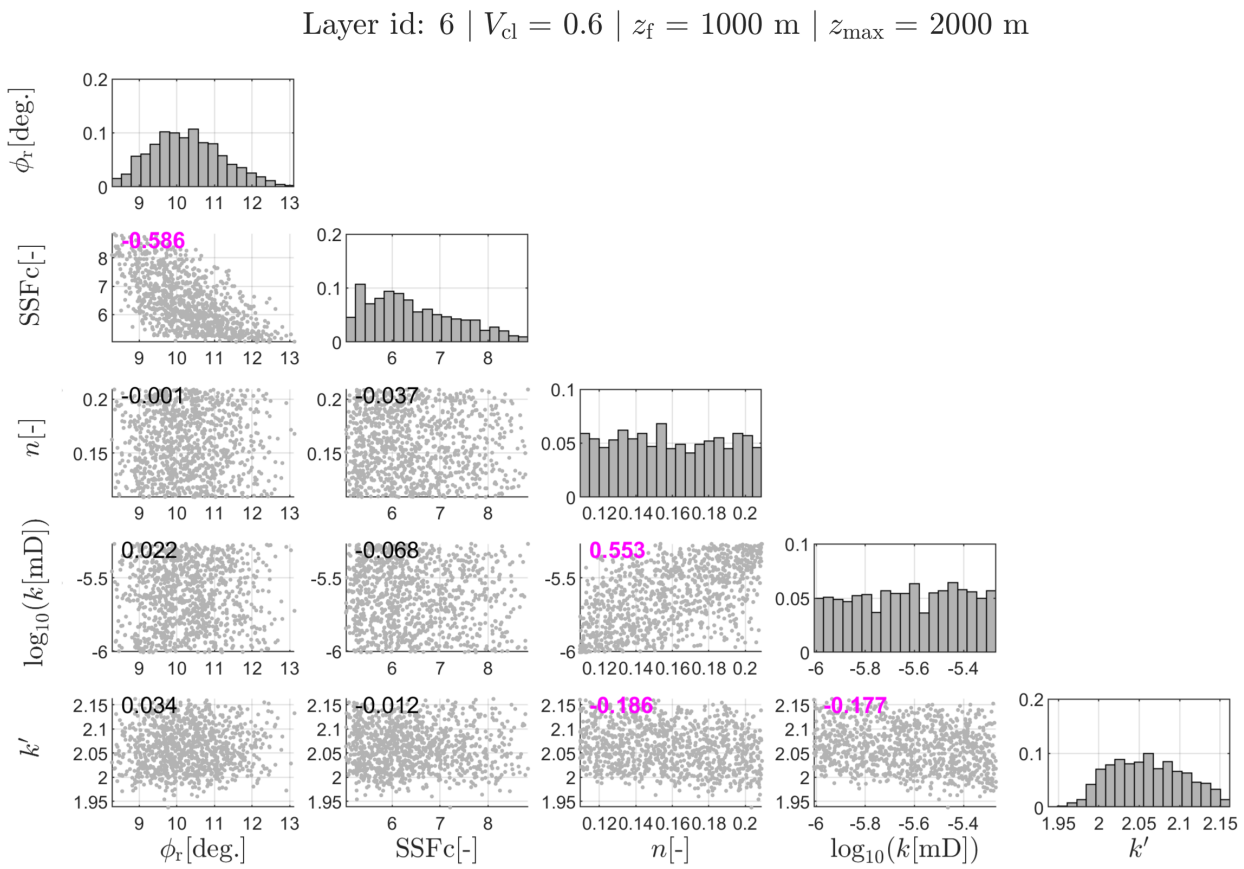

Figure B.15: Correlation between intermediate variables for a given material. *A posteriori* correlation coefficients are displayed in bold magenta when the correlation is statistically significant. $k = \hat{k}_{xx}$ is the permeability across the resulting smear. $N = 1000$.

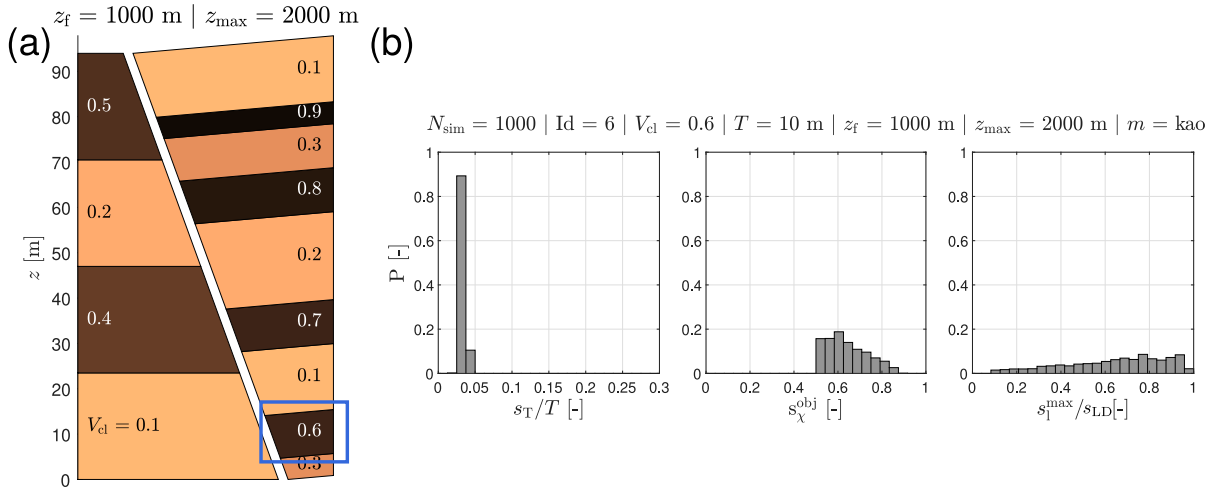

Figure B.16: **(a)**: Faulting interval, with the studied clay source highlighted in blue. **(b)**: Relative clay smear dimensions.

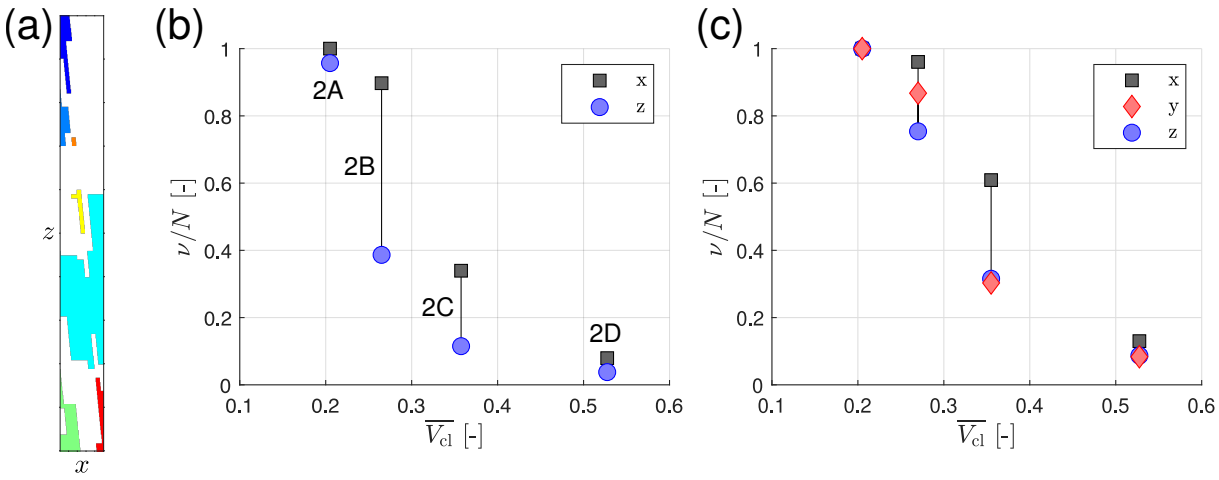

Figure B.17: **(a)**: Example of an individual fault section in which there is a continuous sand pathway through the fault core in x (cyan object), but not in z. Clay smears are shown in white. **(b)**: Relative frequency of continuous sand pathways, for each of the 4 sequences shown in Fig. 3 in the main text. Consistent with MPFA, we used 8-connected pixel (cell) connectivity. $N = 5000$ fault sections (2D). **(c)**: Relative frequency of continuous sand pathways, for each of the 4 sequences shown in Fig. 3 in the main text. Consistent with TPFA, we used 6-connected pixel (cell) connectivity. $N = 2000$ realizations (3D).

B.3.1 Computation hydraulic conductivity from normalized flux measurements

1. Using Darcy's law Darcy (1856), the hydraulic conductivity (K, [L/T]) can be calculated as follows (Eq. B.2):

$$K = \frac{QL}{\Delta h A} \tag{B.2}$$

   Where Q is the flow rate [L^3/T], L is the length of the porous medium [L], A is the cross-sectional area [L^2] and Δh is the hydraulic head difference [L].

2. We took the $Q/\Delta h$ measurements in Fig. 14 in Kettermann et al. (2017) for the experiments giving the most spread of the data (3 and 4 for one-layer experiments, and 7 and 8 for two-layer experiments). Specifically, we manually selected value pairs of normalized flux and SSF for each experiment from the figure.

3. For each value pair, we estimated K using Eq. B.2, the height of the sandbox ($L = 0.28$ m), and the outflow area ($A = 0.5 \times 0.3$ m). Variations in L due to deformation of the sandbox do not lead to significantly different permeability values.

4. We computed the intrinsic permeability (k) from K following Eq. B.3 and the same water density and viscosity employed to obtain the input k for clay and sand materials (see below).

B.3.2 Computation of intrinsic permeability from hydraulic conductivity

PREDICT allows inputing measured material permeabilities (instead of computing them as described in sect. B.1.2, which is the default), for cases when these data are available. Kettermann et al. (2017) report that the sand and clay have an average hydraulic conductivity (K) of $1 \pm 0.4 \times 10^{-4}$ and $4 \pm 2 \times 10^{-8}$ m/s, respectively. These values can be converted to intrinsic permeability ($k, [\mathrm{L}^2]$) as shown in Eq. B.3:

$$k = \frac{K\mu}{\rho g} \tag{B.3}$$

Where μ and ρ are the dynamic viscosity and density of the fluid, respectively, here taken to be 10^{-3} Pa·s and 998.23 kg/m^3 for water at 20 °C and atmospheric pressure, and g is the gravitational acceleration. We used the central measurement value, which results in $k_\mathrm{s} = 10.347$ D and $k_\mathrm{c} = 4.1388$ mD. To obtain the results in Fig. 2 in the main text, these permeabilities were passed into PREDICT and directly assigned to sand-based fault materials and clay smears, respectively.

Appendix C

Methods (Ch. 5)

Nomenclature for Ch. 5 and Appendix C

Acronyms

CB CO_2-Brine
CZ Fault architectural domain: Fault core or Core Zone
DZ Fault architectural domain: Damage Zone
FW Footwall block of the fault
GCS Geologic Carbon Sequestration or Geologic CO_2 Storage
GoM Gulf of Mexico
HW Hangingwall block of the fault
IEA International Energy Agency (https://www.iea.org/)
IEAGHG IEA Greenhouse Gas R&D Programme (https://ieaghg.org/)
IPCC Intergovernmental Panel on Climate Change (https://www.ipcc.ch/)
LM Lower Miocene
MICP Mercury-intrusion capillary pressure
MIP Macroscopic invasion-percolation
MM-UM Middle Miocene - Upper Miocene
MRST MATLAB Reservoir Simulation Toolbox Lie 2019
MZ Fault architectural domain: Mixed Zone
OR_i Overlying reservoir i. $i = 1$ is the first sand unit within the TS, and $i = 10$ the last one.
OTSW Offshore Texas State Waters
`PREDICT` PeRmEability DIstributions of Clay-smeared faulTs Saló-Salgado et al. 2023a
PVT Pressure, Volume, Temperature
S_i Numerical simulations: Scenario i
S_iC_j Numerical simulations: Scenario i, Case j
SGR Shale Gouge Ratio Yielding et al. 1997
SR Storage Reservoir
TS Top Seal

Notation

Gt Unit of mass: Gigaton (10^9 tons). We do not distinguish between tons (imperial)

and metric tonnes.

Mt Unit of mass: Megaton (10^6 tons). In our simulations, Mt refers to metric tonnes (1 Mt = 10^9 kg).

RMSE Root mean squared error: RMSE = $\sqrt{\frac{\sum_{i=1}^{N}(\hat{x}_i - x_i)^2}{N}}$

Ca Capillary number

f_D Fault displacement [m]

f_L Fault length (strike-parallel) [m]

f_T Fault thickness [m]

$f_{V_{cl}}$ Average clay volume fraction in the fault core [-]

h Cell size, measured as the length of an edge [m]

k Intrinsic or absolute permeability. When bold, $\mathbf{k}$ is the permeability tensor. k_{ii} refers to the main permeability components: For the fault, k_{xx}, k_{yy}, and k_{zz} refer to dip-perpendicular, strike-parallel, and dip-parallel permeability components. For sedimentary formations, $k_{xx} = k_{yy}$ is the horizontal permeability, and k_{zz} is the vertical permeability [mD] or [m^2]

k' Permeability anisotropy, i.e., k_{yy}/k_{xx} and/or k_{zz}/k_{xx} [-]

k_e Effective permeability, where $\mathbf{k}_e = \mathbf{k}k_r$

k_r Relative permeability, a function of fluid saturation (S) [-]

P Probability [-]

p Pore pressure, i.e., the pressure of the brine [bar]

P_c Capillary pressure, a function of fluid saturation (S). The subscript r refers to the reference curve, obtained from laboratory experiments. Specific values of the capillary pressure curve distinguished here include: (1) P_e, the entry capillary pressure, defined as the value at which CO_2 first enters a given unit/fault. In our simulations, it is defined at $S_g = 10^{-3}$. (2) P_b, the breakthrough or displacement pressure, defined as the minimum P_c value required to form a connected pathway (of the nonwetting phase) through the medium. For MICP curves, we define P_b as the value at $S_g = 0.1$. $P_b > P_e$ [bar]

S_α Saturation of fluid phase α [-]

S_{gt} Trapped gas saturation [-]

S_w^* Normalized water saturation, where $S_w^* = \frac{S_w - S_{wi}}{1 - S_{wi}}$ [-]

S_{wi} Irreducible or connate water saturation [-]

T Temperature [°C]

t Time [y]

V_c Clay volume fraction [-]

V_s Shale fraction [-]

W_i Fault throw window i, i.e., a vertical fault section limited by the fault offset. We define six throw windows W_1 to W_6 covering the TS thickness (Fig. 5.3a).

γ Interfacial tension [mN/m]

θ Wetting or contact angle between the solid grains and the wetting phase (brine). Values close to 0° indicate strongly water-wet media, while values close to 90° indicate intermediate wettability. [deg=°]

λ Correlation length [m]

μ Dynamic viscosity [cP] or [Pa· s]

ρ Mass density [kg/m^3]

σ Stress. When bold, $\boldsymbol{\sigma}$ is the stress tensor (as opposed to specific components such as the mean, normal or vertical stress). We use a positive compression sign convention, and define total ($\boldsymbol{\sigma}$) and effective stress ($\boldsymbol{\sigma}_{\text{eff}}$), where $\boldsymbol{\sigma}_{\text{eff}} = \boldsymbol{\sigma} - bp\mathbf{1}$. $\mathbf{1}$ is the identity tensor, and here we assume $b = 1$, where b is Biot's coefficient [bar]

ϕ Porosity [-]

C.1 Upscaling of fault multiphase flow properties

C.1.1 Relative permeability

Drainage sand relative permeability curves were obtained from fitting a Corey-type model (Brooks and Corey 1964) to ExxonMobil coreflood data for sandstones from a similar geologic location (Fig. C.1a, left). In this model, $k_{\text{rw}} = (S^*_{\text{w}})^{n_{\text{w}}}$ and $k_{\text{rg}} = (1 - S^*_{\text{w}})^{n_{\text{g}}}$, where $S^*_{\text{w}} = \frac{S_{\text{w}} - S_{\text{wi}}}{1 - S_{\text{wi}}}$ is the normalized water saturation and S_{wi} is the irreducible water saturation. No measurements on clays were conducted, so we used Corey curves with the same exponents and higher irreducible water saturation (S_{wi}; e.g., Ghomian et al. 2008) (solid lines in Fig. C.1a, left). Based on the extensive review by Iglauer et al. (2015), we consider two θ cases for clay material. To obtain the clay curves for $\theta = 60$ (discontinuous line in Fig. C.1a, left), we modified the curve by reducing S_{wi} from 0.3 to 0.2, decreasing the brine exponent from 4.8 to 3.5, and increasing the CO_2 exponent from 1.7 to 2.5. These changes are based on the trends reported in previous studies assessing the control of wettability on relative permeability (Morrow et al. 1973; Anderson 1987; Tang and Firoozabadi 2002; Blunt 2017, and references therein).

Upscaling of rock curves to the scale of a throw window is also performed using fault core material realizations from `PREDICT`: For a given realization, the corresponding curves are assigned to sand and clay smears. Then, we perform immiscible CO_2-brine flow simulations (Buckley and Leverett 1942), where CO_2 enters the brine-saturated domain from the bottom boundary at a constant flow rate ($S_g = 1$). The top boundary is kept at constant hydrostatic pressure, and the sides are no-flow boundaries. At each timestep, depth-averaged CO_2 saturation profiles from these 3D simulations are compared to 1D displacement profiles (Fig. C.1a, middle). We run 256 1D simulations changing Corey exponents (n_{w} and n_{g} for brine and gas, respectively) around the rock curve values, while S_{wi} is from capillary pressure upscaling (described below); the parameter combination that minimizes the L^1-norm in time of the mean absolute error in gas saturation (i.e., Eq. C.1) is selected, which leads to upscaled k_{r} curves with endpoints between those of the rock curves (e.g., Fig. C.1c, right). Throughout this process, P_{c} is set to 0. Flow is driven from the bottom boundary because this is analogous to updip CO_2 migration, which is our main focus. Note that we take a conservative view of residual trapping in the fault zone and do not consider relative permeability hysteresis in the fault. The Corey exponent values are provided in Table C.1, and the upscaled curves shown in Fig. 5.4b,c.

$$\min_{n_{\text{w}}, n_{\text{g}}} \sum_{i=1}^{n_t} \frac{\sum^{n_z} |S_{\text{1D}} - S_{\text{3D}}|^i}{n_z} \tag{C.1}$$

where, in Eq. C.1, n_z and n_t refer to the number of cells in the z dimension (≈ 100) and number of timesteps, respectively.

Table C.1: Results of capillary pressure and relative permeability upscaling (see also Fig. 5.4b,c and main text for nomenclature).

Fault throw window	θ [°]	Case	P_e [bar]	S_{wi} [-]	n_w [-]	n_g [-]
W_1	30	S2C2	0.334	0.2241	3.4	1.6
		S2C3	0.396	0.2189	3.4	1.6
	60	S2C4	0.334	0.1557	4.4	2.2
		S2C5	0.396	0.1529	4.4	2.2
W_2	30	S2C2	0.333	0.2579	5	1.8
		S2C3	5.789	0.2661	4	1.6
	60	S2C4	0.298	0.1623	3.8	2.2
		S2C5	4.58	0.1856	3.8	2.4
W_3	30	S2C2	0.3	0.2656	5	1.8
		S2C3	0.272	0.2775	4	1.6
	60	S2C4	0.3	0.1801	3.4	2.2
		S2C5	0.272	0.1875	3.8	2.4
W_4	30	S2C2	0.204	0.2465	4.2	1.6
		S2C3	0.212	0.2417	4.4	1.6
	60	S2C4	0.204	0.1691	3.6	2.2
		S2C5	0.24	0.1781	4	2.4
W_5	30	S2C2	0.197	0.2565	4.2	1.6
		S2C3	0.224	0.2630	4	1.6
	60	S2C4	0.196	0.1748	3.4	2.2
		S2C5	0.191	0.1876	3.6	2.4
W_6	30	S2C2	0.258	0.2023	5.6	1.8
		S2C3	0.263	0.2347	6	1.8
	60	S2C4	0.277	0.1499	3.8	2.2
		S2C5	3.177	0.1602	3.4	2.2

C.1.2 Capillary pressure

To model fault P_c, we first obtained reference curves for sand and clay materials (Fig. C.1b, left). Drainage sand capillary pressure curves were generated by fitting a Brooks and Corey (1964) model to ExxonMobil porous plate measurements (samples from the same location used for k_r measurements above). For clay material, the reference MICP curve is from Lu et al. (2017); in particular, we used the green curve reported in their Fig. 3.4a as a representation of a medium seal (sect. 5.3.2; Fig. 5.4e). We converted their MICP values to CO_2-brine according to Eq. 5.1 and used it as the reference curve for clay smears. For the conversion, however, the following θ values are considered based on the extensive review by Iglauer et al. (2015): 30° and 60°, for water-wet and intermediate-wet conditions, respectively (specific cases in Table 5.1). Note that these are different from $\theta = 70°$ used for the clay layers in the TS.

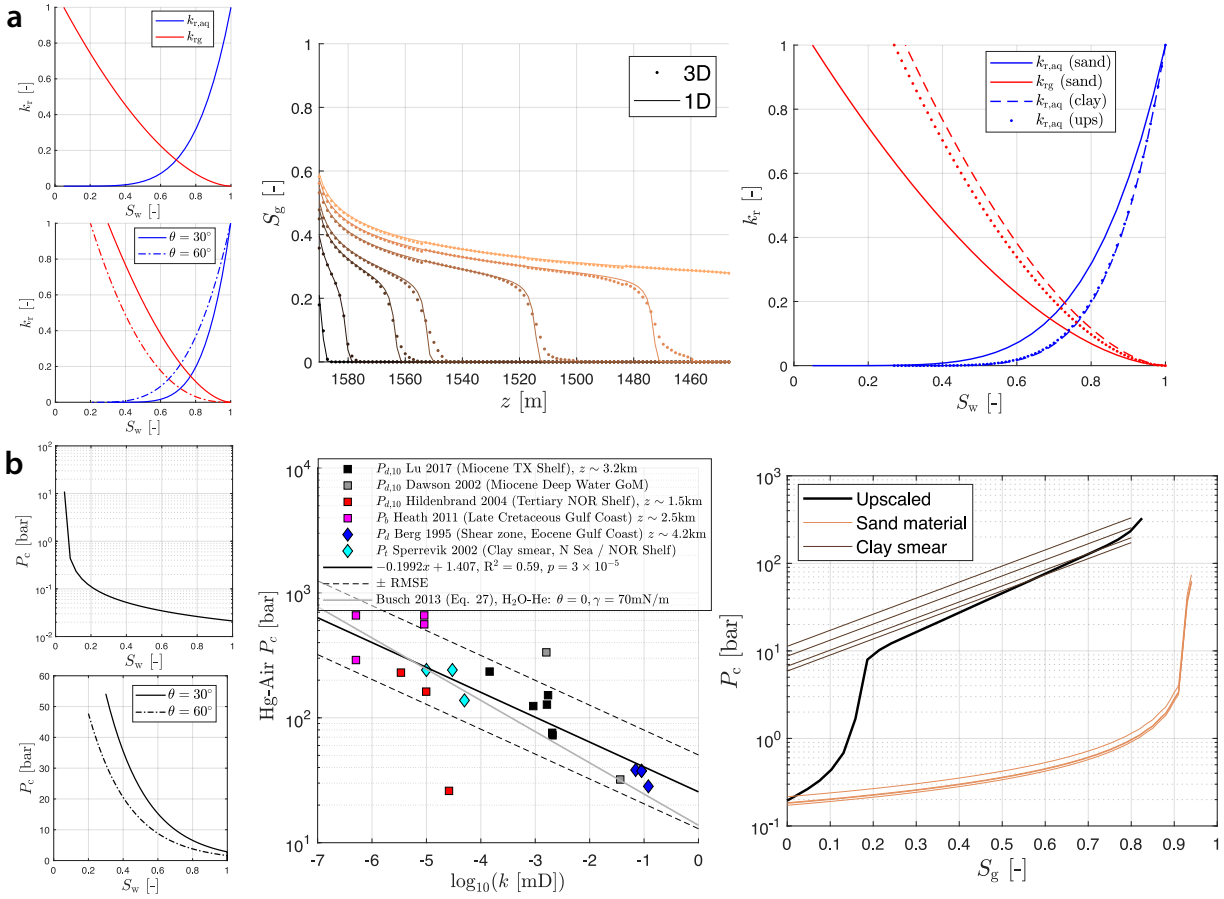

Figure C.1: Application of PREDICT to model fault multiphase flow properties in a given throw window (W_5; see Fig. 5.3 in the main text). **a** Left: CO_2-brine rock curves for sand smears (top) and clay smears (bottom). Middle: Best-match gas saturation profiles between the 1D (solid lines) and 3D (dotted lines) models for an arbitrary realization. Right: Resulting upscaled curves (dotted lines). **b** Left: Reference CO_2-brine rock curves for sand smears (top) and clay smears (bottom). Middle: Determined relationship between mudrock permeability and breakthrough or displacement pressure (P_b). Right: Upscaled CO_2-brine Pc curve for a high-permeability realization ($\theta = 60°$).

Next, fault core material realizations from PREDICT are also employed to generate P_c curves for each throw window: Leverett scaling of the reference sand curve (Eq. C.3) is used to assign a P_c curve to each sand smear. For clay smears, the scaling of P_c with the square root of the permeability ratio in Eq. C.3 may yield unrealistic values. Instead, we first determined a relationship between MICP displacement or breakthrough pressure (P_b) and k from measurements in mostly Tertiary mudrocks (Berg and Avery 1995; Dawson and Almon 2002; Sperrevik et al. 2002; Hildenbrand et al. 2004; Heath et al. 2011; Busch and Amann-Hildenbrand 2013; Lu et al. 2017) (solid black line in Fig. C.1b, middle). Due to scatter, we sample a random P_b value between the best fit line ± RMSE, according to a uniform probability law, for each clay smear (based on their permeability). MICP P_b values are converted to CO_2-brine similar to the reference curve, as described above. Then, $P_c(S_g)$ can be computed from this relationship as:

$$P_c(S_g) = P_{cr}(S_g) \times \frac{P_b}{P_{br}} \tag{C.2}$$

Eq. C.2 simply scales the reference curve (Fig. C.1b, left) according to the P_b ratio for each clay smear in the fault. After assigning a P_c curve to each fault material, we obtain an equivalent P_c, at the scale of a throw window, using macroscopic invasion-percolation (MIP) simulations. Similar to dynamic k_r upscaling, we perform this process in the z (dip-parallel) direction, starting from the bottom of a given fault core realization. Upscaled P_c values range from P_c^{min}, the minimum entry pressure among all sand smears, to P_c^{max}, the maximum capillary pressure among all clay smears. Our implementation is based on Ioannidis et al. (1996) and Yang et al. (2013), and a representative upscaled curve for a high permeability realization in W_5 is provided in Fig. C.1b, right. The upscaled capillary entry pressure values (P_e) are provided in Table C.1, and all upscaled curves shown in Fig. 5.4b,c. Note that we ignored gravity forces, given that $h_z \ll \frac{P_b}{\Delta\rho g}$, where $h_z \approx 1$ m is the vertical cell size of the upscaling grid (Ioannidis et al. 1996).

C.2 SGR modeling of base cases

For comparison purposes, a base case for each of the two scenarios (S1C1 and S2C1) is modeled using the well-established shale gouge ratio method (SGR; Yielding et al. 1997) (Fig. C.2). This requires an estimate of the stratigraphic clay volume fraction (V_c), which we obtained from the shale fraction (V_s) determined from a Gamma-ray well log (Fig. 4.12 in Meckel et al. 2017) as $V_c = 0.65V_s$ (e.g., Grant 2020). Using the SGR as a proxy for fault V_c, fault dip-perpendicular permeability (k_{xx}) is from Sperrevik et al. (2002)'s empirical model. We consider $k' = k_{yy}/k_{xx} = k_{zz}/k_{xx} = 10$, where k' is the permeability anisotropy (Fig. C.2b). Porosity (ϕ) is modeled according to the sand-clay mixture model described by Revil et al. (2002), with $\phi = 0.4$ for the pure sand (e.g., Revil et al. 2002; Haugen et al. 2023) and a compaction-dependent curve for the pure shale (Revil et al. 2002, their Eq. 10). We use Corey-type curves for the relative permeability (Fig. 5.4a), where the irreducible water saturation (S_{wi}) is set to 0.37, between that of SR (S_{wi}=0.31) and TS (S_{wi}=0.43) (Fig. 5.4e). Each fault cell is assigned a specific capillary pressure curve, $P_c(S_w)$, based on

Leverett's J-function (Leverett 1941). Assuming that the contact angle, surface tension and shape remain unchanged (e.g., Saadatpoor et al. 2010):

$$P_c = P_{cr}\sqrt{\frac{k_r\phi}{k\phi_r}} \tag{C.3}$$

where subscript r refers to the reference curve in Fig. 5.4e (Fig. C.2d, Fig. 5.4).

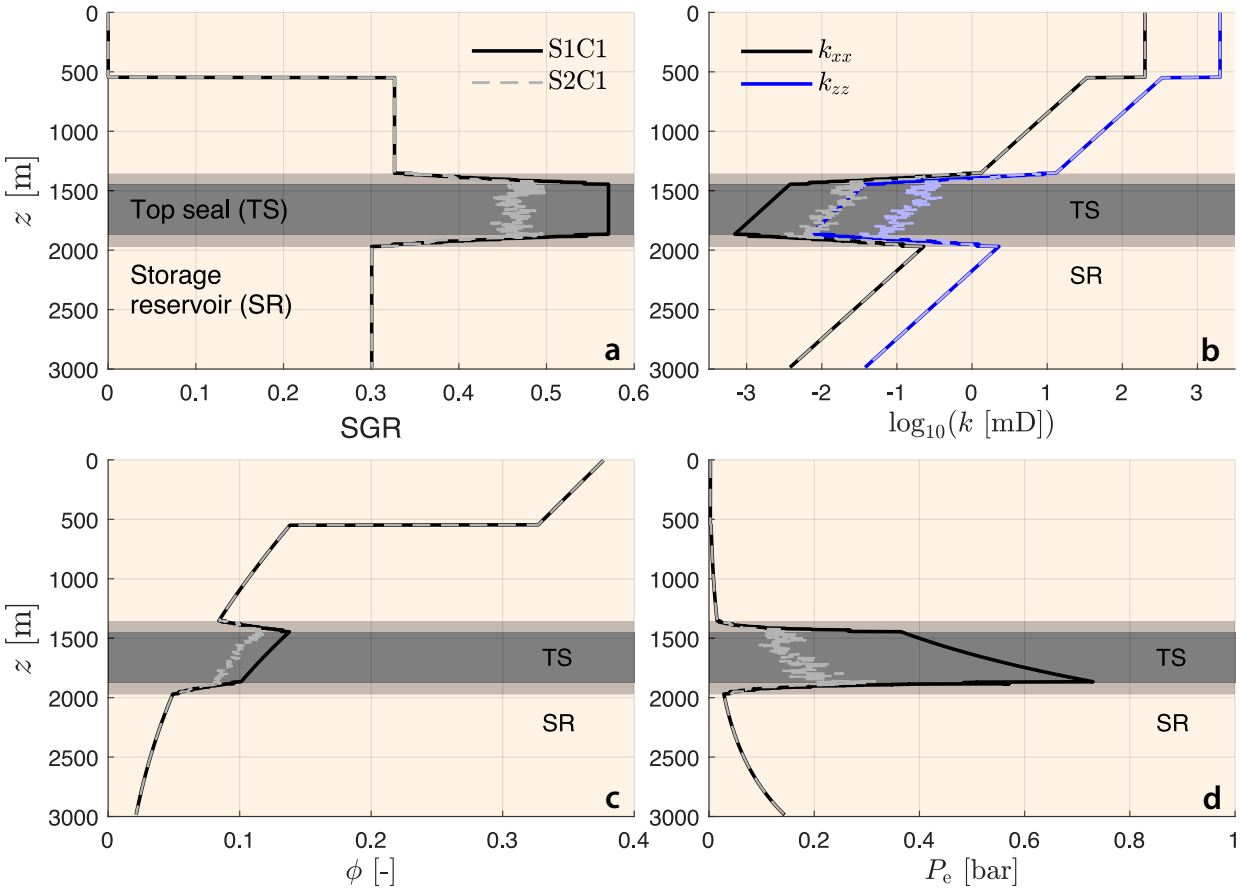

Figure C.2: Mapping of fault properties for the base cases as a function of depth (stratigraphy and fault properties remain constant along the fault strike). Solid lines are for S1C1, and dashed lines are for S2C1. **a** SGR (Yielding et al. 1997). **b** Permeability perpendicular (k_{xx}) and parallel ($k_{yy} = k_{zz}$) to the fault. **c** Porosity. **d** Capillary entry pressure, $P_e = P_c(S_g = 10^{-3})$.

References

AANONSEN, S. I., G. NŒVDAL, D. S. OLIVER, A. C. REYNOLDS, and B. VALLÈS (2009). "The ensemble Kalman filter in reservoir engineering—a review". In: *SPE Journal* 14.03, pp. 393–412. DOI: 10.2118/117274-PA.

AISSAOUI, A. (1983). "Etude théorique et expérimentale de l'hystérésis des pressions capillaries et des perméabilitiés relatives en vue du stockage souterrain de gaz". PhD thesis. Paris, France: École des Mines de Paris.

AJIBOYE, O. and S. NAGIHARA (2012). "Stratigraphic and structural framework of the Clemente-Tomas and Corsair growth fault systems in the Texas continental shelf". In: *GCAGS Journal* 1, pp. 107–117. URL: https://archives.datapages.com/data/gcags-journal/data/001/001001/pdfs/107.htm.

AKBARABADI, M. and M. PIRI (2013). "Relative permeability hysteresis and capillary trapping characteristics of supercritical CO_2/brine systems: An experimental study at reservoir conditions". In: *Advances in Water Resources* 52, pp. 190–206. DOI: 10.1016/j.advwatres.2012.06.014.

ALGHANNAM, M. and R. JUANES (2020). "Understanding rate effects in injection-induced earthquakes". In: *Nature Communications* 11, p. 3053. DOI: 10.1038/s41467-020-16860-y.

ALIZADEH, A. H. and M. PIRI (2014). "Three-phase flow in porous media: A review of experimental studies on relative permeability". In: *Reviews of Geophysics* 52.3, pp. 468–521. DOI: 10.1002/2013RG000433.

ANDERSON, W. G. (1987). "Wettability literature survey part 5: The effects of wettability on relative permeability". In: *Journal of Petroleum Technology* 39.11, pp. 1453–1468. DOI: 10.2118/16323-PA.

ARTS, R., O. EIKEN, A. CHADWICK, P. ZWEIGEL, L. van der MEER, and B. ZINSZNER (2004). "Monitoring of CO_2 injected at Sleipner using time-lapse seismic data". In: *Energy* 29.9–10, pp. 1383–1392. DOI: 10.1016/j.energy.2004.03.072.

ASKAR, A. H., T. H. ILLANGASEKARE, and A. M. C. ILIE (2021). "Monitoring Brine Leakage From Deep Geologic Formations Storing Carbon Dioxide: Design Framework Validation Using Intermediate-Scale Experiment". In: *Water Resources Research* 57.12, e2021WR031005. DOI: https://doi.org/10.1029/2021WR031005.

AVANSI, G. D., C. MASCHIO, and D. J. SCHIOZER (2016). "Simultaneous history-matching approach by use of reservoir-characterization and reservoir-simulation studies". In: *SPE Reservoir Evaluation & Engineering* 19.04, pp. 694–712. DOI: 10.2118/179740-PA.

AZIZ, K. and A. SETTARI (1979). *Petroleum Reservoir Simulation*. London, UK: Applied Science Publishers. DOI: 10.2118/9781613999646.

BACHU, S. (2015). "Review of CO_2 storage efficiency in deep saline aquifers". In: *International Journal of Greenhouse Gas Control* 40, pp. 188–202. DOI: 10.1016/j.ijggc.2015.01.007.

BACHU, S., W. GUNTER, and E. PERKINS (1994). "Aquifer disposal of CO_2: Hydrodynamic and mineral trapping". In: *Energy Conversion and Management* 35.4, pp. 269–279. DOI: 10.1016/0196-8904(94)90060-4.

BAKER, L. (Apr. 1988). "Three-Phase Relative Permeability Correlations". In: SPE Improved Oil Recovery Conference, SPE-17369–MS. DOI: 10.2118/17369-MS.

BALDWIN, B. and C. O. BUTLER (1985). "Compaction curves". In: *AAPG Bulletin* 69.4, pp. 622–626. DOI: 10.1306/AD462547-16F7-11D7-8645000102C1865D.

BALSAMO, F., F. STORTI, F. SALVINI, A. SILVA, and C. LIMA (2010). "Structural and petrophysical evolution of extensional fault zones in low-porosity, poorly lithified sandstones of the Barreiras Formation, NE Brazil". In: *Journal of Structural Geology* 32.11, pp. 1806–1826. DOI: 10.1016/j.jsg.2009.10.010.

BAO, K., K.-A. LIE, O. MØYNER, and M. LIU (2017). "Fully implicit simulation of polymer flooding with MRST". In: *Computational Geosciences* 21.5-6, pp. 1219–1244. DOI: 10.1007/s10596-017-9624-5.

BATZLE, M. and Z. WANG (1992). "Seismic properties of pore fluids". In: *Geophysics* 57.11, pp. 1396–1408. DOI: 10.1190/1.1443207.

BEAR, J. (1972). *Dynamics of Fluids in Porous Media*. New York, USA: Dover.

BEAR, J. (2018). *Modeling Phenomena of Flow and Transport in Porous Media*. Cham, Switzerland: Springer. DOI: 10.1007/978-3-319-72826-1.

BEARD, D. and P. WEYL (1973). "Influence of texture on porosity and permeability of unconsolidated sand". In: *AAPG Bulletin* 57.2, pp. 349–369. DOI: 10.1306/819A4272-16C5-11D7-8645000102C1865D.

BENNION, B. and S. BACHU (2008). "Drainage and imbibition relative permeability relationships for supercritical CO_2/brine and H_2S/brine systems in intergranular sandstone, carbonate, shale, and anhydrite rocks". In: *SPE Reservoir Evaluation & Engineering* 11.03, pp. 487–496. DOI: 10.2118/99326-PA.

BENSE, V. F., T. GLEESON, S. E. LOVELESS, O. BOUR, and J. SCIBEK (2013). "Fault zone hydrogeology". In: *Earth-Science Reviews* 127, pp. 171–192. DOI: 10.1016/j.earscirev.2013.09.008.

BENSE, V. F. and M. PERSON (2006). "Faults as conduit-barrier systems to fluid flow in siliciclastic sedimentary aquifers". In: *Water Resources Research* 42.5. DOI: 10.1029/2005WR004480.

BENSON, S., P. COOK, J. ANDERSON, S. BACHU, H. B. NIMIR, B. BASU, J. BRADSHAW, G. DEGUCHI, J. GALE, G. von GOERNE, W. HEIDUG, S. HOLLOWAY, et al. (2005). "Underground geological storage". In: *IPCC Special Report on Carbon Dioxide Capture and Storage*. Ed. by B. METZ, O. DAVIDSON, H. DE CONINCK, M. LOOS, and L. MEYER. The Edinburgh Building Shaftesbury Road, Cambridge CB2 2RU, UK: Cambridge University Press. Chap. 5, pp. 195–276. URL: https://www.ipcc.ch/report/carbon-dioxide-capture-and-storage/.

BERG, R. R. and A. H. AVERY (1995). "Sealing properties of Tertiary growth faults, Texas Gulf Coast". In: *AAPG Bulletin* 79.3, pp. 375–392. DOI: 10.1306/8D2B1534-171E-11D7-8645000102C1865D.

BERGE, R. L., Ø. S. KLEMETSDAL, and K.-A. LIE (2019). "Unstructured Voronoi grids conforming to lower dimensional objects". In: *Computational Geosciences* 23, pp. 169–188. DOI: 10.1007/s10596-018-9790-0.

BERGE, R. L., Ø. S. KLEMETSDAL, B. SKAFLESTAD, and K.-A. LIE (2021). *The UPR module*. Accessed on: August 25, 2023. URL: https://github.com/rbe051/UPR.

BICKLE, M. J. (2009). "Geological carbon storage". In: *Nature Geoscience* 2.12, p. 815. DOI: 10.1038/ngeo687.

BIRKHOLZER, J. T. and Q. ZHOU (2009). "Basin-scale hydrogeologic impacts of CO_2 storage: Capacity and regulatory implications". In: *International Journal of Greenhouse Gas Control* 3.6, pp. 745–756. DOI: 10.1016/j.ijggc.2009.07.002.

BIRKHOLZER, J., Q. ZHOU, A. CORTIS, and S. FINSTERLE (2011). "A sensitivity study on regional pressure buildup from large-scale CO_2 storage projects". In: *Energy Procedia* 4, pp. 4371–4378. DOI: 10.1016/j.egypro.2011.02.389.

BJØRNARÅ, T. I., E. A. H. MICHIE, and E. SKURTVEIT (2021). "Upscaled geocellular flow model of potential across-and along-fault leakage using shale gouge ratio". In: *TCCS–11. CO2 Capture, Transport and Storage, Trondheim 22nd–23rd June 2021*. SINTEF Academic Press. URL: https://hdl.handle.net/11250/2786524.

BLUNT, M. J. (2000). "An empirical model for three-phase relative permeability". In: *SPE Journal* 5.04, pp. 435–445. DOI: 10.2118/67950-PA.

BLUNT, M. J. (2017). *Multiphase Flow in Permeable Media: A Pore-scale Perspective*. University Printing House, Cambridge CB2 8BS, United Kingdom: Cambridge University Press. DOI: 10.1017/9781316145098.

BOAIT, F., N. WHITE, M. BICKLE, R. CHADWICK, J. NEUFELD, and H. HUPPERT (2012). "Spatial and temporal evolution of injected CO_2 at the Sleipner Field, North Sea". In: *Journal of Geophysical Research: Solid Earth* 117.B03309. DOI: 10.1029/2011JB008603.

BOND, C. E., Y. KREMER, G. JOHNSON, N. HICKS, R. LISTER, D. G. JONES, R. S. HASZELDINE, I. SAUNDERS, S. M. GILFILLAN, Z. K. SHIPTON, and J. PEARCE (2017). "The physical characteristics of a CO_2 seeping fault: the implications of fracture permeability for carbon capture and storage integrity". In: *International Journal of Greenhouse Gas Control* 61, pp. 49–60. DOI: 10.1016/j.ijggc.2017.01.015.

BOURZAC, K. (2017). "We have the technology". In: *Nature* 550, S66–S69. DOI: 10.1038/550S66a.

BRAATHEN, A., J. TVERANGER, H. FOSSEN, T. SKAR, N. CARDOZO, S. SEMSHAUG, E. BASTESEN, and E. SVERDRUP (2009). "Fault facies and its application to sandstone reservoirs". In: *AAPG Bulletin* 93.7, pp. 891–917. DOI: 10.1306/03230908116.

BROCK, D. and F. ORR (1991). "Flow visualization of viscous fingering in heterogeneous porous media". In: *SPE Annual Technical Conference and Exhibition* SPE-22614-MS. DOI: 10.2118/22614-MS.

BROOKS, R. H. and A. T. COREY (1964). *Hydraulic properties of porous media*. Tech. rep. Hydrology Paper no. 3. Fort Collins, CO: Colorado State University.

BRYANT, S. and M. BLUNT (1992). "Prediction of relative permeability in simple porous media". In: *Physical Review A* 46.4, p. 2004. DOI: 10.1103/PhysRevA.46.2004.

BRYANT, S. L., S. LAKSHMINARASIMHAN, and G. A. POPE (2008). "Buoyancy-dominated multiphase flow and its effect on geological sequestration of CO_2". In: *SPE Journal* 13.04, pp. 447–454. DOI: 10.2118/99938-PA.

BUCKLEY, S. E. and M. LEVERETT (1942). "Mechanism of fluid displacement in sands". In: *Transactions of the AIME* 146.01, pp. 107–116. DOI: 10.2118/942107-G.

BURNSIDE, N. and M. NAYLOR (2014). "Review and implications of relative permeability of CO_2/brine systems and residual trapping of CO_2". In: *International Journal of Greenhouse Gas Control* 23, pp. 1–11. DOI: 10.1016/j.ijggc.2014.01.013.

BUSCH, A. and A. AMANN-HILDENBRAND (2013). "Predicting capillarity of mudrocks". In: *Marine and Petroleum Geology* 45, pp. 208–223. DOI: 10.1016/j.marpetgeo.2013.05.005.

CAINE, J. S., J. P. EVANS, and C. B. FORSTER (1996). "Fault zone architecture and permeability structure". In: *Geology* 24.11, pp. 1025–1028. DOI: 10.1130/0091-7613(1996)024<1025:FZAAPS>2.3.CO;2.

CAINE, J. S. and S. A. MINOR (2009). "Structural and geochemical characteristics of faulted sediments and inferences on the role of water in deformation, Rio Grande Rift, New Mexico". In: *Geological Society of America Bulletin* 121.9-10, pp. 1325–1340. DOI: 10.1130/B26164.1.

CAPPA, F., Y. GUGLIELMI, C. NUSSBAUM, L. DE BARROS, and J. BIRKHOLZER (2022). "Fluid migration in low-permeability faults driven by decoupling of fault slip and opening". In: *Nature Geoscience* 15, pp. 747–751. DOI: 10.1038/s41561-022-00993-4.

CAPPA, F. and J. RUTQVIST (2011). "Impact of CO_2 geological sequestration on the nucleation of earthquakes". In: *Geophysical Research Letters* 38.17, p. L17313. DOI: 10.1029/2011GL048487.

CARLSON, F. M. (1981). "Simulation of Relative Permeability Hysteresis to the Nonwetting Phase". In: SPE Annual Technical Conference and Exhibition. Society of Petroleum Engineers, SPE-10157–MS. DOI: 10.2118/10157-MS.

CELIA, M. A. (2021). "The Role of Subsurface Engineering in the Net-zero Energy Transition". In: *IOP Conference Series: Earth and Environmental Science*. Vol. 861. IOP Publishing, p. 072017. DOI: 10.1088/1755-1315/861/7/072017.

CELIA, M. A., S. BACHU, J. NORDBOTTEN, and K. BANDILLA (2015). "Status of CO_2 storage in deep saline aquifers with emphasis on modeling approaches and practical simulations". In: *Water Resources Research* 51.9, pp. 6846–6892. DOI: 10.1002/2015WR017609.

CHADWICK, R., P. ZWEIGEL, U. GREGERSEN, G. KIRBY, S. HOLLOWAY, and P. JOHANNESSEN (2004). "Geological reservoir characterization of a CO_2 storage site: The Utsira Sand, Sleipner, northern North Sea". In: *Energy* 29.9-10, pp. 1371–1381. DOI: 10.1016/j.energy.2004.03.071.

CHANG, Y.-B., B. K. COATS, and J. S. NOLEN (1998). "A Compositional Model for CO_2 Floods Including CO_2 Solubility in Water". In: *SPE Reservoir Evaluation & Engineering* 1.2. Paper Number: SPE-35164-PA, pp. 155–160. DOI: 10.2118/35164-PA.

CHILDS, C., T. MANZOCCHI, J. J. WALSH, C. G. BONSON, A. NICOL, and M. P. SCHÖPFER (2009). "A geometric model of fault zone and fault rock thickness variations". In: *Journal of Structural Geology* 31.2, pp. 117–127. DOI: 10.1016/j.jsg.2008.08.009.

CHILDS, C., A. NICOL, J. J. WALSH, and J. WATTERSON (1996). "Growth of vertically segmented normal faults". In: *Journal of Structural Geology* 18.12, pp. 1389–1397. DOI: 10.1016/S0191-8141(96)00060-0.

CHILDS, C., J. J. WALSH, T. MANZOCCHI, J. STRAND, A. NICOL, M. TOMASSO, M. P. SCHÖPFER, and A. C. APLIN (2007). "Definition of a fault permeability predictor from outcrop studies of a faulted turbidite sequence, Taranaki, New Zealand". In: *Geological Society, London, Special Publications* 292, pp. 235–258. DOI: 10.1144/SP292.14.

CHRISTIE, C. H. and S. NAGIHARA (2016). "Geothermal gradients of the northern continental shelf of the Gulf of Mexico". In: *Geosphere* 12.1, pp. 26–34. DOI: 10.1130/GES01163.1.

ÇIFTÇI, N. B., S. B. GIGER, and M. B. CLENNELL (2013). "Three-dimensional structure of experimentally produced clay smears: Implications for fault seal analysis". In: *AAPG Bulletin* 97.5, pp. 733–757. DOI: 10.1306/10161211192.

CINAR, Y., K. JESSEN, R. BERENBLYUM, R. JUANES, and F. M. ORR (2006). "An experimental and numerical investigation of crossflow effects in two-phase displacements". In: *SPE Journal* 11.02, pp. 216–226. DOI: 10.2118/90568-PA.

CLAUSEN, J. A. and R. H. GABRIELSEN (2002). "Parameters that control the development of clay smear at low stress states: an experimental study using ring-shear apparatus". In: *Journal of Structural Geology* 24.10, pp. 1569–1586. DOI: 10.1016/S0191-8141(01)00157-2.

COREY, A. T. (1954). "The interrelation between gas and oil relative permeabilities". In: *Producers Monthly* 19, pp. 38–41.

CRAWFORD, B. R., P. F. SANZ, B. ALRAMAHI, and N. L. DEDONTNEY (2011). "Modeling and prediction of formation compressibility and compactive pore collapse in siliciclastic reservoir rocks". In: *45th US Rock Mechanics/Geomechanics Symposium*. Accessed on: August 25, 2023. OnePetro. URL: https://onepetro.org/ARMAUSRMS/proceedings-abstract/ARMA11/All-ARMA11/ARMA-11-384/120368/.

CRAWFORD, B. R., D. R. FAULKNER, and E. H. RUTTER (2008). "Strength, porosity, and permeability development during hydrostatic and shear loading of synthetic quartz-clay fault gouge". In: *Journal of Geophysical Research: Solid Earth* 113.B3. DOI: 10.1029/2006JB004634.

CUSINI, M., A. FRANCESCHINI, L. GAZZOLA, T. GAZZOLA, J. HUANG, F. HAMON, R. SETTGAST, N. CASTELLETTO, and J. WHITE (2022). "Field-scale simulation of geologic carbon sequestration in faulted and fractured natural formations". In: *16th Greenhouse Gas Control Technologies Conference (GHGT-16), 23-24 Oct 2022*. IEA Greenhouse Gas R&D Programme (IEAGHG). URL: https://www.osti.gov/biblio/1897350.

DAIGLE, H. and B. DUGAN (2011). "Permeability anisotropy and fabric development: A mechanistic explanation". In: *Water Resources Research* 47.12, W12517. DOI: 10.1029/2011WR011110.

DARCY, H. P. (1856). *Les Fontaines publiques de la ville de Dijon. Exposition et application des principes à suivre et des formules à employer dans les questions de distribution d'eau, etc.* Accessed on: August 25, 2023. Paris, France: Victor Dalmont. URL: https://gallica.bnf.fr/ark:/12148/bpt6k624312/f1.item.

DAVIDSON, T. A. (1993). *A simple and accurate method for calculating viscosity of gaseous mixtures*. Report of Investigations 9456. Accessed on: August 25, 2023. Washington, DC, USA: Bureau of Mines, US Department of the Interior. URL: https://stacks.cdc.gov/view/cdc/10045.

DAWSON, W. C. and W. R. ALMON (2002). "Top seal potential of Tertiary deep-water Gulf of Mexico shales". In: *GCAGS Transactions* 52, pp. 167–176. URL: https://archives.datapages.com/data/gcags/data/052/052001/0167.htm.

DE CONINCK, H. and S. M. BENSON (2014). "Carbon dioxide capture and storage: issues and prospects". In: *Annual Review of Environment and Resources* 39.1, pp. 243–270. DOI: 10.1146/annurev-environ-032112-095222.

DELOGKOS, E., T. MANZOCCHI, C. J. CHILDS, G. CAMANNI, and V. ROCHE (2020). "The 3D structure of a normal fault from multiple outcrop observations". In: *Journal of Structural Geology* 136, p. 104009. DOI: 10.1016/j.jsg.2020.104009.

DEMIDOV, D. and R. ROSSI (2018). "Subdomain Deflation Combined with Local AMG: A Case Study Using AMGCL Library". In: *arXiv:1710.03940*. DOI: 10.48550/arXiv.1710.03940.

DEWHURST, D. N., K. M. BROWN, M. B. CLENNELL, and G. K. WESTBROOK (1996). "A comparison of the fabric and permeability anisotropy of consolidated and sheared silty clay". In: *Engineering Geology* 42.4, pp. 253–267. DOI: 10.1016/0013-7952(95)00089-5.

DICARLO, D. A., A. SAHNI, and M. J. BLUNT (2000). "Three-phase relative permeability of water-wet, oil-wet, and mixed-wet sandpacks". In: *SPE Journal* 5.01, pp. 82–91. DOI: 10.2118/60767-PA.

DOUGHTY, C. and C. M. OLDENBURG (2020). "CO_2 plume evolution in a depleted natural gas reservoir: Modeling of conformance uncertainty reduction over time". In: *International Journal of Greenhouse Gas Control* 97, p. 103026. DOI: 10.1016/j.ijggc.2020.103026.

DUAN, Z. and R. SUN (2003). "An improved model calculating CO_2 solubility in pure water and aqueous NaCl solutions from 273 to 533 K and from 0 to 2000 bar". In: *Chemical Geology* 193.3-4, pp. 257–271. DOI: 10.1016/S0009-2541(02)00263-2.

DURLOFSKY, L. J. (1991). "Numerical calculation of equivalent grid block permeability tensors for heterogeneous porous media". In: *Water Resources Research* 27.5, pp. 699–708. DOI: 10.1029/91WR00107.

DURLOFSKY, L. J. and Y. CHEN (2012). "Uncertainty Quantification for Subsurface Flow Problems Using Coarse-Scale Models". In: *Numerical Analysis of Multiscale Problems*. Ed. by I. G. GRAHAM, T. Y. HOU, O. LAKKIS, and R. SCHEICHL. Springer Berlin Heidelberg, pp. 163–202. ISBN: 978-3-642-22061-6. DOI: 10.1007/978-3-642-22061-6_6.

EASAC (2018). *Negative emission technologies: What role in meeting Paris Agreement targets?* Policy Report 35. Accessed on 01.20.2023. URL: https://easac.eu/publications/details/easac_net.

EGHOLM, D. L., O. R. CLAUSEN, M. SANDIFORD, M. KRISTENSEN, and J. A. KORSTGÅRD (2008). "The mechanics of clay smearing along faults". In: *Geology* 36.10, pp. 787–790. DOI: 10.1130/G24975A.1.

EIKEHAUG, K., M. HAUGEN, O. FOLKVORD, B. BENALI, E. L. LARSEN, A. TINKOVA, A. ROTEVATN, J. M. NORDBOTTEN, and M. FERNØ (2023). "Engineering meter-scale porous media flow experiments for quantitative studies of geological carbon sequestration". In: *Transport in Porous Media*. preprint available on *arXiv* through https://doi.org/10.48550/arXiv.2301.06397.

EIKEN, O., P. RINGROSE, C. HERMANRUD, B. NAZARIAN, T. A. TORP, and L. HØIER (2011). "Lessons learned from 14 years of CCS operations: Sleipner, In Salah and Snøhvit". In: *Energy Procedia* 4, pp. 5541–5548. DOI: 10.1016/j.egypro.2011.02.541.

EINSTEIN, H. H. and G. B. BAECHER (1982). "Probabilistic and statistical methods in engineering geology I. Problem statement and introduction to solution". In: *Engineering Geology and Geomechanics as Fundamentals of Rock Engineering*. Ed. by L. MÜLLER. Suppl. Volume 12 of the series Rock Mechanics. Springer Vienna. Chap. 4, pp. 47–61. DOI: 10.1007/978-3-7091-8665-7_4.

EINSTEIN, H. H. and G. B. BAECHER (1983). "Probabilistic and statistical methods in engineering geology. Specific methods and examples part I: Exploration". In: *Rock Mechanics and Rock Engineering* 16, pp. 39–72. DOI: 10.1007/BF01030217.

ELLSWORTH, W. L. (2013). "Injection-induced earthquakes". In: *Science* 341.6142, p. 1225942. DOI: 10.1126/science.1225942.

ELY, J., W. HAYNES, and B. BAIN (1989). "Isochoric (p, Vm, T) measurements on CO_2 and on (0.982 CO_2 + 0.018 N_2) from 250 to 330 K at pressures to 35 MPa". In: *The Journal of Chemical Thermodynamics* 21.8, pp. 879–894. DOI: 10.1016/0021-9614(89)90036-0.

ENNIS-KING, J. and L. PATERSON (2005). "Role of Convective Mixing in the Long-Term Storage of Carbon Dioxide in Deep Saline Formations". In: *SPE Journal* 10.03, pp. 349–356. DOI: 10.2118/84344-PA.

FÆRSETH, R. B. (2006). "Shale smear along large faults: continuity of smear and the fault seal capacity". In: *Journal of the Geological Society* 163.5, pp. 741–751. DOI: 10.1144/0016-76492005-162.

FÆRSETH, R. B., E. JOHNSEN, and S. SPERREVIK (2007). "Methodology for risking fault seal capacity: Implications of fault zone architecture". In: *AAPG Bulletin* 91.9, pp. 1231–1246. DOI: 10.1306/03080706051.

FAULKNER, D. R., C. A.-L. JACKSON, R. J. LUNN, R. W. SCHLISCHE, Z. K. SHIPTON, C. A. WIBBERLEY, and M. O. WITHJACK (2010). "A review of recent developments concerning the structure, mechanics and fluid flow properties of fault zones". In: *Journal of Structural Geology* 32.11, pp. 1557–1575. DOI: 10.1016/j.jsg.2010.06.009.

FENGHOUR, A., W. WAKEHAM, and J. WATSON (1995). "Amount-of-substance density of CO_2 at temperatures from 329 K to 698 K and pressures up to 34 MPa". In: *The Journal of Chemical Thermodynamics* 27.2, pp. 219–223. DOI: 10.1006/jcht.1995.0019.

FENGHOUR, A., W. A. WAKEHAM, and V. VESOVIC (1998). "The viscosity of carbon dioxide". In: *Journal of Physical and Chemical Reference Data* 27.1, pp. 31–44. DOI: 10.1063/1.556013.

FERNÁNDEZ-GARCÍA, D., T. H. ILLANGASEKARE, and H. RAJARAM (2004). "Conservative and sorptive forced-gradient and uniform flow tracer tests in a three-dimensional laboratory test aquifer". In: *Water Resources Research* 40.10, W10103. DOI: 10.1029/2004WR003112.

FERNØ, M., M. HAUGEN, K. EIKEHAUG, O. FOLKVORD, B. BENALI, J. W. BOTH, E. STORVIK, C. W. NIXON, R. L. GAWTHORPE, and J. M. NORDBOTTEN (2023). "Room-scale CO_2 injections in a physical reservoir model with faults". In: *Transport in Porous Media*. DOI: 10.1007/s11242-023-02013-4.

FICK, A. (1855). "V. On liquid diffusion". In: *The London, Edinburgh, and Dublin Philosophical Magazine and Journal of Science,* 10.63, pp. 30–39. DOI: 10.1080/14786445508641925.

FISHER, Q. and S. JOLLEY (2007). "Treatment of faults in production simulation models". In: *Geological Society, London, Special Publications* 292, pp. 219–233. DOI: 10.1144/SP292.13.

FISHER, Q. J. and R. J. KNIPE (1998). "Fault sealing processes in siliciclastic sediments". In: *Geological Society, London, Special Publications* 147.1, pp. 117–134. DOI: 10.1144/GSL.SP.1998.147.01.08.

FLEMISCH, B., M. DARCIS, K. ERBERTSEDER, B. FAIGLE, A. LAUSER, K. MOSTHAF, S. MÜTHING, P. NUSKE, A. TATOMIR, M. WOLFF, and R. HELMIG (2011). "DuMux: DUNE for multi-{phase, component, scale, physics,...} flow and transport in porous media". In: *Advances in Water Resources* 34.9, pp. 1102–1112. DOI: 10.1016/j.advwatres.2011.03.007.

FLEMISCH, B. et al. (2023). "The FluidFlower Validation Benchmark Study for the Storage of CO_2". In: *Transport in Porous Media*. DOI: 10.1007/s11242-023-01977-7.

FLORIS, F. J. T., M. D. BUSH, M. CUYPERS, F. ROGGERO, and A.-R. SYVERSVEEN (2001). "Methods for quantifying the uncertainty of production forecasts: a comparative study". In: *Petroleum Geoscience* 7.S, S87–S96. DOI: 10.1144/petgeo.7.S.S87.

FOSSEN, H. and A. ROTEVATN (2016). "Fault linkage and relay structures in extensional settings—A review". In: *Earth-Science Reviews* 154, pp. 14–28. DOI: 10.1016/j.earscirev.2015.11.014.

FREDMAN, N., J. TVERANGER, S. SEMSHAUG, A. BRAATHEN, and E. SVERDRUP (2007). "Sensitivity of fluid flow to fault core architecture and petrophysical properties of fault rocks in siliciclastic reservoirs: a synthetic fault model study". In: *Petroleum Geoscience* 13.4, pp. 305–320. DOI: 10.1144/1354-079306-721.

FU, X., L. CUETO-FELGUEROSO, D. BOLSTER, and R. JUANES (2015). "Rock dissolution patterns and geochemical shutdown of CO_2-brine-carbonate reactions during convective mixing in porous media". In: *Journal of Fluid Mechanics* 764, pp. 296–315. DOI: 10.1017/jfm.2014.647.

GARABEDIAN, S. P., D. R. LEBLANC, L. W. GELHAR, and M. A. CELIA (1991). "Large-scale natural gradient tracer test in sand and gravel, Cape Cod, Massachusetts: 2. Analysis of spatial moments for a nonreactive tracer". In: *Water Resources Research* 27.5, pp. 911–924. DOI: 10.1029/91WR00242.

GARCIA, J. E. (2001). *Density of aqueous solutions of CO_2*. Technical report LBNL-49023. Berkeley, CA, USA: Lawrence Berkeley National Laboratory. DOI: 10.2172/790022.

GASDA, S., E. KEILEGAVLEN, T. H. SANDVE, R. BERGE, P. PETTERSSON, and S. KRUMSCHEID (2022). "Practical field-scale simulation approaches for quantification of fault-related leakage under uncertainty". In: *16th Greenhouse Gas Control Technologies Conference (GHGT-16), 23-24 Oct 2022*. IEA Greenhouse Gas R&D Programme (IEAGHG). DOI: 10.2139/ssrn.4277020.

GASDA, S. E., J. M. NORDBOTTEN, and M. A. CELIA (2011). "Vertically averaged approaches for CO_2 migration with solubility trapping". In: *Water Resources Research* 47.5, W05528. DOI: 10.1029/2010WR009075.

GAUCHER, D. and D. LINDLEY (1960). "Waterflood Performance in a Stratified, Five-Spot Reservoir-A Scaled-Model Study". In: *Transactions of the AIME* 219.01, pp. 208–215. DOI: 10.2118/1311-G.

GELHAR, L. W., C. WELTY, and K. R. REHFELDT (1992). "A critical review of data on field-scale dispersion in aquifers". In: *Water Resources Research* 28.7, pp. 1955–1974. DOI: 10.1029/92WR00607.

GHOMIAN, Y., G. A. POPE, and K. SEPEHRNOORI (2008). "Reservoir simulation of CO_2 sequestration pilot in Frio brine formation, USA Gulf Coast". In: *Energy* 33.7, pp. 1055–1067. DOI: 10.1016/j.energy.2008.02.011.

GIGER, S. B., M. B. CLENNELL, N. B. ÇIFTÇI, C. HARBERS, P. CLARK, and M. RICCHETTI (2013). "Fault transmissibility in clastic-argillaceous sequences controlled by clay smear evolution". In: *AAPG Bulletin* 97.5, pp. 705–731. DOI: 10.1306/10161211190.

GOSSELIN, O., S. AANONSEN, I. AAVATSMARK, A. COMINELLI, R. GONARD, M. KOLASINSKI, F. FERDINANDI, L. KOVACIC, and K. NEYLON (2003). "History matching using time-lapse seismic (HUTS)". In: *SPE Annual Technical Conference and Exhibition* SPE 84464. DOI: 10.2118/84464-MS. URL: https://doi.org/10.2118/84464-MS.

GRANT, N. T. (2017). "A geometrical model for shale smear: implications for upscaling in faulted geomodels". In: *Petroleum Geoscience* 23, pp. 39–55. DOI: 10.1144/petgeo2016-021.

GRANT, N. T. (2020). "Stochastic modelling of fault gouge zones: implications for fault seal analysis". In: *Integrated Fault Seal Analysis: Geological Society, London, Special Publications*. Ed. by S. R. OGILVIE, S. J. DEE, R. W. WILSON, and W. R. BAILEY. Vol. 496. Geological Society of London. DOI: 10.1144/SP496-2018-135.

HAGER, B. H., J. DIETERICH, C. FROHLICH, R. JUANES, S. MANTICA, J. H. SHAW, F. BOTTAZZI, F. CARESANI, D. CASTINEIRA, A. COMINELLI, M. MEDA, L. OSCULATI, S. PETROSELLI, and A. PLESCH (2021). "A process-based approach to understanding and managing triggered seismicity". In: *Nature* 595.7869, pp. 684–689. DOI: 10.1038/s41586-021-03668-z.

HASSANZADEH, H., M. POOLADI-DARVISH, A. M. ELSHARKAWY, D. W. KEITH, and Y. LEONENKO (2008). "Predicting PVT data for CO_2–brine mixtures for black-oil simulation of CO_2 geological storage". In: *International Journal of Greenhouse Gas Control* 2.1, pp. 65–77. DOI: 10.1016/S1750-5836(07)00010-2.

HASSANZADEH, H., M. POOLADI-DARVISH, and D. W. KEITH (2007). "Scaling behavior of convective mixing, with application to geological storage of CO_2". In: *AIChE Journal* 53.5, pp. 1121–1131. DOI: 10.1002/aic.11157.

HAUGEN, M., L. SALÓ-SALGADO, K. EIKEHAUG, B. BENALI, J. W. BOTH, E. STORVIK, O. FOLKVORD, R. JUANES, J. M. NORDBOTTEN, and M. FERNØ (2023). "Physical variability in meter-scale laboratory CO_2 injections in faulted geometries". In: *Transport in Porous Media*. preprint available on *arXiv* through https://doi.org/10.48550/arXiv.2301.07347.

HEATH, J. E., T. A. DEWERS, B. J. O. L. MCPHERSON, R. PETRUSAK, T. C. CHIDSEY JR, A. J. RINEHART, and P. S. MOZLEY (2011). "Pore networks in continental and marine mudstones: Characteristics and controls on sealing behavior". In: *Geosphere* 7.2, pp. 429–454. DOI: 10.1130/GES00619.1.

HEBACH, A., A. OBERHOF, and N. DAHMEN (2004). "Density of water + carbon dioxide at elevated pressures: measurements and correlation". In: *Journal of Chemical & Engineering Data* 49.4, pp. 950–953. DOI: 10.1021/je034260i.

HEINEMANN, Z., C. BRAND, M. MUNKA, and Y. CHEN (1991). "Modeling Reservoir Geometry With Irregular Grids". In: *SPE Reservoir Engineering* 6.2, pp. 225–232. DOI: 10.2118/18412-PA.

HESSE, M. and A. WOODS (2010). "Buoyant dispersal of CO_2 during geological storage". In: *Geophysical Research Letters* 37.1, p. L01403. DOI: 10.1029/2009GL041128.

HESSE, M. A., F. ORR JR, and H. TCHELEPI (2008). "Gravity currents with residual trapping". In: *Journal of Fluid Mechanics* 611, pp. 35–60. DOI: 10.1017/S002211200800219X.

HEYNEKAMP, M. R., L. B. GOODWIN, P. S. MOZLEY, and W. C. HANEBERG (1999). "Controls on fault-zone architecture in poorly lithified sediments, Rio Grande Rift, New Mexico: Implications for fault-zone permeability and fluid flow". In: *Faults and Subsurface Fluid Flow in the Shallow Crust*. Ed. by W. HANEBERG, P. MOZLEY, J. MOORE, and G. L.B. Vol. 113. American Geophysical Union, pp. 27–49. DOI: 10.1029/GM113p0027.

HIDALGO, J. J. and J. CARRERA (2009). "Effect of dispersion on the onset of convection during CO_2 sequestration". In: *Journal of Fluid Mechanics* 640, pp. 441–452. DOI: 10.1017/S0022112009991480.

HIDALGO, J. J., J. FE, L. CUETO-FELGUEROSO, and R. JUANES (2012). "Scaling of convective mixing in porous media". In: *Physical Review Letters* 109.26, p. 264503. DOI: 10.1103/PhysRevLett.109.264503.

HILDENBRAND, A., S. SCHLÖMER, B. KROOSS, and R. LITTKE (2004). "Gas breakthrough experiments on pelitic rocks: comparative study with N_2, CO_2 and CH_4". In: *Geofluids* 4.1, pp. 61–80. DOI: 10.1111/j.1468-8123.2004.00073.x.

HOLSTE, J., K. HALL, P. EUBANK, G. ESPER, M. WATSON, W. WAROWNY, D. BAILEY, J. YOUNG, and M. BELLOMY (1987). "Experimental (p, Vm, T) for pure CO_2 between 220 and 450

K". In: *The Journal of Chemical Thermodynamics* 19.12, pp. 1233–1250. DOI: 10.1016/0021-9614(87)90001-2.

HOMMEL, J., E. COLTMAN, and H. CLASS (2018). "Porosity–permeability relations for evolving pore space: a review with a focus on (bio-) geochemically altered porous media". In: *Transport in Porous Media* 124.2, pp. 589–629. DOI: 10.1007/s11242-018-1086-2.

IEA (2021). *Net Zero by 2050: A Roadmap for the Global Energy Sector*. Flagship report. 9, rue de la Fédération, Paris, France: International Energy Agency. URL: https://www.iea.org/reports/net-zero-by-2050.

IEAGHG (2016). *Fault Permeability*. Technical report 2016/13. Accessed on: August 25, 2023. Pure Offices, Cheltenham Office Park, Hatherley Lane, Cheltenham, GLOS, GL51 6SH, UK: IEA Greenhouse Gas R&D Programme. URL: https://ieaghg.org/publications/technical-reports.

IGLAUER, S., C. PENTLAND, and A. BUSCH (2015). "CO_2 wettability of seal and reservoir rocks and the implications for carbon geo-sequestration". In: *Water Resources Research* 51.1, pp. 729–774. DOI: doi.org/10.1002/2014WR015553.

INGRAM, G. M. and J. L. URAI (1999). "Top-seal leakage through faults and fractures: the role of mudrock properties". In: *Geological Society, London, Special Publications* 158, pp. 125–135. DOI: 10.1144/GSL.SP.1999.158.01.10.

IOANNIDIS, M. A., I. CHATZIS, and F. A. DULLIEN (1996). "Macroscopic percolation model of immiscible displacement: Effects of buoyancy and spatial structure". In: *Water Resources Research* 32.11, pp. 3297–3310. DOI: 10.1029/95WR02216.

IPCC (2005). *Special Report on Carbon Dioxide Capture and Storage*. Ed. by B. METZ, O. DAVIDSON, H. DE CONINCK, M. LOOS, and L. MEYER. The Edinburgh Building Shaftesbury Road, Cambridge CB2 2RU, UK: Cambridge University Press. URL: https://www.ipcc.ch/report/carbon-dioxide-capture-and-storage/.

IPCC (2022). "Climate Change 2022: Mitigation of Climate Change". In: *Contribution of Working Group III to the Sixth Assessment Report of the IPCC*. Ed. by P. R. SHUKLA, J. SKEA, R. SLADE, A. AL KHOURDAJIE, R. van DIEMEN, D. MCCOLLUM, M. PATHAK, S. SOME, P. VYAS, R. FRADERA, M. BELKACEMI, A. HASIJA, G. LISBOA, S. LUZ, and J. MALLEY. Cambridge University Press, Cambridge, UK and New York, NY, USA. DOI: 10.1017/9781009157926. URL: https://www.ipcc.ch/report/ar6/wg3/.

ISLAM, A. W. and E. S. CARLSON (2012). "Viscosity models and effects of dissolved CO_2". In: *Energy & fuels* 26.8, pp. 5330–5336. DOI: 10.1021/ef3006228.

ISLAM, M. S. and T. MANZOCCHI (2021). "A novel flow-based geometrical upscaling method for representing fault zones with two-phase fault rock properties into a dynamic reservoir model". In: *Scientific Reports* 11, p. 19511. DOI: 10.1038/s41598-021-99024-2.

JACKSON, S. J. and S. KREVOR (2020). "Small-scale capillary heterogeneity linked to rapid plume migration during CO_2 storage". In: *Geophysical Research Letters* 47.18, e2020GL088616. DOI: https://doi.org/10.1029/2020GL088616.

JADHUNANDAN, P. P. and N. R. MORROW (1995). "Effect of wettability on waterflood recovery for crude-oil/brine/rock systems". In: *SPE Reservoir Engineering* 10.01, pp. 40–46. DOI: 10.2118/22597-PA.

JAGALUR-MOHAN, J., B. JHA, Z. WANG, R. JUANES, and Y. MARZOUK (2018). "Inferring Fault Frictional and Reservoir Hydraulic Properties From Injection-Induced Seismicity". In: *Geophysical Research Letters* 45.3, pp. 1313–1320. DOI: 10.1002/2017GL075925.

JHA, B. and R. JUANES (2014). "Coupled multiphase flow and poromechanics: A computational model of pore pressure effects on fault slip and earthquake triggering". In: *Water Resources Research* 50.5, pp. 3776–3808. DOI: 10.1002/2013WR015175.

JIA, W., B. MCPHERSON, F. PAN, Z. DAI, N. MOODIE, and T. XIAO (2018). "Impact of three-phase relative permeability and hysteresis models on forecasts of storage associated with CO_2-EOR". In: *Water Resources Research* 54.2, pp. 1109–1126. DOI: 10.1002/2017WR021273.

JIN, L., H. LU, and G. WEN (2019). "Fast uncertainty quantification of reservoir simulation with variational U-Net". In: *arXiv:1907.00718*. DOI: 10.48550/arXiv.1907.00718.

JOLLEY, S. J., H. DIJK, J. LAMENS, Q. J. FISHER, T. MANZOCCHI, H. EIKMANS, and Y. HUANG (2007). "Faulting and fault sealing in production simulation models: Brent Province, northern North Sea". In: *Petroleum Geoscience* 13.4, pp. 321–340. DOI: 10.1144/1354-079306-733.

JONK, R., K. M. BOHACS, and J. S. DAVIS (2022). "Evaluating Top Seals within a Sequence-Stratigraphic Framework: Impact on Geological Carbon Sequestration". In: *Marine and Petroleum Geology* 146, p. 105920. DOI: 10.1016/j.marpetgeo.2022.105920.

JU, X., F. P. HAMON, G. WEN, R. KANFAR, M. ARAYA-POLO, and H. A. TCHELEPI (2019). "Learning CO_2 plume migration in faulted reservoirs with Graph Neural Networks". In: *arXiv:2306.09648*. DOI: 10.48550/arXiv.2306.09648.

JUANES, R., B. H. HAGER, and H. J. HERZOG (2012). "No geologic evidence that seismicity causes fault leakage that would render large-scale carbon capture and storage unsuccessful". In: *Proceedings of the National Academy of Sciences* 109.52, E3623–E3623. DOI: 10.1073/pnas.1215026109.

JUANES, R., J. SAMPER, and J. MOLINERO (2002). "A general and efficient formulation of fractures and boundary conditions in the finite element method". In: *International Journal for Numerical Methods in Engineering* 54.12, pp. 1751–1774. DOI: 10.1002/nme.491.

JUANES, R., E. SPITERI, F. ORR JR, and M. BLUNT (2006). "Impact of relative permeability hysteresis on geological CO_2 storage". In: *Water Resources Research* 42.12, W12418. DOI: 10.1029/2005WR004806.

JUNG, N.-H., W. S. HAN, Z. WATSON, J. P. GRAHAM, and K.-Y. KIM (2014). "Fault-controlled CO_2 leakage from natural reservoirs in the Colorado Plateau, East-Central Utah". In: *Earth and Planetary Science Letters* 403, pp. 358–367. DOI: 10.1016/j.epsl.2014.07.012.

KAM, P., M. NADEEM, A. NOVLESKY, A. KUMAR, and E. N. OMATSONE (2015). "Reservoir characterization and history matching of the Horn River shale: an integrated geoscience and reservoir-simulation approach". In: *Journal of Canadian Petroleum Technology* 54.06, pp. 475–488. DOI: 10.2118/171611-PA.

KARIMI-FARD, M., L. J. DURLOFSKY, and K. AZIZ (2004). "An efficient discrete-fracture model applicable for general-purpose reservoir simulators". In: *SPE Journal* 9.02, pp. 227–236. DOI: 10.2118/88812-PA.

KEILEGAVLEN, E., R. BERGE, A. FUMAGALLI, M. STARNONI, I. STEFANSSON, J. VARELA, and I. BERRE (2021). "PorePy: An open-source software for simulation of multiphysics processes in fractured porous media". In: *Computational Geosciences* 25, pp. 243–265. DOI: 10.1007/s10596-020-10002-5.

KETTERMANN, M., S. THRONBERENS, O. JUAREZ, J. L. URAI, M. ZIEGLER, S. ASMUS, and U. KRÜGER (2016). "Mechanisms of clay smear formation in unconsolidated sediments—insights from 3-D observations of excavated normal faults". In: *Solid Earth* 7, pp. 789–815. DOI: 10.5194/se-7-789-2016.

KETTERMANN, M., J. L. URAI, and P. J. VROLIJK (2017). "Evolution of structure and permeability of normal faults with clay smear: Insights from water-saturated sandbox models and numerical simulations". In: *Journal of Geophysical Research: Solid Earth* 122.3, pp. 1697–1725. DOI: 10.1002/2016JB013341.

KILLOUGH, J. E. (1976). "Reservoir simulation with history-dependent saturation functions". In: *SPE Journal* 16.01, pp. 37–48. DOI: 10.2118/5106-PA.

KING, M., A. MUBARAK, J. KIM, and T. BOTT (1992). "The mutual solubilities of water with supercritical and liquid carbon dioxides". In: *The Journal of Supercritical Fluids* 5.4, pp. 296–302. DOI: 10.1016/0896-8446(92)90021-B.

KLIMECK, J., R. KLEINRAHM, and W. WAGNER (2001). "Measurements of the (p, ρ, T) relation of methane and carbon dioxide in the temperature range 240 K to 520 K at pressures up to 30 MPa using a new accurate single-sinker densimeter". In: *The Journal of Chemical Thermodynamics* 33.3, pp. 251–267. DOI: 10.1006/jcht.2000.0711.

KNEAFSEY, T. J. and K. PRUESS (2010). "Laboratory flow experiments for visualizing carbon dioxide-induced, density-driven brine convection". In: *Transport in Porous Media* 82, pp. 123–139. DOI: 10.1007/s11242-009-9482-2.

KOVSCEK, A. R., J. M. NORDBOTTEN, and M. A. FERNO (2023). "Scaling up FluidFlower results for carbon dioxide storage in geological media". In: *Transport in Porous Media*. preprint available on *arXiv* through https://doi.org/10.48550/arXiv.2301.09853.

KRAEMER, T. F. and D. F. REID (1984). "The occurrence and behavior of radium in saline formation water of the US Gulf Coast region". In: *Chemical Geology* 46.2, pp. 153–174. DOI: 10.1016/0009-2541(84)90186-4.

KRAUSE, M. H. and S. M. BENSON (2015). "Accurate determination of characteristic relative permeability curves". In: *Advances in Water Resources* 83, pp. 376–388. DOI: 10.1016/j.advwatres.2015.07.009.

KREVOR, S., M. J. BLUNT, S. M. BENSON, C. H. PENTLAND, C. REYNOLDS, A. AL-MENHALI, and B. NIU (2015). "Capillary trapping for geologic carbon dioxide storage–From pore scale physics to field scale implications". In: *International Journal of Greenhouse Gas Control* 40, pp. 221–237. DOI: 10.1016/j.ijggc.2015.04.006.

KREVOR, S., H. de CONINCK, S. E. GASDA, N. S. GHALEIGH, V. de GOOYERT, H. HAJIBEYGI, R. JUANES, J. NEUFELD, J. J. ROBERTS, and F. SWENNENHUIS (2023). "Subsurface carbon dioxide and hydrogen storage for a sustainable energy future". In: *Nature Reviews Earth & Environment*, pp. 1–17. DOI: 10.1038/s43017-022-00376-8.

KREVOR, S., R. PINI, L. ZUO, and S. M. BENSON (2012). "Relative permeability and trapping of CO_2 and water in sandstone rocks at reservoir conditions". In: *Water Resources Research* 48.2. DOI: 10.1029/2011WR010859.

KRISHNAMURTHY, P. G., D. DICARLO, and T. MECKEL (2022). "Geologic Heterogeneity Controls on Trapping and Migration of CO_2". In: *Geophysical Research Letters* 49.16, e2022GL099104. DOI: 10.1029/2022GL099104.

KRISHNAMURTHY, P. G., T. A. MECKEL, and D. DICARLO (2019). "Mimicking geologic depositional fabrics for multiphase flow experiments". In: *Water Resources Research* 55.11, pp. 9623–9638. DOI: 10.1029/2019WR025664.

KROGSTAD, S., K.-A. LIE, O. MØYNER, H. M. NILSEN, X. RAYNAUD, and B. SKAFLESTAD (2015). "MRST-AD – an Open-Source Framework for Rapid Prototyping and Evaluation of Reservoir Simulation Problems". In: *SPE Reservoir Simulation Conference*, pp. 1–20. DOI: SPE-173317-MS. URL: https://doi.org/SPE-173317-MS.

LAND, C. S. (1968). "Calculation of imbibition relative permeability for two-and three-phase flow from rock properties". In: *Society of Petroleum Engineers Journal* 8.02, pp. 149–156. DOI: 10.2118/1942-PA.

LANDA-MARBÁN, D., T. H. SANDVE, J. W. BOTH, J. M. NORDBOTTEN, and S. E. GASDA (2023). *Performance of an open-source image-based history matching framework for CO_2 storage*. Forhtcoming.

LANDA-MARBÁN, D., S. TVEIT, K. KUMAR, and S. E. GASDA (2021). "Practical approaches to study microbially induced calcite precipitation at the field scale". In: *International Journal of Greenhouse Gas Control* 106, p. 103256. DOI: 10.1016/j.ijggc.2021.103256.

LASSEN, R. N., M. R. PLAMPIN, T. SAKAKI, T. H. ILLANGASEKARE, J. GUDBJERG, T. O. SONNENBORG, and K. H. JENSEN (2015). "Effects of geologic heterogeneity on migration of gaseous CO_2 using laboratory and modeling investigations". In: *International Journal of Greenhouse Gas Control* 43, pp. 213–224. DOI: 10.1016/j.ijggc.2015.10.015.

LEHNER, F. and W. PILAAR (1997). "The emplacement of clay smears in synsedimentary normal faults: inferences from field observations near Frechen, Germany". In: *Norwegian Petroleum Society Special Publications*. Ed. by P. MØLLER-PEDERSEN and A. KOESTLER. Vol. 7. Elsevier, pp. 39–50. DOI: 10.1016/S0928-8937(97)80005-7.

LENHARD, R. J. and J. C. PARKER (1987). "A model for hysteretic constitutive relations governing multiphase flow: 2. Permeability-saturation relations". In: *Water Resources Research* 23.12, pp. 2197–2206. DOI: 10.1029/WR023i012p02197.

LENHARD, R., M. OOSTROM, C. SIMMONS, and M. WHITE (1995). "Investigation of density-dependent gas advection of trichloroethylene: Experiment and a model validation exercise". In: *Journal of Contaminant Hydrology* 19.1, pp. 47–67. DOI: 10.1016/0169-7722(94)00055-M.

LEVERETT, M. C. (1941). "Capillary behavior in porous solids". In: *Transactions of the AIME* 142.01, pp. 152–169. DOI: 10.2118/941152-G.

LI, B. and S. M. BENSON (2015). "Influence of small-scale heterogeneity on upward CO_2 plume migration in storage aquifers". In: *Advances in Water Resources* 83, pp. 389–404. DOI: 10.1016/j.advwatres.2015.07.010.

LIANG, Y., B. WEN, M. A. HESSE, and D. DICARLO (2018). "Effect of dispersion on solutal convection in porous media". In: *Geophysical Research Letters* 45.18, pp. 9690–9698. DOI: 10.1029/2018GL079849.

LIE, K.-A. (2019). *An Introduction to Reservoir Simulation Using MATLAB/GNU Octave: User Guide for the MATLAB Reservoir Simulation Toolbox (MRST)*. University Printing House, Cambridge CB2 8BS, UK: Cambridge University Press. ISBN: 9781108492430. DOI: 10.1017/9781108591416.

LIE, K.-A., S. KROGSTAD, I. S. LIGAARDEN, J. R. NATVIG, H. M. NILSEN, and B. SKAFLESTAD (2012). "Open-source MATLAB implementation of consistent discretisations on complex grids". In: *Computational Geosciences* 16, pp. 297–322. DOI: 10.1007/s10596-011-9244-4.

LIE, K.-A. and O. MØYNER, eds. (2021). *Advanced Modeling with the MATLAB Reservoir Simulation Toolbox*. University Printing House, Cambridge CB2 8BS, UK: Cambridge University Press. DOI: 10.1017/9781009019781.

LIE, K.-A., H. M. NILSEN, O. ANDERSEN, and O. MØYNER (2016). "A simulation workflow for large-scale CO_2 storage in the Norwegian North Sea". In: *Computational Geosciences* 20, pp. 607–622. DOI: 10.1007/s10596-015-9487-6.

LIN, L. I.-K. (1989). "A concordance correlation coefficient to evaluate reproducibility". In: *Biometrics* 45.1, pp. 255–268. DOI: 10.2307/2532051.

LINDSAY, N., F. MURPHY, J. J. WALSH, J. WATTERSON, S. FLINT, and I. BRYANT (1993). "Outcrop studies of shale smears on fault surfaces". In: *The Geological Modelling of Hydrocarbon Reservoirs and Outcrop Analogues*. Ed. by S. FLINT and I. BRYANT. Vol. 15. International Association of Sedimentology, pp. 113–123. DOI: 10.1002/9781444303957.ch6.

LIU, Y. and L. J. DURLOFSKY (2020). "Multilevel strategies and geological parameterizations for history matching complex reservoir models". In: *SPE Journal* 25.01, pp. 081–104. DOI: 10.2118/193895-PA.

LOVELESS, S., V. F. BENSE, and J. TURNER (2011). "Fault architecture and deformation processes within poorly lithified rift sediments, Central Greece". In: *Journal of Structural Geology* 33.11, pp. 1554–1568. DOI: 10.1016/j.jsg.2011.09.008.

LU, H., L. SALÓ-SALGADO, R. JUANES, and Y. MARZOUK (2023). "Uncertainty Quantification of CO_2 Leakage and Risk Analysis of Induced Seismicity for Large-scale Geological CO_2 Sequestration". In: *ASCE Engineering Mechanics Institute 2023 Conference, Atlanta, GA, June 6–9*. Engineering Mechanics Institute and Georgia Institute of Technology. URL: https://www.emi-conference.org/.

LU, J., D. L. CARR, R. H. TREVIÑO, J.-L. T. RHATIGAN, and R. FIFARIZ (2017). "Evaluation of Lower Miocene Confining Units for CO_2 Storage, Offshore Texas State Waters, Northern Gulf of Mexico, USA". In: *Geological CO_2 Sequestration Atlas of Miocene Strata, Offshore Texas State Waters*. Ed. by R. H. TREVIÑO and T. A. MECKEL. Austin, TX: Bureau of Economic Geology, The University of Texas at Austin. Chap. 3, pp. 14–25. DOI: 10.23867/RI0283D.

LUNN, R. J., Z. K. SHIPTON, and A. M. BRIGHT (2008). "How can we improve estimates of bulk fault zone hydraulic properties?" In: *Geological Society, London, Special Publications* 299.1, pp. 231–237. DOI: 10.1144/SP299.14.

MACMINN, C. W. and R. JUANES (2013). "Buoyant currents arrested by convective dissolution". In: *Geophysical Research Letters* 40.10, pp. 2017–2022. DOI: 10.1002/grl.50473.

MACMINN, C. W., M. L. SZULCZEWSKI, and R. JUANES (2010). "CO_2 migration in saline aquifers. Part 1. Capillary trapping under slope and groundwater flow". In: *Journal of Fluid Mechanics* 662, pp. 329–351. DOI: 10.1017/S0022112010003319.

MACMINN, C. W., M. L. SZULCZEWSKI, and R. JUANES (2011). "CO_2 migration in saline aquifers. Part 2. Capillary and solubility trapping". In: *Journal of Fluid Mechanics* 688, pp. 321–351. DOI: 10.1017/jfm.2011.379.

MANZOCCHI, T., A. E. HEATH, B. PALANANTHAKUMAR, C. CHILDS, and J. J. WALSH (2008). "Faults in conventional flow simulation models: a consideration of representational assumptions and geological uncertainties". In: *Petroleum Geoscience* 14.1, pp. 91–110. DOI: 10.1144/1354-079306-775.

MANZOCCHI, T., J. J. WALSH, P. NELL, and G. YIELDING (1999). "Fault transmissibility multipliers for flow simulation models". In: *Petroleum Geoscience* 5.1, pp. 53–63. DOI: 10.1144/petgeo.5.1.53.

MARCUCCI, A., S. KYPREOS, and E. PANOS (2017). "The road to achieving the long-term Paris targets: energy transition and the role of direct air capture". In: *Climatic Change* 144.2, pp. 181–193. DOI: 10.1007/s10584-017-2051-8.

MECKEL, T. A., J. A. NICHOLSON, and R. H. TREVIÑO (2017). "Capillary Aspects of Fault-Seal Capacity for CO_2 Storage, Lower Miocene, Texas Gulf of Mexico". In: *Geological CO_2 Sequestration Atlas of Miocene Strata, Offshore Texas State Waters*. Ed. by R. H. TREVIÑO and T. A. MECKEL. Austin, TX: Bureau of Economic Geology, The University of Texas at Austin. Chap. 4, pp. 26–36. DOI: 10.23867/RI0283D.

MECKEL, T. A. and J. T. RHATIGAN (2017). "Implications of Miocene Petroleum Systems for Geologic CO_2 Storage beneath Texas Offshore Lands". In: *Geological CO_2 Sequestration Atlas of Miocene Strata, Offshore Texas State Waters*. Ed. by R. H. TREVIÑO and T. A. MECKEL. Austin, TX: Bureau of Economic Geology, The University of Texas at Austin. Chap. 2, pp. 7–13. DOI: 10.23867/RI0283D.

MEGUERDIJIAN, S. and B. JHA (2021). "Quantification of fault leakage dynamics based on leakage magnitude and dip angle". In: *International Journal for Numerical and Analytical Methods in Geomechanics* 45.16, pp. 2303–2320. DOI: 10.1002/nag.3267.

MEGUERDIJIAN, S., R. J. PAWAR, D. R. HARP, and B. JHA (2022). "Thermal and solubility effects on fault leakage during geologic carbon storage". In: *International Journal of Greenhouse Gas Control* 116, p. 103633. DOI: 10.1016/j.ijggc.2022.103633.

MERRELL, M. P., P. B. FLEMINGS, and G. L. BOWERS (2014). "Subsalt pressure prediction in the Miocene Mad Dog field, Gulf of Mexico". In: *AAPG bulletin* 98.2, pp. 315–340. DOI: 10.1306/06251312156.

MESRI, G. and A. CEPEDA-DIAZ (1986). "Residual shear strength of clays and shales". In: *Géotechnique* 36.2, pp. 269–274. DOI: 10.1680/geot.1986.36.2.269.

MILLS, R. T., C. LU, P. C. LICHTNER, and G. E. HAMMOND (2007). "Simulating subsurface flow and transport on ultrascale computers using PFLOTRAN". In: *Journal of Physics: Conference Series*. Vol. 78. 1. IOP Publishing, p. 012051.

MORROW, N. R., P. J. CRAM, and F. MCCAFFERY (1973). "Displacement studies in dolomite with wettability control by octanoic acid". In: *SPE Journal* 13.04, pp. 221–232. DOI: 10.2118/3993-PA.

MØYNER, O. (2021). "Compositional simulation with the AD-OO framework". In: *Advanced Modeling with the MATLAB Reservoir Simulation Toolbox (MRST)*. Ed. by K.-A. LIE and O. MØYNER. University Printing House, Cambridge CB2 8BS, UK: Cambridge University Press, pp. 324–374. DOI: 10.1017/9781009019781.

MØYNER, O. and H. M. NILSEN (2019). "Multiresolution coupled vertical equilibrium model for fast flexible simulation of CO_2 storage". In: *Computational Geosciences* 23.1, pp. 1–20. DOI: 10.1007/s10596-018-9775-z.

MUNKEJORD, S. T., M. HAMMER, and S. W. LØVSETH (2016). "CO_2 transport: Data and models–A review". In: *Applied Energy* 169, pp. 499–523. DOI: 10.1016/j.apenergy.2016.01.100.

MUSKAT, M. (1949). *Physical Principles of Oil Production*. New York City, New York, USA: McGraw-Hill Book Co.

MYERS, R. D., A. ALLGOOD, A. HJELLBAKK, P. VROLIJK, and N. BRIEDIS (2007). "Testing fault transmissibility predictions in a structurally dominated reservoir: Ringhorne Field, Norway". In: *Geological Society, London, Special Publications* 292.1, pp. 271–294. DOI: 10.1144/SP292.16.

MYERS, R. D., P. J. VROLIJK, C. W. KIVEN, and M. TSENN (2014). "Method for predicting fluid flow". Utility Patent US8793110B2. Accessed on: August 25, 2023. URL: https://patents.google.com/patent/US8793110B2.

NAAR, J., R. WYGAL, and J. HENDERSON (1962). "Imbibition relative permeability in unconsolidated porous media". In: *SPE Journal* 2.01, pp. 13–17. DOI: 10.2118/213-PA.

NELSEN, R. B. (2006). *An Introduction to Copulas*. New York, NY, USA: Springer Science & Business Media. DOI: https://doi.org/10.1007/0-387-28678-0.

NEUFELD, J. A., M. A. HESSE, A. RIAZ, M. A. HALLWORTH, H. A. TCHELEPI, and H. E. HUPPERT (2010). "Convective dissolution of carbon dioxide in saline aquifers". In: *Geophysical Research Letters* 37.22, p. L22404. DOI: 10.1029/2010GL044728.

NEWELL, P. and M. J. MARTINEZ (2020). "Numerical assessment of fault impact on caprock seals during CO_2 sequestration". In: *International Journal of Greenhouse Gas Control* 94, p. 102890. DOI: 10.1016/j.ijggc.2019.102890.

NI, H., S. BAKHSHIAN, and T. MECKEL (2023). "Effects of grain size and small-scale bedform architecture on CO_2 saturation from buoyancy-driven flow". In: *Scientific Reports* 13, p. 2474. DOI: 10.1038/s41598-023-29360-y.

NICHOLSON, A. J. (2012). "Empirical analysis of fault seal capacity for CO_2 sequestration, Lower Miocene, Texas Gulf Coast". MA thesis. The University of Texas at Austin. URL: https://repositories.lib.utexas.edu/handle/2152/ETD-UT-2012-05-5606.

NILSEN, H. M., K.-A. LIE, and O. ANDERSEN (2016). "Robust simulation of sharp-interface models for fast estimation of CO_2 trapping capacity in large-scale aquifer systems". In: *Computational Geosciences* 20, pp. 93–113. DOI: 10.1007/s10596-015-9549-9.

NILSEN, H. M., K.-A. LIE, O. MØYNER, and O. ANDERSEN (2015). "Spill-point analysis and structural trapping capacity in saline aquifers using MRST-co2lab". In: *Computers & Geosciences* 75, pp. 33–43. DOI: 10.1016/j.cageo.2014.11.002.

NOORSALEHI-GARAKANI, S., G. K. VENNEKATE, P. VROLIJK, and J. URAI (2013). "Clay-smear continuity and normal fault zone geometry–first results from excavated sandbox models". In: *Journal of Structural Geology* 57, pp. 58–80. DOI: 10.1016/j.jsg.2013.09.008.

NORDBOTTEN, J. M., B. FLEMISCH, S. E. GASDA, H. NILSEN, Y. FAN, G. E. PICKUP, B. WIESE, M. A. CELIA, H. K. DAHLE, G. T. EIGESTAD, and K. PRUESS (2012). "Uncertainties in practical simulation of CO_2 storage". In: *International Journal of Greenhouse Gas Control* 9, pp. 234–242. DOI: 10.1016/j.ijggc.2012.03.007.

NORDBOTTEN, J. M., M. FERNØ, B. FLEMISCH, R. JUANES, and M. JØRGENSEN (2022). *Final Benchmark Description: FluidFlower International Benchmark Study*. DOI: 10.5281/zenodo.6807102. URL: https://doi.org/10.5281/zenodo.6807102.

NORDBOTTEN, J. M., B. BENALI, J. W. BOTH, B. BRATTEKÅS, E. STORVIK, and M. FERNØ (2023). "DarSIA: An open-source Python toolbox for two-scale image processing of dynamics in porous media". In: *Transport in Porous Media*. DOI: 10.1007/s11242-023-02000-9.

NORDBOTTEN, J. M. and M. A. CELIA (2012). *Geological Storage of CO_2: Modeling Approaches for Large-scale Simulation*. Hoboken, NJ, USA: John Wiley and Sons. ISBN: 978-0-470-88946-6. URL: https://www.wiley.com/en-sg/Geological+Storage+of+CO2:+Modeling+Approaches+for+Large+Scale+Simulation-p-9780470889466.

OLDENBURG, C. M. (2018). "Are we all in concordance with the meaning of the word conformance, and is our definition in conformity with standard definitions?" In: *Greenhouse Gases: Science and Technology* 8.2, pp. 210–214. DOI: 10.1002/ghg.1773.

OLIVER, D. S. and Y. CHEN (2011). "Recent progress on reservoir history matching: a review". In: *Computational Geosciences* 15.1, pp. 185–221. DOI: 10.1007/s10596-010-9194-2.

PANARETOS, V. M. and Y. ZEMEL (2019). "Statistical aspects of Wasserstein distances". In: *Annual Review of Statistics and Its Application* 6, pp. 405–431.

PAWAR, R. J., G. S. BROMHAL, S. CHU, R. M. DILMORE, C. M. OLDENBURG, P. H. STAUFFER, Y. ZHANG, and G. D. GUTHRIE (2016). "The National Risk Assessment Partnership's integrated assessment model for carbon storage: A tool to support decision making amidst uncertainty". In: *International Journal of Greenhouse Gas Control* 52, pp. 175–189. DOI: 10.1016/j.ijggc.2016.06.015.

PEACOCK, D. C. and D. SANDERSON (1992). "Effects of layering and anisotropy on fault geometry". In: *Journal of the Geological Society* 149.5, pp. 793–802. DOI: 10.1144/gsjgs.149.5.0793.

PENSADO, A. S., A. A. PADUA, M. J. COMUÑAS, and J. FERNANDEZ (2008). "Viscosity and density measurements for carbon dioxide+ pentaerythritol ester lubricant mixtures at low lubricant concentration". In: *The Journal of Supercritical Fluids* 44.2, pp. 172–185. DOI: 10.1016/j.supflu.2007.10.004.

PENTLAND, C. H., E. ITSEKIRI, S. K. AL MANSOORI, S. IGLAUER, B. BIJELJIC, and M. J. BLUNT (2010). "Measurement of nonwetting-phase trapping in sandpacks". In: *SPE Journal* 15.02, pp. 274–281. DOI: 10.2118/115697-PA.

PENTLAND, C. H., R. EL-MAGHRABY, S. IGLAUER, and M. J. BLUNT (2011). "Measurements of the capillary trapping of super-critical carbon dioxide in Berea sandstone". In: *Geophysical Research Letters* 38.6, p. L06401. DOI: 10.1029/2011GL046683.

PERSON, M., J. P. RAFFENSPERGER, S. GE, and G. GARVEN (1996). "Basin-scale hydrogeologic modeling". In: *Reviews of Geophysics* 34.1, pp. 61–87. DOI: 10.1029/95RG03286.

PLUG, W.-J. and J. BRUINING (2007). "Capillary pressure for the sand–CO_2–water system under various pressure conditions. Application to CO_2 sequestration". In: *Advances in Water Resources* 30.11, pp. 2339–2353. DOI: 10.1016/j.advwatres.2007.05.010.

PYRCZ, M. J. and C. V. DEUTSCH (2014). *Geostatistical Reservoir Modeling*. 198 Madison Avenue, New York, NY 10016, USA: Oxford University Press. ISBN: 9780199731442. URL: https://global.oup.com/academic/product/geostatistical-reservoir-modeling-9780199731442?cc=us&lang=en&.

QIU, Y., K. XU, A. A. PAHLAVAN, and R. JUANES (2023). "Wetting transition and fluid trapping in a microfluidic fracture". In: *Proceedings of the National Academy of Sciences* 120.22, e2303515120. DOI: 10.1073/pnas.2303515120.

RANAEE, E., F. INZOLI, M. RIVA, and A. GUADAGNINI (2019). "Hysteresis effects of three-phase relative permeabilities on black-oil reservoir simulation under WAG injection protocols". In: *Journal of Petroleum Science and Engineering* 176, pp. 1161–1174. DOI: 10.1016/j.petrol.2019.01.044.

RASMUSSEN, A. F., T. H. SANDVE, K. BAO, A. LAUSER, J. HOVE, B. SKAFLESTAD, R. KLÖFKORN, M. BLATT, A. B. RUSTAD, O. SÆVAREID, K.-A. LIE, and A. THUNE (2021). "The open porous media flow reservoir simulator". In: *Computers & Mathematics with Applications* 81, pp. 159–185. DOI: 10.1016/j.camwa.2020.05.014.

AL-RAWAJFEH, A. E. (2004). "Modelling and simulation of CO_2 release in multiple effect distillers for seawater desalination". PhD thesis. Martin Luther University Halle-Wittenberg. DOI: 10.25673/3764.

RAWLING, G. C. and L. B. GOODWIN (2006). "Structural record of the mechanical evolution of mixed zones in faulted poorly lithified sediments, Rio Grande rift, New Mexico, USA". In: *Journal of Structural Geology* 28.9, pp. 1623–1639. DOI: 10.1016/j.jsg.2006.06.008.

RAWLING, G. C., L. B. GOODWIN, and J. L. WILSON (2001). "Internal architecture, permeability structure, and hydrologic significance of contrasting fault-zone types". In: *Geology* 29.1, pp. 43–46. DOI: 10.1130/0091-7613(2001)029<0043:IAPSAH>2.0.CO;2.

REDLICH, O. and J. N. KWONG (1949). "On the thermodynamics of solutions. V. An equation of state. Fugacities of gaseous solutions." In: *Chemical Reviews* 44.1, pp. 233–244. DOI: 10.1021/cr60137a013.

REVIL, A., D. GRAULS, and O. BRÉVART (2002). "Mechanical compaction of sand/clay mixtures". In: *Journal of Geophysical Research: Solid Earth* 107.B11, ECV11-1–ECV11-15. DOI: 10.1029/2001JB000318.

REVIL, A. and L. M. CATHLES III (2002). "Fluid transport by solitary waves along growing faults: A field example from the South Eugene Island Basin, Gulf of Mexico". In: *Earth and Planetary Science Letters* 202.2, pp. 321–335. DOI: 10.1016/S0012-821X(02)00784-7.

REYNOLDS, C. and S. KREVOR (2015). "Characterizing flow behavior for gas injection: Relative permeability of CO_2-brine and N_2-water in heterogeneous rocks". In: *Water Resources Research* 51.12, pp. 9464–9489. DOI: 10.1002/2015WR018046.

REZK, M. G., J. FOROOZESH, A. ABDULRAHMAN, and J. GHOLINEZHAD (2022). "CO_2 Diffusion and Dispersion in Porous Media: Review of Advances in Experimental Measurements and Mathematical Models". In: *Energy & Fuels* 36.1, pp. 133–155. DOI: 10.1021/acs.energyfuels.1c03552.

RIAZ, A., M. HESSE, H. TCHELEPI, and F. ORR (2006). "Onset of convection in a gravitationally unstable diffusive boundary layer in porous media". In: *Journal of Fluid Mechanics* 548, pp. 87–111. DOI: 10.1017/S0022112005007494.

RIAZ, A., C. PANKIEWITZ, and E. MEIBURG (2004). "Linear stability of radial displacements in porous media: influence of velocity-induced dispersion and concentration-dependent diffusion". In: *Physics of Fluids* 16.10, pp. 3592–3598. DOI: 10.1063/1.1775431.

RICE, J. R. (1992). "Fault stress states, pore pressure distributions, and the weakness of the San Andreas Fault". In: *International Geophysics*. Vol. 51. Elsevier, pp. 475–503. DOI: 10.1016/S0074-6142(08)62835-1.

RINALDI, A. P., P. JEANNE, J. RUTQVIST, F. CAPPA, and Y. GUGLIELMI (2014). "Effects of fault-zone architecture on earthquake magnitude and gas leakage related to CO_2 injection in a multi-layered sedimentary system". In: *Greenhouse Gases: Science and Technology* 4.1, pp. 99–120. DOI: 10.1002/ghg.1403.

RINGROSE, P. S. and T. A. MECKEL (2019). "Maturing global CO_2 storage resources on offshore continental margins to achieve 2DS emissions reductions". In: *Scientific Reports* 9.1, pp. 1–10. DOI: 10.1038/s41598-019-54363-z.

ROWE, A. M. and J. C. CHOU (1970). "Pressure-volume-temperature-concentration relation of aqueous sodium chloride solutions". In: *Journal of Chemical and Engineering Data* 15.1, pp. 61–66. DOI: 10.1021/je60044a016.

SAADATPOOR, E., S. L. BRYANT, and K. SEPEHRNOORI (2010). "New trapping mechanism in carbon sequestration". In: *Transport in Porous Media* 82.1, pp. 3–17. DOI: 10.1007/s11242-009-9446-6.

SALÓ-SALGADO, L., J. S. DAVIS, and R. JUANES (2023a). "Fault permeability from stochastic modeling of clay smears". In: *Geology* 51.1, pp. 91–95. DOI: 10.1130/G50739.1.

SALÓ-SALGADO, L., M. HAUGEN, K. EIKEHAUG, M. FERNØ, J. M. NORDBOTTEN, and R. JUANES (2023b). "Direct Comparison of Numerical Simulations and Experiments of CO_2 Injection and Migration in Geologic Media: Value of Local Data and Forecasting Capability". In: *Transport in Porous Media*. DOI: 10.1007/s11242-023-01972-y.

SALÓ-SALGADO, L., O. MØYNER, K.-A. LIE, and R. JUANES (2023c). *Three-dimensional simulation of geologic carbon dioxide sequestration using MRST*. In preparation.

SALÓ-SALGADO, L., J. A. SILVA, L. LUN, J. S. DAVIS, and R. JUANES (2023d). *Updip migration of sequestered CO_2 along Gulf Coast Miocene growth faults is unlikely*. In preparation.

SANTOSO, R. K., X. HE, M. ALSINAN, H. KWAK, and H. HOTEIT (2021). "Bayesian long-short term memory for history matching in reservoir simulations". In: *SPE Reservoir Simulation Conference* SPE-203976-MS. DOI: 10.2118/203976-MS.

SCHULZ, R., N. RAY, S. ZECH, A. RUPP, and P. KNABNER (2019). "Beyond Kozeny–Carman: predicting the permeability in porous media". In: *Transport in Porous Media* 130.2, pp. 487–512. DOI: 10.1007/s11242-019-01321-y.

SCHULZE-MAKUCH, D. (2005). "Longitudinal dispersivity data and implications for scaling behavior". In: *Groundwater* 43.3, pp. 443–456. DOI: 10.1111/j.1745-6584.2005.0051.x.

SCIBEK, J. (2020). "Multidisciplinary database of permeability of fault zones and surrounding protolith rocks at world-wide sites". In: *Scientific Data* 7.1, pp. 1–14. DOI: 10.1038/s41597-020-0435-5.

SILLIMAN, S. and E. SIMPSON (1987). "Laboratory evidence of the scale effect in dispersion of solutes in porous media". In: *Water Resources Research* 23.8, pp. 1667–1673. DOI: 10.1029/WR023i008p01667.

SILVA, J. A., H. BYRNE, A. PLESCH, J. H. SHAW, and R. JUANES (2021a). "Revisiting the Classical Experiment in Earthquake Control at the Rangely Oil Field, Colorado, 1970, Using a Coupled Flow and Geomechanical Model". In: *Bulletin of the Seismological Society of America* 111.6, pp. 3136–3159. DOI: 10.1785/0120210020.

SILVA, J. A., M. ROKROK, H. YOON, M. FEHLER, S. FRAILEY, and R. JUANES (2021b). "Mechanisms for microseismicity occurrence due to CO_2 injection at Decatur, Illinois: A coupled multiphase flow and geomechanics perspective". In: *American Geophysical Union Fall Meeting 2021*. Vol. 2021. American Geophysical Union, T22C–02. URL: https://ui.adsabs.harvard.edu/abs/2021AGUFM.T22C..02A/abstract.

SILVA, J. A., L. SALÓ-SALGADO, J. PATTERSON, G. R. DASARI, and R. JUANES (2023). "Assessing the viability of CO_2 storage in offshore formations of the Gulf of Mexico at a scale relevant for climate-change mitigation". In: *International Journal of Greenhouse Gas Control* 126, p. 103884. DOI: 10.1016/j.ijggc.2023.103884.

SKEMPTON, A. W. (1964). "Long-term stability of clay slopes". In: *Géotechnique* 14.2, pp. 77–102. DOI: 0.1680/geot.1964.14.2.77.

SLB (2014a). *ECLIPSE Reference Manual*. 2014.1. Manual for the ECLIPSE reservoir simulator. Schlumberger Ltd., Houston, TX, USA.

SLB (2014b). *ECLIPSE Technical description*. 2014.1. Technical description for the ECLIPSE reservoir simulator. Schlumberger Ltd., Houston, TX, USA.

SMITH, D. A. (1966). "Theoretical considerations of sealing and non-sealing faults". In: *AAPG Bulletin* 50.2, pp. 363–374. DOI: 10.1306/5D25B48F-16C1-11D7-8645000102C1865D.

SMITS, K. M., T. SAKAKI, A. LIMSUWAT, and T. H. ILLANGASEKARE (2010). "Thermal conductivity of sands under varying moisture and porosity in drainage–wetting cycles". In: *Vadose Zone Journal* 9.1, pp. 172–180. DOI: 10.2136/vzj2009.0095.

SNÆBJÖRNSDÓTTIR, S. Ó., B. SIGFÚSSON, C. MARIENI, D. GOLDBERG, S. R. GISLASON, and E. H. OELKERS (2020). "Carbon dioxide storage through mineral carbonation". In: *Nature Reviews Earth & Environment* 1.2, pp. 90–102. DOI: 10.1038/s43017-019-0011-8.

SNIPPE, J., N. KAMPMAN, K. BISDOM, T. TAMBACH, R. MARCH, C. MAIER, T. PHILLIPS, N. F. INSKIP, F. DOSTER, and A. BUSCH (2022). "Modelling of long-term along-fault flow of CO_2 from a natural reservoir". In: *International Journal of Greenhouse Gas Control* 118, p. 103666. DOI: 10.1016/j.ijggc.2022.103666.

SOSIO DE ROSA, S., Z. K. SHIPTON, R. J. LUNN, Y. KREMER, and T. MURRAY (2018). "Along-strike fault core thickness variations of a fault in poorly lithified sediments, Miri (Malaysia)". In: *Journal of Structural Geology* 116, pp. 189–206. DOI: 10.1016/j.jsg.2018.08.012.

SPERREVIK, S., R. B. FÆRSETH, and R. H. GABRIELSEN (2000). "Experiments on clay smear formation along faults". In: *Petroleum Geoscience* 6.2, pp. 113–123. DOI: 10.1144/petgeo.6.2.113.

SPERREVIK, S., P. A. GILLESPIE, Q. J. FISHER, T. HALVORSEN, and R. J. KNIPE (2002). "Empirical estimation of fault rock properties". In: *Norwegian Petroleum Society Special Publications*. Ed. by A. G. KOESTLER and R. HUNSDALE. Vol. 11. Elsevier, pp. 109–125. DOI: 10.1016/S0928-8937(02)80010-8.

SPITERI, E. J., R. JUANES, M. J. BLUNT, and F. M. ORR (2008). "A new model of trapping and relative permeability hysteresis for all wettability characteristics". In: *SPE Journal* 13.03, pp. 277–288. DOI: 10.2118/96448-PA.

SPITERI, E. J. and R. JUANES (2006). "Impact of relative permeability hysteresis on the numerical simulation of WAG injection". In: *Journal of Petroleum Science and Engineering* 50.2, pp. 115–139. DOI: 10.1016/j.petrol.2005.09.004.

SPYCHER, N. and K. PRUESS (2005). "CO_2-H_2O mixtures in the geological sequestration of CO_2. II. Partitioning in chloride brines at 12–100 C and up to 600 bar". In: *Geochimica et Cosmochimica Acta* 69.13, pp. 3309–3320. DOI: 10.1016/j.gca.2005.01.015.

SPYCHER, N., K. PRUESS, and J. ENNIS-KING (2003). "CO_2-H_2O mixtures in the geological sequestration of CO_2. I. Assessment and calculation of mutual solubilities from 12 to 100 C and up to 600 bar". In: *Geochimica et Cosmochimica Acta* 67.16, pp. 3015–3031. DOI: 10.1016/S0016-7037(03)00273-4.

STONE, H. L. (1970). "Probability model for estimating three-phase relative permeability". In: *Journal of Petroleum Technology* 22.02, pp. 214–218. DOI: 10.2118/2116-PA.

STORK, A. L., J. P. VERDON, and J.-M. KENDALL (2015). "The microseismic response at the In Salah Carbon Capture and Storage (CCS) site". In: *International Journal of Greenhouse Gas Control* 32, pp. 159–171. DOI: 10.1016/j.ijggc.2014.11.014.

SZULCZEWSKI, M. L., M. HESSE, and R. JUANES (2013). "Carbon dioxide dissolution in structural and stratigraphic traps". In: *Journal of Fluid Mechanics* 736, pp. 287–315. DOI: 10.1017/jfm.2013.511.

SZULCZEWSKI, M. L., C. W. MACMINN, H. J. HERZOG, and R. JUANES (2012). "Lifetime of carbon capture and storage as a climate-change mitigation technology". In: *Proceedings of the National Academy of Sciences* 109.14, pp. 5185–5189. DOI: 10.1073/pnas.1115347109.

SZULCZEWSKI, M. L., C. W. MACMINN, and R. JUANES (2014). "Theoretical analysis of how pressure buildup and CO_2 migration can both constrain storage capacity in deep saline aquifers". In: *International Journal of Greenhouse Gas Control* 23, pp. 113–118. DOI: 10.1016/j.ijggc.2014.02.006.

TANG, G.-Q. and A. FIROOZABADI (2002). "Relative permeability modification in gas/liquid systems through wettability alteration to intermediate gas wetting". In: *SPE Reservoir Evaluation & Engineering* 5.06, pp. 427–436. DOI: 10.2118/81195-PA.

THE MATHWORKS, INC. (2021). *Copulas: Generate correlated samples.* https://www.mathworks.com/help/stats/copulas-generate-correlated-samples.html. Accessed: 2021-05-26.

TIMUR, A. (1968). "An Investigation Of Permeability, Porosity, & Residual Water Saturation Relationships For Sandstone Reservoirs". In: *The Log Analyst* 9.04, pp. 8–17. URL: https://onepetro.org/petrophysics/article-pdf/2197575/spwla-1968-vixn4a2.pdf.

TREVIÑO, R. H. and T. A. MECKEL (2017). *Geological CO_2 Sequestration Atlas of Miocene Strata, Offshore Texas State Waters.* Reports of Investigations RI0283. Austin, TX: Bureau of Economic Geology, The University of Texas at Austin, p. 74. DOI: 10.23867/RI0283D.

TREVIÑO, R. H. and J.-L. T. RHATIGAN (2017). "Regional Geology of the Gulf of Mexico and the Miocene Section of the Texas Near-Offshore Waters". In: *Geological CO_2 Sequestration Atlas of Miocene Strata, Offshore Texas State Waters.* Ed. by R. H. TREVIÑO and T. A. MECKEL. Austin, TX: Bureau of Economic Geology, The University of Texas at Austin. Chap. 1, pp. 3–6. DOI: 10.23867/RI0283D.

TREVISAN, L., A. CIHAN, F. FAGERLUND, E. AGARTAN, H. MORI, J. T. BIRKHOLZER, Q. ZHOU, and T. H. ILLANGASEKARE (2014). "Investigation of mechanisms of supercritical CO_2 trapping in deep saline reservoirs using surrogate fluids at ambient laboratory conditions". In: *International Journal of Greenhouse Gas Control* 29, pp. 35–49. DOI: 10.1016/j.ijggc.2014.07.012.

TREVISAN, L., R. PINI, A. CIHAN, J. T. BIRKHOLZER, Q. ZHOU, A. GONZÁLEZ-NICOLÁS, and T. H. ILLANGASEKARE (2017). "Imaging and quantification of spreading and trapping of carbon dioxide in saline aquifers using meter-scale laboratory experiments". In: *Water Resources Research* 53.1, pp. 485–502. DOI: https://doi.org/10.1002/2016WR019749.

TVERANGER, J., A. BRAATHEN, T. SKAR, and A. SKAUGE (2005). "Centre for Integrated Petroleum Research: Research activities with emphasis on fluid flow in fault zones". In: *Norwegian Journal of Geology* 85, pp. 63–71. URL: https://njg.geologi.no/vol-81-90/details/17/363-363.

VERDON, J. P., J.-M. KENDALL, A. L. STORK, R. A. CHADWICK, D. J. WHITE, and R. C. BISSELL (2013). "Comparison of geomechanical deformation induced by megatonne-scale CO_2 storage at Sleipner, Weyburn, and In Salah". In: *Proceedings of the National Academy of Sciences* 110.30, E2762–E2771. DOI: 10.1073/pnas.1302156110.

VESOVIC, V., W. WAKEHAM, G. OLCHOWY, J. SENGERS, J. WATSON, and J. MILLAT (1990). "The transport properties of carbon dioxide". In: *Journal of Physical and Chemical Reference Data* 19.3, pp. 763–808. DOI: 10.1063/1.555875.

VILARRASA, V. and J. CARRERA (2015). "Geologic carbon storage is unlikely to trigger large earthquakes and reactivate faults through which CO_2 could leak". In: *Proceedings of the National Academy of Sciences* 112.19, pp. 5938–5943. DOI: 10.1073/pnas.1413284112.

VROLIJK, P. J., J. L. URAI, and M. KETTERMANN (2016). "Clay smear: Review of mechanisms and applications". In: *Journal of Structural Geology* 86, pp. 95–152. DOI: 10.1016/j.jsg.2015.09.006.

WALLACE, K. J., C. H. RHATIGAN, R. H. TREVIÑO, and T. A. MECKEL (2017). "Estimating CO_2 Storage Capacity in a Saline Aquifer Using 3D Flow Models, Lower Miocene, Texas Gulf of Mexico". In: *Geological CO_2 Sequestration Atlas of Miocene Strata, Offshore Texas State Waters*. Ed. by R. H. TREVIÑO and T. A. MECKEL. Austin, TX: Bureau of Economic Geology, The University of Texas at Austin. Chap. 7, pp. 57–61. DOI: 10.23867/RI0283D.

WALLACE, K. J. (2013). "Use of 3-Dimensional Dynamic Modeling of CO_2 Injection for Comparison to Regional Static Capacity Assessments of Miocene Sandstone Reservoirs in the Texas State Waters, Gulf of Mexico". MA thesis. The University of Texas at Austin. URL: https://repositories.lib.utexas.edu/handle/2152/21899.

WANG, S., M. LEE, M. K. PARK, and J.-M. KIM (2010). "Box experiments on monitoring the CO_2 migration in a homogeneous medium using electrical resistivity survey". In: *Geosciences Journal* 14, pp. 77–85. DOI: 10.1007/s12303-010-0009-1.

WANG, Y., D. FERNÀNDEZ-GARCIA, and M. W. SAALTINK (2023). "Modeling reactive multi-component multi-phase flow for Geological Carbon Sequestration (GCS) with Matlab". In: *Computers & Geosciences* 172, p. 105300. DOI: 10.1016/j.cageo.2023.105300.

WEBER, K., G. MANDL, W. PILAAR, B. LEHNER, and R. PRECIOUS (1978). "The role of faults in hydrocarbon migration and trapping in Nigerian growth fault structures". In: *10th Annual OTC, Houston, TX*. Offshore Technology Conference, pp. 2643–2653. DOI: 10.4043/3356-MS.

WEIR, G. J., S. P. WHITE, and W. M. KISSLING (1996). "Reservoir storage and containment of greenhouse gases". In: *Transport in Porous Media* 23, pp. 37–60. DOI: 10.1007/BF00145265.

WHITE, D. (2009). "Monitoring CO_2 storage during EOR at the Weyburn-Midale Field". In: *The Leading Edge* 28.7, pp. 838–842. DOI: 10.1190/1.3167786.

WOOD, B. D., C. N. DAWSON, J. E. SZECSODY, and G. P. STREILE (1994). "Modeling contaminant transport and biodegradation in a layered porous media system". In: *Water Resources Research* 30.6, pp. 1833–1845. DOI: 10.1029/94WR00434.

YAN, W., S. HUANG, and E. H. STENBY (2011). "Measurement and modeling of CO_2 solubility in NaCl brine and CO_2–saturated NaCl brine density". In: *International Journal of Greenhouse Gas Control* 5.6, pp. 1460–1477. DOI: 10.1016/j.ijggc.2011.08.004.

YANG, Y. and A. C. APLIN (2010). "A permeability–porosity relationship for mudstones". In: *Marine and Petroleum Geology* 27.8, pp. 1692–1697. DOI: 10.1016/j.marpetgeo.2009.07.001.

YANG, Z., L. TIAN, A. NIEMI, and F. FAGERLUND (2013). "Upscaling of the constitutive relationships for CO_2 migration in multimodal heterogeneous formations". In: *International Journal of Greenhouse Gas Control* 19, pp. 743–755. DOI: 10.1016/j.ijggc.2012.11.015.

YIELDING, G., P. BRETAN, and B. FREEMAN (2010). "Fault seal calibration: a brief review". In: *Geological Society, London, Special Publications* 347.1, pp. 243–255. DOI: 10.1144/SP347.14.

YIELDING, G. (2012). "Using probabilistic shale smear modelling to relate SGR predictions of column height to fault-zone heterogeneity". In: *Petroleum Geoscience* 18, pp. 33–42. DOI: 10.1144/1354-079311-013.

YIELDING, G., B. FREEMAN, and D. T. NEEDHAM (1997). "Quantitative fault seal prediction". In: *AAPG Bulletin* 81.6, pp. 897–917. DOI: 10.1306/522B498D-1727-11D7-8645000102C1865D.

ZEE, W. van der and J. L. URAI (2005). "Processes of normal fault evolution in a siliciclastic sequence: a case study from Miri, Sarawak, Malaysia". In: *Journal of Structural Geology* 27.12, pp. 2281–2300. DOI: 10.1016/j.jsg.2005.07.006.

ZHANG, Y., C. JACKSON, and S. KREVOR (2022). "An Estimate of the Amount of Geological CO_2 Storage over the Period of 1996–2020". In: *Environmental Science & Technology Letters* 9.8, pp. 693–698. DOI: 10.1021/acs.estlett.2c00296.

ZHAO, B., C. W. MACMINN, and R. JUANES (2016). "Wettability control on multiphase flow in patterned microfluidics". In: *Proceedings of the National Academy of Sciences* 113.37, pp. 10251–10256. DOI: 10.1073/pnas.1603387113.

ZHAO, B., C. W. MACMINN, B. K. PRIMKULOV, Y. CHEN, A. J. VALOCCHI, J. ZHAO, Q. KANG, K. BRUNING, J. E. MCCLURE, C. T. MILLER, et al. (2019). "Comprehensive comparison of pore-scale models for multiphase flow in porous media". In: *Proceedings of the National Academy of Sciences* 116.28, pp. 13799–13806. DOI: 10.1073/pnas.1901619116.

ZHENG, X. and D. N. ESPINOZA (2021). "Measurement of unloading pore volume compressibility of Frio sand under uniaxial strain stress path and implications on reservoir pressure management". In: *Rock Mechanics and Rock Engineering* 54, pp. 5745–5760. DOI: 0.1007/s00603-021-02571-3.

ZHENG, X. and D. N. ESPINOZA (2022). "Stochastic quantification of CO_2 fault sealing capacity in sand-shale sequences". In: *Marine and Petroleum Geology* 146, p. 105961. DOI: 10.1016/j.marpetgeo.2022.105961.

ZOBACK, M. and D. SMIT (2023). "Meeting the challenges of large-scale carbon storage and hydrogen production". In: *Proceedings of the National Academy of Sciences* 120.11, e2202397120. DOI: 10.1073/pnas.2202397120.

ZOBACK, M. D. and S. M. GORELICK (2012). "Earthquake triggering and large-scale geologic storage of carbon dioxide". In: *Proceedings of the National Academy of Sciences* 109.26, pp. 10164–10168. DOI: 10.1073/pnas.1202473109.

ZULQARNAIN, M., M. ZEIDOUNI, and R. G. HUGHES (2018). "Implications of fault structure heterogeneities, dissolution and capillary trapping mechanisms for CO_2 storage integrity". In: *International Journal of Greenhouse Gas Control* 76, pp. 53–61. DOI: 10.1016/j.ijggc.2018.06.013.

ZULQARNAIN, M., M. ZEIDOUNI, and R. G. HUGHES (2020). "Hydromechanical modelling to evaluate impact of fault structure on CO_2 migration in stacked storage system". In: *International Journal of Greenhouse Gas Control* 93, p. 102886. DOI: 10.1016/j.ijggc.2019.102886.